Modelling and Analysis of the Hydraulic Energy Conversion Processes for Offshore Hydro-Pneumatic Energy Storage Systems

Andrew Borg

A thesis submitted to the University of Malta

in partial fulfilment of the requirements for the degree of

Doctor of Philosophy

at the Faculty of Engineering

Department of Mechanical Engineering

January 2025

L-Università ta' Malta

University of Malta Library – Electronic Thesis & Dissertations (ETD) Repository

The copyright of this thesis/dissertation belongs to the author. The author's rights in respect of this work are as defined by the Copyright Act (Chapter 415) of the Laws of Malta or as modified by any successive legislation.

Users may access this full-text thesis/dissertation and can make use of the information contained in accordance with the Copyright Act provided that the author must be properly acknowledged. Further distribution or reproduction in any format is prohibited without the prior permission of the copyright holder.

L-Università ta' Malta

FACULTY/~~INSTITUTE/CENTRE/SCHOOL~~ Engineering

DECLARATION OF AUTHENTICITY FOR DOCTORAL STUDENTS

(a) Authenticity of Thesis/Dissertation

I hereby declare that I am the legitimate author of this Thesis/Dissertation and that it is my original work.

No portion of this work has been submitted in support of an application for another degree or qualification of this or any other university or institution of higher education.

I hold the University of Malta harmless against any third party claims with regard to copyright violation, breach of confidentiality, defamation and any other third party right infringement.

(b) Research Code of Practice and Ethics Review Procedure

I declare that I have abided by the University's Research Ethics Review Procedures. Research Ethics & Data Protection form code 9789_29092021_Andrew Borg.

☑ As a Ph.D. student, as per Regulation 66 of the Doctor of Philosophy Regulations, I accept that my thesis be made publicly available on the University of Malta Institutional Repository.

□ As a Doctor of Sacred Theology student, as per Regulation 17 (3) of the Doctor of Sacred Theology Regulations, I accept that my thesis be made publicly available on the University of Malta Institutional Repository.

□ As a Doctor of Music student, as per Regulation 26 (2) of the Doctor of Music Regulations, I accept that my dissertation be made publicly available on the University of Malta Institutional Repository.

□ As a Professional Doctorate student, as per Regulation 55 of the Professional Doctorate Regulations, I accept that my dissertation be made publicly available on the University of Malta Institutional Repository.

COPYRIGHT NOTICE

1. Copyright in text of this dissertation rests with the Author. Copies (by any process) either in full, or of extracts may be made only in accordance with the regulations held by the Library of the University of Malta. Details may be obtained from the Librarian. This page must form part of any such copies made. Further copies (by any process) made in accordance with such instructions may only be made with the permission (in writing) of the Author.

2. Ownership of the right over any original intellectual property which may be contained in, or derived from, this thesis is vested in the University of Malta and may not be made available for use by third parties without the written permission of the University, which will prescribe the terms and conditions of any such agreement.

ABSTRACT

Energy storage systems are imperative for addressing instability issues in the electricity network arising from a high penetration of intermittent sources of renewable energy, such as wind and solar power. The integration of storage will avoid the curtailment of renewable energy production and revenue loss during periods of low energy demand and grid congestion.

This thesis investigates the performance of an offshore Hydro-Pneumatic Energy Storage (HPES) system consisting of a subsea accumulator pre-charged with compressed air. Unlike conventional pumped hydro systems, HPES systems operate under a highly variable head. As a result, designing the hydraulic machinery to be able to maintain high energy conversion efficiencies over a wide pressure range is a major engineering challenge.

The present study applies numerical modelling to understand the hydraulic performance of a megawatt-scale, topside Energy Conversion Unit (ECU) of an offshore HPES system when used to smoothen the intermittent supply of energy from offshore wind and solar parks. The ECU comprises a centrifugal pump to store excess energy in the HPES system and a Pelton turbine to convert the stored energy back into electricity during periods of low renewable energy production. Three different numerical models are used to investigate the ECU performance: The first model (Alpha) is a quasi-steady state and computationally efficient model of the storage system implemented in Python™. The second model (Beta), modelled in MATLAB® Simulink® and Simscape™ is a more comprehensive model which provides more realistic operation due to the addition of transients, losses and inertias. The third model (Alpha Plus) is the Alpha model that has been upgraded to integrate Time Series Forecasting to simulate a smoothened power output from an intermittent power input.

The simulations have shown that the power absorbing capacity of the large scale centrifugal pump is highly dependent on the state of charge (pressure) of the subsea HPES accumulator. Additionally, a single centrifugal pump is limited in its ability to meet the smoothing requirements of the wind turbine when operating under the HPES system's variable head constrains. While the Pelton turbine model showed excellent operational flexibility over a wide range of pressure and power levels, maintaining a high efficiency over the same wide range with a centrifugal pump remains challenging given that the pressure and power are hydraulically coupled.

The final stage of this study involved a techno-economic feasibility assessment of a floating breakwater integrating the proposed HPES system in deep waters. The proposed hybrid breakwater is modelled to generate multiple revenue streams, including the provision of energy storage services to offshore wind and solar parks as well as sheltered waters for facilitating multi-use of space at sea. The hybridisation is aimed at reducing costs for integrating the HPES offshore. However the techno-economic assessment showed that the overall revenue generation, including that involving the use of the storage system, is insufficient to cover the high investment costs of the hybrid breakwater.

SELECTED CONTRIBUTIONS

Journal Publications

Borg, A.; Sant, T.; Buhagiar, D.; Farrugia, R.N.; Micallef, C. A Numerical Model Comparison of the Energy Conversion Process for an Offshore Hydro-Pneumatic Energy Storage System. *Appl. Sci.* **2023**, *13*, 7189. https://doi.org/10.3390/app13127189

Borg, A.; Cutajar, C.; Sant, T.; Farrugia, R.N.; Buhagiar, D. Techno-Feasibility Assessment of a Floating Breakwater Concept for Supporting Marine Renewables in Deep Waters. *Energies* **2024**, *17*, 2574. https://doi.org/10.3390/en17112574

Conference Papers

Borg A.; Sant, T.; Buhagiar, D.; Cutajar, C.; Farrugia, R.N. Numerical modelling of a hydro-pneumatic energy storage system for smoothing power fluctuations from offshore wind. In Proceedings of the Journal of Physics: Conference Series, Volume 2626, EERA DeepWind conference, Trondheim, Norway, 18 January 2023. DOI: 10.1088/1742-6596/2626/1/012014

Borg A.; Cutajar C.; Sant, T.; Farrugia, R.N.; Buhagiar, D. Statistical analysis for evaluating the energy storage requirements of offshore wind and solar plants in the Mediterranean Sea. In Proceedings of the 7th Offshore Energy & Storage Symposium (OSES 2023), St. Julians, Malta, 12 July 2023. DOI: 10.1049/icp.2023.1564

Other Contributions

Cutajar C.; Borg A.; Sant, T.; Farrugia, R.N.; Buhagiar, D. Numerical modelling of the wave attenuation of floating breakwaters in deep waters. In Proceedings of the 7th Offshore Energy & Storage Symposium (OSES 2023), St. Julians, Malta, 12 July 2023. DOI: 10.1049/icp.2023.1561

Cassar, A.; Sant, T.; Borg, A. Modelling the hydraulic performance of an array of centrifugal pumps operating under a variable pressure in a hydro-pneumatic energy storage system. In Proceedings of the 8th Offshore Energy & Storage Symposium (OSES 2024), New Bedford, Massachusetts, 10 July 2024. DOI: 10.1088/1742-6596/2929/1/012004

ACKNOWLEDGEMENTS

First and foremost, I am humbled and appreciative for my principal supervisor, Prof Ing. Tonio Sant, who has helped me throughout the entirety of my PhD journey. Tonio's dedication to his students and his proactive approach to finding a solution and contribute to scientific knowledge is second to none. He has taught me valuable lessons, both on a technical level, as well as on a personal level. I will forever be grateful to him for my early career professional development.

I would also like to my express my sincere gratitude towards my co-supervisor, Dr Ing. Daniel Buhagiar for his regular check-ins and constant suggestions on how to conduct and present my research.

A special thanks also goes to Malta's and Delft's FLASC teams, where I am privileged to now call the latter team my colleagues. Their support, willingness to collaborate and open-minded approach to listening to my research has been very inspiring.

A special thank you also goes to Mr Robert Bonello, for constantly being of support whenever a software issue arose. I appreciate all his patience and little talks about life throughout the project.

Finally, I would like to sincerely thank Eliza, my closest friends and family, especially my parents and brother, Mark Anthony, for all their support and provision of clarity in my decision-making. I appreciate their influence in my life more and more every day, from motivating me to take the leap to pursue a PhD, to supporting me in moving country to exercise the knowledge I have gained through this study in industry overseas.

FUNDING

This research is financed by The Energy and Water Agency under the Maltese National Strategy for Research and Innovation in Energy and Water, grant number EWA 63/22 (Project FORTRESS) and by the Research Excellence Fund of the University of Malta (Project FLASC-Optima).

TABLE OF CONTENTS

LIST OF FIGURES

LIST OF TABLES

LIST OF ABBREVIATIONS

AR	Auto Regressive
ADF	Augmented Dickey-Fuller
AIC	Akaike Information Criterion
ARMA	Auto Regressive Moving Average
ARIMA	Auto Regressive Integrated Moving Average
BEP	Best Efficiency Point
BESS	Battery Energy Storage System
CAES	Compressed Air Energy Storage
CAPEX	Capital Expenditure
CFD	Computational Fluid Dynamics
DECEX	Decommissioning Expenditure
ECU	Energy Conversion Unit
EnTEC	Energy Transition Expertise Centre
ESS	Energy Storage System
EWA	Energy and Water Agency
FBW	Floating Break Water
FES	Flywheel Energy Storage
FIT	Feed-in Tariff
FLASC	Floating Liquid-piston Accumulator using Seawater under Compression
FOWT	Floating Offshore Wind Turbine
HES	Hydrogen Energy Storage
HFB	Hybrid Flow Battery
HPES	Hydro-Pneumatic Energy Storage
HSF	High Speed Flywheel
IRR	Internal Rate of Return
kW	Kilowatt
LCOE	Levelized Cost of Energy
LDES	Long Duration Energy Storage
LHS	Latent Heat Storage
LSF	Low Speed Flywheel
MA	Moving Average
MW	Megawatt
$NPSH_A$	Net Positive Suction Head Available
$NPSH_R$	Net Positive Suction Head Required
NPV	Net Present Value
OPEX	Operational Expenditure
PCM	Phase Change Material
PCS	Pressure Containment System
PHES	Pumped Hydro Energy Storage

PID	Proportional Integral Derivative
PV	Photovoltaic
RE	Renewable Energy
RES	Renewable Energy Source
RFB	Redox Flow Batteries
RMSE	Root Mean Square Error
$RMSE_N$	Normalised Root Mean Square Error
SAC	Special Area of Conservation
SARIMA	Seasonal Auto Regressive Integrated Moving Average
SDES	Short Duration Energy Storage
SHS	Sensible Heat Storage
SMA	Simple Moving Average
SPA	Special Protection Area
SPP	Simple Payback Period
TES	Thermal Energy Storage
VSD	Variable Speed Drive
WT	Wind Turbine

LIST OF SYMBOLS

α	Needle Angle (°)
a	Annuity Factor
A_{nv}	Needle Valve Area (m^2)
A_p	Pipe Cross-sectional Area (m^2)
β	Jet Angle (°)
B	Bucket Width (m)
C_D	Discharge Coefficient
C_f	Air Friction Coefficient
C_H	Head Coefficient
C_n	Cash Flow (€)
C_P	Power Coefficient
C_Q	Flow Coefficient
C_v	Velocity Coefficient
$\Delta HPES$	HPES Net Power
d_j	Jet Diameter (m)
d_{nv}	Needle Valve Diameter (m)
d_{wire}	Wire Diameter (m)
D_i	Impeller Diameter (m)
D_p	Pipe Diameter (m)
D_{Pel}	Viscous Damping ($Nmsrad^{-1}$)
D_r	Runner Diameter (m)
$E_{generated}$	Annual Energy Generated (MWh)
f	Friction Factor

F	Bucket Force (N)
h	Needle Valve Position (m)
h_f	Secondary Head Losses (m)
H	Discharge Head
H_{NE}	Nozzle Entry (m)
I	Initial Investment (€)
J	Motor Inertia (kgm^2)
J_{Pel}	Wheel Inertia (kgm^2)
k	Skin Friction Coefficient
K_b	Bearing Friction Coefficient
K_s	Shape Factor
l	Mesh Size (m)
L	Pipe Length (m)
L_f	Pipe Resistance Length (m)
N_s	Specific Speed
M_b	Bearing Friction Torque (Nm)
M_B	Bucket Torque (Nm)
M_F	Frictional Moment (Nm)
M_G	Generator Torque (Nm)
η_{gen}	Generator Efficiency
η_H	Hydraulic Efficiency
η_{mech}	Mechanical Efficiency
η_{nozzle}	Nozzle Efficiency
η_{ovr}	Turbine Efficiency
$\eta_{pipeline}$	Pipeline Efficiency
η_{pump}	Hydraulic Efficiency
n	Number of Mesh Layers
N	Number of Nozzles
N_s	Specific Speed
ρ_{air}	Air Density (kgm^{-3})
ρ_{sw}	Seawater Density (kgm^{-3})
$\emptyset$	Bucket to Jet Speed Ratio
p_A	Atmospheric Pressure (bar)
p_{crack}	Crack Pressure (bar)
p_{CR}	Critical Pressure (bar)
p_G	PCS Gauge Pressure (bar)
p_{hyd}	Hydrostatic Pressure (bar)
p_{loss}	Pressure Loss (bar)
p_{max}	Pressure Limit (bar)
p_{pr}	Pre-charge Pressure (bar)
$P_{ECU,I}$	Input ECU Power
$P_{ECU,O}$	Output ECU Power

$P_{forecasted}$	One-step-ahead Intermittent Power
$P_{Friction}$	Friction Power Loss (MW)
P_{Hp}	Pump Hydraulic Power (MW)
P_{Ht}	Turbine Hydraulic Power (MW)
P_I	Input Power (MW)
P_J	Turbine Jet Power (MW)
P_N	Nozzle Power (MW)
P_O	Output Power (MW)
P_{raw}	Intermittent Power
P_{smt}	SMA Power
$P_{smt,I}$	Theoretical SMA Power
$P_{smt,O}$	Output SMA Power
$P_{S_{ref}}$	Reference Shaft Power (MW)
P_S	Shaft Power (MW)
$P_{Windage}$	Windage Power Loss (MW)
Q	Flow rate (m^3s^{-1})
r	Internal Rate of Return
r_r	Surface Roughness Height (m)
r_p	Pressure Ratio
r_v	Volume Ratio
Re	Reynolds Number
R_r	Relative Roughness
σ	Layer Spacing (m)
θ	Bucket Angle (°)
T_e	Electromagnetic Torque (NmA^{-1})
T_m	Mechanical Torque (Nm)
ϑ	Kinematic Viscosity (m^2s^{-1})
v_{bucket}	Bucket Velocity (ms^{-1})
v_{fluid}	Fluid Velocity (ms^{-1})
v_{jet}	Jet Velocity (ms^{-1})
V_F	Fluid Volume (m^3)
V_T	Total Volume (m^3)
ω	Rotational Speed (RPM)
ω_{ref}	Reference Rotational Speed (RPM)
ω_{Pelton}	Turbine Rotational Speed ($rads^{-1}$)
Z	Number of Buckets

1 INTRODUCTION

The transition of the global energy supply system from one that relies heavily on fossil fuels, which unequivocally are causing climate change, to an environmentally sustainable system that exploits the vast clean and renewable sources of energy available in nature has now become one of the most important challenges faced by mankind in the history of civilisation. For such a transition to be successful, it is essential to integrate energy storage technologies that are able to convert the intermittent supply of renewable energy, such as wind and solar power, into a stable and schedulable supply of electricity.

This dissertation deals with the numerical performance modelling of an offshore Hydro-Pneumatic Energy Storage (HPES) system. The modelling couples models for mechanical hardware, including hydraulic machinery, piping systems and the compressed gas storage accumulator, with control schemes to simulate the time series operation of the HPES system when the latter is used to smoothen the intermittent supply of energy originating from offshore wind and solar parks. The power smoothing will ultimately reduce the need for conventional spinning reserves, which often consists of fossil-fuel powered gas turbine plants. This chapter covers the main topics relevant to the study and presents the main research questions and objectives. The organisation of this dissertation is also described briefly.

1.1 The Need for Energy Storage

Climate change and current international events are the main motivations for the recent renewed international efforts to exploit renewable energy sources (RES) on a wider scale. In fact, the collective European Union Renewables Directive target of a 40% share of renewables by 2030 is expected to be revised and raised to 45%, including a combination of both onshore and offshore-based renewable energy systems [1]. According to DNV's Energy Transition Outlook [1], offshore wind alone is expected to make up approximately 11.4% of the world's electricity generation if net zero greenhouse gas emissions are to be achieved by 2050. This value implies an average annual growth in offshore wind of approximately 13% up to the mid-21st century, without considering other renewable energy sources (RES), such as offshore solar photovoltaics (PVs) [1].

An increase in RES installations directly implies increases in energy curtailment, given that the supply of intermittent wind and solar power often does not match the actual demand of energy consumers. The Energy Transition Expertise Centre (EnTEC) [2] reported that power market arbitrage became profitable in 2021 and 2022, with profitability only expected to increase with further cost reductions due to technological advancements in the energy storage sector. EnTEC highlighted that an economic key performance indicator is the cost variation based on the type of storage technology and any geological limitations which may impact the ESSs viability [2]. Energy storage is a primary solution for reducing intermittency issues associated with renewables and thus, for avoiding curtailment, as explained in Figure 1.1 [3]. Energy storage is divided into three main processes; Firstly, the ability of absorbing energy in, the ability of retaining the energy stored through a storage technology and finally being readily available to discharge the energy required. Energy storage helps to regulate the electricity supply and demand mismatch. Energy storage may be classified into two main groups: Short duration energy storage (SDES) and long duration energy storage (LDES) systems. Twitchell et al. [4] summarise the definitions of energy storage duration based on different sources, where typically SDES is known to be classified as storage of less than 4 to 8 hours and LDES is classified as storage of more than 8 or 10 hours. According to Shan et al. [5], LDES is best defined as energy storage solutions which offer intra-day energy storage applications.

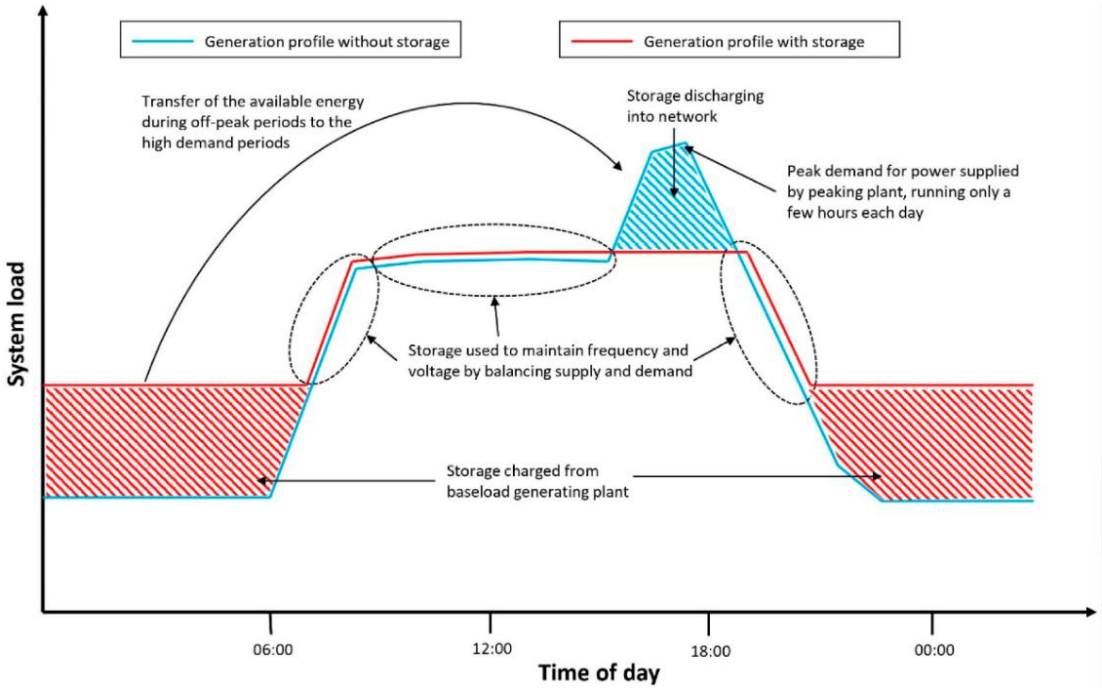

Figure 1.1: The role of energy storage for reducing intermittency issues associated with renewables [3].

While LDES typically considers storage exceeding 8 hours, longer timeframes such as seasonal storage also fall under this category. While lithium-ion batteries are expected to be the front-running SDES technology, LDES is made up of a wider range of competing technologies, with mechanical systems such as pumped-hydro and compressed air energy storage considered optimal for long discharge, and thus longer supply applications [6], [7].

Cárdenas et al. [8] presented a UK-based case study evaluating the impacts of SDES and LDES in avoiding curtailment of a renewable energy mix based on wind turbines and solar photovoltaics (PVs). Meanwhile, the European Commission stated that the only way that renewable energy (RE) generation can reach full capacity is if energy storage systems (ESSs) are applied in tandem with renewable energy sources (RESs), with an increasing relevance set on long-duration energy storage (LDES) requirements due to their potential for avoiding up to 88% of generation curtailment [5], [6]. Thus so far, LDES has been limited solely due to technological immaturity and economic feasibility. LDES has the potential to provide better grid stability and reliability compared to SDES [9]. In fact, research has shown that the LDES market is expected to continue to grow, reaching a valuation of $223 billion by 2044 [10].

1.2 Why Store Energy Offshore?

Wang et al. [11] present a classification and review of different offshore renewable sources of energy, energy storage systems and expected future trends in the renewable offshore sector, highlighting the advantages of moving offshore when compared to having the same projects onshore. With respect to environmental detriment, Slocum et al. [12] found that aquaculture damage is far less likely at deeper offshore systems as opposed to systems which are in shallower waters or along coastal areas. Additionally, offshore structures offer far more safety compared to onshore structures since structures offshore are isolated in an environment of their own. Arellano-Prieto et al. [13] assess energy storage technologies that are viable for offshore applications due to the increasing interest in the co-deployment of RES and Energy Storage Systems (ESSs). Their research explains that offshore co-location is mainly driven by environmental constraints onshore and can provide a secure and large-scale energy supply.

The research also stated that offshore energy storage solutions are advantageous since they minimise land usage, make more efficient use of space and may re-use already-deployed offshore structures instead of decommissioning them. Additionally, locating energy storage systems 'behind the meter' offshore allows RES operators to improve their business cases due to improved grid visibility, as described in [14].

In heavily populated areas such as coastal regions, the rationale for moving offshore is even greater due to overpopulation and increasing land prices [15]. Figure 1.2 shows the worldwide population dispersion, highlighting how approximately 38% of the Earth's population live within 100 kilometres from the shore [16], [17].

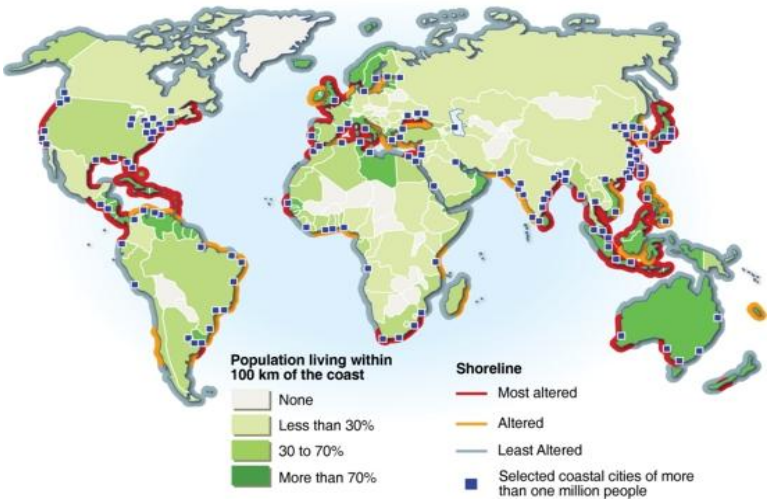

Figure 1.2: The worldwide population dispersion [12].

1.3 Problem Statement

While Section 1.2 provided reason as to why having energy storage offshore in lieu of onshore may be advantageous, marinising storage technologies imposes substantial challenges due to the rough nature of the offshore environment, logistical planning due to co-location as well as scheduling regular maintenance checks while maintaining economic competitiveness [13]. Thus, developing offshore storage technologies that rely on well-known hardware and established operating principles offers important strategic benefits for co-locating large-scale storage infrastructure with renewable energy parks offshore. As already highlighted earlier, this dissertation focuses on the performance modelling of offshore-based HPES systems.

Figure 1.3 presents the basic principle of operation of an HPES system. HPES systems are a form of energy storage technology in which energy is stored by injecting a liquid, normally water, into a container that is pre-charged with compressed air [18], [19]. Ortego et al. [20] described hydro-pneumatic energy storage to be a combination of the high-power density advantage offered by PHES and the spatial flexibility and high energy density of a CAES system.

In fact, HPES systems are essentially a variation of CAES: hydro-pneumatic energy storage systems use hydraulics to compress the air, hence attaining higher efficiencies compared to conventional, solid piston CAES systems [20], [21]. The use of a liquid piston in HPES as opposed to a solid piston in CAES has a number of advantages as follows [22]:

1. Firstly, gas leakage is eliminated, and viscous fluid forces replace the sliding friction generated in the solid piston setup; and
2. A hydraulic pump-turbine also yields higher power densities, thus using a smaller turbomachine for the same power output while simultaneously increasing response speed.

In comparison to other well-known energy storage technologies such as Pumped-Hydro Energy Storage (PHES), further described in Sub-section 2.1.2, HPES has a highly variable head which is constantly varying as the system charges and discharges. As a result, designing the hydraulic machinery to be operable across a wide pressure range is an engineering challenge, which is one of the problems tackled in this study. Additionally, due to the intermittent nature of the RES (explained in Section 1.1), which are to operate in tandem with each other and in co-location with the ESS, reliable forecasting of expected power production is highly useful to reap maximum benefits of the installed ESS.

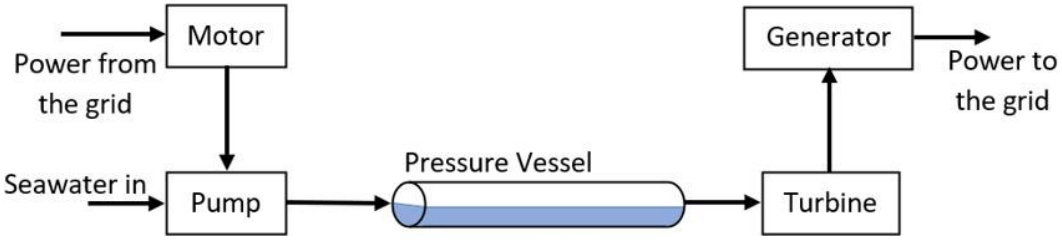

Figure 1.3: The principle of operation of a HPES system.

Due to the working principle of HPES systems, integration of HPES offshore can be done in a variety of ways, being placed topside on floating structures or subsea, on the seabed. Gao et al. [23] performed a techno-economic assessment of offshore hybrid wind-wave farms with integrated energy ESSs. The study found that reducing ESS requirements by generating energy from hybrid, offshore wind-wave farms instead of solely an offshore wind farm leads to more competitive lifecycle costs. The study also highlights that overall costs are heavily dependent on the local renewable energy resources (RESs).

Similarly, Rönkkö et al. [24] performed a case study comparing three hybrid, offshore wind-wave systems, highlighting the importance of a shared infrastructure to reap the most benefit. A relatable idea is that of integrating the ESS with floating breakwaters. The hybridization would enable cost reductions by being able to have the breakwaters serving two purposes:

1. The provision of shelter to offshore renewables, such as floating solar, and other infrastructure, such as aquaculture cages; and
2. The provision of storage [23], [24].

1.4 Research Objectives

The overall aim of the subject research is to investigate the behaviour of a megawatt-scale Energy Conversion Unit (ECU) of an offshore Hydro-Pneumatic Energy Storage (HPES) system when smoothing the intermittent power output from offshore-based wind and solar power plants through various numerical simulations. The research also aims to understand how system relationships and control can be affected and improved by performing a series of parametric analyses to identify what parameters affect how an ECU performs and how such effects could be exploited or reduced, depending on their assets or liabilities.

Additionally, the research aims to explore the feasibility of integrating the proposed offshore energy storage system in a floating breakwater deployed in multi-use deep water parks in order to challenge the motive of co-locating and utilising the same offshore space for multiple applications.

Specific objectives include:

O1. to familiarise with the theoretical performance modelling of pumps for high pressure performance, Pelton turbines, energy storage, HPES systems, power regulation and artificial intelligence techniques to model the steady and unsteady performance of ECUs from intermittency into a schedulable supply (smoothened).

O2. to develop numerical models in Python™, MATLAB® Simulink® and Simscape™ to simulate the time series operation of centrifugal pump and Pelton turbine of a MW-scale ECU operating under different conditions .

O3. to integrate time-forecasting techniques in the numerical models to simulate the unsteady operation of the ECU when smoothing the intermittent renewable power from offshore wind and solar parks.

O4. to carry out a case study exploring the feasibility of hybrid floating breakwaters integrating the proposed HPES system and deployed in Maltese waters to support multi-use of marine space.

The research questions which arise are:

Q1. What parameters will limit the pump and turbine speed variability during the charging and discharging processes, respectively?

Q2. What is the pump and turbine efficiency when operating with a variable speed and time-varying accumulator head while converting intermittent power into a smoothened output?

Q3. How can Time-series Forecasting be used for improving the time response of the ECU in smoothing the intermittent supply of power from RES?

Q4. To what extent are transient effects, such as those arising from the inertia of hydraulic machines and hydraulic lines, important in modelling the unsteady operation of the ECU?

Q5. What is the economic viability of HPES systems when integrated in floating breakwaters located in deep water multi-use offshore parks?

The presented research tests the following hypothesis:

'The energy conversion unit consisting of a pump and a turbine, coupled hydraulically to an accumulator in a hydro-pneumatic energy storage system, is an energy efficient and viable system for converting intermittent power into a schedulable form in an offshore environment'.

1.5 Organisation of Work

This research work presented in this dissertation is mainly organized in three parts: **Part 1** presents a detailed literature review in various areas relevant to the undertaken research work. **Part 2** outlines the methodology followed and the numerical model development of the megawatt-scale Energy Conversion Unit (ECU) of an offshore Hydro-Pneumatic Energy Storage (HPES) system. **Part 3** presents the Case Study exploring different scenarios involving the integration of an offshore HPES system in a floating breakwater in a Central Mediterranean context.

Part 1 is split up into two chapters. Chapter 2 is a comprehensive literature review on a variety of hydraulic machinery, energy storage systems as well as forecasting techniques. Chapter 3 discusses the theoretical background required for the development and implementation of the numerical models. Part 1 is aimed at achieving objective O1.

Part 2 tackles the methodology adopted and the justification of the different numerical models developed through Chapter 4. Chapter 5 involves the description and verification of the first two numerical models, the Alpha and Beta models respectively. The Alpha model is also validated against the Beta model. Chapter 6 looks into the development of the third numerical model, the Alpha Plus model, which introduces time-series forecasting and is a continuation of the first numerical model (the Alpha model). Finally, Chapter 6 also presents numerous time-series simulations using the Alpha and Alpha Plus models. Part 2 tackles objectives O2 and O3 and research questions Q1, Q2, Q3 and Q4.

Part 3 consists of Chapters 7 and 8. Chapter 7 analyses the energy storage requirements of offshore wind and solar plants based on implementing different power moving averages. Chapter 8 performs a techno-economic feasibility study by integrating the megawatt-scale ECU and HPES system in a novel breakwater design. Part 3 tackles objective O4 and research question Q5.

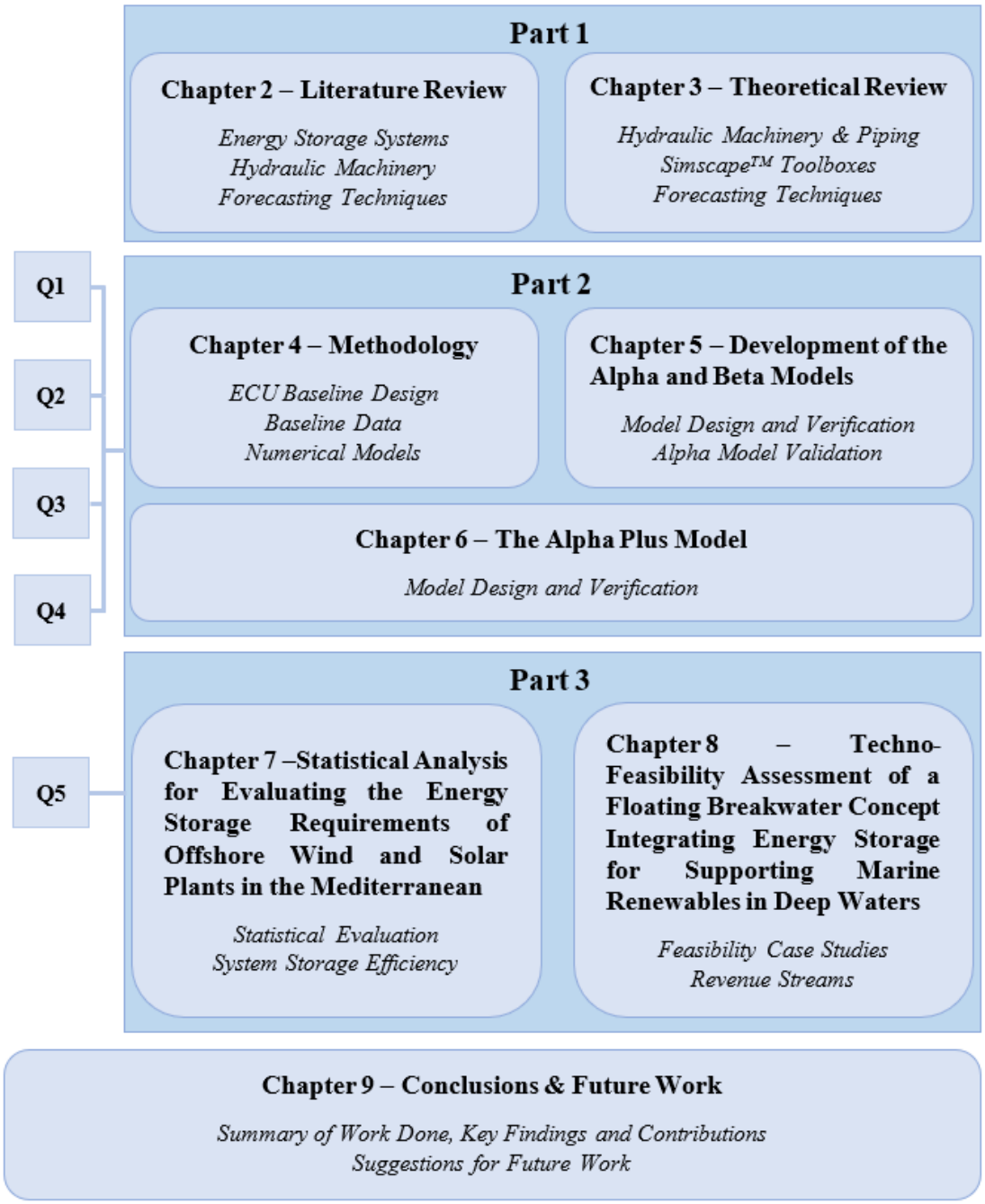

Figure 1.4: A breakdown of each chapter making up the thesis, with Q1 to Q5 representing where each research question is tackled.

2 LITERATURE REVIEW

The literature review section covers extensive research on the main areas that are relevant to this project. Detailed research on the qualitative information about the different types of energy storage systems, hydraulic pumps and turbines and time series forecasting are all critically analysed. Critical knowledge gaps in open literature are identified and discussed.

2.1 Energy Storage Systems

As previously mentioned in Section 1.1, energy storage is required to regulate the electricity supply and demand mismatch, in order to avoid curtailment of renewable sources of energy. Energy storage technologies are classified into different categories, depending on the mechanism used to store the energy. These include electrochemical, mechanical, thermodynamics and chemical storage [25], [26], [27]. Figure 2.1 presents a basic diagram of the main technologies in their respective sub-divisions [28], [29].

2.1.1 Electrochemical Energy Storage (EES)

According to Oliveira et al. [30], electrochemical technologies are best suited for micro-grids. When considering rechargeable EES solutions such as batteries, the positive and negative electrodes are referred to as the positrode and negatrode respectively, as opposed to the typical referral to a cathode and anode. Xia et al. [31] explain that the reasoning is due to the specification as to whether an EES device is re-chargeable or not.

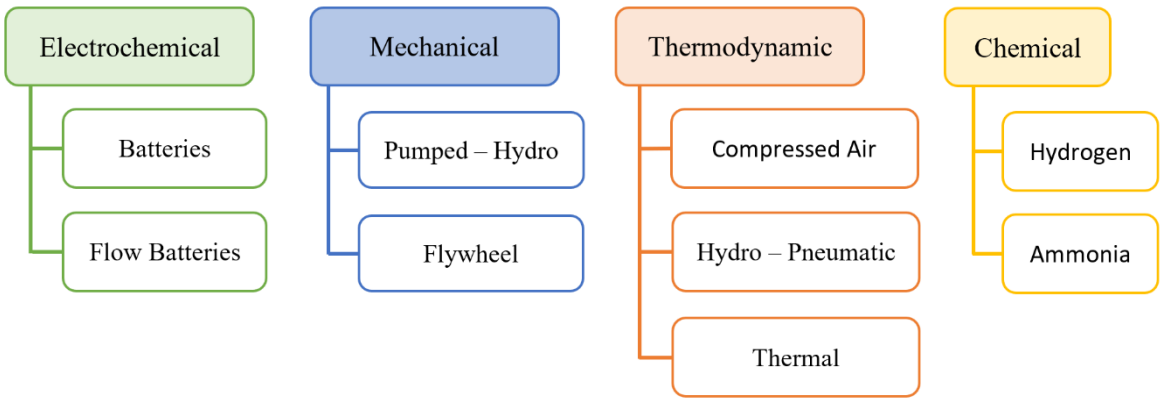

Figure 2.1: A breakdown of the main energy storage technologies.

When re-chargeable, the use of the terms anode and cathode is incorrect since a positrode always maintains positive polarity, despite being a cathode during discharging and an anode during charging. The advantages of EES systems are their modularity, providing customer requirement flexibility, high efficiency, fast start and response time and high-power achievability. Additionally, EES is a well-developed storage system, which makes it more widely accepted due to market familiarity. However, several up-and-coming sub-types are also being created. EES systems face several challenges, where their investment costs can be high. Furthermore, their environmental impact prior and post-use is problematic due to the specific chemicals used in the system [28].

There are risks related to electrochemical energy storage in the form of batteries. Firstly, electrical isolation is a definitive requirement to avoid shock hazards at operating voltages of 230 Volt. Secondly, due to the energies being in the kilowatt (kW) and megawatt (MW) scale, an electrical explosion, known as an arc flash, is possible. An arc flash may lead to the battery reaching temperatures of 12,000˚C or more. By nature, a battery is typically made up of numerous chemicals, some of which may be combustible liquids or gases. Problems such as electrolyte leakage or accidental mixing between the liquids separated by the membrane can occur. Adding on, moving such a storage system offshore undoubtedly increases risks. Jeevarajan et al. [32] reported that battery energy storage system catastrophic failures typically occurred as a result of pre-mature product degradation due to temperature changes, dirt and moisture present in the operating environment of the batteries. Lithium batteries are the most commonly used electrochemical battery type within industry. Due to their maturity, improvements in energy density and battery lifespan have been consistent over the past few years. Lithium batteries exist as many different models, however developed models can commonly be generalised as having good power and energy densities together with high efficiencies. Disadvantages of such systems are the high costs due to various raw materials (such as Cobalt), a short lifetime and post-lifecycle recycling [30].

Flow batteries convert chemical energy into electrical energy through an oxidation-reduction reaction between two different liquids, leading to the flow of ions through a membrane. Flow batteries have increased in popularity due to their long life-cycle compared to lithium batteries, competitive maintenance and operational costs and their high reliability. Flow batteries suffer from lower power and energy densities, thus being at a disadvantage in terms of financial competitiveness and spatial requirements, since flow battery capacity is directly proportional to storage tank size [28], [30], [33].

Flow batteries are divided into two different types: Redox Flow Batteries (RFB) and Hybrid Flow Batteries (HFB). HFBs consist of a cell with active matter and an external tank where the liquid electrolyte is stored. HFB types include zinc-bromine and zinc- cerium. HFB systems are best suited for short and medium duration energy storage (2 to 10 hours) and achieve efficiencies greater than 70% [34]. Meanwhile, RFBs differ from HFBs since their electrolytes are both liquids. RFBs consist of liquid electrolytes which are physically separated by a membrane. The purpose of the membrane is that ions can flow without causing the separate electrolytes to mix. RFBs have been able to tap into the energy storage market, being advantageous in rapid discharge situations (for example in the case of an emergency). Furthermore, RFBs are highly durable (lifetime in excess of 20 years) and reliable, making them a potential up and coming offshore energy storage option [30], [35].

2.1.2 Pumped-Hydro Energy Storage (PHES)

Pumped-hydro energy storage involves having at least two reservoirs which are located at a different altitude. PHES exists in two forms: the river-based system and the off-river PHES system. In both system types, the lower reservoir is the larger of the two and is usually setup near a water source, for example by a riverside or at the seaside. As shown in Figure 2.2, water is pumped from the lower to the upper reservoir when excess energy is available, but energy demand is low. Water is fed from the upper to the lower reservoir for generation when energy demand is high [36]. Rehman et al. [37] described the PHES system as the most cost-effective energy storage method available, however applying such a system is contingent on geographical location, spatial requirements due to PHES low energy density and capital costs.

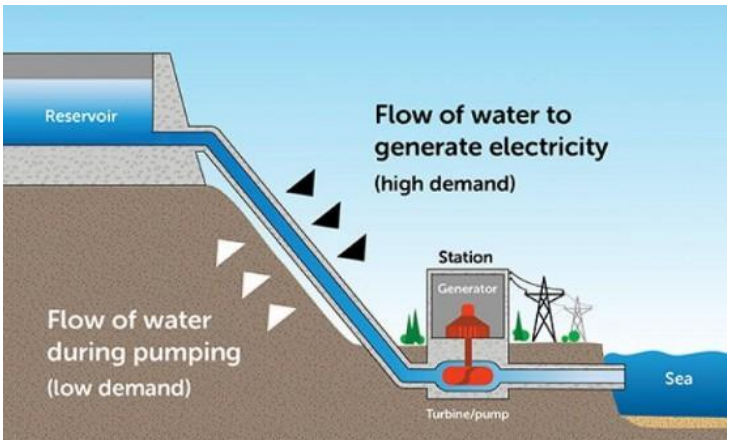

Figure 2.2: A schematic diagram of a PHES system [47].

While PHES has its disadvantages, it is one of the most established storage types used due to its high round trip efficiency, reaching 75 to 80%. Furthermore, PHES can reach MW scale power ratings and has a long lifecycle, reaching up to 40 years of operation with regular maintenance [30].

2.1.3 Flywheels

Flywheel energy storage (FES) is a short duration energy storage system. The working principle of flywheels involves three main operational modes: the charging, discharging and standby states. During charging, excess energy is used to drive the flywheel, thus increasing its speed and storing the energy as rotational kinetic energy. During discharging, the flywheel is allowed to rotate while losing speed, until all rotational kinetic energy is consumed. The standby mode simply involves the flywheel maintaining its stored energy while not receiving or producing energy from or to the grid [30], [38]. Flywheel energy storage for large-scale renewable energy sources exists in two main variations, characterised mainly by their operating speed. Low-speed flywheels (LSF) are most useful for a low-cost solution, however at the expense of higher spatial requirements. As mentioned previously, flywheels are usually used for short duration storage. However, high-speed flywheels (HSF) are a flywheel type which can store energy for up to 24 hours, while having smaller spatial requirements compared to LSF [39], [40]. Figure 2.3 shows the main components of a FES system [41]. Flywheel energy storage competes with the battery energy storage market but is also suited to be used in conjunction with batteries [39]. They are an advantageous system type since they offer high round-trip efficiencies (reaching 95%), are environmentally friendly and can charge and discharge at high rates [30].

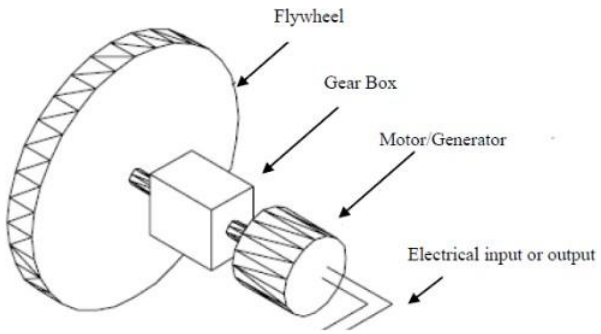

Figure 2.3: A schematic of a FES system [41].

Zakeri et al. [42] reported that flywheel lifecycle costs are lower in comparison to batteries. This may be due to negligible maintenance costs despite the initial high capital investment needed [40]. The high capital investment mentioned is needed due to the specific materials necessary to last for approximately 20 years and to handle the required high speeds. Similar to batteries, a disadvantage of flywheel energy storage for large-scale applications are the safety hazards related to their operation [30].

2.1.4 Compressed Air Energy Storage (CAES)

Compressed air energy storage is a type of mechanical energy storage which operates by utilising excess power to compress air within an air-tight reservoir. Energy storage capacity within CAES systems is dependent on the air pressure ratio attainable, the storage volume available and the compressed air temperature when stored [43], [44]. Figure 2.4 shows the working principle of a typical CAES system. CAES works by using excess energy and operating a motor, which in turn drives a compressor. As a result, during a charging cycle of the system, the compressor increases the pressure of the air within the reservoir. When discharging, the compressed air is released to drive an expander, which operates a generator, thus feeding energy to the grid when required. The recuperator is utilised to improve the overall efficiency of the system by reducing fuel consumption. The recuperator extracts waste heat from the low-pressure turbine to pre-heat the air from the cavern [30], [45], [46].

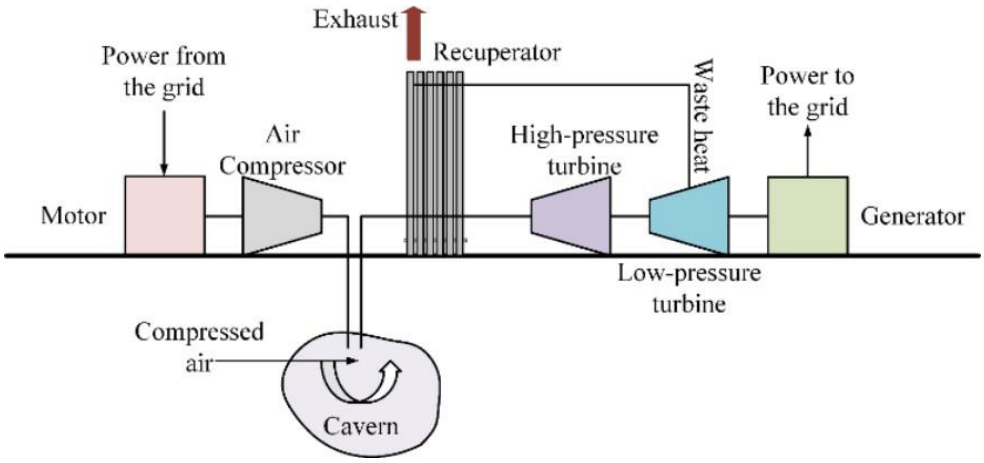

Figure 2.4: A schematic diagram of a CAES system [46].

CAES systems are most utilised for large-scale energy storage and are capable of LDES. Dooner et al. [45] explained that another advantage of CAES is that their life cycle is typically expected to reach approximately 40 years, making the technology a long-term investment due to its low cost per unit power, despite a high initial investment.

Oliveira et al. [30] reported that one of the main challenges with CAES is the geographical restrictions associated with the technology. CAES is only possible by making use of natural, underground reservoirs and due to their low energy density, large spaces are a necessity. Hossain et al. [47] describe the different types of CAES systems. While minimal losses occur during storage, CAES round-trip efficiency varies between 40 to 75%. The traditional CAES system involves heat losses to atmosphere and the use of fossil fuel combustion to generate the required heat during expansion. Meanwhile, an adiabatic thermodynamic process is the most efficient CAES system type to be implemented in terms of efficiency (reaching figures of > 70%) and environmental friendliness [48]. However, the advantages come at the expense of a more complex system which integrates thermal energy storage to minimise the heat release to atmosphere, thus also increasing costs [30]. CAES has different applications in the grid service industry which are based on the system's size. Small CAES systems in the low megawatt scale are suitable for power regulation due to their quick response. Meanwhile, large-scale CAES is best suited for energy management due to prolonged discharge times [45].

2.1.5 Hydro-Pneumatic Energy Storage (HPES)

A schematic of the HPES system's working principle has already been previously shown and described in Figure 1.3 in Section 1.3. Such systems also achieve high thermal efficiencies, where the round trip (overall) efficiency is pre-dominantly based on the system thermodynamics [18]. As explained in Section 1.3, liquid piston-type accumulators are preferred when it comes to large-scale projects due to their compact sizing and flow capacity handling. The liquid piston cools the air undergoing compression while it heats it up during expansion. The liquid inside the pressure containment system enables the air compression and expansion processes to approach isothermal conditions, as long as the charging and discharging rates are not too high [18].

HPES is highly adaptable for offshore deployment. Hazim et al. [49] proposed an innovative re-purposing solution which utilises offshore pipelines as energy storage based on a hydro-pneumatic energy storage (HPES) system. Their research found a compromise between providing a feasible energy storage solution while also saving time and decommissioning costs by applying existing infrastructure. Additionally, deploying the pressure containment subsea allows the system to exploit the excellent heat sink characteristics of open sea water, thus allowing the HPES to achieve higher isothermal conditions. This eliminates the need for thermal energy storage normally integrated in AA-CAES systems, thus further simplifying marinisation of the technology [50]. Furthermore, HPES for offshore applications allows spatial requirements to be less restricted compared to an onshore plant, thus allowing for even more system flexibility due to more public acceptance. HPES systems offer an improvement over CAES systems since they obtain higher efficiencies via hydraulic use. In fact, adiabatic CAES systems usually obtain efficiencies of 70 to 75% while HPES systems can reach efficiencies of 80% [43], [46], [51]. Another advantage of HPES systems is their lifetime, where they can last for a minimum of 20 years, comparing well with electro-chemical storage [52], [53]. The main variation to be made with respect to HPES as an offshore application is in the type of steel to be used. According to DNV-GL standards [54], duplex stainless steel is a requirement for offshore applications, as opposed to stainless steel grades 304 and 316.

Finally, hydro-pneumatic storage also has an advantage on its energy density capacity, edging both PHES and CAES substantially, while also not being geographically- dependent like CAES [52]. Additionally, it is also cost-competitive compared to the aforementioned energy storage technologies. In terms of offshore use applicability, the advantages of HPES over other storage technologies such as batteries include [55]:

1. High reliability by using well-proven components.
2. Long lifetime (> 25 years).
3. High safety levels (no fire risk).
4. No use of rare/hazardous materials.

The Floating Liquid-piston Accumulator using Seawater under Compression (FLASC) Technology

FLASC (Floating Liquid-piston Accumulator using Seawater under Compression) is a novel, offshore-based hydro-pneumatic accumulator energy storage system. FLASC is based on the non-linear relationship between pressure and gas volumes [51]. FLASC consists of one or more connected pressure vessels. The differences between FLASC and conventional HPES systems is that FLASC is not geographically constrained by a large water body at high head. In the case of FLASC, pressure head is obtained by pre-charging the pressure vessel prior to deployment [51]. The FLASC Energy Conversion Unit (ECU) consists of a pump, turbine or a combined pump-turbine system. In the case of a combined pump-turbine system, operation in pump or turbine mode depends on whether the system is charging or discharging respectively. Due to the compression and expansion processes involved, temperature must be managed appropriately. As shown in the graph in Figure 2.5, the compression ratio of FLASC is relatively low, thus allowing the concept to achieve high thermal efficiency (> 96%) [51], [56].

Adding on, since the pressure ratio is so small, heat generation during compression is low, thus minimising thermal energy losses. Due to the thermodynamic process being carried out below the sea surface, the sea acts as an excellent heat sink and source during compression and expansion respectively. The liquid piston itself facilitates heat transfer, hence enabling the thermodynamic process to approximate to an isothermal one. Moreover, the system is not sensitive to sea depths, thus being useful at depths of 20 to 30 metres, or deeper depths, such as at a depth of 300 metre [57].

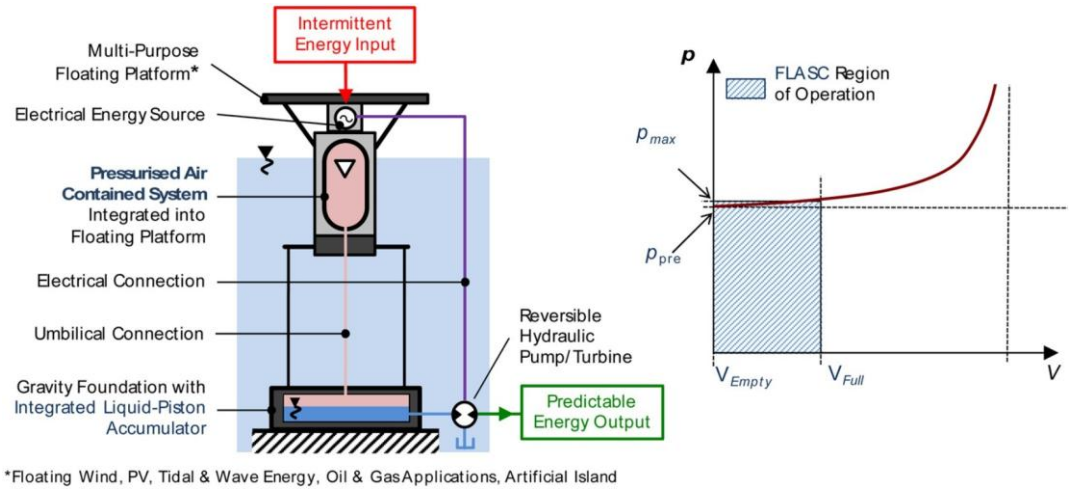

Figure 2.5: The working principle of FLASC, including labelling of its fundamental components [45].

2.1.6 Thermal Energy Storage (TES)

According to Sarbu et al. [58], although thermal energy storage is already popular within building and industrial processes to provide heat originating from conventional sources of energy, TES is also nowadays being used in various applications exploiting renewable energy sources. TES is typically employed in order to improve system efficiency by re-purposing energy which would otherwise be lost [25]. TES is classified into three main types, differentiated by storage duration, cost and their rates of charging and discharging. The three types are thermochemical heat storage, sensible heat storage (SHS) and latent heat storage (LHS) [25].

SHS involves the heating or cooling of the specific storage material, which is usually a solid or a liquid for the said type of storage. SHS is suitable for offshore-based storage since one of the storage media used is typically water, due to its high specific heat capacity. As a result, SHS is a heat storage system which is known for being cheap and safe since hazardous materials are not utilised [25]. LHS systems make use of phase change materials (PCMs) since PCMs have the ability to absorb and release energy through a physical state change. The procedure is known as phase transition enthalpy, as described by Jain et al. [59]. Charging occurs when the PCM melts, thus changing from a solid state to a liquid and increasing vibrational energy at a molecular level. During discharging, the opposite process occurs, thus releasing the stored energy when reaching its solid state. LHS is useful in the RES industry since it can be used in conjunction with photovoltaic (PV) systems to reduce their panel operating temperature, thus enhancing the PV system's performance. Furthermore, using long term storage helps to reduce curtailment of solar power during the summer peaks [60]. Dincer [60] explains that there is a trade-off between storage size and heat losses, whereby with greater storage sizes, the lower are the losses.

Thermochemical heat storage makes use of a thermochemical material to store energy. During charging, an endothermic chemical reaction occurs, thus supplying thermal energy to the thermochemical material. The involved material splits into multiple compounds. Due to the storage occurring at ambient temperatures, heat losses are negligible in comparison to other storage methods.

Energy discharge involves an exothermic chemical reaction, where the separated compounds rejoin, releasing heat in the process [25], [59].

Sensible heat energy storage is deemed to be the most economical TES type due to its simplicity and due to being the most established TES type. Compared to LHS and thermochemical heat storage, SHS has the lowest energy density, thus not being suitable for large scale projects. However, the cost of setting up such systems (i.e., SHS) is much higher, reaching 56 $/kWh and 111 $/kWh respectively due to increased storage system complexity [59].

2.1.7 Hydrogen Energy Storage (HES)

Hydrogen Energy Storage (HES) is a form of chemical energy storage with great potential due to it being a low-carbon energy source and because of its versatility. Hydrogen is produced from water, where the gas obtained can be utilised directly in industrial plants. HES is nowadays being explored in tandem with RES plants, where any excess or off-peak power can be used to produce and store hydrogen. Figure 2.6 shows a schematic of a HES system together with a variety of RES [61].

Ekpotu et al. [62] described the different states of hydrogen storage; namely as a gas or a liquid. The main advantage of storage in its gaseous state is that it is highly economically feasible, with compressible pressures reaching 700 bar according to Breeze [61] and Ali et al. [63]. HES in liquid form was studied, with results by Faye et al. [64] showing that energy density is improved in this way.

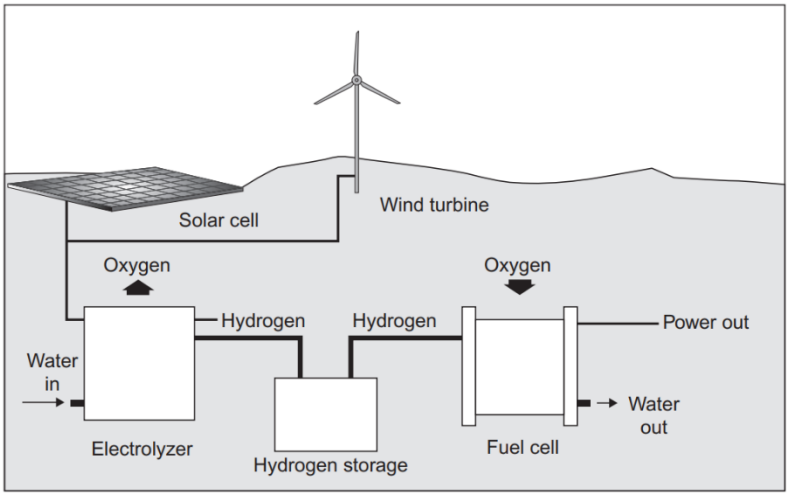

Figure 2.6: A basic schematic of a HES system [61].

However, liquid storage is more complex and requires additional processes such as refrigeration to reduce energy loss during liquefaction. When HES is primarily purposed for power generation, its storage occurs through compression in order to obtain high-volume energy density. Storage size is limited to the pressure vessel size utilised. HES can also be performed by taking advantage of geographical location through the use of underground caverns, similar to CAES [61]. Ali et al. [63] explain how gaseous HES can store energy for long durations and has a very low rate of performance degradation. The expected round trip efficiency from HES plants is usually approximately 54%, however fuel cell systems can reach higher efficiencies of 70 to 75%. The former low efficiency is satisfactory in relation to RES storage since otherwise the power would be completely lost if not harvested [61].

2.2 Co-Location of Offshore Energy Storage

Wang et al. [11] present a classification and review of different offshore renewable sources of energy, energy storage systems and expected future trends in the renewable offshore sector, highlighting the advantages of moving offshore when compared to having the same projects onshore. Arellano-Prieto et al. [65] assess energy storage technologies viable for offshore applications due to the increasing interest in the co-deployment of RES and Energy Storage Systems (ESSs). Their research explains that offshore co-location is mainly driven by environmental constraints onshore. In heavily populated areas such as coastal regions, the rationale for moving offshore is even greater due to overpopulation and increasing land prices [15]. An increase in the installation and use of offshore renewables directly implies an increase in energy intermittency, thereby requiring ESSs to resolve this limitation and stabilise the renewable energy (RE) output [66].

LDES approximately considers storage exceeding 8 hours, but also includes longer timeframes such as seasonal storage. While lithium-ion batteries are expected to be the front running SDES technology, LDES is made up of a wider range of competing technologies, with pumped-hydro and compressed air energy storage considered optimal for long discharge, and thus longer supply applications [6], [7]. Depending on the system design, different LDES technologies may be re-purposed to offset costs from replacing ageing systems and infrastructure [5], [67], [68].

A case study by Child et al. [69] concluded that a combination of flexible generation and ESSs at an hourly rate can provide a more secure provision of renewable energy year wide. The study also suggests that a fully renewable system across Europe by 2050 is achievable if policy is set based on a regional case-by-case basis, while still reaching European Energy Union requirements. Cárdenas et al. [8] presented a UK-based case study to assess and indicate that both SDES and LDES have significant effects in avoiding curtailment of a renewable energy mix based on wind and solar photovoltaics (PVs). A detail of importance reported is that when renewables' penetration reaches 100%, the storage capacity requirements increase considerably in comparison to penetrations of approximately 80%. The case study also showed that the energy storage period of 4 to 200 hours would be the most important storage duration to handle daily renewable generation variability, with SDES being required for the sole use of high frequency imbalance smoothing.

Nayak et al. [70] and Marcos et al. [71] applied a Simple Moving Average (SMA) to smoothen PV power output, thus optimising the battery energy storage system sizing used to avoid RE curtailment. The results of the latter research indicated that the strategies of applying a SMA and a power ramp rate control improved battery life due to reduced system cycling. Lastly, Torres et al. [72] apply a SMA and a prediction model to predict a SMA to smoothen power fluctuations by means of a flywheel energy storage system. Results showed that power fluctuations were minimised by 50% with the inclusion of a SMA and energy storage.

2.3 Hydraulic Pumps

The following section presents an overview of the three main types of hydraulic pumping machinery, highlighting their working principles, advantages and disadvantages while also providing a technological update of the current state-of-the-art in industry.

2.3.1 Centrifugal Pumps

A centrifugal pump is characterised by the diameter of the impeller. The impeller consists of vanes fitted inside shroud plates. The impeller is always immersed in water and when it rotates, the fluid surrounding it also rotates. The centrifugal force is thus imparted to the water particles, and the water flows radially outwards.

Since rotational energy is transferred to the fluid, both pressure and kinetic energy rise at discharge sides of the impeller. At suction (the inlet), water is displaced so negative pressure ($p < p_{atm}$) is induced at the inlet. Such low pressure allows suction of water into the system.

Operating pressures are often expressed in terms of head since it is more practical to quantify how high a pump can raise fluid in metres [73], [74]. Priming is important since when there is no pressure initially, the negative pressure developed by rotating air at the impeller inlet will be negligibly small to create a water suction. The casing area increases along the flow direction (shown in Figure 2.7), and this is important for two reasons [75], [76]:

1. The volute casing may accommodate newly added water; and
2. A greater area results in reduced exit flow velocity. Reduced velocity at the outlet induces an increase in static pressure. This is necessary to overcome resistance of the fluid flow path.

The rotating impeller is mounted on a cantilever shaft. Centrifugal pumps can have different impeller types; Open, semi-open or closed. While open impellers are used in small, low cost pumps or pumps requiring fluid suction which consists of solids and contaminants, semi-open pumps are used in medium-sized pumps which only take in fluids with limited amounts of suspended solids. Semi-open impellers obtain higher efficiencies compared to open impellers. Furthermore, open impellers lose efficiency over time due to slippage losses as the pump wears. Finally, closed impellers are the most common pump impeller design used.

They are best applied to large pumps and attain the best efficiencies of all impeller types. With respect to closed impellers, a compromise must be found since the more suspended solids flow through the pump, the higher is the wear rate of the impeller.

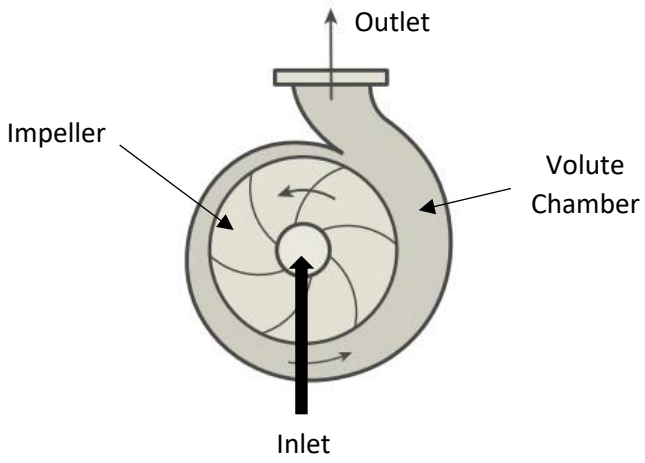

Figure 2.7: A centrifugal pump schematic diagram [78].

However, an open impeller becomes the preferred option the cloggier the working fluid is, albeit at the expense of efficiency. Impellers are typically manufactured using bronze due to the more favourable properties related to casting, machining and corrosion resistance. Use of bronze is only limited by temperature and pump speed [73].

The net positive suction head available ($NPSH_A$) is the head available at the pump's suction flange. $NPSH_A$ is defined as the pressure difference between the pressure at the lowest pressure region of the pump and the vaporisation pressure of the fluid being pumped.

Meanwhile, net positive suction head required ($NPSH_R$) is the inlet head amount needed for proper pump operation. The total discharge head is the inlet head and differential head summation [76], [77]. If the inlet pressure is less than the vapour pressure, cavitation will occur since water starts to boil and forms vapour bubbles, inducing hardware damage. A greater suction head implies less pressure at the suction and therefore, pumps are limited by the head they can [75], [78].

The centrifugal pump casing is designed whereby the suction flange is one or two pipe sizes larger compared to the discharge flange, thus managing inlet fluid velocity and reducing friction losses. Friction loss is defined as the fluid's resistance to movement inside the pipe. Head losses due to pipe friction, turbulence and secondary losses also count as types of friction loss. Head losses are caused due to energy in the flow being dissipated into heat, which is eventually lost to the surroundings. Such losses are typically estimated due to the complexity associated with calculating them.

Approximations can be made by assuming the pipes have a rectangular or square cross-section. Gibson [79] calculated head loss based on straight pipes, however in practice, the pipes are curved and thus, losses will be greater than those predicted by Gibson [79]. Furthermore, shock losses at impeller discharge are difficult to determine since the exit velocity of fluid exiting the impeller is unknown. Finally, leakage losses also occur at the neckring and at the balance disc (if the pump is multistage). Neckring and balance disc leakage usually cause a maximum of 2% of the total flow to be lost. Power losses occur due to phenomena such as disc, gland and bearing friction. For both single and multistage pumps, disc friction is usually valued at a maximum of 2% of the total power. Finally, pump total loss is defined as the percentage difference between maximum efficiency (100%) and the achieved efficiency [79].

Figure 2.8 shows the relationship between the net positive suction head (NPSH) and the flow rate (Q). Pump range of operation is of importance in order to avoid problems such as excessive thrust, undesirable temperature changes and cavitation. If the pump is operating in a range on the left of the best efficiency point (BEP), then temperature rises must be checked, and the maximum rise must be noted to ensure it is not exceeded. Exceeding or reaching the maximum temperature rise can cause problems such as cavitation (due to vaporisation) as well as material problems depending on what material the pump is made of. If the pump's operation range is to the right of the BEP, then overloading may be the problem, potentially leading to the motor tripping since more power is being asked for than available (requirement > availability). When operating to the right of the BEP, the static pressure must also be increased if a higher flow is desired to be maintained (higher $NPSH_R$ needed). Therefore, the pump operating range is limited anywhere between 70 to 120% [80]. Stewart [73] created a pump selection guide explaining that centrifugal pumps are widely used for several operations due to their reliability and low available suction head management. Moreover, centrifugal pumps are very minimally prone to leakages, as long as high temperatures are not reached (> 350 °F). Other advantages include their ability to handle a wide range of flow rates and heads (i.e., pressures), their ease of access in the market and have the lowest capital and operating expenses (CAPEX and OPEX).

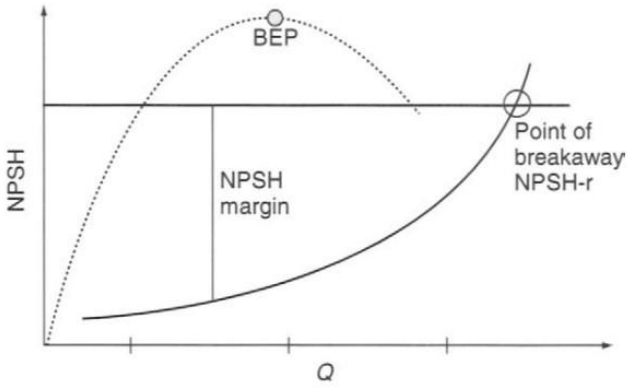

Figure 2.8: Pump range of operation [80].

Centrifugal pumps have a basic operation principle, can handle high flow rates at low pressures, are the most classic and most established pump technology on the market, and are on the lower end of investment and maintenance costs, especially for their long life cycle [81], [82].

Centrifugal pumps also contain disadvantages; pump design and performance are strongly dependent on pressure. Throttling causes energy losses, thus making the pump type less efficient compared to positive displacement pumps. Adding on, centrifugal pumps are not safe to be run dry (without a fluid). As a result, they must be filled with fluid prior to start up, thus preventing dry run damage [82].

Furthermore, centrifugal pumps require priming and while some pumps are designed to be self-priming, there are market limitations with respect to pumps offered with the self-priming feature [73]. In practical terms, it is damaging to operate centrifugal pumps on the left side of the BEP plot since such pumps create vibration and re-circulation problems since the flow rate may be less than minimum on the left side graph region. Centrifugal pumps can either be single stage or multi-stage. Multistage pumps differ since they consist of numerous impellers rather than just one, where each impeller generates a slightly higher pressure compared to the previous impeller. Typically, transitions from single stage to multistage only affect the head and the shaft power, whereby fluid flow rate remains the same. Multistage pumps are useful since they can operate in a range of high pressures and achieve higher efficiencies compared to single stage pumps since the impellers are in series to each other.

2.3.2 Rotary Positive Displacement Pumps

Rotary positive displacement pumps consist of a rotating mechanical device, also known as a displacer, which transfers the medium and increases the medium's potential energy in the process due to mechanical compression of the fluid. Performance of this pump type is specified by the fluid flow, power input, suction and discharge port pressures, drive shaft speed and fluid kinematic viscosity. Like all positive displacement pumps, the pump's flow rate is directly proportional to the pump speed. Nevertheless, the discharge pressure is independent of flow rate or speed. However, unlike reciprocating positive displacement pumps, rotary type pumps do not require valves since the suction and discharge parts of the pump are separated by a sealing gap. Rotary type pumps are useful for pumping media which are defined as self – lubricating or are of a higher viscosity than what a centrifugal pump is able to handle [78]. Figure 2.9 shows a schematic of the pump [78].

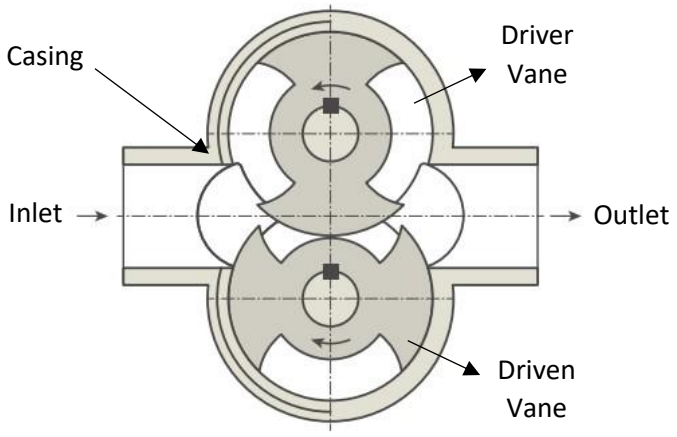

Figure 2.9: A rotary positive displacement pump schematic [78].

Rotary pumps are typically rated by means of their capacity (flow rate), rather than their displacement, where their flow rate is affected by slip losses. Slip is an amount of fluid which leaks from high-pressure discharge back to low-pressure suction, hence causing a loss in the calculated capacity of the pump. Its occurrence is inevitable since it is caused by the clearance between the pumps' moving parts and stationary parts (i.e., the pump casing). Rotary pump capacity is also reduced with low viscosity fluids, larger clearances (hence why machining must be done to a high degree) and reduced pump speed. A rotary pumps' overall efficiency ranges between 60 to 70%, however some rotary pumps have even reached percentages of 80 or more in ideal conditions [73].

Rotary pumps exist in different types. Eccentric rotors are a type which differ based on their vane design, having either sliding or flexible vanes. Sliding vanes slide in and out of the rotor and seal the cavities of fluid, thus increasing the fluid pressure during rotation. Such vanes are best applied to lower-viscosity fluids but are not reliable due to wear and vane mechanical failure. Meanwhile, flexible vanes are made of a softer and more flexible material. Flexible vane rotor design is more simplistic and must also be used in situations which are low pressure, low temperature and not demanding. Twisted vanes are needed if the efficiency is desired to be completely maximised, however the cost of such vanes is also highest. The next type of rotary pumps are the gear pumps. External gear pumps provide good sizing, are useful for fluids of high viscosity and are capable of creating high pressures. Meanwhile, internal gear pumps are similar however make use of internal teeth at the ring gear. They are useful with clear fluids or fluids which consist of small amounts of suspended solids. Internal gears are reliable and cheap, however are limited by back pressure and suspended solids handling nonetheless. The final category of rotary pumps are screw pumps. Such pumps are mostly used in the oil and gas industry.

Screw pumps can either be single, double or triple screw however they are expensive, require maintenance and do not last as long as centrifugal pumps [73]. The advantages of rotary positive displacement pumps are that the pump has reversible flow directions, maintains a constant flow rate during operation irrespective of back pressure, can be run dry apart from specific exceptions and also have low investment costs. Furthermore, positive displacement pumps are able to reach efficiencies between 10 to 35% higher compared to centrifugal pumps [78], [82]. However, while being cheap, they do require a lot of maintenance (higher number of mechanical moving parts) and must be produced to a degree of excellent quality due to the tight spaces and clearances which make a part of its design.

2.3.3 Reciprocating Positive Displacement Pumps

In the case of a reciprocating positive displacement pump, the displacer is typically represented by a piston, which varies the pump's space, thus compressing or expanding space for water to be pumped into. The pump's piston space is enclosed by two valves; One opens during the first half revolution of pumping (from reservoir to piston) and the other opens during the second half revolution of pumping (from piston to desired head). During the first half revolution, the space increases as the piston is retracted. As a result of the vacuum and pressure difference, the first valve opens and fluid flows into the piston region and the suction valve closes. During the second half, the piston retracts in the opposite direction, thus increasing the pressure [78]. Once the discharge pressure is reached, the second valve is triggered, and water is able to flow upwards. An important note is that both valves cannot be open simultaneously. The reciprocating positive displacement pump flow rate is dependent on the pump's design; specifically, the stroke length and frequency since these two parameters have a linear relationship with flow rate [78]. Furthermore, the pump speed is the main factor in determining the its capacity [73].

Different types of reciprocating pumps are plunger and piston pumps and diaphragm pumps. Plunger and piston pumps can either be single-acting or double-acting. Single-acting means that the fluid flows in one direction from suction to discharge, while double-acting means that liquid can be pumped in both directions when the piston moves.

Figure 2.10 shows the flow difference between the single-acting and double-acting pumps [73]. Diaphragm pumps have a similar working principle to piston pumps; however the piston is replaced by a flexible diaphragm. Such pumps can be driven mechanically or hydraulically, and they are limited by flow rate and temperature. Despite diaphragm pumps are simple to operate, they have a short life cycle.

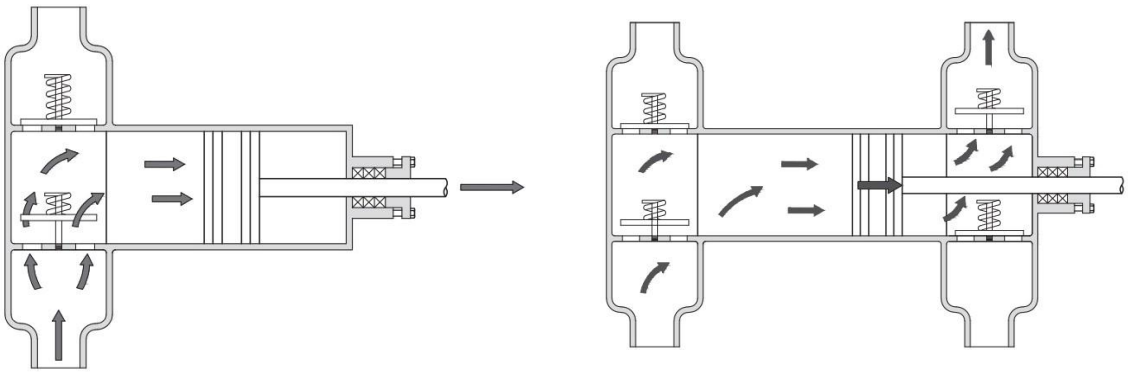

Figure 2.10: A single-acting (left) and double-acting (right) reciprocating pump schematic [78].

The diaphragm itself is typically made of stainless steel or Teflon. They are capable of pumping highly corrosive materials (unless the pump is a packed plunger) and are self-priming, an advantage which exists over some centrifugal and rotary pumps [73]. While several different reciprocating pump types exist (piston, plunger, diaphragm), reciprocating pumps are classified into two sectors: power and direct-acting pumps.

Power pumps are driven by a motor or an engine. Direct-acting pumps operate via pressure from a gas present within the pump (e.g., air or compressed air). Reciprocating pumps are standardised via API Standard 674, which looks into pump pressure and speed ratings, together with pump design and allowable materials [73], [83]. The main advantage of the reciprocating pump is its flexibility in piston driving, whereby this can be done mechanically, hydraulically (expensive) or pneumatically. The pressure curve is not affected by the pump performance, making the pump flexible over a wide range of pressures and flow rates. The pump type is also safe to run dry and can be self-primed [82]. Self-priming means that the pump is able to repeatedly turn a mixture of air and water into a pumpable fluid. Moreover, the pump head achieved is almost completely independent of flow rate (apart from minor slippage losses). Reciprocating operating speeds are far lower, hence making such pump types suitable for high viscosity fluids [73]. Moreover, despite the pressure, positive displacement pumps are consistent in the volume flowrate delivered, independent of pressure [84].

Despite the positives, reciprocating pumps have numerous disadvantages. Firstly, such pumps work in pulsations due to their working principle. As a result, there will be time during operation where pumping is not taking place. Hence, the flow rate reached by these pumps does not compete with other pump types (example centrifugal pumps) and is in fact limited to a maximum of 1,500 m^3/h. Finally, reciprocating positive displacement pumps also come at high costs, high demands for pre-pump inlet filtration, as well as high maintenance due to a higher number of moving parts (valves, sliding contacts, springs). [73], [78], [82].

2.3.4 Pump Type Comparison

While reciprocating positive displacement pumps (metering pumps) have their flow rate almost negligibly affected by pressure, rotary positive displacement and centrifugal pumps are dependent on pressure in different ways.

Rotary pumps are dependent on pressure since pressure is what influences any leakage losses in between the tight gaps of the rotary pump design. Meanwhile, discharge pressure is what affects centrifugal pumps [78]. Figure 2.11 shows the relationship that flow rate and pressure have for different pump types. As previously mentioned, centrifugal pumps are best suited for applications which require low pressures and high flow rates, while displacement pumps are most applicable for high pressure and low flow rate situations. In terms of cost, centrifugal and rotary positive displacement pumps are cheaper than positive displacement pumps, with the latter two requiring more maintenance compared to centrifugal pumps. According to API 610 [75], centrifugal pumps are to be designed whereby they can start off by undergoing a minimum of three years of continuous operation without human interference (i.e., maintenance).

Another important factor is the power ratings of the different pumps. Centrifugal pumps, specifically high speed, multi-stage and radial centrifugal pumps, are almost the only pumps in existence which have thus far been able to generate a power rating of greater than one megawatt. Meanwhile, positive displacement pumps are incapable of reaching the high speeds centrifugal pumps are able to reach [84]. The only positive displacement category pump exception which is able to generate one megawatt, or more, is the rotary positive displacement pump, as shown in Figure 2.12 [78]. Table 2.1 compares the three main pump types by looking into the factors of importance in relation to the desired application (i.e., the marine industry). While efficiency and flexibility were also important, the most important factor apart from being able to reach MW-scale rating was low maintenance, due to such machinery being deployed offshore. Hence, the centrifugal pump option was deemed the most attractive solution in this case. Centrifugal pumps are best applied when fluid containing impurities and matter such as sand and fine solids is required to be suctioned and passed through pipelines. If the pump is set on the seafloor, a centrifugal pump is ideal since it is able to obtain high flow rates at low pressures and can deal with the abrasion associated with some of the impurities absorbed [85].

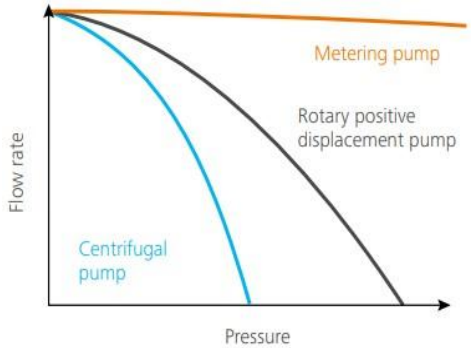

Figure 2.11: A comparison of flow rate versus pressure for different pump types [78].

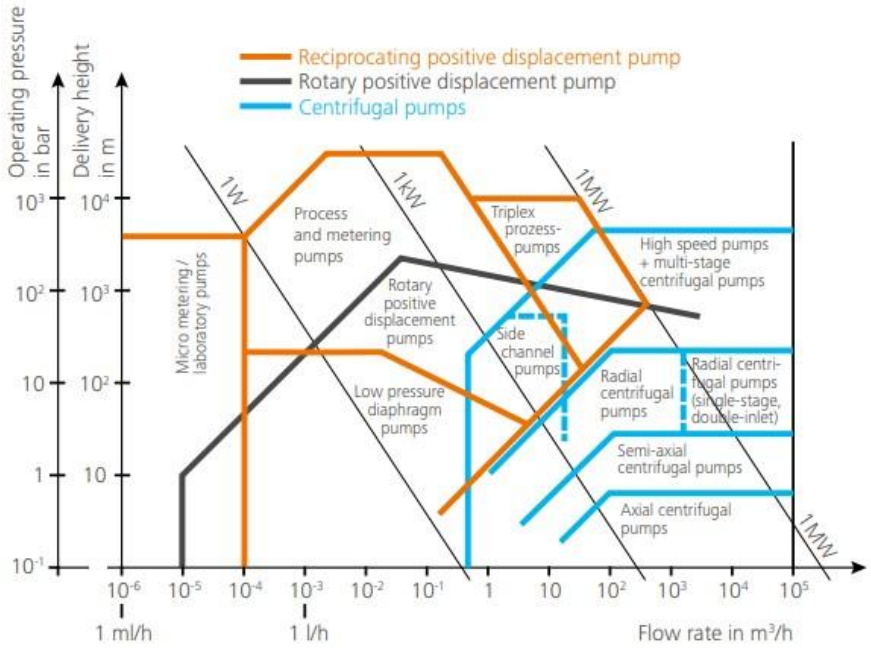

Figure 2.12: A comparison of the operability of the different pump types [78].

A disadvantage of such pumps is that they are highly sensitive to contaminants or large particles, thus requiring a good filtration system prior to the water entering such a pump [86]. Rotary positive displacement pumps are used in industries which require the handling of high-viscosity fluids, rather than a relatively low viscous fluid such as seawater. A positive displacement pump which is competitive with the centrifugal pump for oil and gas applications is known as the screw pump or screw spindle pump. The screw pump is able to handle a wide range of pressures, a low flow rates range (50 m^3/h to 2498 m^3/h) and viscosity. The pump also obtains a constant flow independent of variations in back pressure (resulting from viscosity alterations) [87].

Table 2.1: Comparison of the different pump types [73], [75], [78], [82].

Pump Type	Low Maintenance	Low Investment Cost	High Efficiency	MW Power Achievable	Flexible Operation Conditions
Centrifugal	✓	✓	X	✓	X
Rotary	X	✓	✓	✓	✓
Reciprocating	X	X	✓	X	✓

2.4 Hydraulic Turbines

The following section presents an overview of the main types of impulse and reaction turbines, highlighting their working principles, advantages and disadvantages while also providing a technological update of what currently exists within industry.

2.4.1 Pelton Turbines

Pelton turbines are hydraulic impulse machines which represent one of the most large-scale power conversion methods in the world. A single turbine is able to convert hundreds of megawatts of hydraulic energy into kinetic energy and such turbines are used in high head (300 to 4000 metres) and low flow rate situations [88]–[90]. The turbine is required to operate in air, and must thus be placed in a separate, air tight chamber or pressure vessel if it is to be used underwater [88]. A high speed water jet is ejected through a nozzle. An impulsive force is induced when the Pelton wheel buckets are hit by the water jet which, in turn, makes the turbine rotate.

For maximum impulse, a 180° water re-direction would be optimal. However, this would feed the water directly back into the jet, where a new supply of water is being ejected. Therefore, in practical turbine design, the exit velocity cannot be zero since water has to move away from the bucket to make way for the following buckets. Therefore, the flow angle for exit flow is usually about 170°. The water jet kinetic energy is transformed into rotational energy. The rotating shaft produces electricity by running a generator. Power demand may fluctuate over time. Therefore, a governing mechanism is used to control the position of a spear head. At low demand, the spear head is moved inwards so that water flow rate is reduced. If power demand increases, the head is moved out, thus increasing flow rate. The spear head ensures that the turbine rotates at a constant, specified RPM while conforming to the power supply frequency, thus acting as a speed governing mechanism of the Pelton wheel [91], [92].

Pelton turbines consist of a number of basic components, the main ones of which are shown in Figure 2.13. The casing is what encapsulates the moving parts of the turbine. The branch pipe is a pipeline which connects where the water is coming from to the nozzle. At the end of the branch pipe is the injector, which consists of a spear valve to control flow and a nozzle to allow the water jet to exit. The runner is a disc which houses the buckets on it.

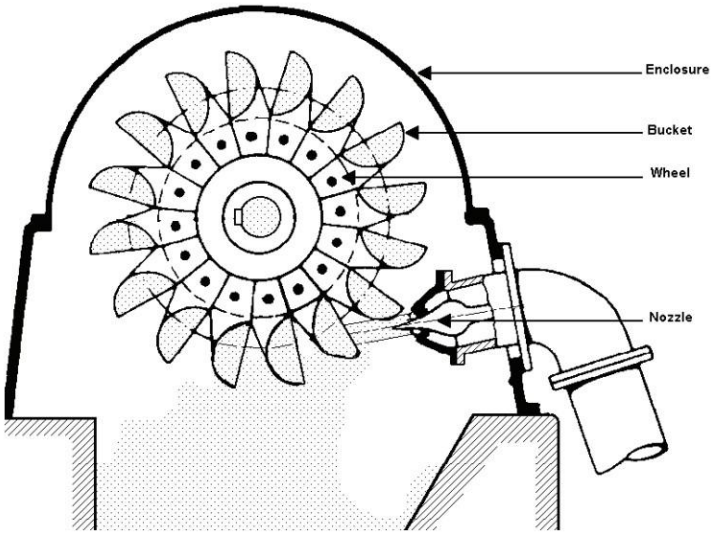

Figure 2.13: A basic schematic of a Pelton turbine [64].

Finally, the buckets are the part which the water jet hits and through which the impulse force is generated [93]. Zhang [91] found that Pelton turbine efficiency is greatly influenced by flow friction inside the turbine buckets. Furthermore, Atthanayake [94] found that bucket surface roughness plays an essential role in reducing losses, attributing directly to friction. Apart from slight variations from dynamic losses in the penstock (pipe), the reservoir consists of a nearly static head. Therefore, a fixed fluid velocity is able to be maintained. A fixed fluid velocity and fixed Pelton turbine speed mean that their ratio is constant. Hence, appropriate sizing based on their ratio can provide an optimum practical bucket to speed ratio, which is to be maintained throughout turbine operation. The optimum theoretical bucket to speed ratio is found to be 0.50, however the ideal practical ratio is approximately typically 0.47-0.48 due to windage, back-splashing, mechanical friction and non-uniform bucket flow losses in the system [92], [95].

Pelton turbine design importance is on the number of buckets on the disc (runner). Too many buckets result in two bucket interference with the jet, while too little causes the jet to completely miss both buckets at a certain moment, reducing efficiency drastically. The number of buckets on the turbine runner is typically around 18 to 22 to maximise efficiency. With respect to their production, buckets are usually casted and then mounted onto the runner. It is cheap, reliable and can produce complex shapes easily. On the other hand, the whole runner and buckets may also be cast into one full piece and are typically made of stainless steel [88], [91].

Pelton turbines can either be configured horizontally or vertically. Horizontal configuration usually allows up to two injectors, while vertical configuration allows up to six, symmetrically distributed injectors. Figure 2.14 shows the setup of a large scale, vertically configured Pelton turbine with multiple injectors [96]. The two important parameters to ensure the production of useful power are the flow rate and the head. Head is the vertical height from the level where the water enters to the level of turbine centreline but may also be defined as the height at which a pump can raise water up. Multiple-jet machines have a number of advantages over single-jet machines [88]. Firstly, multi-jet machines offer a higher rotational speed while also making use of a smaller runner and casing. Flow can be controlled without the aforementioned spear valve and due to surge pressure reductions, there is a lower chance of blockage associated with the use of multiple jets. Pelton turbines are advantageous since their work environment is atmosphere, obtain efficiencies of 80 to 90% over a wide range of rated power operation and are easy and cheap to maintain due to their simplicity. Meanwhile, a disadvantage of such turbines is that their efficiency decreases with time due to hydro-abrasive erosion [97]. Moreover, Pelton turbines have a large spatial requirement due to the runner disc and generator.

Figure 2.14: A multi-jet, vertical Pelton turbine [96].

2.4.2 Francis Turbines

Francis turbines are known as reaction turbines and are most ideal for applications which involve low head and high flow rates. Francis turbines consist of guide vanes which can either be stationary or adjustable. The water enters through the inlet tangentially to these fixed or adjustable vanes and is guided towards the rotating blades. Fixed vanes are known to typically have lower efficiencies compared to adjustable vanes and also generate vortex swirling [98]. The purpose of the vanes is to prevent shock from occurring when water enters through the inlet [99].

The working principle of the Francis turbine is opposite to that of a centrifugal pump. The inlet is the section which is of larger diameter, and the outlet is narrowed down, thus increasing the velocity of the fluid as it passes through the turbine before exiting axially [100]. The velocity increase generates a momentum, thus causing the rotating blades to rotate and cause a pressure drop on impact of the water onto the blades. Francis turbines can either be radial flow or mixed flow. The main difference between the two turbine types is that the flow enters tangentially for the radial flow while a mixed flow turbine has flow entering at an angle which is between radial and axial. Mixed flow turbines are more popular since they are used for greater turbine speeds since the flow rate is limited with radial flow Francis turbines [92], [100], [101]. Figure 2.15 shows examples of a radial flow Francis turbine (left) and a mixed flow Francis turbine (right).

A main problem associated with Francis turbines is cavitation. Since the turbine operates with pressure drops due to the rotation of the blades, cavitation is generated and may potentially lead to excessive vibrations and pre-mature mechanical wear and tear in the form of erosion, pitting and crevice corrosion [98], [101]. The type of cavitation which occurs in Francis turbines is hydrodynamic and flow cavitation [92].

Hydrodynamic cavitation typically increases noise and vibrations while also throttling the fluid flow due to bubble formation. Cavitation within Francis turbines occurs at the runner outlet or at the tube inlet of the turbine due to the pressure drops that occur there. Duncan [102] found that the typical areas of pitting corrosion due to cavitation within a Francis turbine were identified at the draft tube liner, the nose cone and the leading edges of both the pressure and suction sides of the turbine. According to Avellan [103], leading edge cavitation is a type of cavitation which is not sensitive to the Thoma number and is thus able to cause substantial blade erosion. Similar to centrifugal pumps, the other cavitation types which occur vary but also include vortex, attached and travelling cavitation.

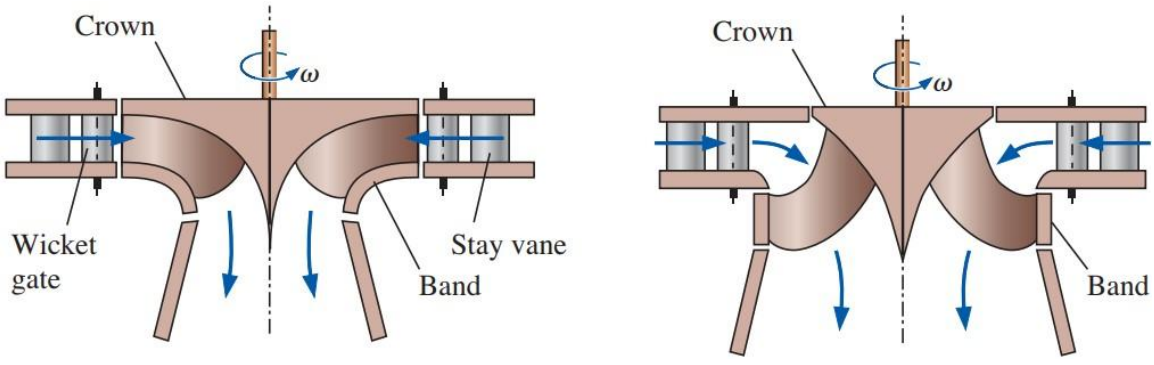

Figure 2.15: Radial flow (left) and mixed flow (right) Francis turbine schematics [100].

While cavitation is inevitable, several studies have looked into preventing cavitation in order to limit performance reduction and corrosion due to cavitation. With Francis turbines, their operation must be below their most efficient operating conditions in order to avoid cavitation [101]. The water quality that the Francis turbine operates with is also fundamental since this turbine type requires filtered water with negligible contaminants and abrasive solids such as sand. While minimal amounts will not affect the turbine efficiency, corrosion and material damage will still occur since cavitation would still be present [104].

Apart from cavitation, a Francis turbine operating in a transient rather than steady-state environment brings along numerous additional challenges. While the turbine has the advantage of obtaining high efficiencies (90 to 95%) if operating at the BEP, operating condition instability, pressure shocks, noise and vibrations all add to the risk of the component failure [101], [103]. A transient Computational Fluid Dynamics (CFD) simulation by Nicolle et al. [105] showed that unnecessary and hard accelerations and decelerations on the turbine caused forces which create severe fatigue on the blades. Francis turbine advantages include the slow decrease in efficiency over time. Furthermore, in comparison to other turbines such as the Pelton turbine, the same power generation by the Francis turbine is obtained while utilising less space compared to the Pelton turbine. Francis turbines have a range of head operation, thus reaching a compromise between the high head requirements of Pelton turbines and the low head requirements of Kaplan turbines. However, the disadvantages are that they are more susceptible to contaminants compared to Pelton turbines, thus requiring better filtering. Due to the runner being completely enclosed within a cast steel casing, maintenance and inspection is far more tedious compared to Pelton turbines [98].

2.4.3 Kaplan Turbines

The Kaplan turbine is a reaction turbine as in the case of the Francis turbine described in Section 2.4.2, however having the geometry similar to that of a propellor. The Kaplan turbine is designed for low head (2 to 40°metre), high flow rate applications and is typically designed to take in flow axially. The main components are almost identical to the Francis turbine, where the Kaplan turbine has a rotor, which consists of a runner and a shaft, guide vanes, the draft tube and the overall casing.

The working principle is also the same as the Francis turbine; Water is guided onto the blades, causing them to rotate which leads to a pressure drop and an increase in velocity [106].

Kaplan turbines (schematics shown in Figure 2.16) can either have fixed or adjustable blades, however the adjustable blade design allows for the turbine to compete in terms of efficiencies reached, especially in low power scenarios [92]. Adjustable blades allow the Kaplan turbine to attain better efficiencies since the flow rate can be controlled in two ways. Firstly, the gates can be adjusted to control the flow rate, however with adjustable blades, the pitch angle gives an additional method on how the flow rate may be controlled [100]. If the guide vanes are fixed, the turbine is referred to as single regulated whereby if the guide vanes are freely adjustable, the turbine is referred to double regulated [106].

For low head purposes, Kaplan turbines are advantageous since they can reach the efficiency levels of Francis turbines, varying between 90 to 95%. Furthermore, Kaplan turbines are smaller in size compared to other hydro power turbines and thus require less space. However, the turbine design has a number of limitations: Firstly, the draft tube must be kept as short as possible, since cavitation problems arise the longer it is due to higher head than what the turbine is designed for. Furthermore, the Kaplan turbine has a minimum flow rate which must be reached or else the turbine will succumb damage. While their maintenance is inexpensive, the initial investment cost for design, manufacture and installation is costly but such machine types have a lifecycle of at least 30 years [104], [106].

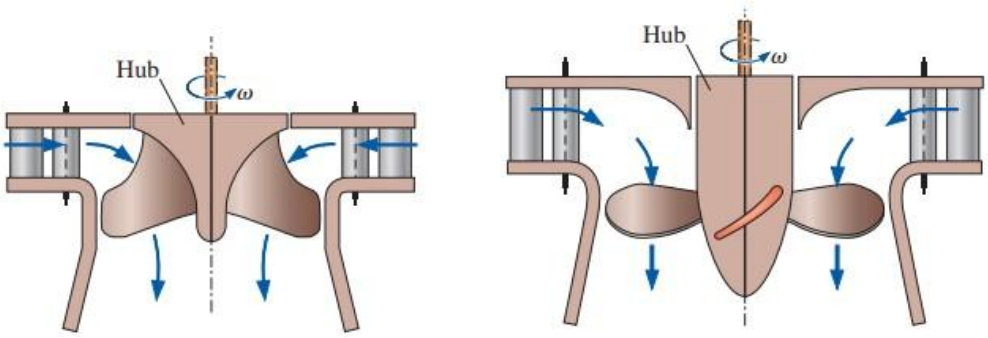

Figure 2.16: Mixed flow (left) and axial flow (right) Kaplan turbine schematics [100].

2.4.4 Turbine Type Comparison

The turbines being compared are split into the categories of reaction and impulse turbines. The reaction turbines working principle involves a pressure difference which occurs through the runner, while impulse turbines do not have a pressure change as the fluid passes through the runner. While Pelton and Francis turbines are capable of low to medium flow rates respectively and high to medium pressures respectively, Kaplan turbines are suited for low pressure, low head and high flow rate applications. The Pelton turbine is designed to operate in air and is found to have the widest operating range (maintaining efficiency between 25 to 100% load) as well as being less sensitive to head changes compared to reaction turbines [107]. The reaction Francis and Kaplan turbines are designed to be surrounded by water during operation. As a result, if the Pelton turbine were to be applied to a sub-sea environment, a compressed air pressure vessel would have to be used, whereby the inner pressure of the chamber is equal to the external hydrostatic pressure of the fluid on the vessel, thus causing changes to the aerodynamic performance of the turbine. A study by Hirtenlehner [108] found that a Pelton turbine operating in a higher ambient pressure (e.g. a compressed air chamber) results in additional losses in the turbine efficiency. Due to the change in air pressure, windage and friction losses were higher since such factors are dependent on the air density in the pressure vessel. Furthermore, vortex losses occur more as the back pressure increases.

Maintenance for the Pelton and Kaplan turbines is relatively low, especially for the Pelton turbine due to the low number of components and the low optimal speeds as a result of the lower stress levels on moving parts during operation [109]. The Kaplan turbine has a high initial investment cost and the amount of moving parts it has leads to higher maintenance requirements compared to a Pelton turbine. Meanwhile, the Francis turbine is tedious when it comes to maintenance since its components are difficult to reach due to the runner being completely enclosed inside a casing [110]. With respect to efficiency, the Pelton turbine achieves an efficiency of approximately 90%, whereby Francis turbines and Kaplan turbines (if double regulated), have a superior performance with efficiencies reaching around 94 to 95%, [109]. However, the Francis turbine is far more sensitive to operation environment changes, causing it to lose efficiency fast as soon as operation is not at or very close to the BEP. The Kaplan turbine behaves similarly to the Francis turbine, but the Pelton turbine is able to maintain close to 90% efficiency over a wide range of rated powers. The Francis turbine is able to maintain its efficiency over the widest range of specific speeds [92].

The Pelton turbine is relatively large in size in comparison to the Francis and Kaplan turbines for the same power output, since the reaction turbines are able to operate at faster speeds. All three turbine types are capable of tapping into the MW scale power region [92]. For low output systems, impulse turbines are more efficient while also being less costly than reaction turbines. The Francis turbine is costlier compared to the Pelton turbine due to the detailed and specific rotor design [111]. Table 2.2 summarises the comparison between the three turbine types analysed. Given the Pelton turbine's ability to achieve high pressures, coupled with its low maintenance requirements and flexible operating conditions, it was considered the most suitable option for the ESS ECU.

Table 2.2: Comparison of the different turbine types [92], [107], [108].

Turbine Type	Pelton	Francis	Kaplan
High Pressures	✓	✓	X
Low Flow Rates	✓	✓	X
Submerged Operation	X	✓	✓
Low Maintenance	✓	X	✓
High Efficiency	X	✓	✓
Low Spatial Requirements	X	✓	✓
Low Investment Costs	✓	X	X
Flexible Operating Conditions	✓	X	X
MW Power Achievable	✓	✓	✓

2.5 Numerical Modelling of the Performance of Centrifugal Pumps and Pelton Turbines

While Sections 2.3 and 2.4 delved into different pumps and turbines, Section 2.5 analyses previous research related to the performance modelling of centrifugal pumps and Pelton turbines, since the ECU within this thesis is made up of the said turbomachinery.

Recent studies have employed various numerical modeling techniques to analyse the performance of centrifugal pumps and Pelton turbines. With respect to centrifugal pumps, Computational Fluid Dynamics (CFD) simulations have been very commonly applied to investigate flow patterns and pump performance characteristics. Huang et al. [112] used OpenFOAM 5.0 to perform both steady-state and transient simulations across a wide operating range. The simulation outcomes demonstrated high accuracy in the prediction of pump performance, with specific insight on the relationship between vortices and hydraulic losses. A study by Zhao et al. [113] applied a mixture of machine learning and high-precision numerical simulations to structurally optimise a series of multistage centrifugal pumps. The research indicated that the optimised structure reduced potential for unstable flow and also improved turbulence distribution. Jenkins and Kuryachy [114] presented a MATLAB Simulink model to simulate the operation of a centrifugal pump as a turbine. The research highlights the usefulness of the software in terms of modelling and pump performance analysis.

With respect to Pelton turbines, Bhuyan et al. [115] performed simulations of a Pelton turbine operating together with a wave energy-harvesting device. The research showed that energy conversion via the turbine was efficient. Decaix et al. [116] used a meshless-based model to simulate the flow within a Pelton turbine. The aim of the study was to analyse the complex interactions between the water jet and turbine buckets. The study provided a more computationally efficient model to validate experimental data in comparison due mesh-based modelling. Setyawan et al. [117] simulated the operation of a Pelton turbine with 3 nozzles and carried out a comparative study with 2 and 1 nozzles. The results showed that the Pelton wheel efficiency had a direct proportionality with the number of nozzles. Chukwuneke et al. [118] studied the effect of bucket splitter angle on the turbine power output. The efficiency and performance of the turbine under fixed-head conditions was studied, with the aim of optimising the turbine's design.

A common factor of the above research related to the relevant turbomachinery within this study is that the vast majority of works, both for steady state and transient simulations, only consider fixed head scenarios. As a result, a knowledge gap is related to the simulation of such turbomachinery under variable head conditions.

2.6 Time Series Forecasting

Time series forecasting is a method which allows researchers to find patterns in captured data and use the said patterns to forecast the future. Due to megawatt-scale RES power fluctuations, introducing time series forecasting may be useful as an information metric to the energy storage system. With an abundance of recorded data from renewable energy sources such as solar energy as well as wind speed data, forecasting can be used to carry out predictive analysis through supervised learning [119]–[121]. Forecasting is useful in amalgamation with hydraulic machinery in order to anticipate which machinery will be required in the near future, rather than reacting based solely off of real-time data [122], [123]. Figure 2.17 shows an overview of the bridge between Artificial Intelligence, Machine Learning, Data Science and which section Time Series Forecasting falls under [124].

Previous research has shown that power smoothing can aid in reducing storage capacity and operational costs [125]–[127]. Sharma et al. [120] specified that forecasting is useful for ESS operation since it aids in storage management and flexibility over the storage system's operational lifecycle. Wurth et al. [128] emphasised the importance of minute-scale forecasting to balance out the power grid, as well as for the validation of forecasting models. The most classic forecasting methods in relation to wind speed and wind power are statistical models, such as the Auto Regressive Moving Average (ARMA), due to their time-series-based modelling.

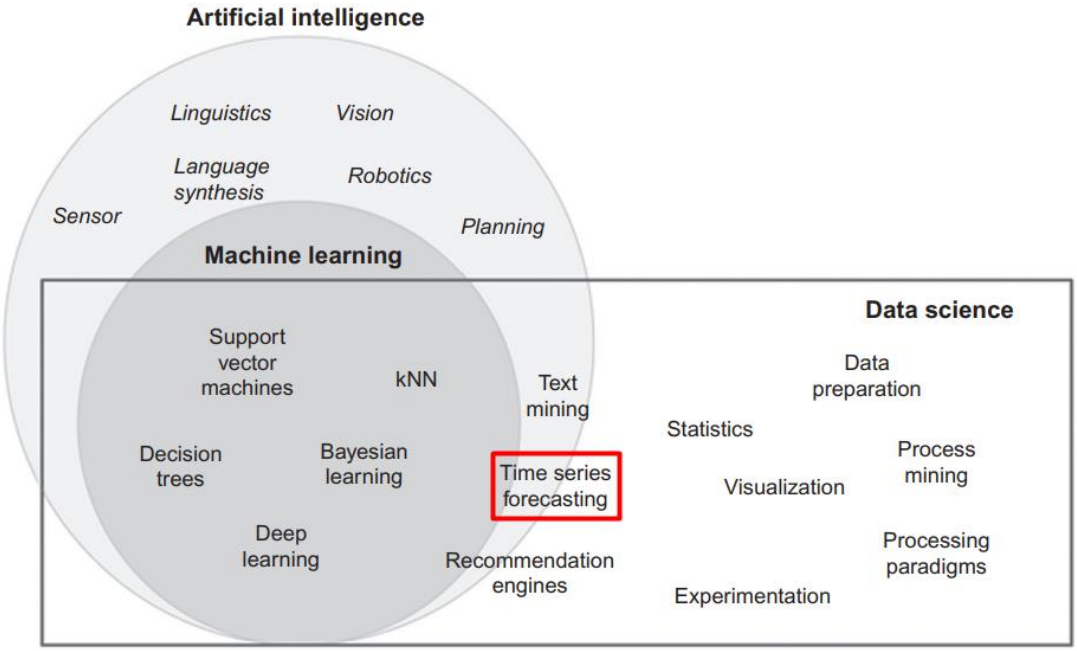

Figure 2.17: An overview of the relationship between AI, ML and Data Science, highlighting which categories Time Series Forecasting falls under [124].

Such forecasting methods are typically used for 10-minute-ahead forecasts, with Wurth et al. [128] highlighting that an existing knowledge gap is understanding how statistical forecasting methods would perform at smaller future timesteps. Johnson et al. [129] applied a simple moving average (SMA) method paired with battery energy storage to reduce power fluctuations from photovoltaic (PV) power. Alam et al. [130] explained that the averaging window is the controlling factor on the charging or discharging of the storage system. A long averaging window causes large power differentials to be handled by the storage system as well as time delays, and a window too short can potentially still lead to an intermittent power output. In order for the forecast to be satisfactory, the forecasting model used, and its statistical accuracy are pivotal in ensuring reliable results. Time series data consist of three main components [122], [123]:

1. Trend: The trend assesses whether the data average is increasing or decreasing.
2. Seasonal: The seasonal component observes if there is a sequence at a fixed interval.
3. Irregular: Purely checks if there are any arbitrary data points within the time series data.

Dennecker [131] found that time series prediction is made more complex without having weather information also considered. For example, scatter clouds caused multiple short peaks in a solar energy source time series. Time series energy forecasting is typically made up of two parts: the AR model and the moving average (MA) model. The amalgamation of both models is termed the ARMA model, which may also be utilised as an Auto Regressive Integrated Moving Average (ARIMA) if the data being worked with is defined as non-stationary. In the scenario of data which has a seasonal component, a Seasonal ARIMA (SARIMA) model can be applied. Dennecker [131] explains that ensuring that the forecasting results are satisfactory by using part of the dataset for training to reduce prediction errors is vital. Optimising such results is a computationally costly exercise since a rolling forecast and forecasting error must be calculated at each point over a full dataset. As a result, the operation of forecasting must be targeted at specific requirements or utilise justified assumptions to improve optimisation efficiency. For example, in relation to energy time forecasting, short-term forecasting including forecasting numerous times within one day allows for a smaller yet more detailed dataset since the electricity market requires a high update rate to exploit its benefits. A high update rate, however, requires high efficiency and flexibility but should never be at the demise of accurate forecasting.

2.7 Identified Knowledge Gaps

The literature review provided insight on what the existing knowledge gaps to be tackled within this dissertation are.

1. When referring to Section 2.1, while HPES systems seem to be a safe, easily co-locatable and reliable storage system for offshore energy storage using existing and well known components, published works concerning their hydraulic performance and techno-feasibility on a megawatt-scale level is limited in open literature. With reference to Section 2.5, it is evident that the majority of literature available about hydraulic machinery is focused on fixed head operation, as is the case in most pump-hydro energy storage plants. The variable head operation characterising HPES systems has not yet been dealt in enough detail in literature.

2. Section 2.3 analysed and compared the different types of pumps which may be implemented with the presented HPES system. Section 2.2.4 concluded that the centrifugal pump is the best choice to satisfy most of the criteria set for the system in particular. Despite this, the challenges in operating the system to tackle unknowns such as operating the system under a variable head while maintaining an efficiency as close to the BEP as possible for different power levels requires in-depth analysis and testing.

3. Section 2.4 delved into understanding hydraulic turbines which have been very well established for decades. The Pelton turbine was selected due to its high head, low flow rate working principle and its operational flexibility. In fact, operating the selected machinery (i.e., Pelton turbine) based on the set criteria in Section 2.3.4 to output a desired power while also maintaining its optimal bucket to jet speed ratio requires a different control strategy. Additionally, understanding the effects of potentially operating a Pelton turbine in an enclosed, subsea environment has not yet been studied.

4. Lastly, Section 2.6 highlights that while statistical models such as the ARMA and SARIMA models are well-established, applying such forecasting methods to forecast the availability of power for timestamps which are at the 1 minute mark (or less) has not been done yet, especially when considering it in the context of utilising RES in tandem with the HPES system to provide a stable power output to the grid.

3 THEORETICAL REVIEW

This chapter presents the underlying theory forming the basis of the numerical models developed in this study, namely the Alpha, Beta and Alpha Plus models. It covers the governing equations for simulating the performance of the megawatt-scale ECU consisting of a multi-stage centrifugal pump, a Pelton turbine and integrated hydraulic circuits. The models for time-series forecasted are also described.

3.1 Performance Modelling of Centrifugal Pumps

Figure 3.1 [73] shows an example of typical centrifugal pump performance characteristic curves. Centrifugal pumps obey a number of affinity laws. The laws show that the flow rate, Q, is directly proportional to the pump speed, ω; The discharge head, H, is directly proportional to the square of the pump speed and the required motor power, P, is directly proportional to the cube of the pump speed, as shown in equations 3.1 to 3.3 [100]:

$$Q \propto \omega \tag{3.1}$$

$$H \propto \omega^2 \tag{3.2}$$

$$P_I \propto \omega^3 \tag{3.3}$$

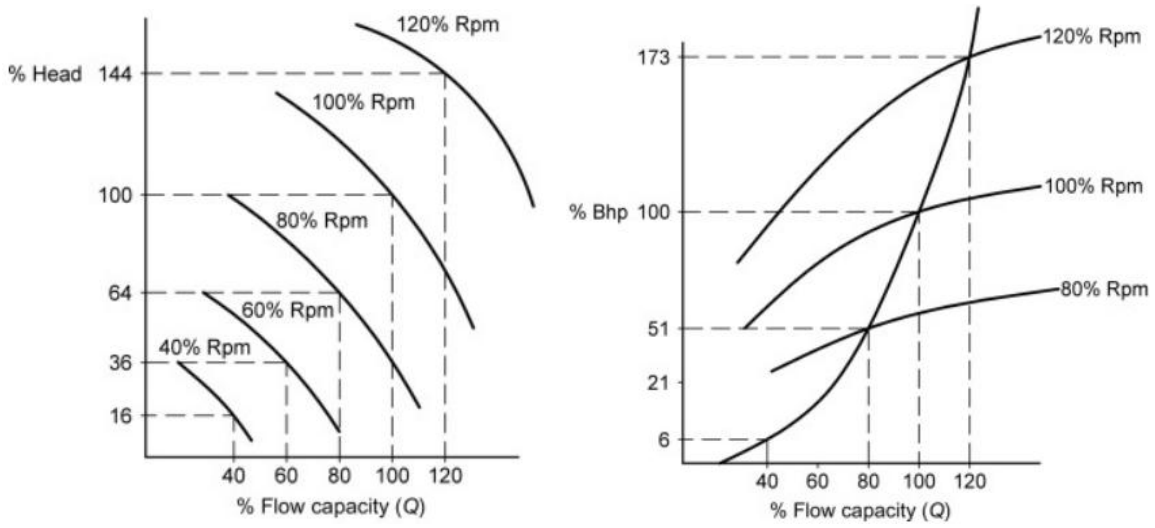

Figure 3.1: An example of typical centrifugal pump characteristic curves at different speeds [73].

Different centrifugal pump types can be selected based on the specific speed of the pump, N_s, presented in equation 3.4 hereunder:

$$N_s = \frac{\omega\sqrt{Q}}{H^{\frac{3}{4}}} \tag{3.4}$$

The discharge head, H, is calculated as shown in equation 3.5 which originates from the Bernoulli equation:

$$H = \overbrace{(z_d - z_s)}^{1} + \frac{\overbrace{p_d - p_s}^{2}}{\rho g} + \frac{\overbrace{v_d^2 - v_s^2}^{3}}{2g} \tag{3.5}$$

Where part 1 is the height difference, part 2 is defined as the pressure head difference and part 3 is the velocity head difference, all between the outlet (d) and inlet (s) ports of the pump. The Net Positive Suction Head (NPSH) is another important parameter which determines whether the pump will experience cavitation during operation at its suction port. Figure 3.2 shows the relationship of the NPSH for a pump transporting fluid to an enclosed tank [92], [100]. The useful (output) power of the pump is defined by multiplying the pump fluid's flow rate by the differential pressure, Δp, as presented in equation 3.6:

$$P_O = Q \times \Delta p \tag{3.6}$$

The centrifugal pump's efficiency may then be determined by finding the ratio between the calculated or observed output power, P_O, and the input power, P_I, which can be directly obtained from a pump's curves, shown previously in Figure 3.1. Equation 3.7 shows the pump efficiency's calculation [92], [100], [132]:

$$\eta_{\text{pump}} = \frac{P_O}{P_I} \tag{3.7}$$

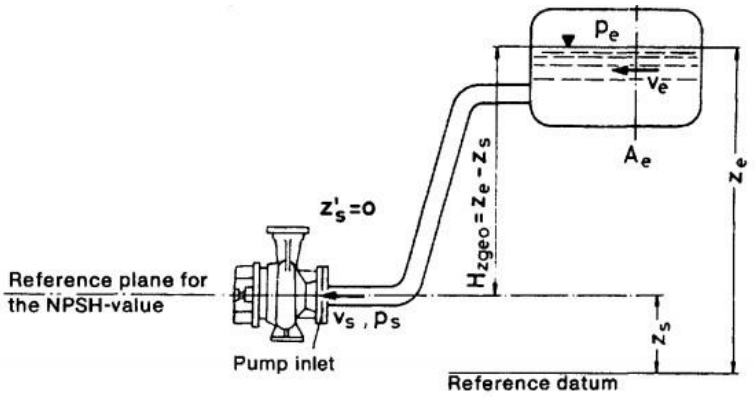

Figure 3.2: A schematic of a basic pump system transporting fluid to an enclosed tank [132].

3.1.1 Centrifugal Pump Upscaling

Since one of the main objectives of the study was to analyse a megawatt-scale system, understanding centrifugal pump upscaling was required since readily available pump curves of such large pumps were not attainable. The pump upscaling process involves the use of dimensionless groups to ensure geometric similarity. The dimensionless groups required are listed below in equations 3.8 to 3.10 [100]:

$$C_H = \frac{gH}{\omega^2 D^2} \tag{3.8}$$

$$C_Q = \frac{Q}{\omega D^3} \tag{3.9}$$

$$C_P = \frac{P}{\rho \omega^3 D^5} \tag{3.10}$$

Where C_H, C_Q, C_P are the head, capacity, and power coefficients respectively, ω is the pump's impeller rotational speed and D is the impeller diameter. Once the coefficient values of the existing pump are established, the new pump's impeller diameter and rotational speed could be found by applying equations 3.11 and 3.12 [100]:

$$D = \frac{Q^2 C_H^*}{\left(C_Q^*\right)^2 gH} \tag{3.11}$$

$$\omega = \frac{Q}{C_Q^* D^3} \tag{3.12}$$

Since the coefficient values are to remain constant for both the existing and upscaled pump, the new impeller diameter and rotational speed values are to be substituted into equations 3.8 to 3.10 to find the new head, flow rate and power values of the upscaled pump. Due to upscaling, the efficiency of the pump is also altered based on the Reynolds numbers of the original and upscaled pumps, as shown in equation 3.13 [133]:

$$\frac{1-\eta_2}{1-\eta_1} = \left(\frac{Re_1}{Re_2}\right)^{0.1} \tag{3.13}$$

Where η_1 and η_2 are the hydraulic efficiencies and Re_1 and Re_2 are the Reynolds numbers of the original and upscaled pumps, respectively.

3.1.2 Simscape™ Centrifugal Pump Modelling

Simscape™ includes a built-in centrifugal pump block which can be modelled via two different two-dimensional characteristics, namely the pressure versus flow rate and the power versus flow rate relationships. The relationships have already previously been graphically presented in Figure 3.1 in Section 3.1. The actual angular velocity of the pump, ω, is compared to the reference angular velocity, ω_{ref}, to obtain the actual pressure, p, in relation to the reference pressure, p_{ref}, within the said curves. The same process is repeated for the actual and reference powers, P and P_{ref}, respectively. Equations 3.14 and 3.15 present the equations applied for this procedure to be performed in Simscape™, with the same affinity laws listed in equations 3.2 and 3.3 being applied hereunder [134]:

$$p = p_{ref}\left(\frac{\omega}{\omega_{ref}}\right)^2 \tag{3.14}$$

$$P = P_{ref}\left(\frac{\omega}{\omega_{ref}}\right)^3 \tag{3.15}$$

3.1.3 Filtration Pressure Drop Modelling

Given that in the present study the centrifugal pump is modelled to operate in an open seawater environment, a water filtration system is to be included in order to model the pressure drop due to the presence of a mesh filter. In the case of centrifugal pumps, filtration of 500 to 1000 microns is sufficient [135]. Luan et al. [136] describe a method to calculate pressure drop across a wire mesh filtration system. Firstly, the fluid velocity, v_{fluid}, must be calculated based on equation 3.16:

$$v_{fluid} = \frac{Q}{A_p} \tag{3.16}$$

Where Q is the flowrate and A_p is the pipe cross-sectional area.

Once the fluid velocity is calculated, the Reynolds numbers with respect to geometric data of the wire diameter, d_{wire}, the layer spacing, σ, and the mesh size, l, could all be calculated as presented in equations 3.17 to 3.19 on the following page:

$$Re_d = \frac{v_{fluid}\, d_{wire}}{\vartheta} \tag{3.17}$$

$$Re_\sigma = \frac{v_{fluid}\, \sigma}{\vartheta} \tag{3.18}$$

$$Re_l = \frac{v_{fluid}\, l}{\vartheta} \tag{3.19}$$

Where ϑ is the kinematic viscosity of the fluid. Once the three Reynolds numbers are calculated, the pressure drop, ΔP_{mesh}, could be determined via equation 3.20 [136]:

$$\Delta P_{mesh} = 10 n_l Re_d^{0.77}\, Re_\sigma^{-0.09}\, Re_l^{-1.03}\, \frac{\rho_{sw} {v_{fluid}}^2}{2} \tag{3.20}$$

Where n_l is the number of mesh layers and ρ_{sw} is the seawater density.

3.2 Performance Modelling of Pelton Turbines

Similar to centrifugal pumps, different turbines have varied specific speeds, where Pelton turbines fall under the spectrum of the lowest specific speeds in comparison to other turbines, such as the Francis and Kaplan turbines. Equation 3.21 presents the specific speed formula, N_s, for hydraulic turbines [92]:

$$N_s = \frac{\omega \sqrt{P}}{H^{\frac{5}{4}}} \tag{3.21}$$

Once confirming that the turbine selected falls within the specific speed range, the water jet speed can be calculated since this parameter is proportional to the square root of the head at nozzle entry, H_{NE}, as shown in equation 3.22 hereunder:

$$v = C_v \sqrt{2 g H_{NE}} \tag{3.22}$$

Where v is the jet speed and C_v is the nozzle velocity coefficient. One of the fundamental parameters related to Pelton turbines is the bucket to jet speed ratio, $\emptyset$.

While it can be theoretically shown that the optimal value for ratio to reach peak hydraulic efficiency is 0.50, values anywhere between 0.46 and 0.48 are typically applied due to losses originating from aerodynamic drag and friction [78]. The bucket speed, v_{bucket}, to jet speed, v_{jet}, ratio is presented in equation 3.23 [91], [137]:

$$\emptyset = \frac{v_{bucket}}{v_{jet}} \tag{3.23}$$

Once the bucket speed is found based on the assumed bucket to jet speed ratio, the force on the buckets, F, could be calculated using:

$$F = \rho A v (v_{jet} - v_{bucket})(1 + kcos(\theta)) \tag{3.24}$$

Where A is the nozzle cross-sectional area, k is the bucket friction coefficient and θ is the bucket angle. The turbine's hydraulic and jet powers, P_H and P_J respectively, can then be calculated via equations 3.25 and 3.26:

$$P_H = F \times v_{bucket} \tag{3.25}$$

$$P_J = \frac{1}{2}\rho A {v_{jet}}^3 \tag{3.26}$$

Additionally, the nozzle power can also be required since this is a pivotal component in calculating the overall efficiency of the Pelton turbine. Equation 3.27 presents the nozzle power, P_N,:

$$P_N = gQH_{NE} \tag{3.27}$$

The overall Pelton turbine efficiency, η_{ovr}, is comprised of a number of efficiencies shown in equation 3.28 hereunder:

$$\eta_{ovr} = \eta_{mech} \times \eta_H \times \eta_{nozzle} \times \eta_{pipeline} \tag{3.28}$$

Where η_{mech} is the mechanical efficiency, η_H is the hydraulic efficiency, η_{nozzle} is the nozzle efficiency and $\eta_{pipeline}$ is the pipeline efficiency [91], [137].

3.2.1 Pelton Turbine Sizing

Zaw Oo et al. [138] described the procedure required in correctly designing a Pelton turbine based on a variety of theoretical and empirical formulae. The first step is to calculate an approximate jet diameter based on the flow rate and head requirements of the Pelton turbine, as shown in equation 3.29 hereunder:

$$d_j = \sqrt[3]{\frac{4Q}{z\pi\sqrt{2gH_{NE}}}} \tag{3.29}$$

Where d_j is the jet diameter, Q is the discharge flow rate and z is the number of nozzles. A number of empirical formulae may then be used in order to obtain the bucket width and the number of buckets making up the turbine. The bucket width is taken to be approximately 4 times the jet diameter, as shown in equation 3.30. The number of buckets is then calculated by applying equation 3.31 [138]:

$$B = 4d_j \tag{3.30}$$

$$Z = 0.5\frac{D}{d_j} + 15 \tag{3.31}$$

Where B is the bucket width, Z is the number of buckets and D is the Pelton runner diameter.

3.2.2 Pelton Turbine Efficiency Losses

To accurately predict the hydraulic turbine performance, the losses associated with Pelton turbine operation have to be quantified. The losses mainly include frictional and windage losses. Zhang [91] explained that aerodynamic losses such as windage are directly related to the effect the air has around the Pelton wheel and buckets during operation. The frictional losses mentioned comprise of bearing friction losses. Equation 3.32 presents the equation applied to calculate the bearing friction power losses, $P_{friction}$:

$$P_{friction} = K_b \times M_b \times \omega \tag{3.32}$$

Where K_b is the bearing friction coefficient which is a function of the bearing type, temperature and lubricant viscosity, M_b is the bearing frictional torque and ω is the turbine rotational speed [91] [139]. In order to calculate the bearing frictional torque, the bearing reaction forces were to be calculated, as shown by Petley et al. [140]. Once calculated, the SKF bearing calculator [141] could be used to obtain the bearing torque, and thus obtain the friction power loss as shown in equation 3.32. Zhang [91] derived an equation whereby windage losses are a resultant of the Pelton turbine rotational speed, runner diameter, as well as a number of geometric ratios of a horizontal axis turbine design. Figure 3.3 shows the geometric values required for accurately obtaining the power losses due to windage, $P_{windage}$. Equation 3.33 provides the windage power loss calculation, which assumes that the Pelton turbine is operating in atmospheric conditions.

$$P_{windage} = 15\left(\frac{\omega}{2\pi}\right)^3 D^5 (R_1)^{\frac{1}{4}} (R_2)^{\frac{3}{4}} (R_3)^{\frac{5}{4}} (R_4)^{\frac{7}{4}} \tag{3.33}$$

Where R1 to R4 are Pelton turbine geometric approximations. As already mentioned previously, the above equation represents frictional power loss for a Pelton turbine operating in atmospheric conditions. If the turbine were to operate in a subsea, encapsulated area, the constant would vary as a function of air density. In the case of the turbine operating in an environment which is not atmospheric, equation 3.33 is updated as shown in equation 3.34 hereunder:

$$P_{windage} = 10^{-4} \times C_f Re \rho_{air} \left(\frac{\omega}{2\pi}\right)^3 D^5 (R_1)^{\frac{1}{4}} (R_2)^{\frac{3}{4}} (R_3)^{\frac{5}{4}} (R_4)^{\frac{7}{4}} \tag{3.34}$$

Where C_f is the air friction coefficient, Re is the Reynolds number and ρ_{air} is the air density of the Pelton turbine's operating environment [90], [108], [142].

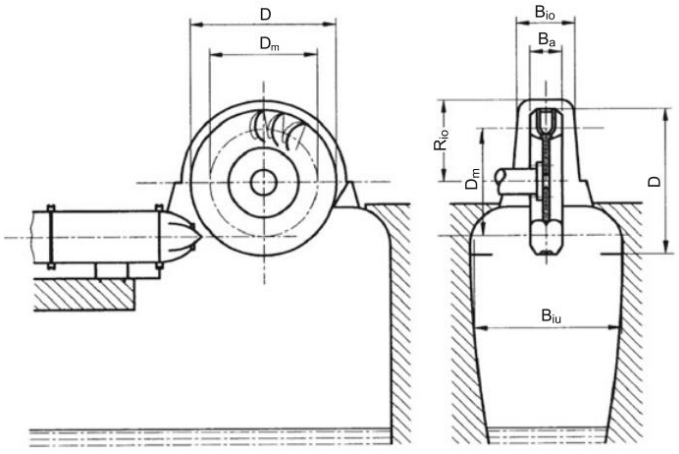

Figure 3.3: Main geometric parameters required for windage loss calculations [91].

3.2.3 Simscape™ Model for the Needle Valve

Figure 3.4 presents a schematic of the needle valve, highlighting all necessary geometric parameters influencing the design of the valve. The flow rate through the valve is calculated via equation 3.35 [143]:

$$Q = C_D A(h)\sqrt{\frac{2}{\rho}}\frac{\Delta p}{(\Delta p^2 + p_{Cr}^2)^{\frac{1}{4}}} \qquad where\ p_{cr} = (\Delta p + p_{atm})(1 - B_{lam}) \qquad (3.35)$$

Where C_D is the discharge coefficient, *A(h)* is the valve area as a function of valve position h, p_{cr} is the minimum pressure for turbulent flow, B_{lam} is the laminar flow pressure ratio and Δp is the differential pressure. The maximum valve position, h_{max} results in the maximum needle valve area, A_{max}, presented in equation 3.36. The maximum valve position, h_{max} is calculated as a function of the valve diameter, d_s, and the needle valve angle, α, as shown in equation 3.37 [143]:

$$A_{max} = \frac{\pi d_s^2}{4} \qquad (3.36)$$

$$h_{max} = d_s \frac{1 - \sqrt{1 - \cos\left(\frac{\alpha}{2}\right)}}{\sin(\alpha)} \qquad (3.37)$$

The maximum valve position, h_{max} results in the maximum needle valve area, A_{max}. The area at the minimum, maximum and in between the extremes is calculated via the relationships presented in equation 3.38:

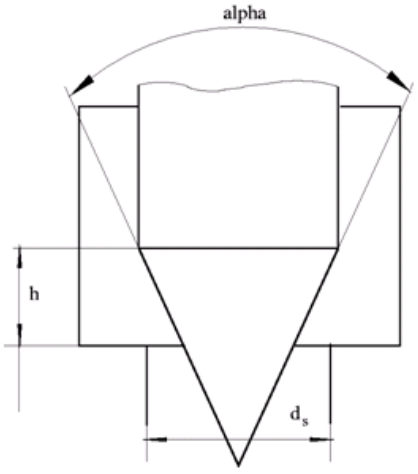

Figure 3.4: Needle Valve schematic model [143].

$$A(h) = \begin{cases} A_{leak} & \text{for } h \leq 0 \\ \pi\,(d_s - h\sin\left(\frac{\alpha}{2}\right)\cos\left(\frac{\alpha}{2}\right))\,h\sin\left(\frac{\alpha}{2}\right) + A_{leak} & \text{for } 0 < h < h_{max} \\ A_{max} + A_{leak} & \text{for } h \geq h_{max} \end{cases} \quad (3.38)$$

Where A_{leak} is a constant value representing fluid flow leakage [143].

3.3 Pipe Sizing

Selecting the correct pipe diameter size involves an iterative process based on the expected fluid flow rate within the piping, the internal roughness of the pipe as well as the secondary head losses within the pipe. The above parameters are all related through the Moody Chart, presented in Figure 3.5. Equation 3.39 calculates the Reynolds number, Re, as follows [100]:

$$Re = \frac{4Q}{\pi D_p \vartheta} \quad (3.39)$$

Where Q is the fluid flow rate, D_p is the pipe diameter and ϑ is the kinematic viscosity of the fluid.

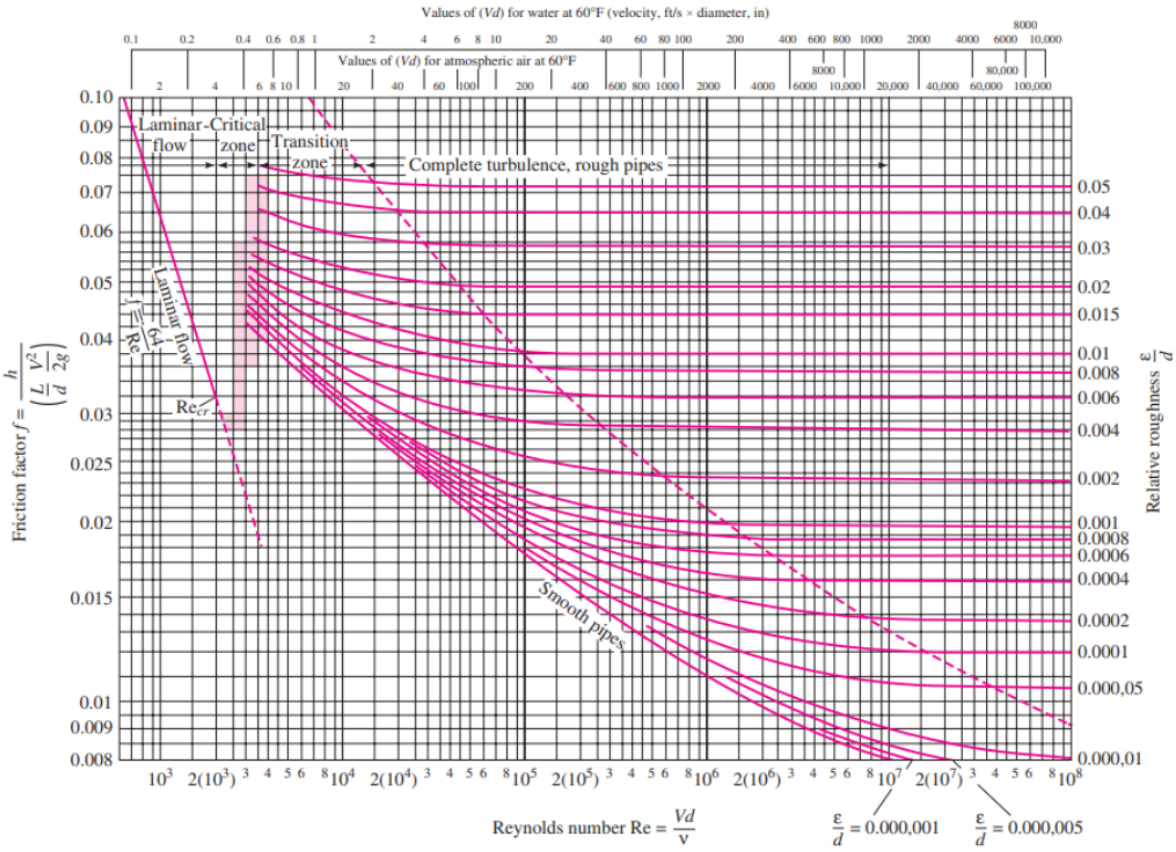

Figure 3.5: The Moody Chart, extracted from [100].

The relative roughness, R_r, can then be obtained based on the pipeline type, as described by Farshad et al. [144],and as presented in equation 3.40 [100]:

$$R_r = \frac{k}{D_p} \tag{3.40}$$

Where k is the roughness constant. Lastly, once the Moody Chart is used to estimate the friction factor, f, equation 3.41 can be implemented to find the secondary head losses, h_f:

$$h_f = \frac{16fLQ^2}{2g\pi D_p^3} \tag{3.41}$$

Where L is the pipe length. Apart from the head losses due to the friction factor, h_f, the resistance coefficients based on other minor or local losses such as valves and elbows must also be considered. As a result, the total secondary head loss, Δh_{total}, is represented via equation 3.42 [100]:

$$\Delta h_{total} = \frac{v_{fluid}^2}{2g}\left(\frac{fL}{D_p} + \sum K\right) \tag{3.42}$$

Where v_{fluid} is the fluid velocity and K is the summation of various resistance coefficients based on the piping system implemented [100]. The above equations are repeated until a pipe diameter which has a satisfactory limit of secondary losses is found.

3.3.1 Simscape™ Model for a Hydraulic Resistive Tube

The Simscape™ model for the piping system is represented by the hydraulic resistive tube. The built-in model assumes that flow is fully developed throughout the pipes' length and also neglects fluid inertia and fluid compressibility. Similarly to Section 3.3, the pressure losses within the Simscape™ pipe model (shown in equation 3.43) are calculated by means of the Darcy Equation, however the pipe length is represented in two parts; Firstly is the pipe actual length, L, and secondly is the pipe's equivalent length of local resistances, L_f. The latter is what replaces K in equation 3.42 presented previously [145].

$$p = f\frac{(L + L_f)}{D_{pipe}}\frac{\rho}{2A_{pipe}^2}\, Q\,|Q| \tag{3.43}$$

Where A_{pipe} is the pipe cross-sectional area and f is the friction factor as a function of Reynolds number, previously shown in equation 3.39.

The friction factor, f, is calculated differently within the Simscape™ model to the iterative process of using the Moody Chart shown previously in Figure 3.5 in Section 3.3. Equation 3.44 presents the friction factor, f, for laminar and turbulent flow respectively:

$$\mathrm{f} = \begin{cases} \dfrac{K_s}{Re} & \text{for } Re \leq Re_L \\ \dfrac{1}{\left(-1.8\log_{10}\left(\dfrac{6.9}{Re} + \left(\dfrac{\frac{r}{D_p}}{3.7}\right)^{1.11}\right)\right)^2} & \text{for } Re \geq Re_T \end{cases} \tag{3.44}$$

Where K_s is the shape factor of the pipe cross-section, r is the surface roughness height, while Re_L and Re_T are the laminar and turbulent Reynolds number limits respectively.

3.4 Pressure Containment System (PCS)

The pressure containment system of the HPES system consists of a accumulator that is pre-charged with a pressurised gas. Energy is stored by injected seawater to compress the gas. The filling or discharging of seawater leads to changes in the air's pressure within the accumulator. Figure 3.6 shows a schematic of the accumulator, and the main parameters associated with its numerical modelling. The calculations of the fluid volume and compressed air pressure within the containment system are obtained via equations 3.45 and 3.46 respectively:

$$V_{F_t} = V_{F_t-1} \pm (Q \times dt) \tag{3.45}$$

$$p_G = \frac{(p_{pr} + p_A)}{(V_T - V_{Ft}) \times V_T} - p_A \tag{3.46}$$

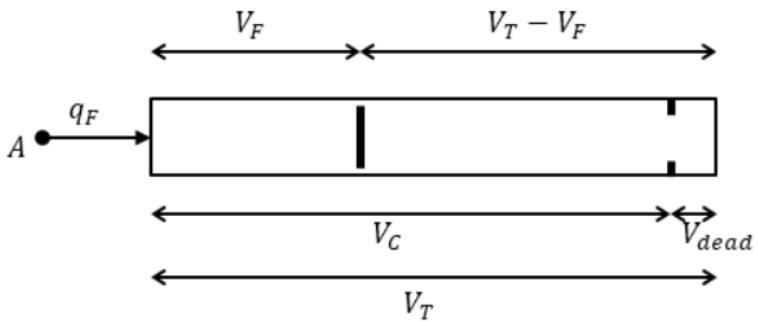

Figure 3.6: A schematic of a gas-charged accumulator [146].

Where V_{F_t} and V_{F_t-1} are the PCS fluid volumes at the current and previous timesteps, Q is the flow rate, where the positive or negative symbols are applied based on if fluid is entering or exiting the PCS respectively, dt is the timestep, p_G is the PCS gauge pressure at the current timestep, V_T is the total PCS volume and p_{PR} and p_A represent the gauge pre-charge (minimum) pressure and atmospheric pressure, respectively. Equation 3.46 is a simplified version of the equation utilised by the Simscape™ gas-charged accumulator model [146], based on the assumption that the HPES system is isothermal since it uses the surrounding seawater as a heat sink [51], [147].

In order to calculate the storage capacity of the containment system, the pressure ratio applied must be established. Equation 3.47 presents the ratios presented by Cutajar et al. [148] as a function of pressure, r_p, or volume, r_v:

$$r_p = \frac{p_{max}}{p_{pr}} = \left(\frac{V_1}{V_2}\right)^n = r_v^n \tag{3.47}$$

Where p_{max} is the upper pressure limit (when fully charged), $p_{pr}$is the pre-charge pressure (when fully discharged) and volumes V_1 and V_2 are the initial and final volumes (i.e., fully discharged and fully charged states). Once the pressure or volume ratios are found, the energy storage capacity, E, measured in kWh, can be calculated by implementing equation 3.48 hereunder:

$$E = \frac{p_{max}V_2\ln(r_v) - p_{hyd}V_2(r_v - 1)}{3600(10^3)} \tag{3.48}$$

Where p_{hyd} is the hydrostatic pressure based on the subsea depth positioning of the accumulator.

3.4.1 Check Valve

Since charging and discharging of the PCS must occur based on power surplus or deficit, a check valve must be included in the accumulator modelling in order to allow fluid flow in one direction only, while blocking it in the opposite direction. Figure 3.7 presents a graph depicting the working principle of the check valve. The valve linearly opens up once the crack differential pressure is reached and opens linearly until the maximum possible opening. If the check valve is desired to be opened fully immediately, the crack pressure, p_{crack}, can be set to be the maximum pressure, p_{max} [149].

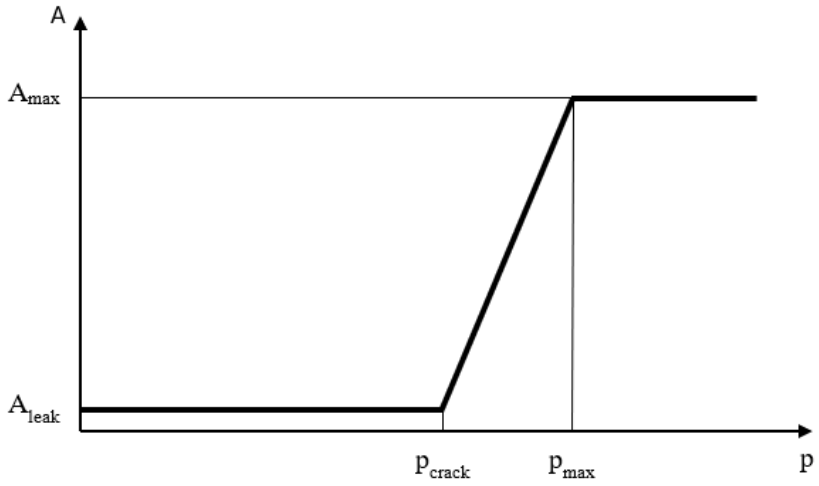

Figure 3.7: The relationship of valve area and differential pressure for check valve operation [149].

The flow rate and critical pressure calculation is once again carried out using equation 3.35 shown previously in Section 3.2.3. While A_{max} is also calculated as previously shown in using equation 3.36 in Section 3.2.3, the check valve area is calculated as a function of pressure instead of a function of horizontal position as in the case of the needle valve. Equation 3.49 presents the relationships based on the pressure experienced at the check valve as a result of centrifugal pump pressure output [149]:

$$A(p) = \begin{cases} A_{leak} & \text{for } p \leq p_{crack} \\ A_{leak} + k(p - p_{crack}) & \text{for } p_{crack} < p < p_{max} \\ A_{max} & \text{for } p \geq p_{max} \end{cases} \quad (3.49)$$

Where A_{leak} is the leakage area and k is a ratio between valve area and differential pressure, presented in equation 3.50:

$$k = \frac{A_{max} - A_{leak}}{p_{max} - p_{crack}} \quad (3.50)$$

3.5 PID Control Theory

Proportional-Integral-Derivative (PID) control consists of an algorithm made up of three coefficients: the proportional, integral and derivative terms. PID control is easily applicable to different applications within the world of engineering due to its robustness and simplicity. The main terms are shown in Figure 3.8 and listed [150]:

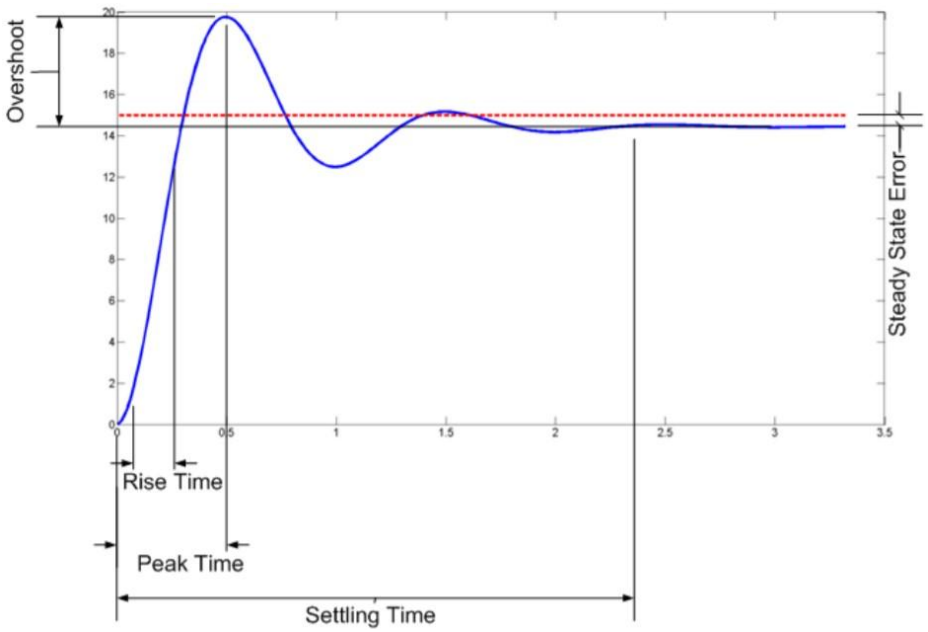

Figure 3.8: A linear system step response, showing parameters for response optimisation [151].

- Overshoot: The percentage of how much the system output exceeds the steady state output value by.
- Dead Time: The time required for the response to plot the occurrence of a change in the system.
- Rise Time: The time taken for the system response to rise from 10 to 90% of its final value (1 if the final value is a step response).
- Settling Time: The time required for the step response to maintain its value within a specified range of the final value (usually 5%).
- Steady State Error: The difference between the desired setpoint and the final response value.

Obtaining a desirable response requires defining various terms to understand the responses' characteristics [151]. The PID control systems can either be open loop or closed loop systems. When feedback is not provided and the system does not respond or react to external factors, the system is referred to as an open loop system. On the other hand, when the system output is fedback into the input signal, thus influencing the said input, the system is a closed loop system. Closed loop systems are more advantageous since they allow for a safer system overall, since the system is able to adapt to external disturbances. Figure 3.9 shows a block diagram representation of an open and closed loop system, respectively [150], [152].

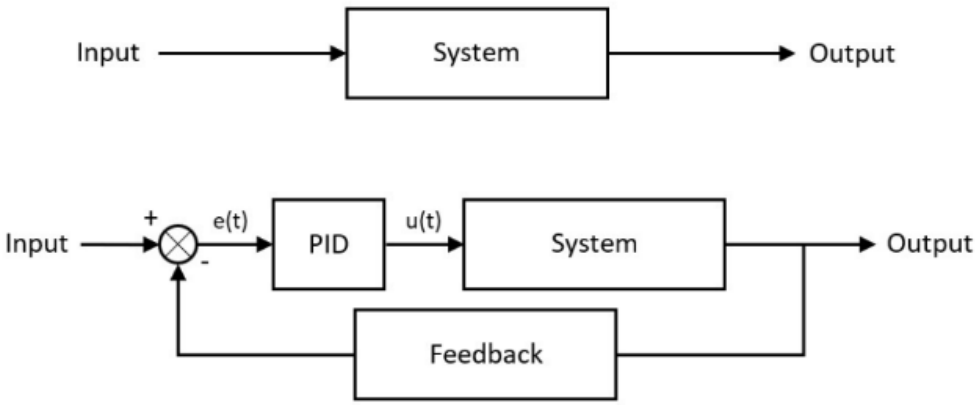

Figure 3.9: An open loop (top) and closed loop (bottom) control system [152].

The P, I and D coefficient values are obtained with the help of existing tuning methods to get the desired response the user requires for the application in question, with manual tuning allowing for minor adjustments to obtain optimal operating conditions [150], [153], [154].

3.6 Overview of the Existing Toolboxes in Simscape™

In order to obtain a fully operative system within the Simscape™ environment, multiple toolboxes with a graphical user interface were implemented where some toolboxes required custom inputs while some did not. The following sub-sections present a brief explanation of what each toolbox was used for and how it is modelled.

3.6.1 Three-Phase Source

The Three-Phase Source was implemented in order to provide electrical power to the Direct Torque Control Induction Motor Drive, explained in detail in the upcoming Section 3.6.2. All parameters were kept at their default value; however the phase-to-phase voltage was adjusted in order to match with the operating voltage of the induction motor connected to the centrifugal pump model [155].

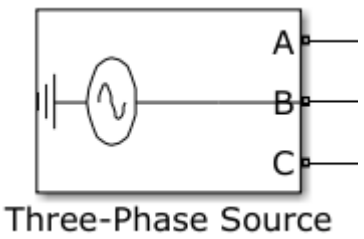

Figure 3.10: The Three-Phase Source Simscape™ block [155].

3.6.2 Direct Torque Control (DTC) Induction Motor Drive

The DTC Induction Motor Drive block (shown in Figure 3.11) is divided into three main parts; namely the Asynchronous Machine directly connected to the centrifugal pump shaft, the converters and DC bus and finally, the speed controller. The Asynchronous Machine parameters consist of a mixture of electrical and mechanical parameters, and the governing equation is presented hereunder in equation 3.51 [156]:

$$T_e = J\frac{d}{dt}\omega_r + F\omega_r + T_m \tag{3.51}$$

Where T_e is the electromagnetic torque, J is the motor inertia, F is the friction factor, ω_r is the pump's motor rotational speed, and T_m is the mechanical torque. The mechanical input of the toolbox block can either be a mechanical torque, T_m or a rotational speed, ω_r. Meanwhile, the output can also be a speed, a torque, or can be a mechanical rotational port which connects to the Simscape environment. The differential equation presented in equation 3.51 applies to all input and output options. The equivalent circuit parameters, namely the main winding of the stator and rotor must be calculated based on the selected generator and then converted to SI units [157]. The electrical components such as the rectifier, braking chopper and inverter all retained default Simscape™ values. Lastly, the block consists of an in-built speed controller to match the desired input speed set. The controller is a Proportional Integral (PI) controller, and also has a ramp rate limiter to restrict the increase or decrease the motor's rpm per second. The DTC controller can be modulated through Hysteresis or Space Vector Modulation (SVM), however the Direct Torque Control methodology is more commonly utilised for the use in this case [158], [159].

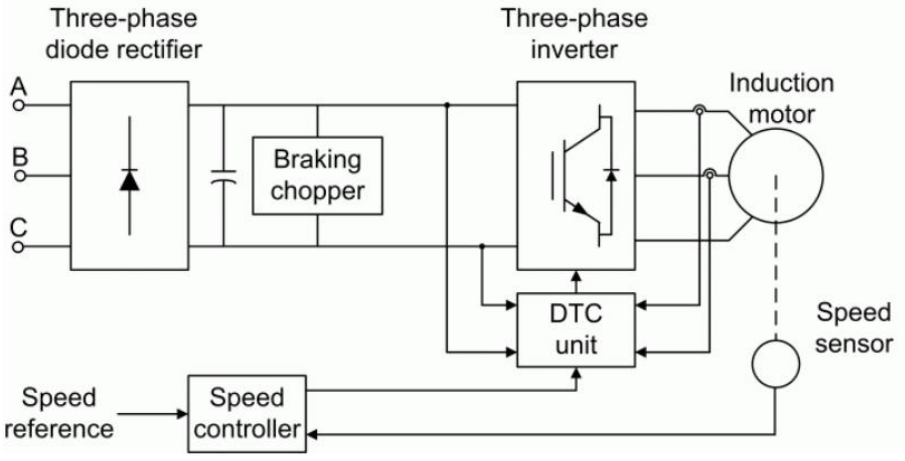

Figure 3.11: A schematic of the Direct Torque Control setup [156].

3.7 Time Series Forecasting Python™ Statistical Models

Python™ consists of a statistical model which gives access to in-built toolboxes with different data science and artificial intelligence models. One of the main models which applies to this study is the SARIMA model, previously explained in Section 2.4. Prior to implementing the SARIMA model, the Augmented Dickey-Fuller (ADF) test is carried out to check for data stationarity by analysing if the Auto Regressive (AR) model has a unit root [160]. Stationarity signifies that the probability distribution of a stochastic process is independent of time [131]. Equation 3.52 shows the ADF equation which tests whether $\gamma = 0$, with the null hypothesis stating that the data is non-stationary.

$$\Delta y_t = \alpha + \beta t + \gamma y_{t-1} + \delta_1 \Delta y_{t-1} + \delta_2 \Delta y_{t-2} + \ ... \tag{3.52}$$

Where y_t is the data input, α is a constant value and β reflects a time trend coefficient. The Seasonal Auto Regressive Integrated Moving Average (SARIMA) forecasting tool in-built in Python™ is best suited whenever the data being dealt with has a seasonality to it [161]. The SARIMA model in Python™ is represented as $(p, d, q) \times (P, D, Q)_s$, where p and q are the AR and moving average (MA) order terms respectively, with d being an integer to represent differencing (only necessary if data is non-stationary). Meanwhile, P, D and Q represent the seasonal component and s is the seasonal period. Equation 3.53 shows the SARIMA model equation.

$$\emptyset_p(L)\widetilde{\emptyset_p}(L^S)\Delta^d\Delta_s^D y_t = A(t) + \theta_q(L)\widetilde{\theta_q}(L^S)\zeta_t \tag{3.53}$$

where $\emptyset_p$ and $\widetilde{\emptyset_p}$ represent the AR and seasonal AR orders respectively, θ_q and $\widetilde{\theta_q}$ are the MA and seasonal MA orders, Δ^d and Δ_s^D are the differencing and seasonal differencing orders (if required), y_t is the time-series data and L, $A(t)$ and ζ_t are the lag operator, the trend component and white noise respectively.

4 METHODOLOGY

This following chapter describes the approach taken in aiming to meet the objectives, answer the research questions and test the hypothesis presented previously in Chapter 1. This chapter outlines the path taken throughout the study, explaining the different numerical codes developed and the correlations between them, while providing a clear rationale for the creation of each software model. The set-up of the ECU system hydraulic machinery and a detailed view of the overall baseline ECU design are also presented.

4.1 Study Roadmap

The study roadmap provides the step-by-step approach taken over the course of the study to meet the objectives set at the start of the study. The roadmap is setup as follows:

1. Prior to commencing the numerical modelling, the hydraulic machinery making up the ECU were selected or designed to meet the main requirement of being megawatt-scale rated machinery. The centrifugal pump was up-scaled from an existing centrifugal pump model, while the Pelton turbine was also modelled based on an existing model. The PCS sizing was obtained via documentation by industrial collaborators FLASC B.V. (explained throughout Section 4.2).
2. Once the baseline design was developed, the different numerical models were developed, each with their specific rationale (explained further in Section 4.3). The models were validated via testing and model results for the same tests were compared (explained further in Section 5.3). Some of the models were also used for more time series simulations to perform parametric analyses related to ESS capacity and power smoothing fluctuations (explained further in Sections 7.3 and 7.4 respectively). The tests performed were carried out using Baseline Data, presented in Section 4.4. The same Baseline Data was once again utilised throughout Chapters 7 and 8.

3. Following the numerical models, a statistical analysis on Excel® was performed (presented in Chapter 7) related to the evaluation of energy storage requirements in the central Mediterranean Sea. The reason for selecting Excel® was to carry out a more long-term analysis (in the order of magnitude of years). For simplification purposes, the efficiency of the hydraulic machinery was fixed and a parametric analysis varying the average operational efficiency was performed.
4. The latter study allowed for a techno-feasibility case study to be performed (presented in Chapter 8), with the aim of studying the incorporation of the HPES system within a novel floating breakwater design making part of a marine park.

4.2 The Baseline Design for the ECU and PCS

Initially, the setup of the ECU design to be used throughout testing and analysis was to be specified. Figure 4.1 presents a schematic of the ECU and PCS system.

The MW-scale ECU consists of a variable speed, multi-stage centrifugal pump and a Pelton turbine. The multi-stage centrifugal pump must operate at variable speeds depending on the PCS state of charge since, unlike in pumped-hydro energy storage, the centrifugal pump will have to operate under large variable-head conditions required by the HPES system [162], [163], [164]. The characteristic curves of the centrifugal pump assumed throughout this study are presented in Figure 4.2.

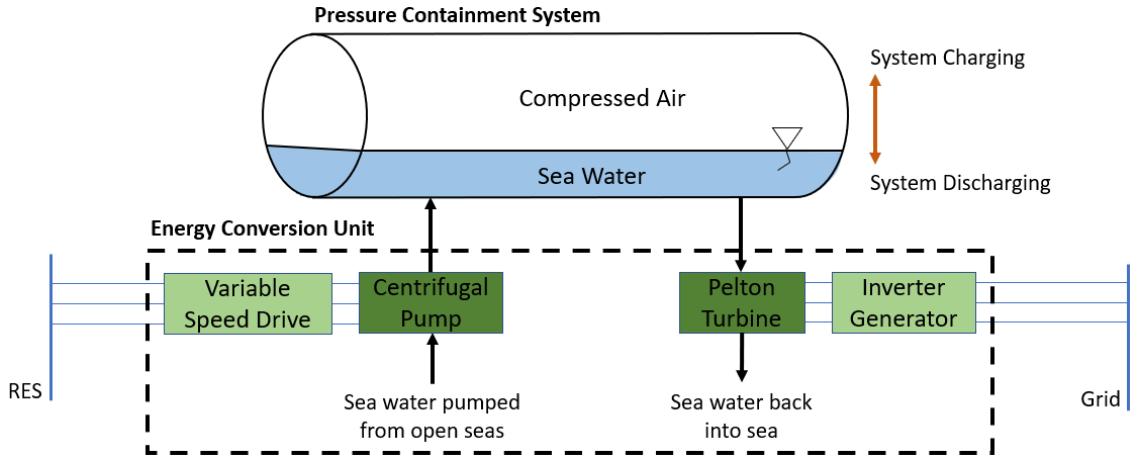

Figure 4.1: Schematic showing the offshore HPES system, highlighting the ECU and PCS.

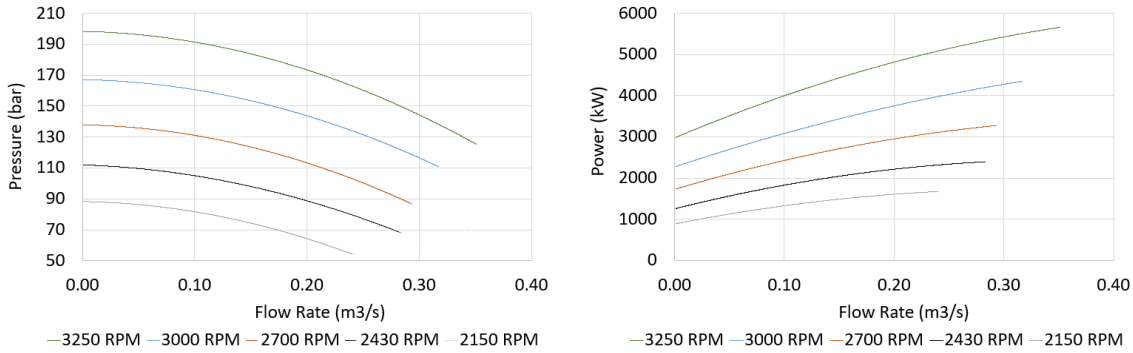

Figure 4.2: Centrifugal pump (left) pressure versus flow rate characteristic curves; (right) power versus flow rate characteristic curves.

Due to the scarcity of open-source MW-scale centrifugal pump curve availability, these curves were derived from an existing MW-scale centrifugal pump curves obtained via a non-disclosure agreement (NDA) by applying dynamic similarity rules based on the Head, Flow rate, and Power coefficients shown in equations 3.8 to 3.10 in Section 3.1.1.

The Reynolds number has been ignored; however, Reynolds number effects were considered to obtain the efficiency changes due to upscaling as previously explained and shown by means of equation 3.13 in Section 3.1.1. Table 4.1 presents the main existing and up-scaled centrifugal pump values.

Similar to the pump, the Pelton turbine operates at a variable speed and with a large variable head, whereby both speed and nozzle orifice are varied to supply the output power required, while also maintaining an optimal bucket to jet speed ratio of approximately 0.48 [91], [137]. This value is taken from the literature, where the theoretical optimal ratio is 0.50; however, it becomes 0.48 due to viscous friction and windage losses due to bucket aerodynamic drag [91], as previously mentioned in Section 2.4.1.

Table 4.1: Existing pump and up-scaled pump model parameters.

	Original Pump	Up-scaled Pump
Impeller Diameter (m)	0.50 m	0.40 m
Number of Stages	8	9
Maximum Efficiency (η_{pump})	0.80	0.82
Rated Power (P_{H_p})	3000 kW	4300 kW
Rated Speed (ω)	1800 RPM	3250 RPM
Maximum Head (H)	1100 m	1987 m

Figure 4.3 shows the hydraulic power curves for the MW-scale PCS system in the study. The ECU components were designed and selected based on the PCS requirements of the full-scale HPES system having an operating pressure range of between 80 and 200 bar [148]. The pressure range selected is based on previous work by Cutajar et al. [148], who found that the most cost-effective design to minimise material requirements in terms of kilogram of steel per unit of stored energy (kg/kWh) occurred at an approximate pressure ratio of 2.5 and for a maximum compressed air pressure of 200 bar, which is the typical working pressure for offshore pipelines. Additionally, the compression and expansion processes of the PCS were assumed to be isothermal since the PCS is considered to be located in a subsea environment, thus using the surrounding seawater as an excellent heat sink and heat source [51], [147]. Table 4.2 summarises the main parameters of the horizontal shaft Pelton turbine wheel and, finally, the PCS parameters are also shown in Table 4.3 [148], [165].

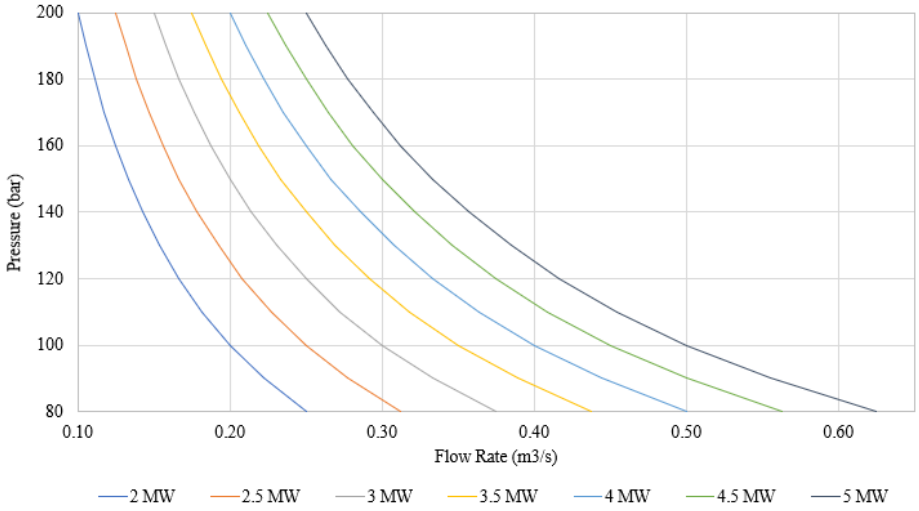

Figure 4.3: The hydraulic power curves of the FLASC system.

Table 4.2: Main parameters of the Pelton turbine.

Pelton Turbine Parameter	Value
Rated Power (P_{H_t})	5.00 MW
Rated Speed (ω_{Pelton})	426 RPM
Maximum Efficiency (η_{Pelton})	92%
Runner Diameter (D)	3.78 m
Bucket to Jet Speed Ratio ($\emptyset$)	0.48
Generator Efficiency (η_{gen})	0.95
Number of Nozzles (N)	2
Skin Friction Coefficient (k)	0.97
Jet Angle (β)	165°

Table 4.3: Main parameters of the PCS.

PCS Parameter	Value
Pre-charge (Minimum) Pressure (p_{pr})	80 bar
Pressure Limit (p_{max})	200 bar
Total Volume (V_T)	4080 m^3

4.2.1 Piping System Sizing

In order to implement a pipe size which did not cause excessive head losses and secondary losses, an iterative process was applied until a satisfactory pipe diameter was calculated. The iterative process applies equations 3.39 to 3.41, previously presented in Section 3.3 [166]. The relative roughness for an assumed internally-coated pipe was extracted from [167]. Once the losses were calculated, the secondary losses resulting from any pipe local resistances were calculated by applying the relevant resistance coefficients to equation 3.42, also presented in Section 3.3 [100]. Table 4.4 presents the final pipe diameter selected, together with the maximum head losses associated with the piping system applied for the study (shown in Figure 4.4). The percentage pressure loss in the pipes was calculated by finding the ratio between the pipe pressure loss and the system's pre-charge pressure (i.e., 80 bar as shown in Table 4.3).

Table 4.4: A summary of the final pipe diameter selected and assumed lengths selected for the piping system presented in Figure 4.4.

Piping Parameter	Value
Pipe Diameter (d_{pipe})	0.36 m
Relative Roughness (k)	0.0000127
Number of Pipe Bends	2
Bend Resistance Coefficient (k_{bend})	0.125
Length of Pipe 1	30 m
Length of Pipe 2	0.50 m
Length of Pipe to Accumulator	100 m
Total Pressure Loss due to Piping (p_{loss})	0.99%

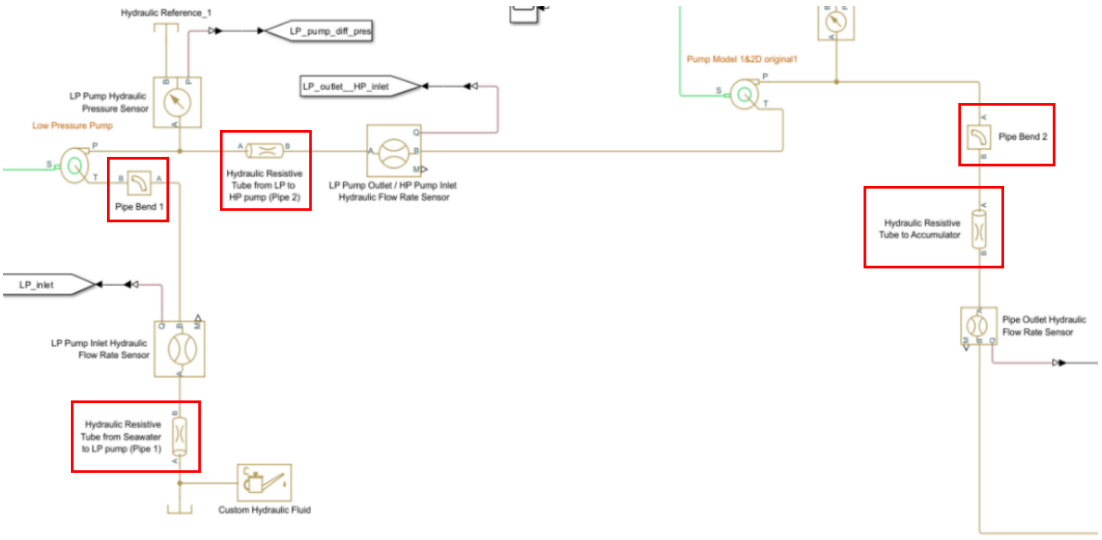

Figure 4.4: An image indicating all pipes considered to calculate the expected head secondary losses in the system, as implemented in MATLAB Simscape™.

4.2.2 Pump Model Verification Tests

Since the pump data was manually inputted in the form of tables from the pump curves, ensuring that the data was being extracted and interpolated correctly by the model was imperative. As a result, the model was built in stages, with the first stage assuming an ideal velocity source. As a result, the focus in Figure 4.5 was to apply different constant speeds and different pressure differentials across the pump's inlet and outlet and in turn, read the corresponding output flow rate and efficiency.

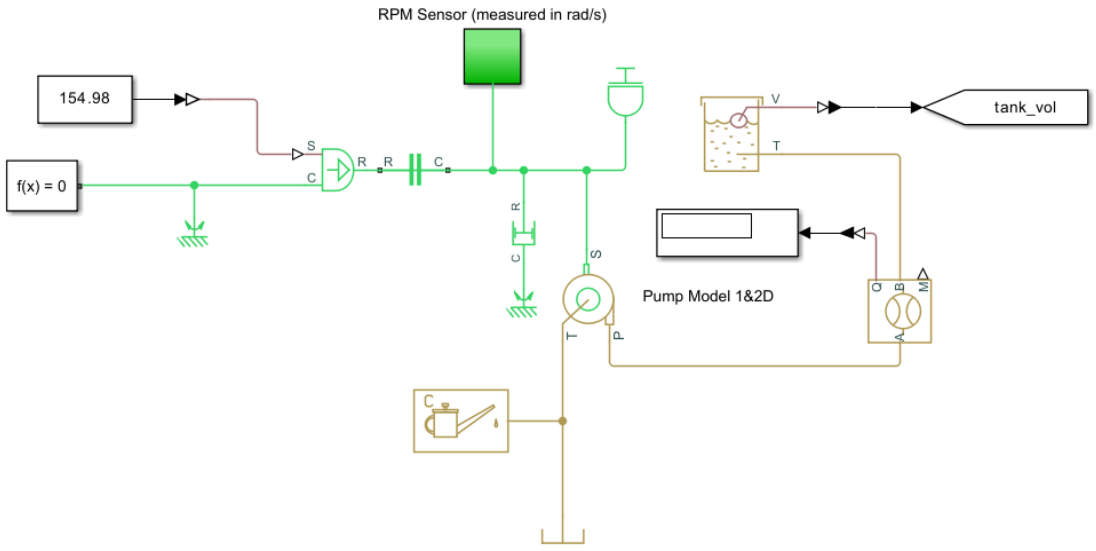

Figure 4.5: A basic model to test the inputting of pump characteristic data.

4.3 Overview of the Developed Numerical Models

The first code development carried out is a code in Python™, titled the Alpha model. This model involves the creation of mathematical equations of a centrifugal pump and a Pelton turbine and includes an accumulator or pressure vessel which is used to carry out the charging and discharging cycles involved in HPES, as explained in Section 2.1.5. The aim of the Alpha model was to create a quasi-steady state and computationally efficient, yet accurate model of the FLASC HPES system which allows the modelling and analysis of a variety of pump and turbine models due to the flexibility in input parameters offered. The novelty of the work is the development of a reliable numerical code which is able to model the performance of the ECU and overall HPES system at MW-scale.

The Beta model is a more detailed and computationally demanding numerical model which aims to provide a more realistic operational scenario by accounting for transients, hydraulic component inertias, hydraulic pipe losses, and includes a number of electrical black boxes. The Beta model is based on MathWorks® Simulink® and Simscape™ and provides an approximation on how a MW-scale system would operate without the need for physical prototyping, which can lead to great expenditure.

The reason for using different compiling codes for above numerical models was that Python™ provided a high degree of computational efficiency and versatility in developing simplified in-house codes. On the other hand, MathWorks® Simulink® and Simscape™ provided in-built toolboxes for modelling complex hydraulic systems that take into account complex phenomena such as transient effects and compressibility, at the expense of higher computational demands.

The Alpha Plus model continues building on the Alpha model. The difference in this model is that the Alpha Plus model includes Time Series Forecasting (explained in Sections 2.6 and 3.7) in addition to the already-existing model. The Alpha Plus model is a novel numerical model for simulating the operation of the megawatt-scale ECU to obtain a smoothened power output based on an input theoretical SMA of intermittent power. The numerical model also applies a one-step-ahead time-series forecasting model to predict the power diverted to the ECU and identifies which hydraulic machine will be required to feed a smoothened power output to the grid. Table 4.5 highlights the different capabilities and limitations of each numerical model, while Figure 4.6 summarises the numerical model development timeline.

Table 4.5: Highlighting the different numerical models.

Numerical Model	Computationally Efficient	Flexible Parameterisation	Transient Analysis	Electrical Components	Time Series Forecasting
Alpha	✓	✓	x	x	x
Beta	x	x	✓	✓	x
Alpha Plus	x	✓	x	x	✓

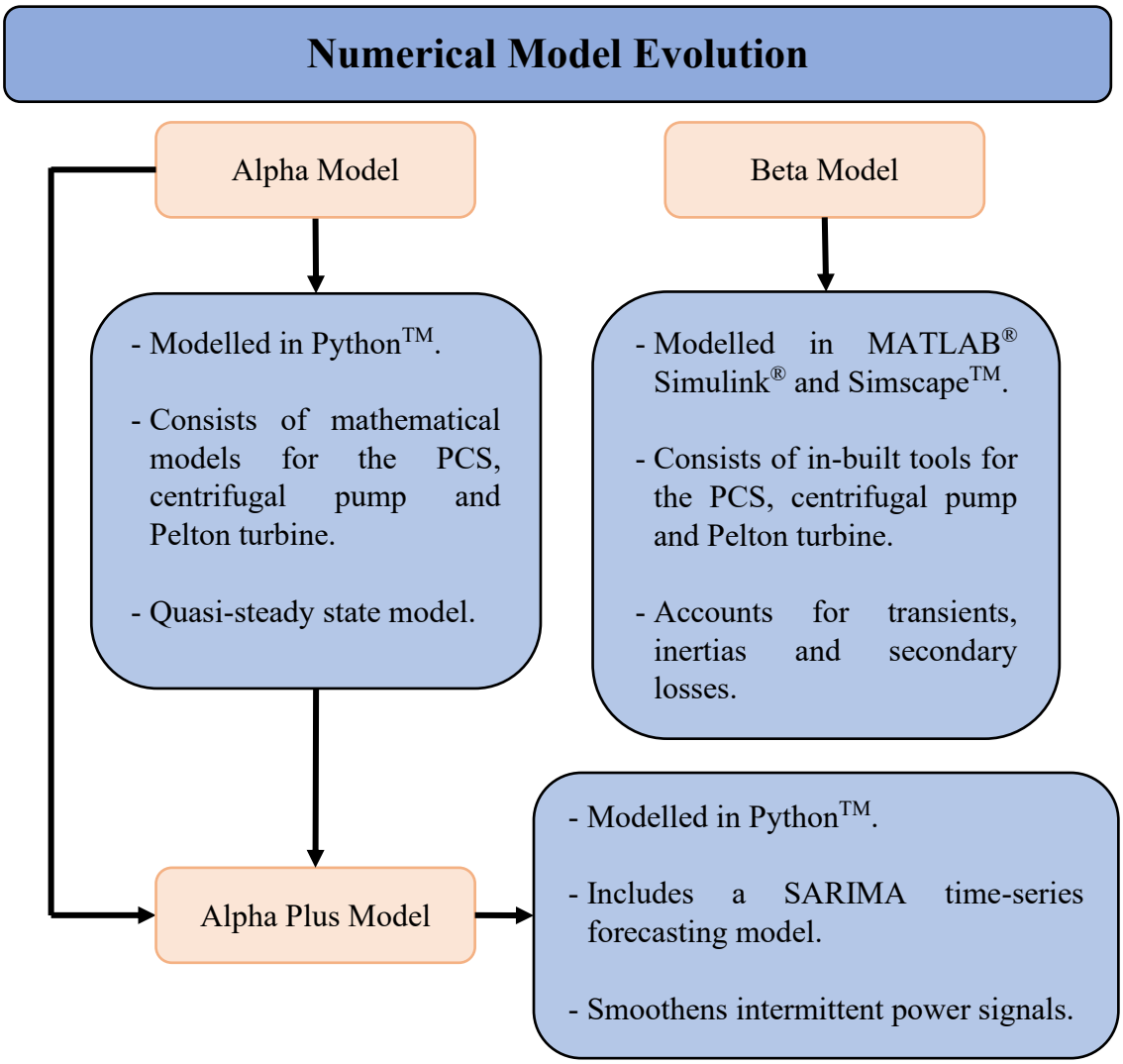

Figure 4.6: A summary of the differences and evolution between the three different numerical models.

4.4 Baseline Data

The following section describes how the wind and solar data obtained were utilised to set up the case studies performed in Chapter 6.

The wind data was obtained from LiDAR 10-minute averaged data collected at Qalet Marku at a height of 100 metres above ground level[1]. The wind speed measurements were applied to a IEA 10 MW wind turbine (WT) [168], with the wind speed being corrected for WT hub height based on a realistic wind shear exponent ($\propto$) [169], as shown in equation 4.1:

$$v = \left(\frac{H}{H_0}\right)^{\propto} \times v_0 \tag{4.1}$$

where v is the wind speed at the height of interest (in this case the hub height of the modelled WT), v_0 is the measured wind speed at a reference height, H_0, for a measurement height of 100 m and where H is the proposed WT's hub height (119 m). An air density correction was also applied, as shown in equation 4.2 hereunder [170]. Despite applying it, no correction was required since the Maltese Islands' average air density across the dataframe was in fact equivalent to the WT reference power curve's air density.

$$v_0 = \left(\frac{\rho_{std}}{\rho_0}\right)^{\frac{1}{3}} \times v_{std} \tag{4.2}$$

Where v_{std} is the original wind speed, ρ_{std} is the standard air density and ρ_0 is the new air density based on the measured wind speeds, v_0.Re-sampling of data was required since the resolution of the 10-minute average data was not fine enough for the numerical models. Figure 4.7 shows an example of how the wind data was resampled based on the original 10-minute average data.

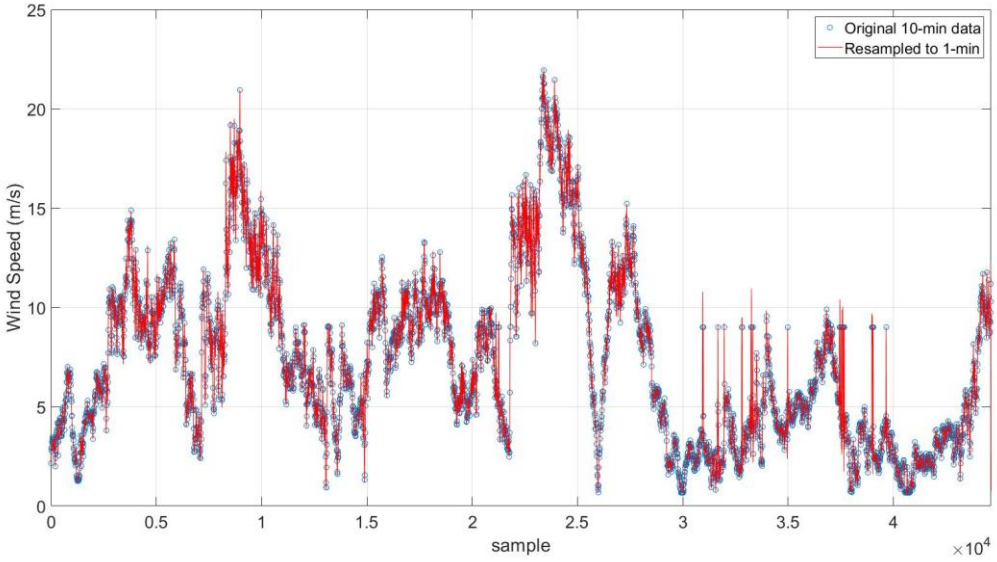

Figure 4.7: A re-sampling plot showing the Original 10-minute average wind speed data and the Resampled 1-minute data.

[1] The LiDAR system was purchased through European Regional Development Fund for the setting up of a Solar Laboratory (ERDF 335), part-financed by the European Union.

Due to the data not being fine enough for the numerical models, both the wind and solar data obtained were up-sampled in MATLAB®. The *upsample* function was implemented, where the sample rate of the dataset inputted is adjusted by inserting zeros between samples. The number of zeros inputted in between the samples is called the upsampling factor, where the output is an upsampled array based on the new sampling factor. Meanwhile, Figure 4.8 presents a histogram comparison to show how the frequency of counts per wind speed bracket varies due to the re-sampling. The histograms were also produced to ensure that the data's trend did not lose its shape due to the data up-sampling. Additionally, the up-sampled data wind speed average was cross-checked with the original data, in order to ensure that the average speed across the original dataset was maintained in the up-scaled dataset. Once the re-sampling of wind data was completed, the power could be obtained based on the IEA 10 MW wind turbine (WT) [168].

In the case of the hourly solar PV data obtained from the University of Malta[2], a multiplication factor of 1.11 was applied to estimate the RES generation if the same installation (kWh) were to be placed offshore, taking into consideration advantages such as less obstacles blocking sunlight and less dust and assuming that the advantages outweigh the disadvantages [11].

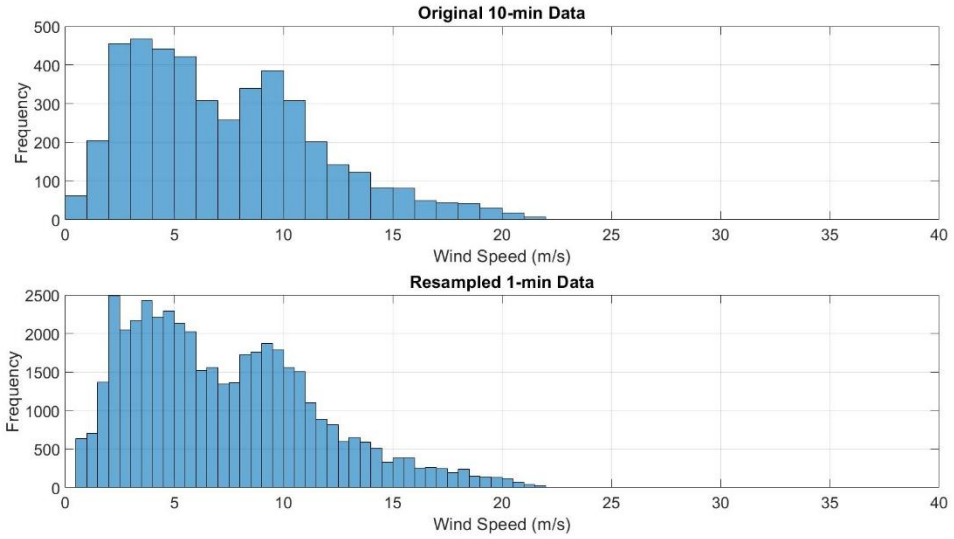

Figure 4.8: A histogram comparison showing the Original 10-minute data and the Resampled 1-minute data.

[2] The solar PV data was provided by Prof. Ing. Joseph Micallef and Dr. Ing. Francarl Galea from the University of Malta.

5 DEVELOPMENT OF THE ALPHA AND BETA MODELS

The following chapter describes the Alpha and Beta models developed during the course of this study to simulate the performance of the mega-watt scale ECU under steady and unsteady flow conditions. As already explained in Chapter 4, while the Alpha model is a more basic yet computationally efficient model, the Beta model is more comprehensive due to including transient effects, inertias and piping to calculate hydraulic losses within the circuits. The numerical verification of the Beta model is presented. Furthermore, this chapter presents the verification of the Alpha model against the results of the Beta model. The latter exercise helped to evaluate the impact of ignoring transient effects on the performance predictions of the ESS.

5.1 The Alpha Model

As previously mentioned in Section 4.3, the Alpha model is a quasi-steady-state numerical model (developed in Python^{TM}) which simulates the operation of the ECU charging and discharging the PCS of the offshore HPES system. The flowchart presented in Figure 5.1 on the following page shows the procedure which the Alpha model implements for the numerical solution. The simulator requires pump, Pelton turbine, and PCS model inputs, mainly based on the parameters shown in Tables 4.1 to 4.3 in Section 4.2. Additionally, the pump requires polynomial curve inputs, taken from the equations of the curves shown in Figure 4.2 in Section 4.2, as a function of rotational speed. The simulation duration and timestep may also be manually adjusted, where a 1-s timestep was considered throughout this study. Opting for a smaller timestep only led to a maximum Normalised Root Mean Square Error ($RMSE_N$) of 1.39% across all criteria analysed in Section 5.3 when implementing finer timesteps of 0.5 and 0.1 s. Finally, a constant power input or a file with a power time-series must be inputted for the system to run. If power is positive, meaning that the RES power generation is greater than a set moving average for scheduling power or greater than grid demand, this implies that the centrifugal pump will be in operation and, thus, the PCS is being charged.

Meanwhile, if power is negative, which means that demand is greater than supply, the PCS will discharge. The numerical simulation working in the time domain is automatically stopped when the time limit set is reached, or when the PCS reaches its upper or lower pressure limits previously presented in Table 4.3 (200 and 80 bar, respectively).

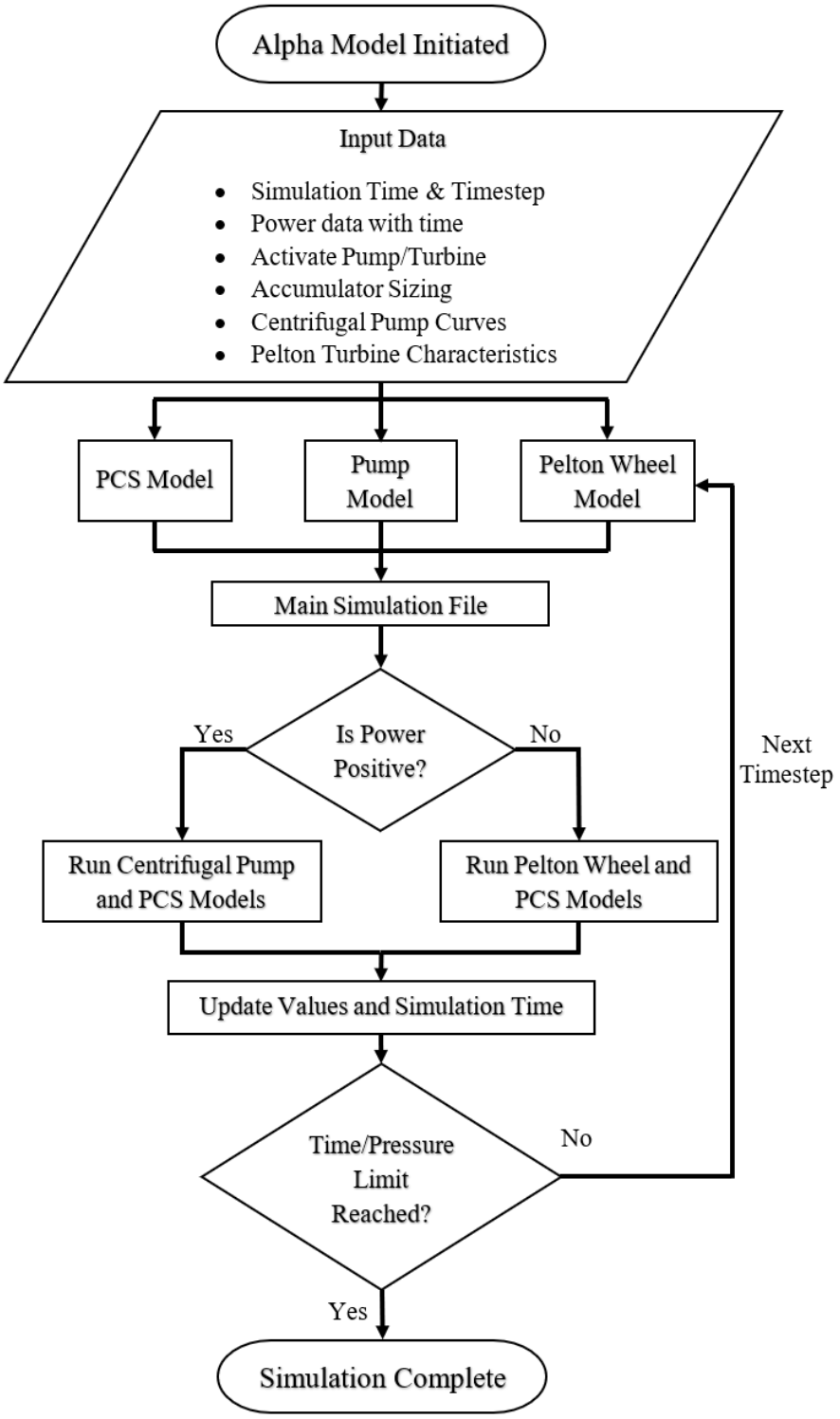

Figure 5.1: The time marching numerical algorithm implemented in the Alpha model.

The PCS modelling involved a time marching approach, where the volume of air within the pressure vessel and its pressure are established at each timestep using equations 3.45 and 3.46 previously presented in Section 3.4. The methodology for operating the pump within the Alpha model for the charging process is summarised in Figure 5.2. The inertia-less pump operation is regulated via a PID controller which translates the differential between desired and shaft power, ΔP, into a speed output due to the centrifugal pump's requirement of operating at variable speed. With speed being a function of both PCS pressure and desired power, interpolation of the pump characteristic curves (Figure 4.2 in Section 4.2) is required to obtain the pressure-flow and power-flow curves at the output speed provided by the PID controller.

The Ziegler-Nichols method [171] was used to obtain baseline PID values. Manual tuning was then applied to fine-tune the controller. Such tuning was acceptable since the study focuses on analysing the quasi-steady-state Alpha model's accuracy for constant power charging and discharging. Once the curves are obtained, a flow rate satisfying both pressure and power requirements is found. Since the pump curves present shaft (electrical motor power output) power (P_s), the pump hydraulic power, P_O, is determined using Equation 3.6 in Section 3.1. Equation 3.7 is used to find the hydraulic efficiency, η_{pump}.

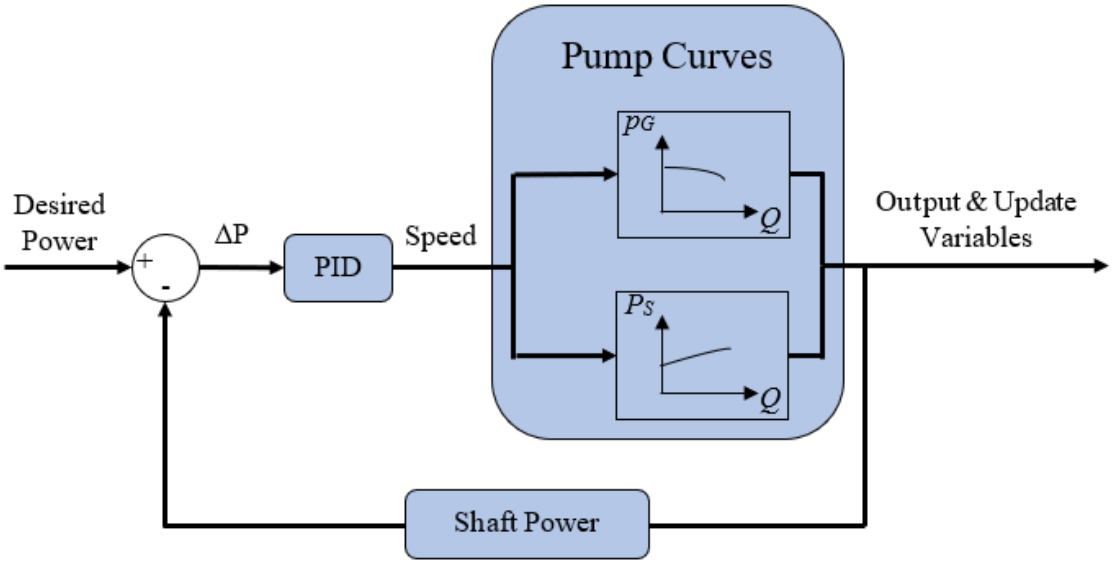

Figure 5.2: A schematic showing the variable speed centrifugal pump's numerical modelling procedure.

For the discharging process of the ECU, the Pelton turbine was modelled as a function of pressure as well as power. The jet velocity was calculated as a function of PCS pressure, as shown in equation 3.22 in Section 3.2, while the desired power was maintained by adjusting the needle valve position, h, interpreted based on the Simscape^{TM} needle valve model explained previously in Section 3.2.3 [143]. Equation 3.38 in Section 3.2.3 was applied at the start of an iterative process, presented in Figure 5.3, within the same timestep. The sequential increase in needle valve position h (where Δh was 0.01 mm) was continued until the Pelton turbine wheel yielded the desired power generation by comparing the desired power with the Pelton turbine's hydraulic power (P_{H_t}), computed by applying Equation 3.25 in Section 3.2.

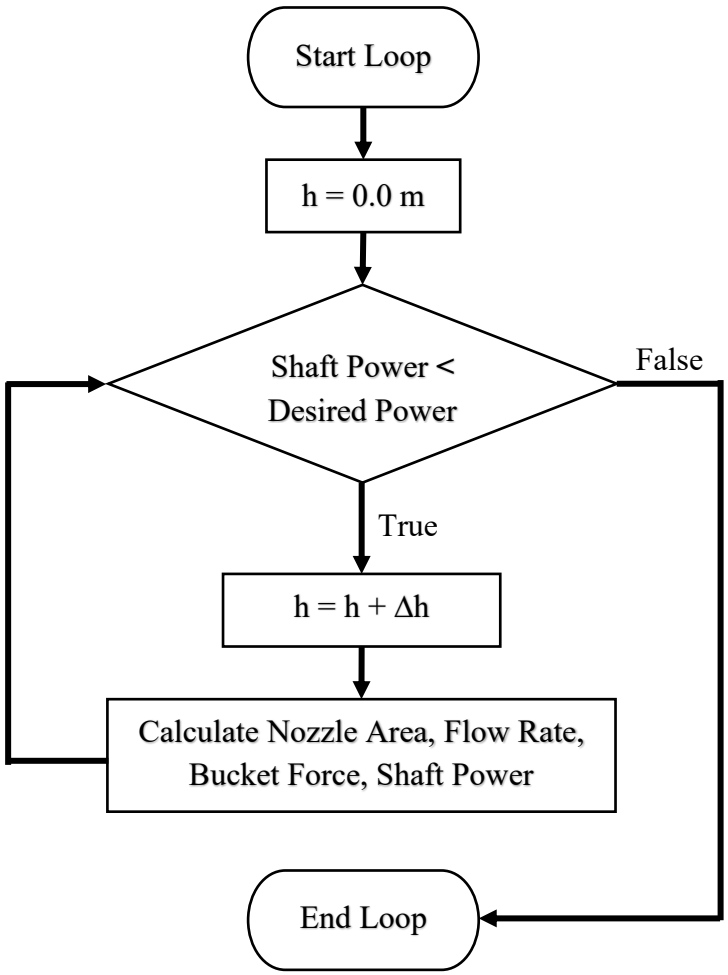

Figure 5.3: A schematic showing the Pelton turbine's iterative needle valve positioning while loop.

5.2 The Beta Model

The Beta model uses Mathworks® Simulink® and Simscape™ to model the same system described in Section 5.1, while including electrical components, such as a three-phase source and a VSD, a piping system which includes fluid inertia and compressibility, and other built-in Simscape models which simulate the PCS as well as the centrifugal pump. The Pelton turbine was modelled using an amalgamation of mathematical functions via Simulink® while also applying some built-in components from the Simscape™ library. Due to computational challenges, the ECU hydraulic machinery and PCS modelling was split into two models, (i) a charging model including the variable speed, multi-stage centrifugal pump and PCS and (ii) a discharging model including the mathematical model of the Pelton turbine and PCS.

While the control system for this model is identical to the system presented and explained previously in Figure 5.2 in Section 5.1, a primary difference was the inclusion of electrical parameters and pump's motor inertia within the Variable Speed Drive (VSD) block described previously in Section 3.6.2. As a result of the introduction of inertia, the pump's speed had a ramp up which was different from the quasi-steady-state solution of the Alpha model since the controller gains affect speed transients and, thus, require tuning through the in-built MATLAB® PID tuner.

Figure 5.4 presents the system modelled in Simscape™ for the operation of the variable speed, multi-stage centrifugal pump charging the PCS at a constant, desired power. The output from the VSD is directly connected to the pump's motor, where the pump takes seawater (defined from an in-built Simscape™ model) in and pumps it to the PCS.

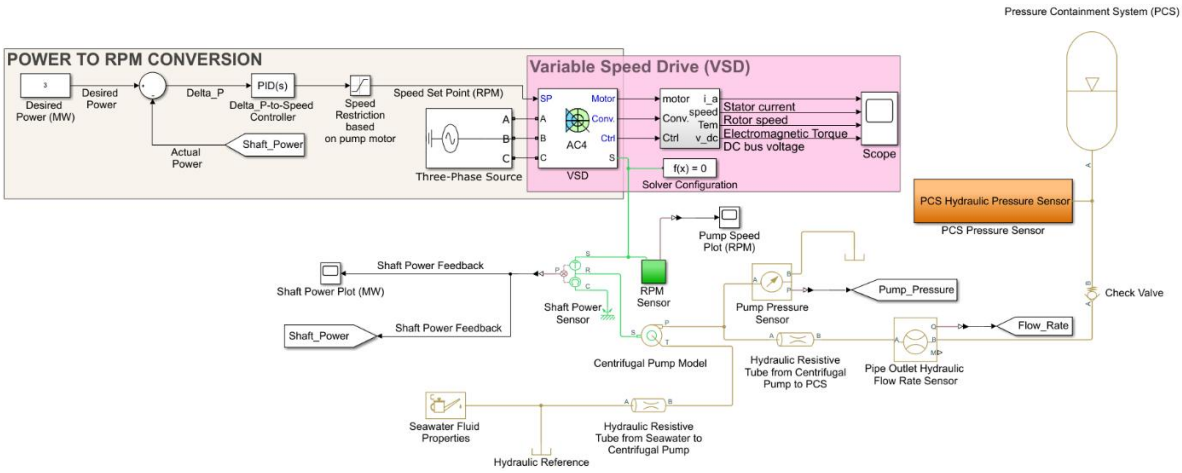

Figure 5.4: A schematic showing the components and blocks required to perform charging simulations in Simscape™.

A check valve was added at the PCS's inlet to prevent backflow to the pump, thus preventing the system pressure from dropping below the stipulated pre-charge pressure of 80 bar. The check valve was modelled based on the needle valve, shown in equations 3.49 and 3.50 in Section 3.4.1, where the only difference is that the check valve opens fully once the pre-charge pressure is reached, while the needle valve has a variable position based on the needle valve position.

With respect to the discharging model, most of the equations across Section 3.2 were used in both the Alpha and Beta models. The Beta model introduces a nested PID control loop, based on previous work by Buhagiar et al. [95], to regulate power requirements and maintain optimal speed based on the bucket-to-speed ratio previously mentioned in Sections 4.2 and 5.1 [91]. Apart from maintaining the optimal bucket speed ratio, the spear valve had to be adjusted based on the said power requirements. Moreover, the Pelton turbine's inertia and damping are also considered to calculate the bucket torque to be matched to the generator's torque for power generation, a step which is omitted in the Alpha model.

Figure 5.5 presents an overview of the Simulink® model of the Pelton turbine, specifically highlighting the aforementioned nested PID control loop and also presenting the inertia and damping transfer function block [40]. Finally, the Beta model also considers frictional ($P_{friction}$) and windage ($P_{windage}$) losses. Equations 3.32 and 3.34 in Section 3.2.2 show how the said losses were calculated [90], [91], [172]. Figure 5.6 on the following page shows part of the Pelton turbine system modelling, where multiple spear valves were implemented due to their advantages as previously discussed previously in Section 2.4.1.

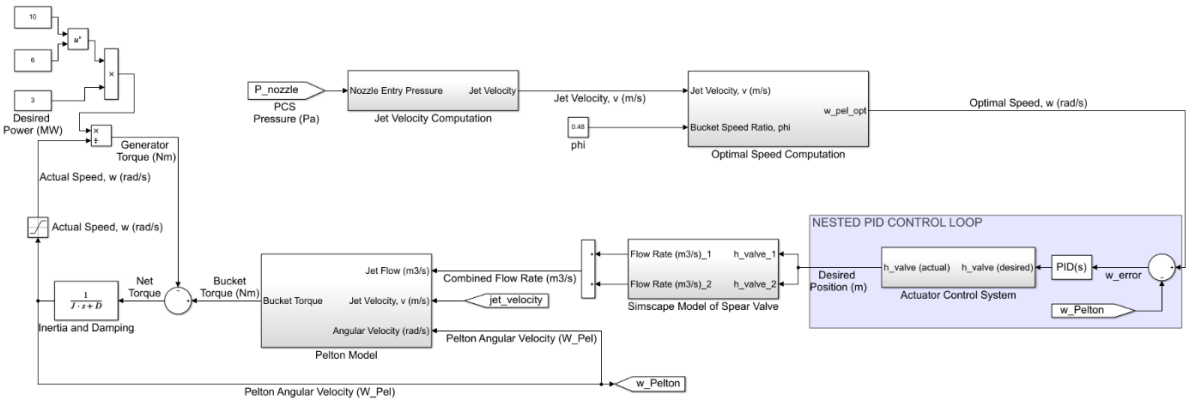

Figure 5.5: A mathematical model of the Pelton turbine system in Simulink.

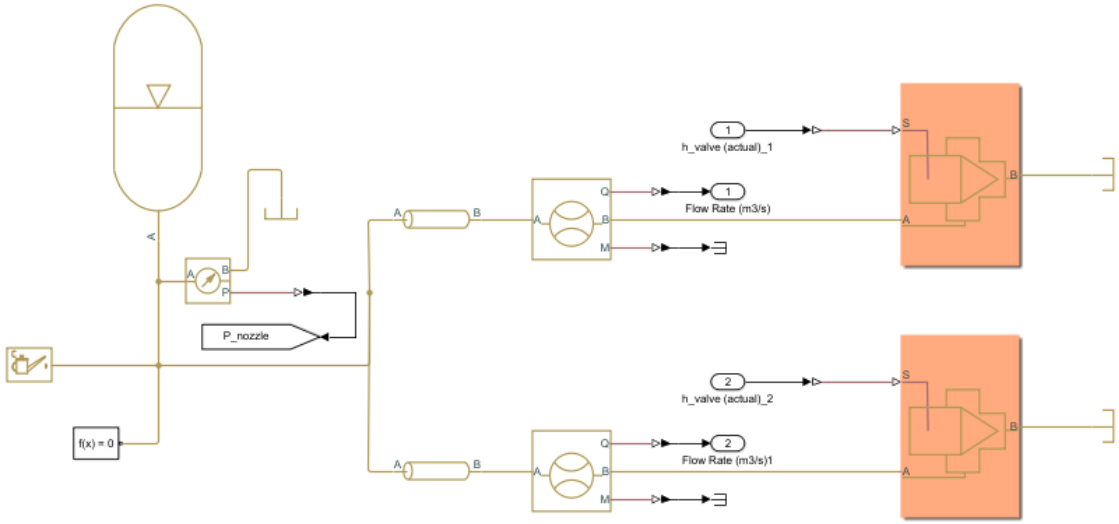

Figure 5.6: A snippet of the Beta model, focusing on the Needle Valve Simscape™ models.

Meanwhile, Figure 5.7 presents one of the innovative capabilities of the Discharging Beta model. As explained in Section 3.2.2, the power loss due to windage presented in equation 3.34 was derived in terms of density, in order to evaluate the change in density if the Pelton turbine were to work in a compressed air environment instead of atmospheric air conditions. Figure 5.7 compares the Pelton turbine's overall efficiency operating under atmospheric conditions and operating at an approximate 100 metres sea depth within a compressed air chamber due to the associated sea depth. Due to the increase in air density as a result of the compressed air environment, the power loss due to windage effects causes a decrease in efficiency reaching 23%. However, the difference in efficiency reduces as the system discharges from 200 to 80 bar, as may be observed from Figure 5.7. The pressurised conditions also cause the system to discharge faster since more energy is lost as a result of the lower efficiencies throughout the simulation.

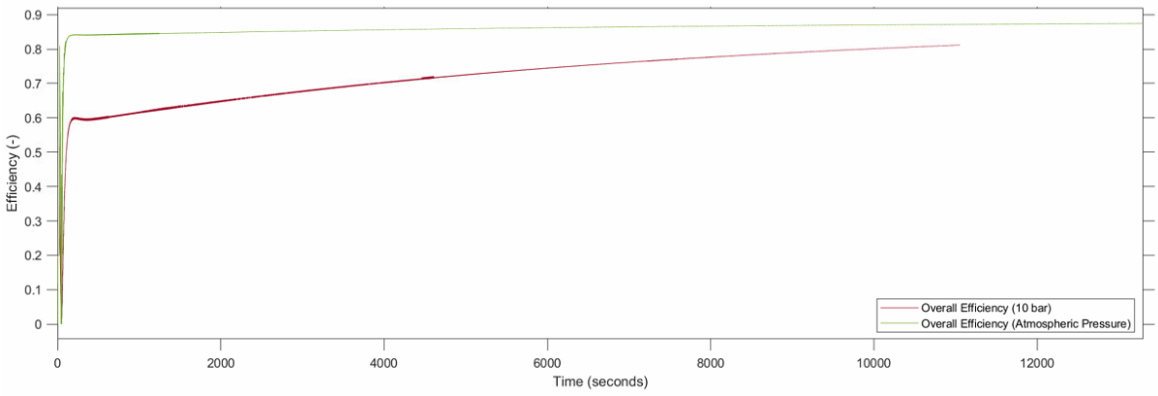

Figure 5.7: A comparison between the Overall Efficiency for a Pelton Turbine operating in atmospheric conditions and at a sea depth of 100 metres.

5.3 Verification of the Alpha Model

The aim of this section is to compare the results of the two novel numerical models explained in Sections 5.1 and 5.2 to evaluate the Alpha model's accuracy and to understand the effect of transients on the overall system performance and efficiency. As previously explained in Section 5.2, the Beta model charging and discharging models were split due to computational restrictions, particularly within the charging model. Since a full charging cycle from 80 to 200 bar was not possible due to the high computational resources required, the charging cycle was divided into six 10 bar increments across the pressure range between 80 and 190 bar. Tables 5.1 and 5.2 summarise all the simulation runs performed using the Alpha and Beta models. The runs were selected based on input powers which were within the operating capabilities of the pump, in accordance with Figure 4.2 in Section 4.2.

Table 5.1: The charging runs performed in the Alpha and Beta models at constant power (MW).

Charging Runs	Input Power (MW)	Pressure Range (bar)
Run 1	1.5	80-90
Run 2	2.0	
Run 3	2.5	100-110
Run 4	3.0	
Run 5	3.0	120-130
Run 6	5.0	
Run 7	3.5	140-150
Run 8	5.0	
Run 9	4.0	160-170
Run 10	5.0	
Run 11	3.6	180-190
Run 12	3.8	

Table 5.2: The discharging runs performed in the Alpha and Beta models at constant power (MW).

Discharging Runs	Input Power (MW)	Pressure Range (bar)
Run 1	1.0	200-80
Run 2	2.0	
Run 3	3.0	
Run 4	4.0	
Run 5	5.0	

For example, charging the system at 1.5 MW at a pressure of 160 bar was not possible according to the pump curves, even when applying variable speeds, since the pump reaching such high pressures would require greater speeds as well as a greater power input. Similarly, if a power of 5.0 MW were to be inputted to charge the system when the PCS is at a pressure of 80 bar, the flowrate limit would be reached, thus also reaching a pump power output limit and not satisfying the requirement of charging the system at the desired 5.0 MW.

The following sub-sections summarise the results of the runs selected for the comparison of the Alpha model to the more comprehensive Beta model, highlighting the key similarities and differences, and assessing the Normalised Root Mean Square Error ($RMSE_N$) generated by the two numerical models, both for charging and discharging cycles.

5.3.1 Verification - HPES System Charging

Figure 5.8 presents a portion of the results obtained specifically from Runs 2 and 7, directly comparing the Alpha and Beta models for the same simulation runs. On observation, the results are highly comparable and follow the same trends, with minimal time differences between the two models. A primary visual difference of the power results between the Alpha and Beta models is the effect of the PID controller and motor inertia within the Beta model, where the controller gain parameters play a crucial role in the pump's power and speed ascent time and overshoot.

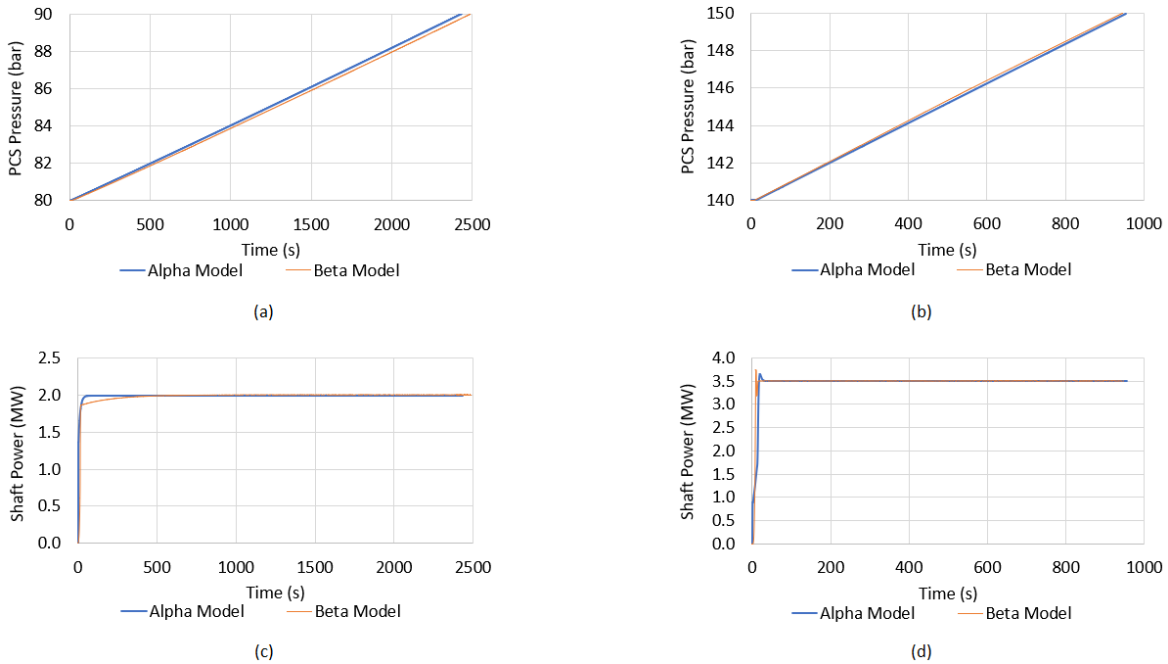

Figure 5.8: Plots during system charging showing (a) Accumulator Pressure variation for Run 2, (b) Accumulator Pressure variation for Run 7, (c) Input Power for Run 2, and (d) Input Power for Run 7.

A finding obtained during simulation runs was that if a full charging cycle were to be performed in the Beta model (from 80 to 200 bar), PID active control would be required. Firstly, due to the large variation in PCS pressure and secondly, owing to the large variation in powers, the system at 120 bar could be charged at powers of between 3.0 and 5.0 MW, thus having a direct influence on the pump's required speed, which is an output of the PID controller, as previously shown in Figure 5.4 in Section 5.2. In Figure 5.8c, d, the response of the Beta model in the two cases indicates different PID controller gain parameters. While the former case experiences undershoot and a longer settling time, the latter case is more aggressive, thus experiencing an overshoot, yet obtains a relatively faster settling time. It must be noted that while the PID controller gain parameters are satisfactory for the purposes of this study, further optimisation of the control system's response is not to be excluded.

Table 5.3 presents the controller gain parameters implemented for every run. Table 5.4 presents a comparison between the controller regulation quality indicators for all the charging runs across the two numerical models. While steady state error remains low across all runs, the overshoot for both models towards the upper pressure limit is large. The Alpha model shows a lot less sensitivity to the controller regulation quality across all runs due to the exclusion of inertia and its quasi-steady-state modelling approach.

Table 5.3: The controller gain parameters for all charging runs performed in the Beta model.

Charging Runs	PID Parameter Gains		
	Proportional (P)	Integral (I)	Derivative (D)
Run 1	0.004	0.0050	5×10^{-7}
Run 2	0.008	0.0045	5×10^{-7}
Run 3	0.005	0.0050	0.50
Run 4	0.005	0.0050	0.00
Run 5	0.006	0.0050	0.15
Run 6	0.003	0.0100	0.02
Run 7	0.200	0.0004	0.15
Run 8	0.003	0.0100	0.02
Run 9	0.009	0.0100	1×10^{-4}
Run 10	0.003	0.0100	0.02
Run 11	0.0095	0.1000	1×10^{-4}
Run 12	0.0095	0.1000	1×10^{-5}

Table 5.4: The controller regulation quality indicators for all charging runs.

Charging Runs	Maximum Overshoot (%)		Settling Time (s)		Steady State Error (MW)	
	Alpha Model	Beta Model	Alpha Model	Beta Model	Alpha Model	Beta Model
Run 1	0	0	8	366	0.001	0.011
Run 2	0	0	21	85	0.001	0.004
Run 3	0	8	19	257	0.002	0.003
Run 4	0	0	21	150	0.002	0.002
Run 5	0	0	18	90	0.002	0.004
Run 6	0	0	18	103	0.002	0.023
Run 7	6.57	5.7	20	50	0.003	0.003
Run 8	0	0	15	67	0.003	0.022
Run 9	6.25	20	15	53	0.004	0.002
Run 10	1.2	0	15	104	0.03	0.022
Run 11	17	16.7	30	139	0.003	0.056
Run 12	15	15.7	30	56	0.004	0.0006

In reality, better-optimised PID control response can lead to even better RMSE results (presented later in Table 5.5) since the results comparison also considers the pump speed ramp up difference between the two numerical models due to the inclusion of machinery inertia and piping inertia and fluid compressibility in the Beta model. The RMSE and $RMSE_N$ are calculated by applying equations 5.1 and 5.2 respectively.

$$RMSE = \sqrt{\sum_{i=1}^{n} \frac{(\hat{y}_i - y_i)^2}{n}} \tag{5.1}$$

Where $\hat{y}_i$ is the actual value, y_i is the predicted value and n is the number of observations.

$$RMSE_N = \frac{RMSE}{y_{max} - y_{min}} \tag{5.2}$$

Where y_{max} and y_{min} are the maximum and minimum values in the observed dataset respectively.

Figure 5.9 presents more results comparing the same runs within the Alpha and Beta models. The two numerical models follow the same trend in each plot. Table 5.5 presents the $RMSE_N$ results to provide a more reliable representation on the models' comparative accuracy. The results obtained clearly illustrate the Alpha model's capabilities of reproducing the Beta model simulation predictions for the same prescribed operational conditions. A particularly important trend is that, despite the maximum $RMSE_N$ across all runs reaching only 13.9%, Runs 6, 8, and 11 experienced the highest errors in the majority of parameters. While variables such as pump speed and flow rate are expected to differ due to the different factors considered in the numerical calculations, such a result also coincides with the fact that the three mentioned runs consisted of the highest constant power, implying that $RMSE_N$ has a direct proportionality with input power.

Although the power was a system input, the $RMSE_N$ was still calculated since minor variations occurred which were regulated by the speed controller to maintain power as close to the desired (input) power as possible. The calculation was thus also used to prove that the Beta model controller gain variations across all runs all provided a stable system, since the power difference between the desired and shaft power was the controller's input value.

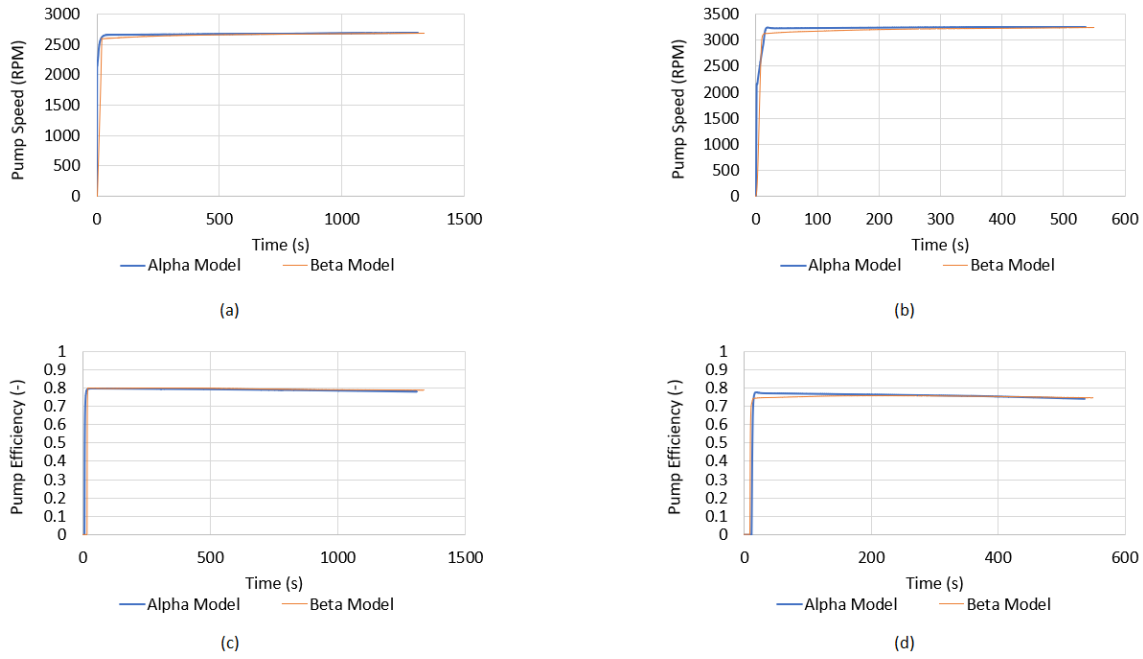

Figure 5.9: Plots showing (a) Pump Speed variation for Run 4, (b) Pump Speed variation for Run 10, (c) Pump Efficiency variation for Run 4, and (d) Pump Efficiency variation for Run 10.

Table 5.5: Summary of all results for the Normalised Root Mean Square Error ($RMSE_N$) comparing the predictions for the Alpha and Beta model PCS charging process.

Charging Runs	Normalised RMSE (%)				
	Input Power	Pump Speed	Flow Rate	PCS Pressure	Pump Efficiency
Run 1	6.94	3.51	10.50	2.51	8.31
Run 2	5.76	4.26	6.38	1.73	7.29
Run 3	4.18	3.93	4.99	2.56	2.13
Run 4	6.79	5.66	7.74	1.99	8.83
Run 5	5.74	5.67	6.01	1.29	6.36
Run 6	9.11	7.73	10.30	2.57	11.30
Run 7	4.18	4.59	6.53	1.12	7.51
Run 8	9.32	8.29	10.30	2.57	11.30
Run 9	5.61	4.84	8.64	2.33	8.55
Run 10	4.81	5.75	6.37	2.37	5.43
Run 11	4.52	4.43	9.07	3.57	13.90
Run 12	6.36	4.36	11.70	2.97	11.20

5.3.2 Verification - HPES System Discharging

While the Alpha and Beta models for the Pelton turbine and PCS are very similar as previously discussed in Sections 5.1 and 5.2, the Beta model includes transients and integrates a nested PID control loop. Additionally, the inertia and damping of the Pelton wheel are also considered (also applied through equation 3.51 in Section 3.6.2) together with power loss calculations in the form of windage and friction. Figure 5.10 presents an example comparison of Run 3 between the typical results yielded from each numerical model.

As may be observed, the plots all follow the same trends, where a minimal difference in simulation time may be noted. Similar to the comparison between the numerical models in Section 5.3.1, the time difference results from the transients experienced in the Beta model, where an overshoot or undershoot within the control systems impacts the time required to fully discharge the PCS.

Figure 5.10f presents the overall efficiency of both models, where a key observation is that while the efficiency is constant across the entire simulation for the Alpha model, a slight variation in efficiency occurs in the Beta model due to the inclusion of the Friction and Windage power losses, since these are directly proportional to the Pelton Wheel speed and the cube of Pelton Wheel speed, as shown in equations 3.32 and 3.34, respectively.

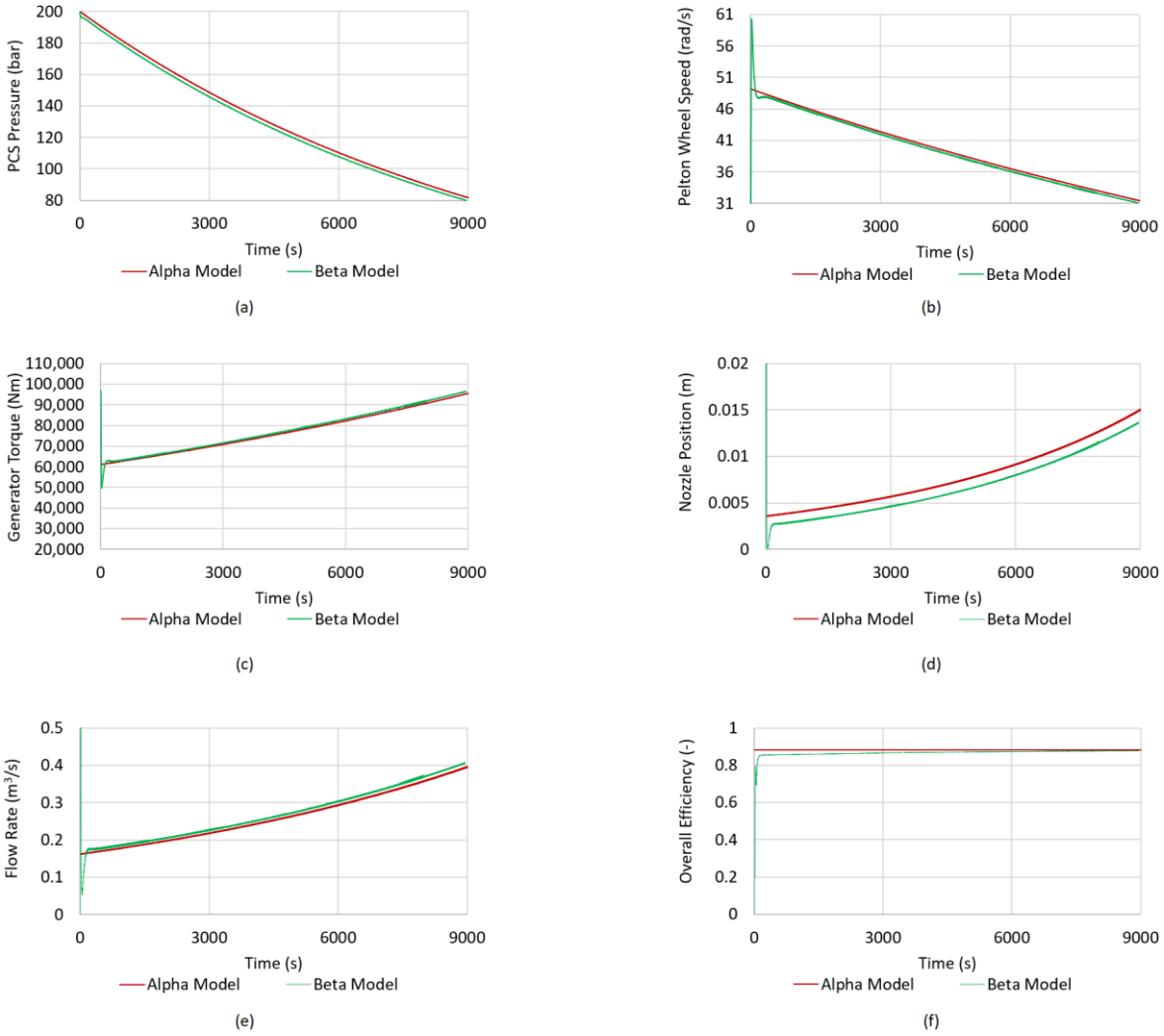

Figure 5.10: Plots showing (a) PCS Pressure variation, (b) Pelton turbine wheel rotational speed variation, (c) Generator Torque variation, (d) Nozzle Position variation, (e) Flow Rate variation, and (f) Overall Efficiency variation. All plots are associated with maintain a constant power of 3 MW (Run 3 in Table 5.2).

Table 5.6 presents the results for the $RMSE_N$ across the five considered runs for the main parameters of the numerical models. While all error results are reasonably low (< 6%) and show the codes' comparability and reliability, several parameters show a trend. The Input Power, Flow Rate, and Nozzle Position all increase with increased constant power input, while the PCS Pressure decreases with increased constant power input. The reason for a PCS Pressure decrease may be due to reduced overshoot and settling time compared to the other runs, since the rated power of the Pelton turbine is 5 MW. The increase in error across the former three variables, however, results from their correlation through the nested PID controller, whereby a higher power requirement seems to increase error within the Beta model, while the Alpha model continues to provide a steady-state solution across all runs. Since the Beta discharging model does not include electrical parameters, the computational time between both models is negligible, only taking a maximum of 45 s to complete a full discharging cycle.

Table 5.6: Summary of all the Normalised Root Mean Square Error ($RMSE_N$) results comparing all the Alpha and Beta model runs for discharging.

Charging Runs	Normalised RMSE (%)					
	Input Power	Pelton Speed	Flow Rate	PCS Pressure	Generator Torque	Nozzle Position
Run 1	3.10	4.52	2.83	4.27	4.39	1.51
Run 2	3.45	2.78	3.80	2.67	3.50	2.26
Run 3	3.76	3.53	4.54	2.13	3.69	2.84
Run 4	3.96	3.98	5.15	1.87	4.08	3.38
Run 5	4.57	4.46	5.66	1.72	4.51	3.91

5.4 Concluding Remarks

The scope of the previous sections was to present the design, testing, and comparison of a simplified numerical model, dubbed the Alpha model, to a more comprehensive numerical model, namely the Beta model. Both models simulate the charging and discharging process of a megawatt-scale offshore HPES system's ECU and PCS. While the two numerical models simulate the same system, the degree of complexity of the integrated models differs, thus resulting in significant differences in the computational resources required.

The Alpha model is a computationally efficient, quasi-steady-state model which provides modularity and flexibility since numerous centrifugal pump, Pelton turbine, and PCS combinations can be simulated by changing the input parameters. A shortcoming of the Alpha model is that its simplified approach disregards transients due to machinery inertia, control system response, piping losses and system pressure losses. Meanwhile, the Beta model, as shown through Figures 5.4 and 5.5 in Sections 5.1 and 5.2, is a more complex model which mimics the physical system and aims to implement as many components as possible at the expense of computational efficiency. The computational challenges mentioned throughout this chapter refer to the fact that either system memory or time requirements to perform a single simulation were not sufficient to complete the tasks in time. Built-in tools such as the Performance Advisor in MATLAB® were utilised to improve processing efficiency, however the simulator was still excessively slow after the suggested changes were implemented. Validation at this stage was not yet possible with experimental data since the study specifically analysed a MW-scale ECU of the ESS, where the scale of such a system is a novelty in itself. Despite this, component testing during setting up the two models was performed and qualitative validation based on previous work and research was also performed [51], [56], [95]. A number of conclusions have been drawn:

- The longest computational time taken by the Beta model was approximately 180 minutes as opposed to the Alpha model's 40 seconds. When considering that the largest Normalised RMSE across all Runs was 13.9%, the Alpha model is a clear front runner in terms of speed and usability. Nevertheless, the Beta model offers an overall system understanding but is more applicable for analysing transients in the design of any HPES or CAES system.
- The Beta model is more suitable for analysing phenomena such as hydraulic machinery ramping, time response over short periods of time due to varying controller parameters, and transient flow analysis through the inclusion of hydraulic piping systems.

- Despite the model differences, the results produced were promising and have demonstrated the reliability of the simplified Alpha model compared to the Beta model by proving that the RMSE results are all consistently low across all runs, both for the charging and the discharging simulations. Lastly, part of the RMSE results is a steady state error since each numerical model commences differently (quasi-steady state versus ramp up to desired speed).

6 THE ALPHA PLUS MODEL

The following chapter describes the Alpha Plus model, an extension of the previously described Alpha model. As explained in Section 4.3, the Alpha Plus model also integrates one-step ahead time series forecasting in order to predict whether the centrifugal pump or Pelton turbine will be required for operation. This chapter delves into the methodology of this software model.

6.1 Development of the Alpha Plus Model

The Alpha Plus numerical model, which was developed in Python™ (version 3.9.13), presents a novel numerical model for simulating the operation of megawatt-scale hydraulic machines (centrifugal pump and Pelton Turbine wheel) to obtain a smoothened power output based on an input theoretical SMA of intermittent power from a 10 MW wind turbine. The motive behind using the SMA as the power to follow stemmed from the focus on understanding how much the ESS could provide a smoothened power output. Additionally, obtaining a smoothened power supply reduces the need of spinning reserves. The numerical model integrates the Alpha model, but also applies a one-step-ahead time-series forecasting model to predict the power diverted to the ECU and identifies which hydraulic machine will be required to feed a smoothened power output to the grid. The model consists of two parts: (i) the dataset was inputted, and the prediction model was selected and tested on the said dataset, and (ii) the time-series simulation was commenced, modelling a twenty-four-hour simulation of ECU performance of the offshore HPES system. Figure 6.1 shows an example of a time-series of power output data from a IEA 10 MW turbine [173]. The trace generated indicates intermittent data, with periods of high power as well as periods of no power, depending on the wind speed experienced. The data required further analysis to help converge towards selecting the correct model for forecasting. The following subsection discusses how the prediction model was selected and tested.

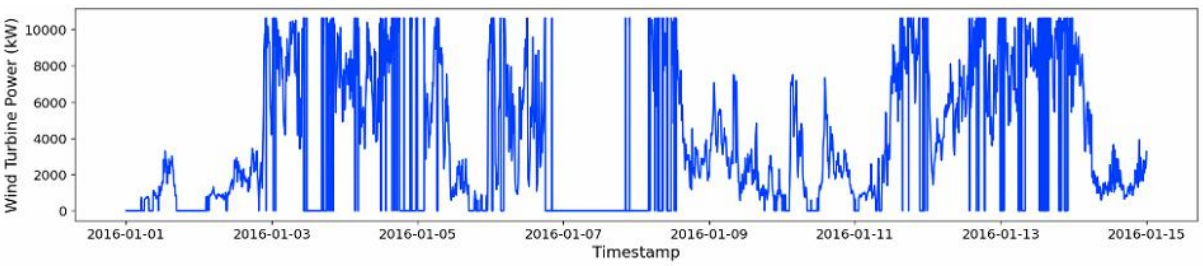

Figure 6.1: Time series power output data based on measured LiDAR data.

6.1.1 Prediction Model and Validation Procedure

Figure 6.2 shows a flowchart of the prediction modelling and validation method of the prediction model adopted. Once the wind turbine power output data were plotted, a moving average (MA) based on the previous 24 hours of data was applied (P_{smt}). Simultaneously, a seasonal decomposition was performed to observe trend and seasonality of the data, which are plotted in Figure 6.3. While no obvious trend was identified, a seasonality was clear, meaning that the data's behaviour repeated itself periodically. The Augmented Dickey-Fuller (ADF) test, presented previously in equation 3.52 in Section 3.7 was used to check for data stationarity by analysing if the Auto Regressive (AR) model has a unit root [160]. Once the ADF test was passed (as shown in Figure 6.4), the dataset could be split into a train-test ratio by using 80% of the data for training and the remaining 20% for testing.

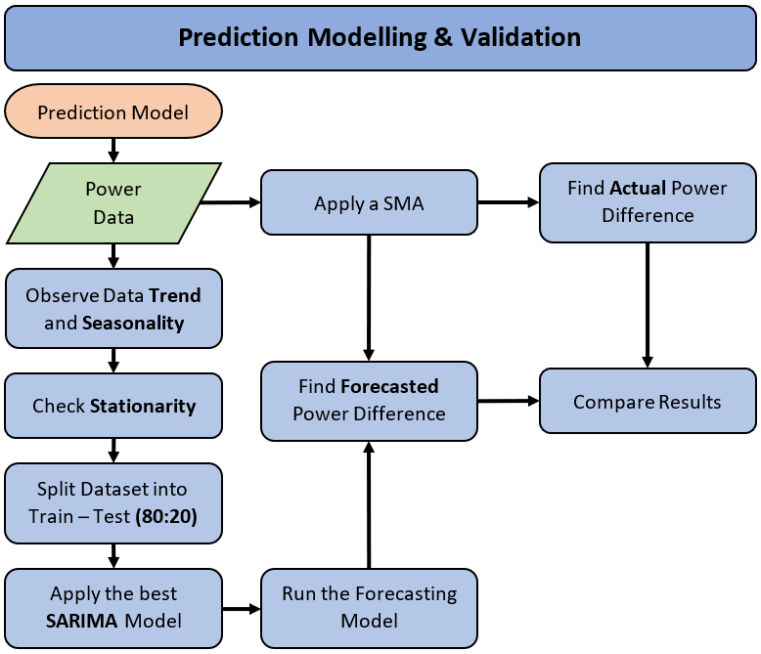

Figure 6.2: A flowchart showing the prediction modelling and validation procedure.

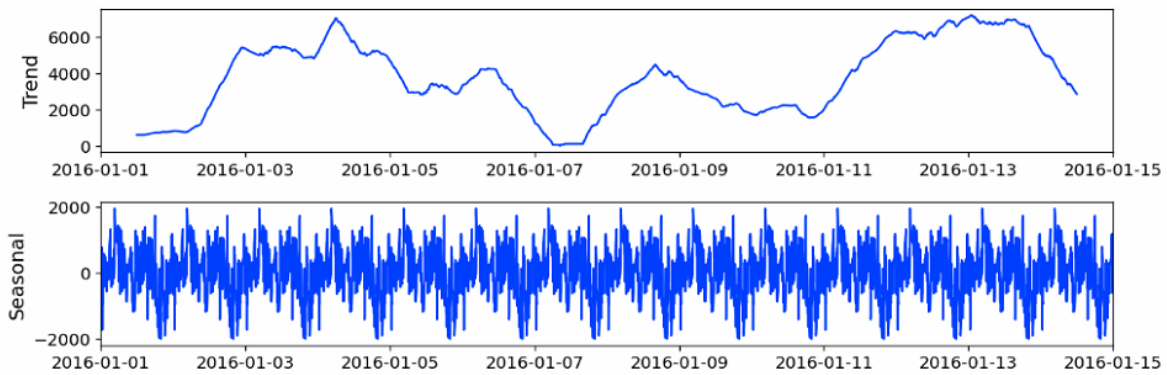

Figure 6.3: The trend and seasonal time series plots.

```
In [11]:  1 ADF_test(y,'raw data')

 > Is the raw data stationary ?
Test statistic = -9.084
P-value = 0.0000000000000398771
Critical values :
        1%: -3.433385280100795 - The data is  stationary with 99% confidence
        5%: -2.8628808769203995 - The data is  stationary with 95% confidence
        10%: -2.567483816537633 - The data is  stationary with 90% confidence
```

Figure 6.4: An example of the ADF test output in the Jupyter Notebook code.

Due to the seasonality in the data, as observed in Figure 6.3, the Seasonal Auto Regressive Integrated Moving Average (SARIMA) forecasting tool in-built in Python™ explained previously in equation 3.53 in Section 3.7 was found to be best suited [161]. The selection of the best SARIMA model involved computing the Akaike Information Criterion (AIC), where the lowest AIC (shown in equation 6.1 hereunder) from the different SARIMA orders tested was deemed the most accurate forecasting model [160], [161].

$$AIC = 2k - 2\ln(\hat{L}) \tag{6.1}$$

Where k and $\hat{L}$ are the number of estimated parameters in the model and the maximum value of the likelihood function for the model respectively. The forecasting model was then run, and the power difference between the actual values and forecasted values could be calculated, with the Root Mean Square Error (RMSE) being computed as a forecasting accuracy metric.

6.1.2 The ECU Simulator

Figure 6.5 shows the working principle of the offshore HPES system operating in tandem with the wind turbine. The system considered is described thoroughly in Section 4.2, where the Pressure Containment System (PCS) is located subsea to make use of the surrounding seawater as an excellent heat source and heat sink [51]. When the intermittent power (P_{raw}) is greater than the SMA (P_{smt}), the excess power is defined as the ECU power input ($P_{ECU,I}$).

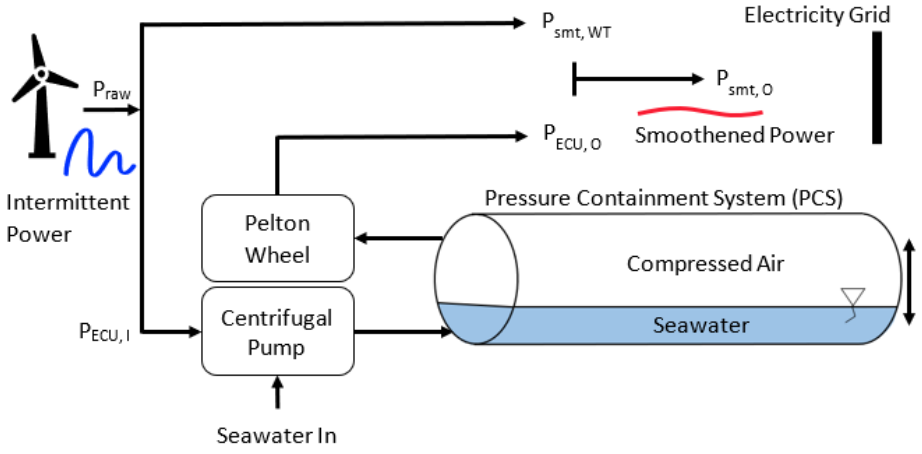

Figure 6.5: The working principle of the overall system.

Meanwhile, when the intermittent power (P_{raw}) is less than the SMA (P_{smt}), the power is represented as $P_{smt,WT}$, depicted in Figure 6.5, and is equal to the intermittent power (P_{raw}) where the input to the ECU ($P_{ECU,I}$) is equal to zero. During such situations, the ECU is to output power ($P_{ECU,O}$) which should be adequate to meet the smoothened power (P_{smt}) required. As a result, the smoothened power output ($P_{smt,O}$) calculation is dependent on whether the system is charging or discharging and is shown in equations 6.2 and 6.3 hereunder:

$$For\ Charging: P_{smt,O} = P_{smt,WT} \qquad where\ P_{ECU,O} = 0 \tag{6.2}$$

$$For\ Discharging: P_{smt,O} = P_{smt,WT} + P_{ECU,O} \tag{6.3}$$

Figure 6.6 summarises the full process of the ECU simulator. The simulator's operation starts off by forecasting the one-step-ahead intermittent power ($P_{forecasted}$) and calculating whether this power was greater or less than the SMA (P_{smt}). When positive, the multi-stage centrifugal pump was to be operated during the following minute based on that power value, while the Pelton Wheel was to be operated when the power difference was negative. As the flowchart depicts, the power difference was updated every minute based on the new forecasted power and SMA. Depending on whether the pump or turbine were in operation, the PCS's state of charge was also updated. Once the simulation was finalised, the overall efficiency comparing the intermittent power and the resulting output power fed into the grid could be computed. Equation 6.4 shows the equation used to calculate the overall efficiency, where $\Delta HPES$ is the net power out or into the HPES system. Additionally, the individual efficiency of the hydraulic machinery, as well as the power flowing through the storage system were also continuously calculated.

$$Overall\ System\ Efficiency = \int_0^t \frac{P_{ECU,O} + P_{smt,WT}}{P_{raw} + \Delta HPES}\, dt \tag{6.4}$$

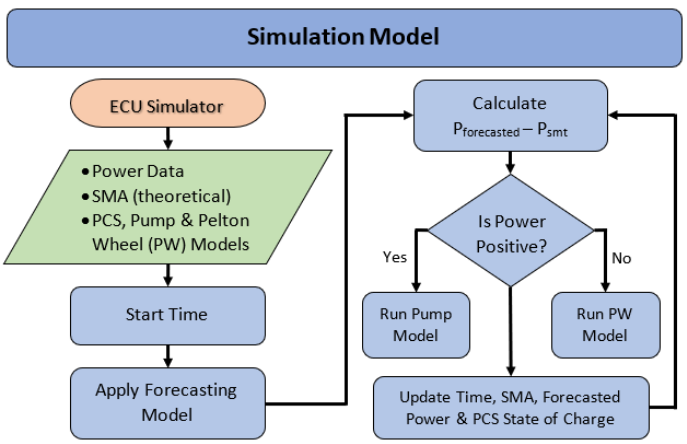

Figure 6.6: A flowchart showing the ECU simulation process.

6.2 Time Series Simulations Using The Alpha & Alpha Plus Models

The following sections presents case study simulations highlighting the difference in operation when implementing the Alpha and Alpha Plus models respectively. This section uses the Alpha and Alpha Plus models to evaluate sensitivities such as ESS capacity and smoothing power fluctuations. Part of this section also uses information which is discussed in further detail in Chapters 7 and 8, particularly in relation to the ESS capacity of the breakwater concept explained in the said chapter.

6.2.1 Energy Storage Sizing Requirements

The wind and solar data used throughout this study are based on time-series wind speed measurement and time-series solar power data obtained across 4 months of the year (January, April, June, October). The specified months were selected to capture the seasonality effects on the storage requirements. The data was corrected in the same manner as previously explained in Section 4.4. This section uses the Alpha Plus model to analyse how the ESS sizing requirements vary the operational performance of the overall HPES system. Since the numerical models (described in Chapter 4) simulate how a singular ECU operates, two case studies which could be handled by one ESS were considered for the renewable energy sources modelled, presented in Table 6.1.

Table 6.1: Table showing the Case Studies sizing considered.

RES	Parameter	Case Study 1	Case Study 2
Wind	Number of WT	1	1
	Capacity (MW)	10	10
	Capacity Factor	31%	31%
	Generation (GWh/annum)	27.2	27.2
Solar	Capacity (MW)	-	2
	PV Generation (kWh/year/kW)		1676
	Generation (GWh/annum)		3.35

One offshore 10 MW wind turbine was involved for Case Study 1 and an amalgamation of one 10 MW offshore wind turbine with a 2 MWp floating solar farm were considered for Case Study 2. The first step to consider was to understand what the required energy storage system sizing would be when implementing a 1-day SMA, based on the Case Studies in Table 6.1. The analytical process was initiated by computing the SMA from the case study data by taking an average power value based on the previous 'n' hours. 'N' is the number of hours considered from which a SMA is obtained. The differential power (ΔP) is calculated using equation 6.5 as follows:

$$\Delta P = P_{raw} - P_{SMA} \tag{6.5}$$

where P_{raw} represents the RES intermittent power generated and P_{SMA} represents the power value based on the SMA applied, both shown in Figure 6.7. Whenever ΔP is positive, the excess power (i.e., anything more than P_{SMA}) drives the centrifugal pump, indicating that the PCS is being charged.

In instances when ΔP is negative (i.e., anything less than P_{SMA}), the Pelton Wheel is operated to represent a PCS discharging process in order to meet the P_{SMA} value. The energy stored or released per hour could then be calculated and the positive or negative values were accumulated to analyse how many consecutive hours are spent in charging mode or in discharging mode. Based on the said cumulative hours of continuous charging or discharging of the PCS of the ESS, the storage requirements were assessed. Once ΔP was calculated, the energies resulting from ΔP and P_{SMA} could be calculated by applying the trapezium rule with the 1-minute data over each monthly period (January, April, June, October).

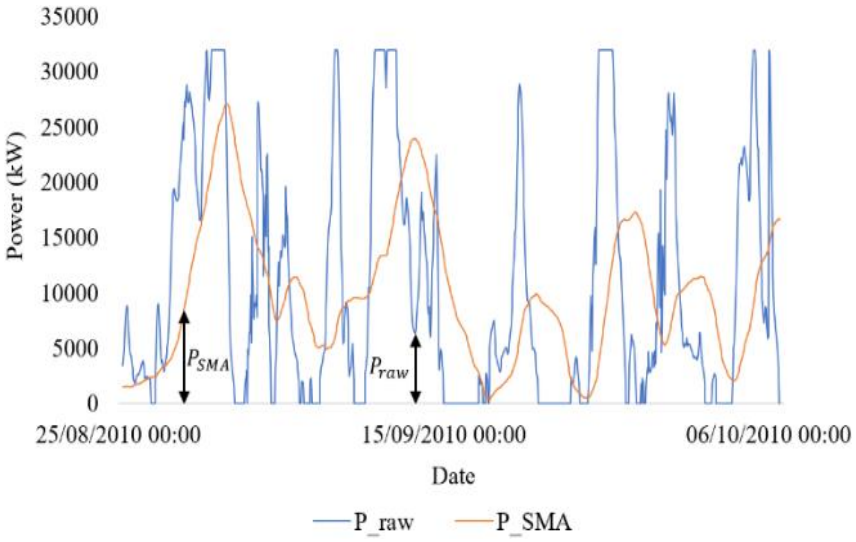

Figure 6.7: Definition of the terms P_raw and P_SMA.

Equations 6.6 and 6.7 show the net energy calculations based on whether the system has positive or negative ΔP respectively:

$$E_{net\_positive} = E_{SMA} + (E_{charging} \times \eta_{pump}) \quad (6.6)$$

$$E_{net\_negative} = E_{SMA} - \frac{(E_{discharging})}{\eta_{Pelton} \times CEF} \quad (6.7)$$

where E_{SMA} is the SMA energy, $E_{charging}$ *and* $E_{discharging}$ are the input energies into the centrifugal pump and Pelton Wheel respectively, η_{pump} and η_{Pelton} are the respective hydraulic machinery efficiencies and where CEF is the Cycle Energy Factor, which indicates the thermal efficiency of the subsea accumulator. For ideal isothermal compression/expansion of the air, the CEF is equal to unity [51]. $E_{net\_positive}$ and $E_{net\_negative}$ are the energies retained from the intermittent energy generated after considering ESS losses.

Table 6.2 summarises the constant values used throughout the statistical analysis, from which the storage capacity of the ESS could be derived. A high average centrifugal pump efficiency (80%) was assumed in order to take a more conservative ESS sizing approach, since higher pumping efficiencies directly imply higher requirements for storage capacity when assuming that the same number of hours of charging will be permitted, independent of pump efficiency.

For each case study, the energy storage requirements providing an availability of at least 80% and 100% were analysed in order to understand how many breakwaters would be required per ECU (see more in Chapter 7).

Table 6.2: Parameters for the HPES system maintained constant for the statistical analysis

Parameter	Value
Simple Moving Average (SMA)	1-day
Centrifugal Pump Rated Power	4.3 MW
Centrifugal Pump Average Efficiency	80%
Pelton Wheel Rated Power	5.0 MW
Pelton Wheel Efficiency	0.85
Cycle Energy Factor (CEF)	0.95
ESS Capacity (per Breakwater)	3.85 MWh

The motive for the inclusion of two percentages is to understand the trade-off in energy storage capacity for having a maximum of 20% more availability. Table 6.3 shows the ESS capacity values for the four different months analysed for a 1-day SMA. The results clearly indicate that sacrificing a small percentage of ESS availability can lead to significant capacity reductions of up to 90%. In most cases, the 10 MWh presented in Table 6.3 provided at least 80% ESS availability. The month of April saw the highest wind speeds, leading to greater energy storage requirements and higher differential power handling requirements by the ECU. Table 6.4 presents the ratio of power between the ESS and the RES power yielded. The values for Case Study 1 are higher in comparison to Case Study 2, indicating that due to having one RES rather than a mix, the ESS requires greater utilisation to avoid RES power curtailment, despite Case Study 2 having a relatively greater energy generation. This finding indirectly shows that more losses will occur in Case Study 1 since more power is diverted into the storage system.

Table 6.3: ESS capacity values for different ESS availabilities for the 4 months analysed.

	ESS Capacity (MWh)			
	Case Study 1 ESS Availability		Case Study 2 ESS Availability	
	≥ 80%	100%	≥ 80%	100%
January	10	55	10	60
April	10	105	10	110
June	10	100	10	95
October	10	100	10	105

Table 6.4: The ratio of power between the ESS and the RES.

	kW (ESS) per kW (RES yielded)	
	Case Study 1	Case Study 2
January	0.815	0.771
April	0.528	0.510
June	0.762	0.698
October	0.656	0.617

Figure 6.8 presents scatter plots for Wind Only data (Case Study 1) and Wind and Solar data combined (Case Study 2) showing the relationship between ESS availability and the number of hours spent in charging or discharging mode based on the applied SMA. All months presented plots of similar trends. The parameters set for the simulation results presented in Sections 6.2.3 to 6.2.5 consider one ECU and three breakwaters, resulting in an overall ESS capacity of 11.55 MWh. This should thus provide an ESS availability greater than 80%.

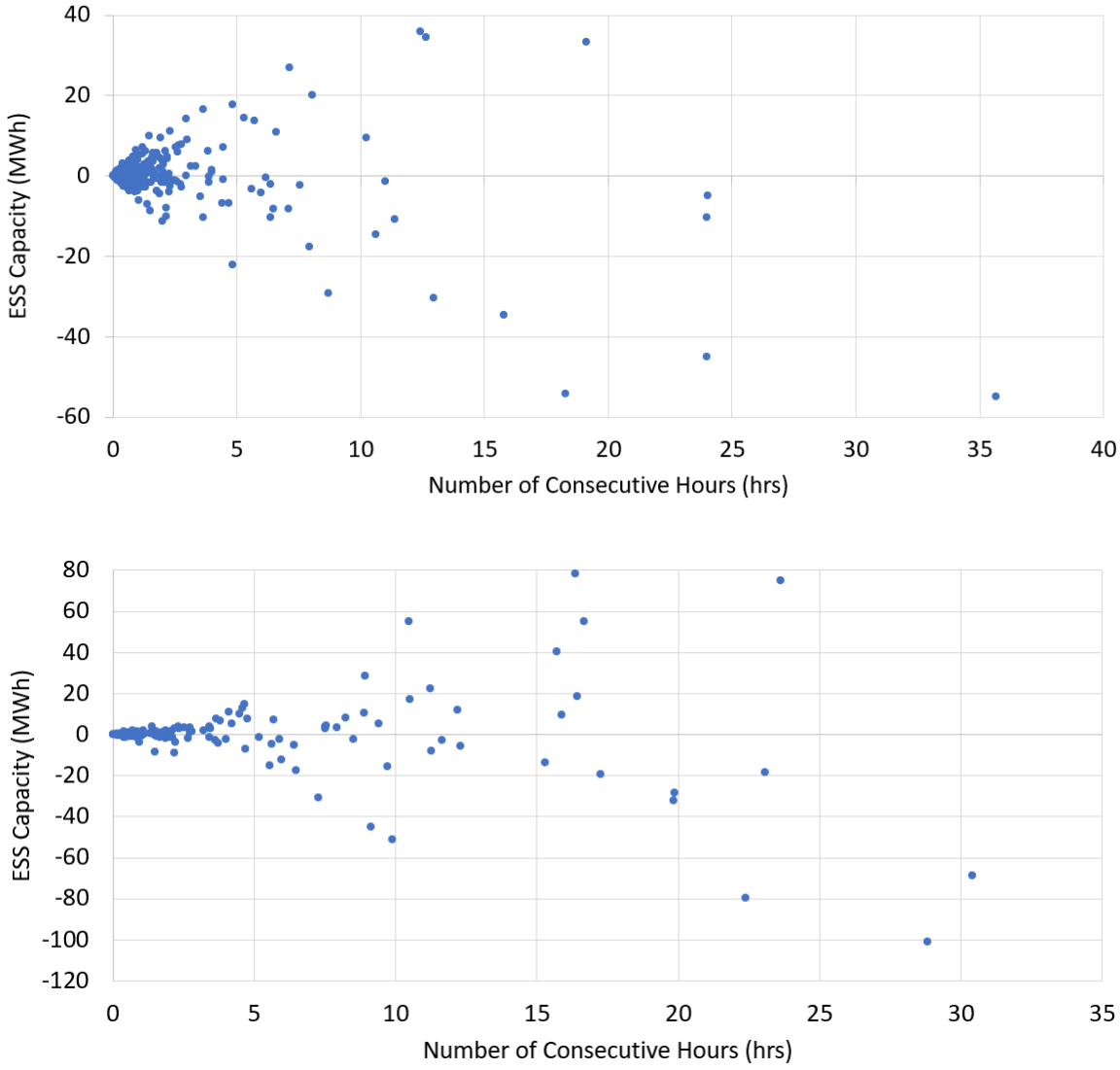

Figure 6.8: The relationship between ESS availability and the number of consecutive hours in charging or discharging mode for (a) Case Study 1 for the month of January and (b) Case Study 2 for the month of October.

6.2.2 Simulation Tests Performed

Once the RES generation data was setup and ESS capacity determined (Section 6.2.1), the simulation tests with the Alpha and Alpha Plus models could be performed. The simulations were carried out in order to understand optimal ESS capacity, the reliability of the Alpha Plus one-step-ahead forecasting model in providing a smoothened power output and the long-term operational performance of the ECU model. All runs were initialised from the mid-pressure value of the energy storage system (140 bar) to mimic a week of typical operation of the ECU based on the data, which would experience variations from the minimum to the maximum pressures (shown in Table 4.3 in Section 4.2) regularly. All simulations were performed with the ECU Baseline design data presented in Section 4.2.

The simulation runs were split into 3 parts; The first part involved analysing the effects of varying the number of breakwaters (and thus ESS capacity) on ECU performance. The study consisted in utilising the Alpha model for the same 1-week simulation for a storage capacity of 1, 3 and 5 breakwaters. The second part involved running the Alpha Plus model for 1 day from each month of RES generation data available to assess the forecasting model's reliability. The reason for having a shorter simulated timeframe is due to the Alpha Plus numerical model being more computationally demanding than the Alpha model as a result of the inclusion of the time-series forecasting model. Finally, the third part involved using the Alpha model to study a week of operation per month of data obtained for the two case studies, described in Table 6.1 in Section 6.2.1. The objective of the latter part was to assess the overall system efficiency for a week of operation. The ECU average efficiency and overall storage system efficiency were evaluated to understand how operation is affected across the four seasons of the year. Tables 6.5 to 6.7 summarise the simulations performed, and the results shown in Sections 6.2.3 to 6.2.5.

Table 6.5: The runs performed in the Alpha model for Section 6.2.3.

Simulation Parameters	1 Breakwater	3 Breakwaters	5 Breakwaters
ESS Capacity (MWh)	3.85	11.55	19.24
Case Study Applied	Case Study 1 (Wind Only)		
SMA Applied	1-day		
Time Period Simulated	1 Week (9 to 16 January 2016)		
Numerical Model Used	Alpha model		

Table 6.6: The runs performed in the Alpha Plus model for Section 6.2.4.

Simulation Parameters	Case Study 1 (Wind Only)
ESS Capacity (MWh)	11.55
SMA Applied	1-day
Time Periods Simulated	1 Day (January 2016) - Winter 1 Day (April 2016) – Spring 1 Day (June 2016) – Summer 1 Day (October 2015) – Autumn
Numerical Model Used	Alpha Plus model

Table 6.7: The runs performed in the Alpha model for Section 6.2.5.

Simulation Parameters	Case Study 1 (Wind Only)	Case Study 2 (Wind+Solar)
ESS Capacity (MWh)	11.55	
SMA Applied	1-day	
Time Periods Simulated	1 Week (January 2016) - Winter 1 Week (April 2016) – Spring 1 Week (June 2016) – Summer 1 Week (October 2015) – Autumn	
Numerical Model Used	Alpha model	

The following sections summarises the results of the runs selected for simulation, highlighting the key findings by analysing ECU performance and understanding the effects, if any, that different seasons of the year could have on the performance of the HPES system.

6.2.3 Evaluating the Impact of ESS Capacity On ECU Performance

In order to understand how ESS capacity affects the performance of the ECU made up of the MW-scale hydraulic machinery, a parametric analysis varying the number of breakwaters (and thus ESS capacity) was carried out as explained in Table 6.5. Table 6.8 presents the key indicators, which highlight the differences due to different ESS capacity sizing. The results show that a proportionality exists between improving the output smoothened power signal and increasing the ESS capacity.

For the 5-Breakwater system, a 34.8% difference in standard deviation was obtained between the intermittent signal and the actual smoothened signal, while this difference was 32.7% for the 1-Breakwater system. An increased ESS capacity of more than 1 breakwater caused the average centrifugal pump efficiency to improve by a maximum difference of 9.1%. The overall system storage efficiency (calculated via Equation 6.3 in Section 6.1.2) also increased since the ECU could operate for longer periods and curtail less power due to the ESS being more available. Despite the low average pump efficiencies, Figure 6.9 shows a histogram analysis comparison of the pump efficiency, where the pump experienced its peak frequency at the higher efficiency values (> 70%).

Table 6.8: The main results of the parametric ESS capacity study.

Simulation Results	1 Breakwater (3.85 MWh)	3 Breakwaters (11.55 MWh)	5 Breakwaters (19.24 MWh)
Standard Deviation (Intermittent Signal)		3.33	
Standard Deviation (Ideal Smoothened Signal)		1.80	
Standard Deviation (Actual Smoothened Signal)	2.24	2.19	2.17
Average Centrifugal Pump Efficiency	59.0%	64.9%	64.7%
Overall System Storage Efficiency	80.58%	83.60%	87.00%

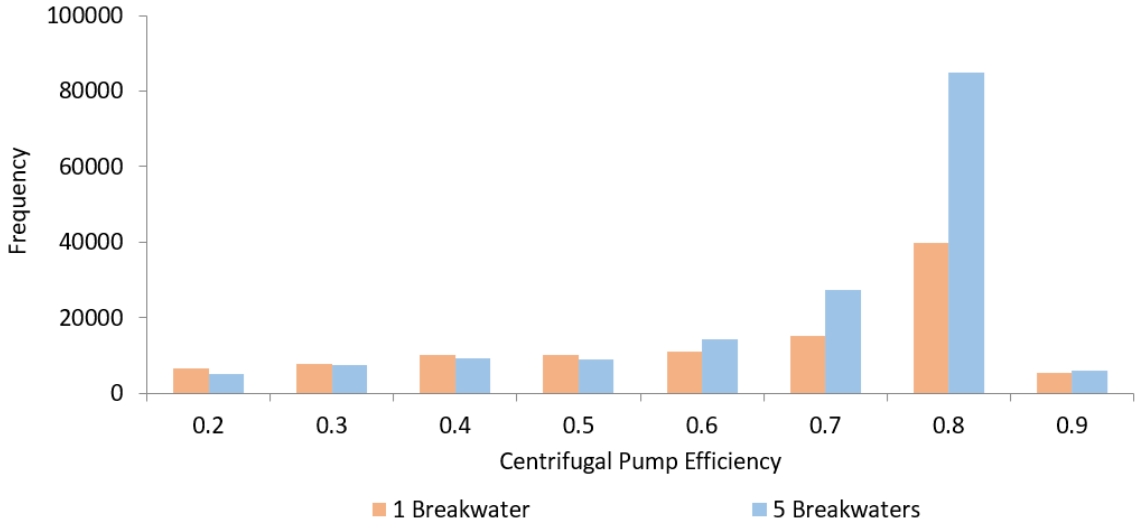

Figure 6.9: Plots showing the Centrifugal Pump Efficiency Histograms over a week of operation for 1 Breakwater and 5 Breakwaters as the ESS.

By visually comparing the two plots (Figure 6.9) it can be immediately concluded that the centrifugal pump is well-designed since the histogram analysis shows that the most common efficiency experienced during centrifugal pump operation is closest to the best efficiency point of the pump, varying between 0.7 and 0.8. Additionally, the 5 Breakwater ESS capacity caused an increase in the pump average efficiency since the lower efficiency values between 0.2 to 0.7 occurred less frequently in comparison to the 1 Breakwater system, thus leading to more pump efficiency frequencies occurring between 0.7 and 0.8. Values including and between 0 and 0.1 were excluded from the histogram analysis since such values occurred whenever the pump was not in operation or whenever there were numerical errors during the interpolation and extrapolation of the pump curve polynomial equations to obtain the desired speed of operation.

Figure 6.10 shows a comparison of the fluctuations in PCS pressure across the simulated week for an ESS capacity of 3.85 MWh (1 Breakwater) and 19.24 MWh (5 Breakwaters) respectively. Due to the smaller capacity, the singular breakwater experiences fluctuations more frequently and will also experience more curtailment due to being fully charged or fully discharged more easily (i.e., one cannot charge or discharge the system further since extreme pressures are reached). Meanwhile, the 5-Breakwater system only experiences a full charge and discharge cycle twice in one week.

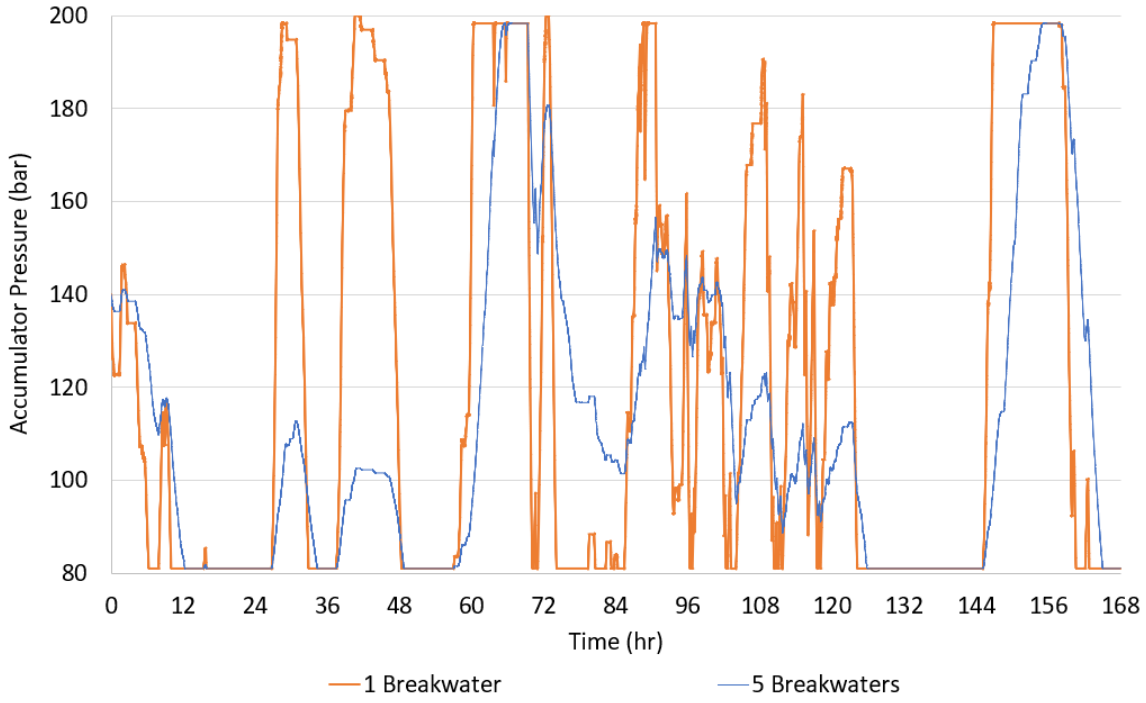

Figure 6.10: Plots showing the PCS Pressure variations over a week of operation for 1 Breakwater and 5 Breakwaters as the ESS.

As a result of the results in the study in Section 6.2.3, it was concluded that the option of a 3-Breakwater system (11.55 MWh) could be considered for the Case Studies performed. The ratio of storage capacity to ECU power for this scenario was approximately three (3:1). This system provided the best compromise between ESS availability, intermittent signal power smoothing and overall system storage efficiency, while also providing a 9.1% advantage in average centrifugal pump efficiency compared to a 1-Breakwater system.

6.2.4 Smoothing Power Fluctuations using Time-Series Forecasting

This section presents the results obtained evaluating the reliability of the Alpha Plus forecasting model and the ECU response to producing a smoothened power output. The data used was solely based on the IEA 10 MWwind turbine [173]. Table 6.9 summarises the results required to confirm if the dataset being used was stationary or not, based on equation 3.52 presented previously in Section 3.7. Since the P-value was less than 0.05, the null hypothesis could be rejected, confirming the data as being stationary. A double check was performed by comparing the test statistic to the stationarity check at different intervals, with a more negative number increasing the confidence that the available data were stationary [160]. Since the test statistic is in fact smaller compared to the different confidence interval checks, the data were confirmed stationary.

Table 6.10 presents the one-step-ahead forecasting model average Root Mean Square Error (RMSE) results across the four twenty-four-hour simulations performed (shown previously in Table 6.7). The average RMSE was calculated by taking the mean value of the difference between the forecasted ($P_{forecasted}$) and actual values (P_{raw}). The difference was squared and then square rooted, thus leading to the RMSE calculation as shown in equation 6.8.

$$\text{RMSE} = \sqrt{\left(P_{forecasted} - P_{raw}\right)^2} \tag{6.8}$$

Table 6.9: The ADF test results.

	Parameter	Values based on a 24-hour simulation			
		January	**April**	**June**	**October**
Stationarity Check	P-value	0.00226	0.000084	0.00227	0.000017
	Test Statistic	-3.871	-4.701	-3.871	-5.052
	99% Confidence	-3.433			
	95% Confidence	-2.863			
	90% Confidence	-2.567			

Table 6.10: The average RMSE results for the simulations performed.

Parameter	Values based on a 24-hour simulation			
	January	**April**	**June**	**October**
Average RMSE Value (kW)	129	16.13	20.75	69.27

Figures 6.11 and 6.12 show the different power curves superimposed for a twenty-four-hour simulation in January and October respectively. The theoretical SMA ($P_{smt,I}$) is the ideal moving average which is ideally to be followed. As may be observed, the smoothened output ($P_{smt,O}$) is identical to the theoretical SMA ($P_{smt,I}$) during Pelton wheel operation since this machinery offers excellent control variability due to its variable speed and spear valve control, as described in Sections 5.1 and 5.2.

During pump operation, the smoothened power output ($P_{smt,O}$) has portions of intermittency, indicated in Figures 6.11 and 6.12, where the intermittent power (P_{raw}) is superimposed by the smoothened power output ($P_{smt,O}$). This occurrence is due to the required power being too low (according to the pump characteristic curves) to reach the high pressures within the PCS at lower powers (typically < 1.3 MW). The reason for the 1.3 MW value is based on the pump characteristic curves (depicted by the grey line), where the centrifugal pump produces a pressure of 80 bar at a power of 1.3 MW.

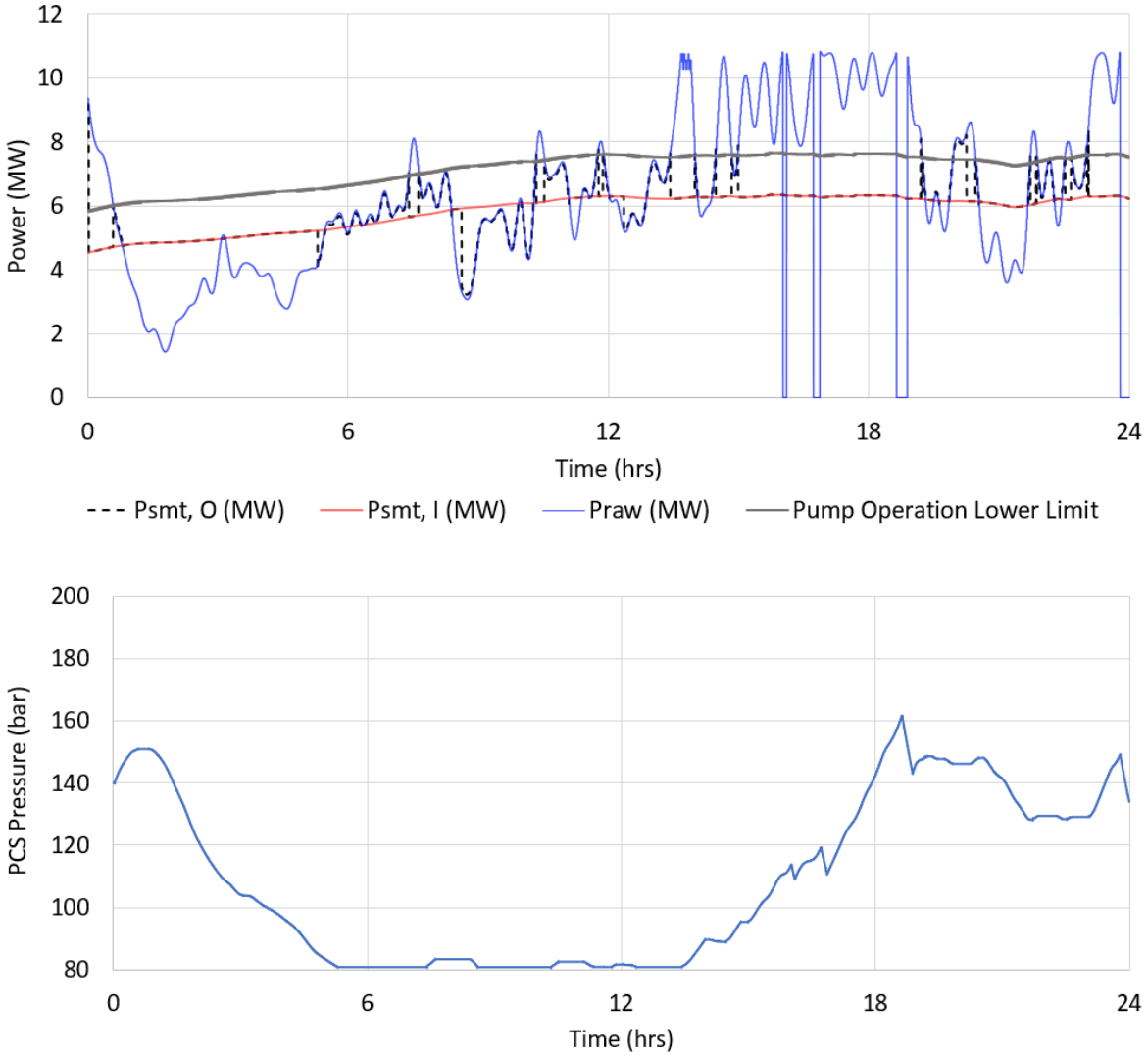

Figure 6.11: The various power curves and the corresponding PCS pressure variation over a 24-hour simulation (SMA of 24 hours) based on January data.

As a result, whenever powers are less than this value, the pump's centrifugal effect cannot utilise the low power input while simultaneously reaching the required pressure based on the PCS state-of-charge. Due to the variable head operation of the pump, another case of intermittency at a higher power than 1.3 MW is seen after approximately 16 hours of operation, where a power differential of 5 MW at a pressure of approximately 160 bar was found to be too high a power for the pump to reach. Figures 6.11 and 6.12 show the pressure variation within the PCS. Table 6.11 summarises the results based on the four different simulations performed.

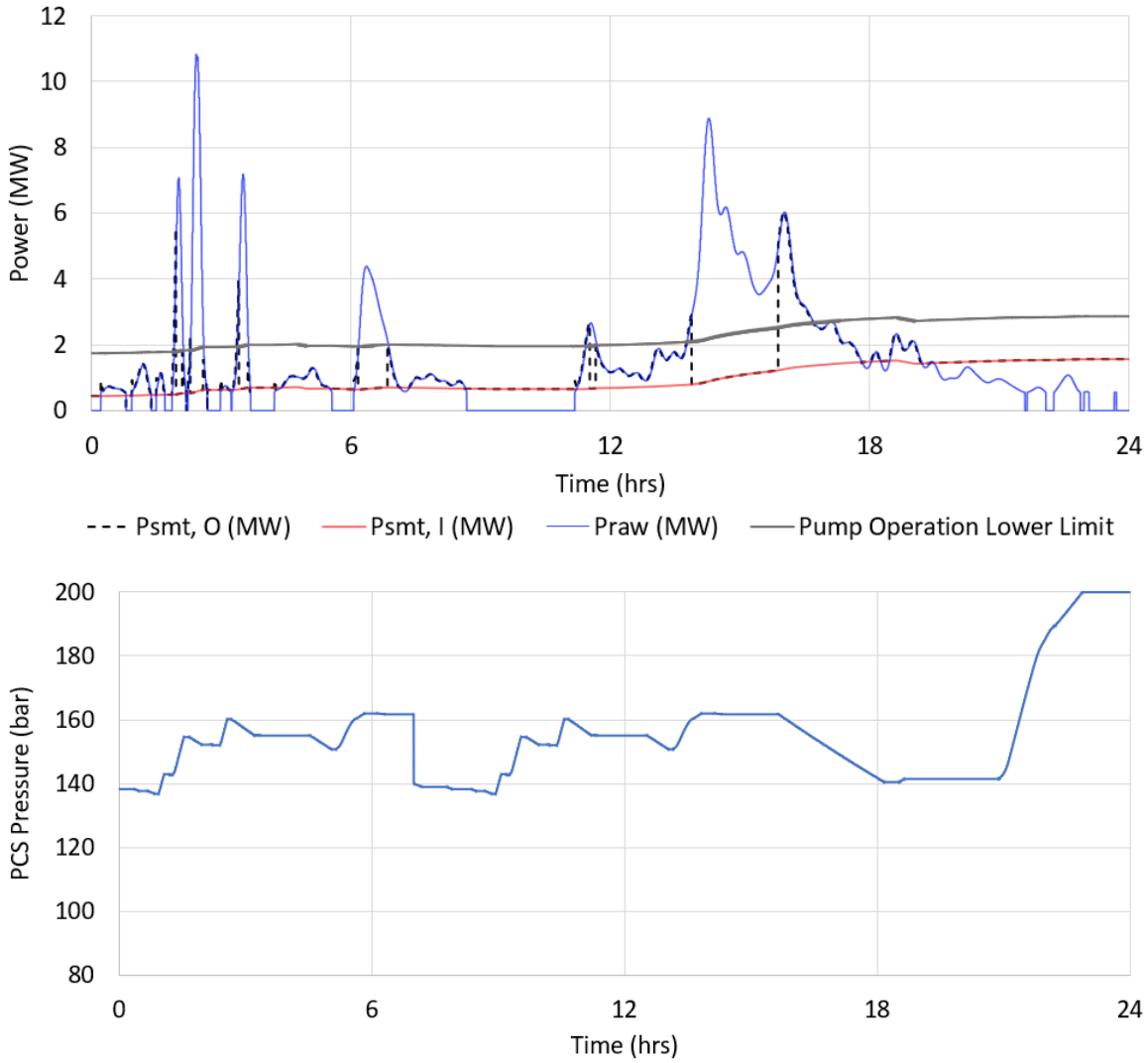

Figure 6.12: The various power curves and the corresponding PCS pressure variation over a 24-hour simulation (SMA of 24 hours) based on October data.

Table 6.11: Summary of the main simulation results.

Parameter	Values based on a 24-hour simulation			
	January	April	June	October
Average Centrifugal Pump Efficiency	64.1%	48.0%	61.0%	53.6%
Average Pelton Turbine Efficiency	88.3%			
% of Energy through the ESS	29.0%	22.6%	71.4%	75.6%
Standard Deviation (P_{raw})	2.56	2.04	1.97	1.81
Standard Deviation ($P_{forecasted}$)	0.79	1.33	0.61	0.78
Overall System Storage Efficiency	91.2%	92.9%	80.4%	60.6%

Despite the pump's average efficiency value, the overall system storage efficiencies calculated using equation 6.3 in Section 6.1.2 were high, apart from the twenty-four-hour simulation based on October's data. The reason for the low overall system storage efficiency is that the pump was utilised most frequently in this case, and thus its low efficiency played a bigger role when computing the efficiency value shown in Table 6.11. Additionally, despite the simulation for April having the lowest average pump efficiency, the overall system storage efficiency attained was the highest relative to the other simulations. This result may be due to more discharging time of the ESS instead of charging time for the time period simulated and due to the pump being inoperable in unfavourable pressure-power conditions. The reason for the high efficiencies despite the low centrifugal pump average efficiencies is that only a portion of the wind turbine's intermittent power passes through the ECU. Furthermore, the standard deviation of the smoothened power output ($P_{smt,O}$) was reduced by at least 34.8% in comparison with the intermittent wind turbine power signal (P_{raw}). These results are expected to reduce the requirements for spinning reserves substantially, which are presently used to balance intermittent loads from large offshore wind farms.

6.2.5 HPES System Performance

The Alpha model is the most computationally efficient numerical model developed, thus allowing longer simulations of the HPES operating. Table 6.6 in Section 6.2.2 presented the runs performed using the Alpha model, with the aim of understanding the long-term ECU performance and how the HPES system handles smoothing the intermittent signals of the powers based on the Case Studies considered. The runs simulated a full week of operation, and the dates selected were kept the same for both Case Studies in order to analyse the similarities and differences in ECU performance between the two studies.

Tables 6.12 and 6.13 present the main results obtained for Case Studies 1 and 2 respectively. For three months out of four, the combination of two RES saw minimal improvements in both the average centrifugal pump and overall system storage efficiencies. Additionally, the SMA was more effective for Case Study 2 in comparison to Case Study 1. In the case of April, the overall system storage efficiency dropped by 0.4% for Case Study 2 compared to Case Study 1, with the decrease being considered negligible.

Table 6.12: Summary of the main simulation results for the Case Study 1 (Wind Only) simulations.

Parameter	Values based on a 7-day simulation (Case Study 1)			
	January	**April**	**June**	**October**
Average Centrifugal Pump Efficiency	64.9%	57.6%	65.2%	58.8%
Standard Deviation (P_{raw})	3.33	3.45	4.04	3.82
Standard Deviation ($P_{smt,O}$)	2.19	2.42	3.09	2.40
Overall System Storage Efficiency	83.6%	75.8%	77.2%	70.5%

Table 6.13: Summary of the main simulation results for the Case Study 2 (Wind+Solar) simulations.

Parameter	Values based on a 7-day simulation (Case Study 2)			
	January	**April**	**June**	**October**
Average Centrifugal Pump Efficiency	64.4%	58.0%	66.5%	58.9%
Standard Deviation (P_{raw})	3.37	3.73	4.07	3.84
Standard Deviation (P_{SMT})	2.22	2.51	3.14	2.39
Overall System Storage Efficiency	83.7%	75.4%	78.8%	71.0%

Figures 6.13 and 6.14 present the power curves and the PCS pressure variation for a week of HPES system operation based on data from the months of January and October. The power curves have been previously described in Section 6.1. The intermittency issues presented during charging are due to pump operation limitations, where the pump can only operate at a minimum power of 1.3 MW. Another reason for intermittency issues are short periods during which the PCS was fully discharged or charged (for example hours 62 to 70 in Figure 6.13). During discharging, the Pelton turbine was always readily available, apart from situations where the power differential exceeded the rated power of the machinery, or when the PCS was fully discharged and could not discharge more seawater (for example hours 72 to 105 in Figure 6.14). Some drops in power are drastic since the WTs inertia was not considered when calculating its power production based on wind speed.

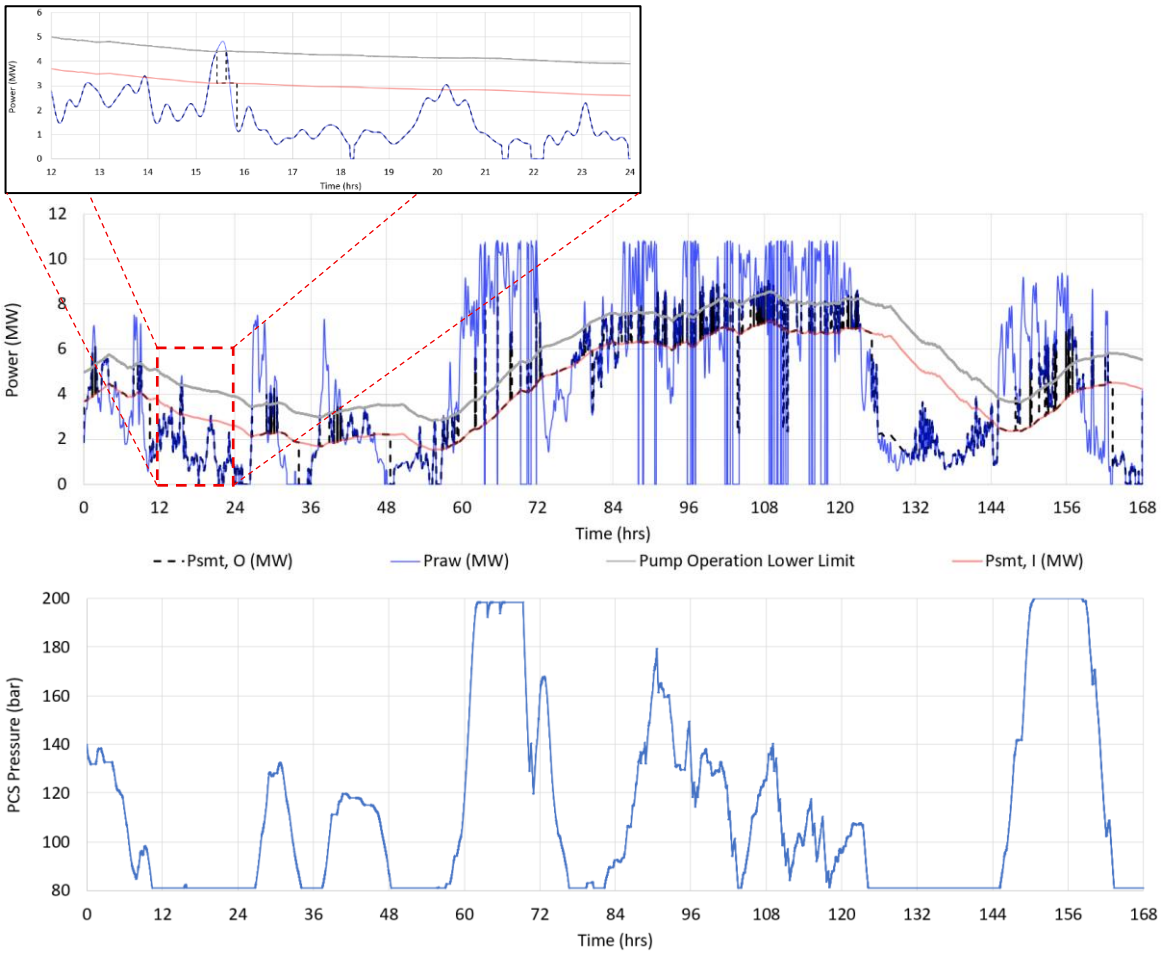

Figure 6.13: The various power curves and the corresponding PCS pressure variation over the 1-week simulation (SMA of 24 hours) based on January data.

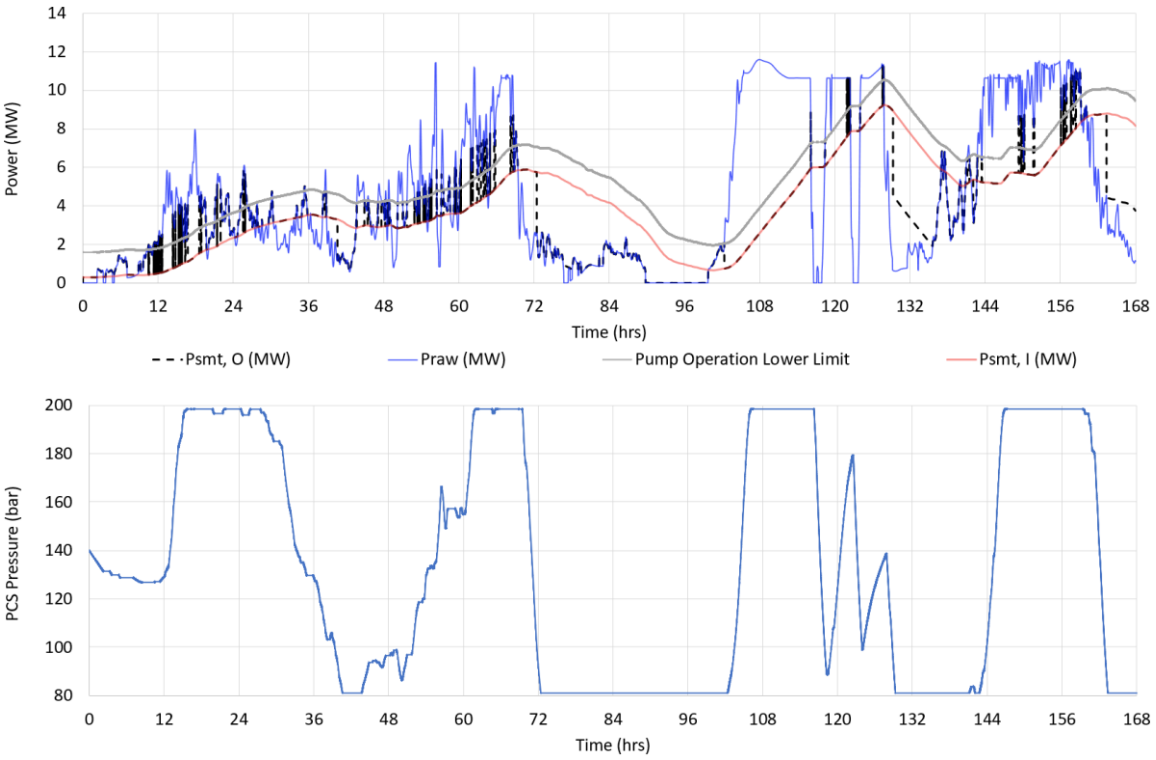

Figure 6.14: The various power curves and the corresponding PCS pressure variation over the 1-week simulation(SMA of 24 hours) based on October data.

Figure 6.15 presents a typical pump rotational speed graph obtained through the simulations performed in order to understand how the pump's speed varied based on pressure and power requirements. The pump operational speeds occurred between speeds of 2,150 and 3,250 RPM, where the former rotational speed represents the minimum operational speed at the pre-charge pressure of 80 bar, while the latter rotational speed is the rated speed of the centrifugal pump.

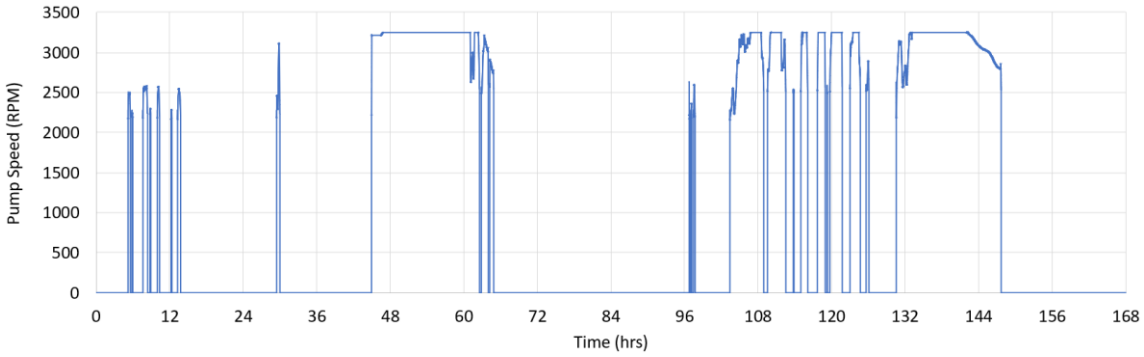

Figure 6.15: The centrifugal pump rotational speed variation for the simulation based on June data.

6.3 Concluding Remarks

The work presented in this chapter provided a better understanding of the performance of the HPES system while presenting the key differences in system operation when implementing the Alpha and Alpha Plus models respectively. This chapter applied the Alpha and Alpha Plus models to evaluate sensitivities such as ESS capacity and smoothing power fluctuations. The main conclusions per section are presented hereunder.

Main conclusions from Section 6.2.1:

1. Sacrificing a maximum of 20% of ESS availability can reduce ESS capacity requirements by up to 90%. This would directly lead to significant cost reductions, with the negative consequence of having to deliberately curtail any RES energy for 20% of the time.

2. The value of kW absorbed or released by the ESS per kW yielded by the RES yield was found to be higher for Case Study 1 (Wind Only) in comparison to Case Study 2 (Wind&Solar). This indicates that due to having one RES rather than a mix, the RES will need to store more energy since the ESS requires greater utilisation to avoid RES power curtailment despite Case Study 2 having a relatively greater energy

generation. This finding indirectly shows that more losses will occur within Case Study 1 since more power is diverted into the storage system.

Main conclusions from Section 6.2.3:

1. A larger storage system provides better overall HPES system storage efficiency for two main reasons; Less RES power is curtailed and the pressure changes during charging are more gradual. The latter is advantageous since if the differential power is at 3 MW, for example, the larger storage will allow the pump to operate at this power for a longer period of time while maintaining higher efficiency. If the storage system is too small, the 3 MW differential power may need to be handled at pressures of 80 bar, as well as higher pressures such as 160 bar, thus yielding highly varied centrifugal pump efficiencies in the meantime.

2. A larger storage system is also superior in smoothing out the intermittent power signal from RES due to being more readily available, thus also curtailing less power.

3. A larger storage system also increases centrifugal pump efficiency by skewing the efficiency histogram towards the higher operating efficiency range. Despite this, the results show that there is a limit as to how much the pump's efficiency can be improved as a function of storage capacity only.

Main conclusions from Section 6.2.4:

1. The Pelton Turbine wheel offers a high degree of flexibility in meeting the necessary smoothened power efficiently due to its variable speed and spear valve controlling the orifice or nozzle.

2. A single centrifugal pump is limited in its ability to meet the smoothing requirements of the RES when operating under the HPES system's variable head constrains, even when operated at variable speeds. This is due to the inherent performance characteristics of a centrifugal pump, making it impossible to operate at low power inputs while also meeting the high-pressure requirements (80 to 200 bar) of the HPES system.

3. Despite the low efficiency of the centrifugal pump, the overall system efficiency of the combined RES plus storage system in delivering a smoothened power output is still high in most cases. However, this is dependent on how much the centrifugal pump is utilised in smoothing out the intermittent signal from the RES.

Main conclusions from Section 6.2.5:

1. The use of a single, variable-speed centrifugal pump under variable head conditions with a pressure ratio of approximately 2.5 means that the operating power (input power) is dependent on the pressure within the PCS. Pump compatibility between input power and pressure must be observed to ensure that the pump is operable and furthermore to ensure that operation occurs at points as close to the pump's best efficiency point as possible.

2. Despite the pump limitations, overall system storage efficiency is satisfactory, with minor improvements being made when storing energy from more than one RES source, despite the fact that multiple RES sources cause higher standard deviations in the raw power data.

7 STATISTICAL ANALYSIS FOR EVALUATING THE ENERGY STORAGE REQUIREMENTS OF OFFSHORE WIND AND SOLAR PLANTS IN THE MEDITERRANEAN SEA

The following chapter presents a statistical analysis for two case studies involving offshore wind and solar farms coupled to an offshore HPES system. The analysis aims to estimate the energy storage capacity and the number of energy conversion units required by the storage system to smoothen the intermittent power from offshore wind and solar plants operating under Central Mediterranean Sea conditions.

Based on the results and conclusions of existing research discussed in Section 2.2, a suitably sized ESS can be obtained with a combination of SDES, LDES and the use of a SMA to smoothen power. This chapter considers two case studies in the Central Mediterranean Sea, specifically in the Maltese Islands. The case studies consider 6 years of hourly data based on wind power only (Case Study 1) and a combination of wind and solar PV power (Case Study 2). The analysis in this chapter involves the HPES system described in Sections 1.3 and 2.1 for providing LDES ($\geq$ 8 hours). In modelling terms, a SMA is applied to the intermittent RES output, where the SMA is assumed to be the demand profile. The ESS charging and discharging modes are based on this key consideration, where charging and discharging represent power above and below the SMA, respectively. By following a SMA, the intermittent power signal from RES can become a smooth power supply when amalgamated with an ESS. The ECU is utilised to assess how storage requirements vary based on different SMAs and the average centrifugal pump efficiencies of the storage system. The overall system storage efficiency, which is the ratio of the energy generated by the combined RES and storage system divided by the energy generated in the absence of storage, is also calculated as a function of the variables being investigated (SMA and centrifugal pump efficiency). The analysis within this Chapter is performed via Excel®.

7.1 Methodology

The wind speed data used throughout this study is 3TIER hourly averaged data for years 2005 to 2010 in a time series format [20] which was corrected based on wind measurements obtained at a coastal location in the Maltese Islands for a height of 80 metres above ground level [21]. The wind speed measurements were applied to a IEA 10 MWwind turbine (WT) [22], with the wind speed being once again corrected for WT hub height based on a realistic wind shear exponent ($\propto$) [21], as shown previously via equation 4.1 in Section 4.4. Section 6.2 already presented the methodology applied for calculating the power difference and energies during charging and discharging through equations 6.2 to 6.4. Meanwhile, the solar data used was the same solar PV data obtained from the University of Malta[3], where the same multiplication factor of 1.11 was applied as explained previously in Section 4.4, which takes into consideration advantages such as less obstacles blocking sunlight, lower ambient temperatures (thus better PV efficiency) and less dust and assuming that the advantages outweigh the disadvantages [11].

Table 7.1 lists parameters related to the case studies under scrutiny. Three different SMAs of 1, 3 and 7 days were considered per case study. Moreover, due to the centrifugal pump operating under variable head conditions (based on the working principle of the offshore HPES system), a sensitivity analysis on the pump's average efficiency across the 6-year timeframe was also performed. The pump efficiency was fixed for the purpose of this study on Excel® since a 6-year analysis duration was utilised. All analysis combinations carried out in the study are shown in Table 7.2.

Table 7.1: Table showing the Case Studies sizing considered.

RES	Parameter	Case Study 1	Case Study 2
Wind	Number of WTs	3	3
	Capacity (MW)	30	30
	Capacity Factor	0.385	0.385
	Generation (GWh/annum)	112.9	112.9
Solar PV	Capacity (MW)	-	40.57
	PV Generation (kWh/year/kW)		1676.03
	Generation (GWh/annum)		68

[3] The solar PV data was provided by Prof. Ing. Joseph Micallef and Dr. Ing. Francarl Galea from the University of Malta.

Table 7.2: A summary of the analyses performed per Case Study.

Analysis Combinations		Centrifugal Pump Average Efficiency		
		60%	70%	80%
SMA	1-day	✓	✓	✓
	3-day	✓	✓	✓
	7-day	✓	✓	✓

Equation 7.1 enables the calculation of the overall system storage efficiency (η_{ovr}), which divides the 6-year duration sum of the energy values calculated using equations 6.3 and 6.4 previously shown in Section 6.2 for the SMA output by the total energy generated by the RES (E_{raw}). The net energy in or out of the ESS, $\Delta HPES$, is also accounted for in the calculation to correct for the fact that the state of charge of the HPES system at the start of the six year period is likely to be different from that at the end of the period. The overall system storage efficiency (η_{ovr}) represents the efficiency of the ESS in smoothing the intermittent-generated RES power.

$$\eta_{ovr} = \sum_{0}^{t} \frac{(E_{net_{positive}} + E_{net_{negative}})}{(E_{raw} + \Delta HPES)} \tag{7.1}$$

Table 7.3 summarises the constant values used throughout the statistical analysis. The Pelton Wheel efficiency was assumed constant since its efficiency is more easily regulated with a variable head compared to that of the centrifugal pump, assuming that both frequency control and spear valve control are being implemented to provide the desired power during discharge [23].

Table 7.3: The HPES system fixed parameters for the analysis.

Parameter	Value
Centrifugal Pump Rated Power	4.3 MW
Pelton Wheel Rated Power	5.0 MW
Pelton Wheel Efficiency	0.85
Cycle Energy Factor (*CEF*) [18]	0.95

7.2 Results

This section demonstrates a selection of the different analyses performed, explained previously in Table 7.2, and of the results generated. The results enable a better understanding of the consecutive number of hours spent in charging and discharging the ESS, of the scatter or distribution of the energy being stored, of the sensitivity between energy curtailment and ESS sizing and of the overall system storage efficiency in each analysis based on equation 7.1.

7.2.1 Peak shaving sensitivity based on the SMA implemented

Figures 7.1 and 7.2 show the effect of the SMA on the two different case studies referred to in Table 7.1. In Figure 7.1, while a 1-day SMA eliminates minimal peaks in Case Study 1, the inclusion of solar PV in Case Study 2 shows relatively more peak shaving for a 1-day SMA. Meanwhile, Figure 7.2 shows considerable smoothing for both 7-day SMA case studies. As a result of the regular 12-hour on and off power generation from the solar PVs, the joint power between the three wind turbines and solar PVs causes higher temporary peaks compared to Case Study 1, resulting in more peak shaving when applying a SMA.

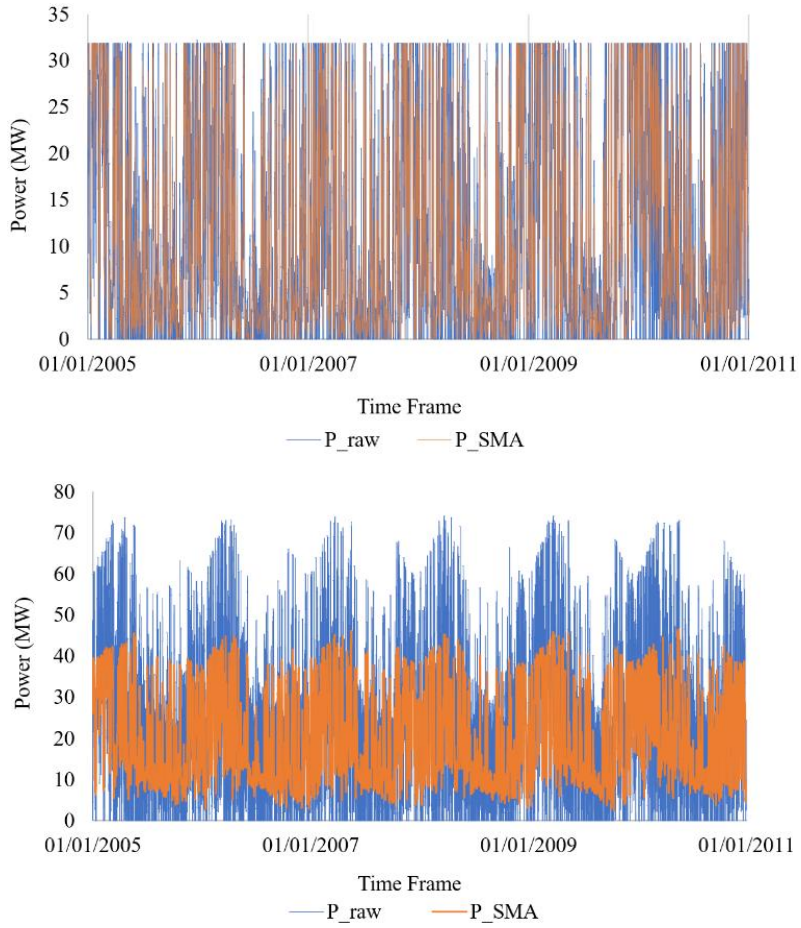

Figure 7.1: A 1 day SMA applied to Case Study 1 (top) and A 1 day SMA applied to Case Study 2 (bottom).

Table 7.4 summarises the standard deviations of the SMAs considered for the two case studies, where the difference in standard deviation in Case Study 2 with and without a SMA is greater compared to Case Study 1.

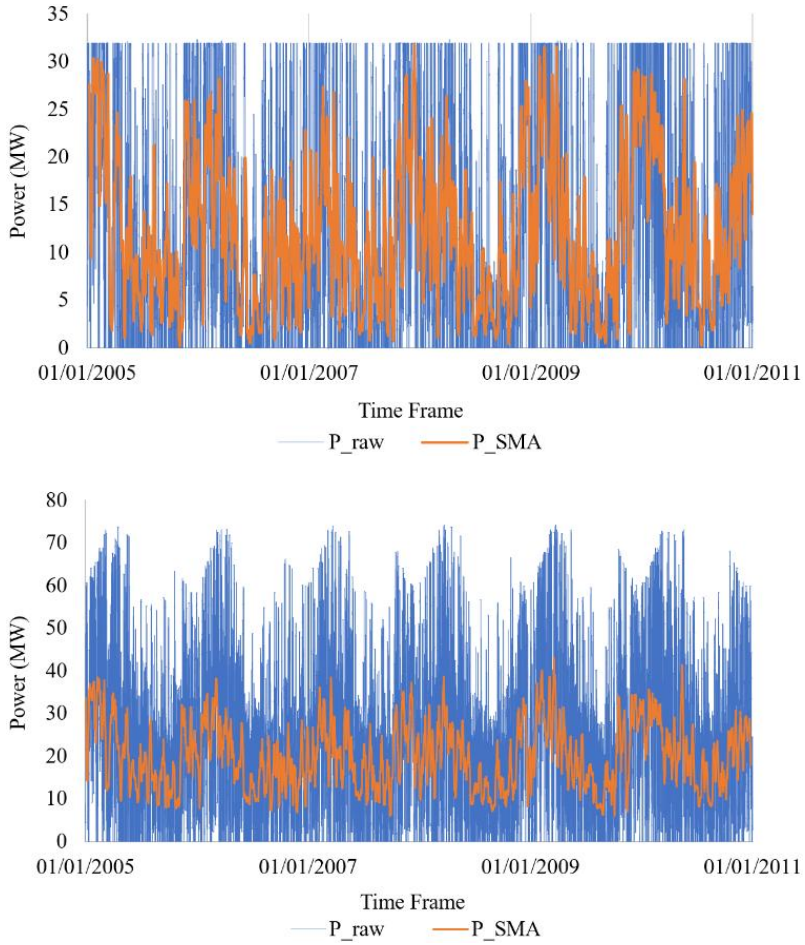

Figure 7.2: A 7 day SMA applied to Case Study 1 (top) and A 7 day SMA to Case Study 2 (bottom).

Table 7.4: SMA standard deviations for each Case Study.

Standard Deviations (MW)	No SMA	SMA		
		1-day	3-day	7-day
Case Study 1	12.24	11.05	9.14	7.39
Case Study 2	16.56	11.24	9.32	7.58

7.2.2 Consecutive number of hours during ESS charging or discharging

Figure 7.3 illustrates histograms for the number of consecutive hours of ESS charging and discharging for an average centrifugal pump efficiency of 70% and SMAs of 1- and 7-days respectively for Case Study 1 across the 6-year period.

While the raw power signal from the RES (P_{raw}) is intermittent by nature, the power set through the SMA (P_{SMA}) causes the differential power (based on equation 6.2 in Section 6.2) in or out of the system to be positive or negative for a consecutive number of hours. Consequently, the net positive or net negative energies follow the same trend ($E_{net\_positive}$ and $E_{net\_negative}$).

Figure 7.3 shows that the trend between a 1-day SMA and a 7-day SMA is the same, but due to the latter's longer SMA smoothing more peaks from the intermittent data, the maximum continuous hours in charging mode reaches 200 hours as opposed to the 1-day SMA maximum of 85 hours.

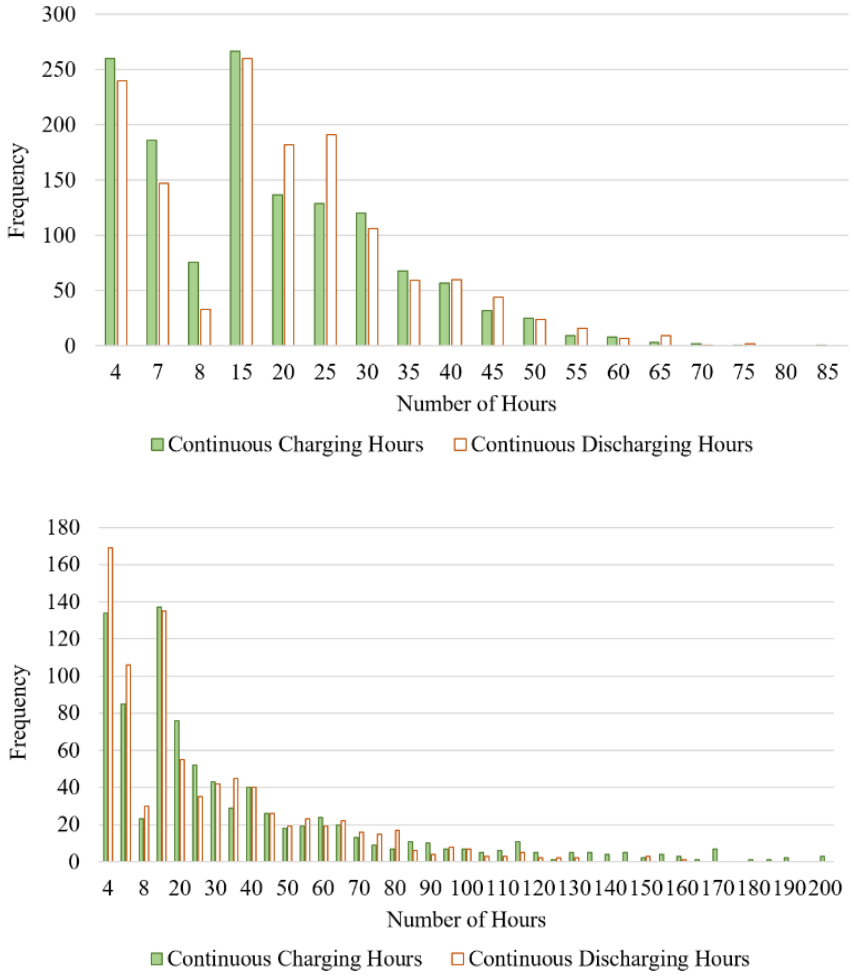

Figure 7.3: Consecutive Hours for a 1-day SMA (top) and Consecutive Hours for a 7-day SMA (bottom).

Table 7.5 shows the percentages of the number of hours which fall within the SDES (≤ 4 hours) and LDES (≥ 8 hours) spectrums across the 6-year period. Case Study 1 indicates a direct proportionality between LDES hours and SMA increase, while Case Study 2 shows an inverse relationship. In Case Study 2, the SDES percentage increases, especially between the 1- and 3-day SMAs. As SMA increases in Case Study 2, an average rise in mid-range hours (> 4 hours and < 8 hours) of 2.78% was observed. Case Study 1 has a decrease in SDES hour occurrences between the 1- and 3-day SMAs, yet its LDES hours increase with increased SMA.

Table 7.5: The percentages of SDES and LDES hours.

	Case Study 1		**Case Study 2**	
	≤ 4 h	**≥ 8 h**	**≤ 4 h**	**≥ 8 h**
1-day	18.10%	69.84%	7.44%	81.24%
3-day	17.36%	70.31%	9.82%	76.64%
7-day	17.61%	71.30%	9.99%	73.13%

7.2.3 The ESS capacity requirements

The analysis in the previous section provided insight on how many consecutive hours were spent in charging or discharging to understand where the amounts fell within the SDES and LDES spectra without accounting for the ESS sizing. Therefore, studying the storage capacity sizing requirements to truly determine if SDES or LDES would be required is discussed next. Figure 7.4 shows a scatter plot relationship between ESS capacity (positive for charging and negative for discharging) and the number of consecutive hours spent in charging or discharging mode for Case Study 2 at the three different SMAs.

It is evident from Figure 7.4 that a greater SMA immediately reflects greater energy storage capacity requirements due to more consecutive hours spent in charging or discharging modes. Additionally, the SDES and LDES limits are also plotted to show how the 6-year data frame is split with respect to duration type. Although ESS capacity varies depending on SMA, the capacity also changes depending on average pump efficiency. As previously described, three different average centrifugal pump efficiencies were considered to analyse how the pump's efficiency affects storage capacity requirements.

Tables 7.6, 7.7 and 7.8 show the maximum energy storage capacity noted for Case Studies 1 and 2 respectively and all the variable parameters considered (shown previously in Table 7.3). An energy storage system providing an availability of 95% and 100% were both examined. The motive for the inclusion of two percentages is to understand the trade-off in storage capacity for having 5% more availability, since the scatter plots in Figure 7.4 show a wide energy storage capacity and consecutive hours dispersion which may, at times, only occur once across the 6-year analysis period.

Table 7.6: ESS capacity values for different centrifugal pump efficiencies for a 1-day SMA.

1-day SMA	**ESS Capacity (MWh)**			
	Case Study 1 ESS Availability		Case Study 2 ESS Availability	
Pump Efficiency	95%	100%	95%	100%
60%	250	310	220	467
70%	265	310	235	467
80%	285	310	255	467

Table 7.7: ESS capacity values for different centrifugal pump efficiencies for a 3-day SMA.

3-day SMA	**ESS Capacity (MWh)**			
	Case Study 1 ESS Availability		Case Study 2 ESS Availability	
Pump Efficiency	95%	100%	95%	100%
60%	580	902	380	1072
70%	640	902	420	1072
80%	680	905	460	1072

Table 7.8: ESS capacity values for different centrifugal pump efficiencies for a 7-day SMA.

7-day SMA	**ESS Capacity (MWh)**			
	Case Study 1 ESS Availability		Case Study 2 ESS Availability	
Pump Efficiency	95%	100%	95%	100%
60%	860	1810	420	1720
70%	880	1810	460	1720
80%	960	1831	500	1720

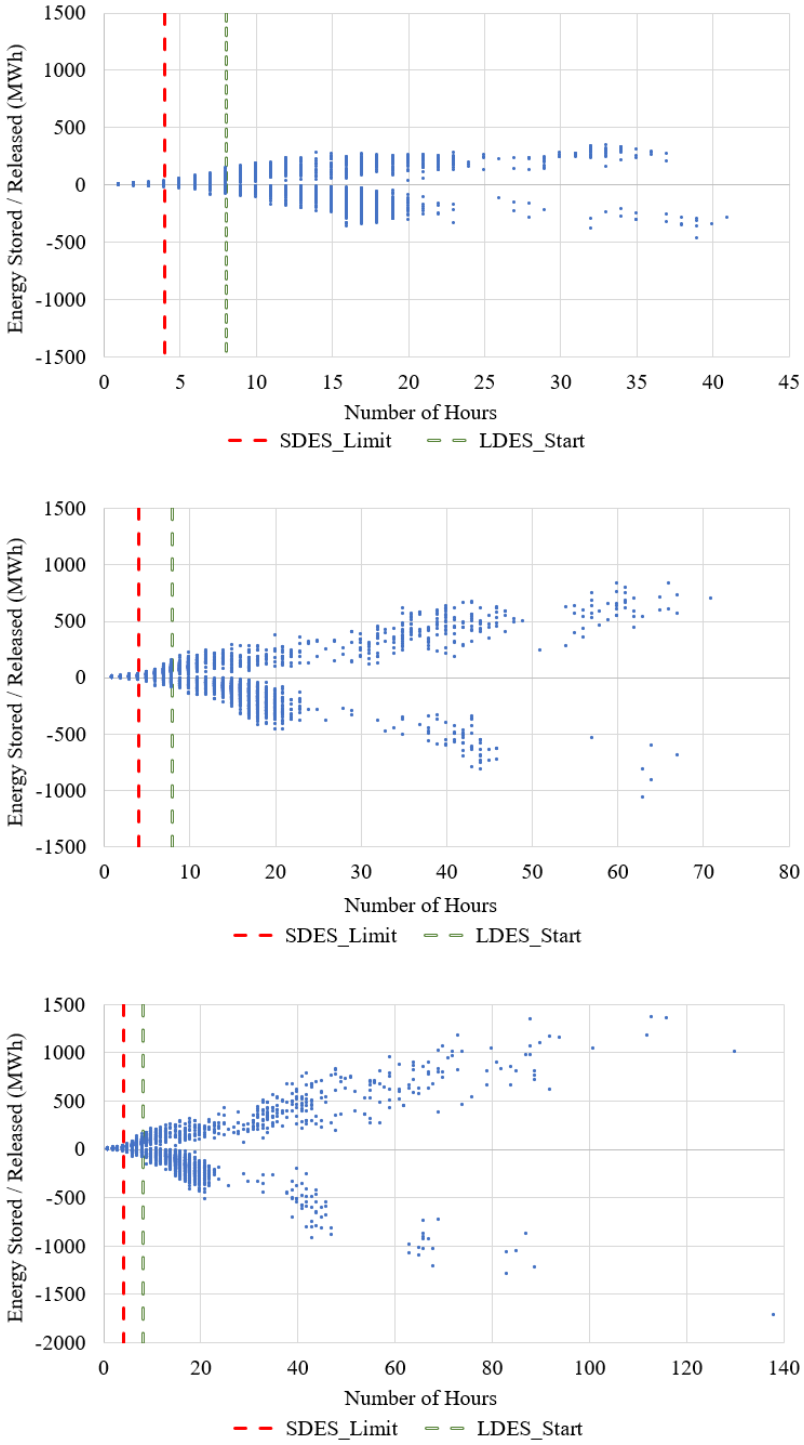

Figure 7.4: The ESS capacity relationship with consecutive charging or discharging hours for: a 1-day SMA (top), 3-day SMA (middle) and a 7-day SMA (bottom).

In Case Study 1, the ESS capacity at 100% availability varied slightly for a 3- and 7-day SMA for a pump efficiency of 80%, thus showing that the maximum ESS capacity requirement happened during charging, since the ESS capacity varied as a function of pump efficiency, unlike Case Study 2 and the 1-day SMA for Case Study 1.

However, in Case Study 2, the ESS capacity remained the same throughout all analyses since the maximum capacity requirement occurred during discharging and the Pelton Wheel efficiency was kept constant. While the powers reached in Case Study 2 are higher due to the amalgamation of 3 wind turbines and a solar plant, the energy storage capacity requirements at the highest SMA of 7 days are lower for Case Study 2 relative to Case Study 1 for all pump efficiencies.

The notable difference between the two case studies for all average pump efficiencies considered is that the 95% availability of ESS capacity decreases the capacity requirements by at least 45%, 57% and 71% respectively for the three different SMAs when considering a 5% sacrifice in ESS availability for Case Study 2. Consequently, a larger SMA leads to a more efficient ESS capacity in terms of MWh at a storage availability of 95% for both case studies. Tables 7.9 to 7.11 quantify the relationship between kWh of the ESS per kWh yielded by the RES for both case studies.

Table 7.9: Ratio of ESS energy to RES energy yielded for a 1-day SMA with 95% ESS availability.

1-day SMA	**kWh (ESS) per kWh (RES yielded)**	
Pump Efficiency	Case Study 1	Case Study 2
60%	0.27	0.57
70%	0.30	0.62
80%	0.32	0.65

Table 7.10: Ratio of ESS energy to RES energy yielded for a 3-day SMA with 95% ESS availability.

3-day SMA	**kWh (ESS) per kWh (RES yielded)**	
Pump Efficiency	Case Study 1	Case Study 2
60%	0.42	0.66
70%	0.46	0.69
80%	0.49	0.74

Table 7.11: Ratio of ESS energy to RES energy yielded for a 7-day SMA with 95% ESS availability.

7-day SMA	**kWh (ESS) per kWh (RES yielded)**	
Pump Efficiency	Case Study 1	Case Study 2
60%	0.48	0.65
70%	0.51	0.69
80%	0.55	0.74

The quantification provides insight on how much energy storage is required per kWh of energy yielded from the RES, irrespective of plant size. As expected, a higher pump efficiency and a larger SMA both increase the energy storage requirement per kWh of RES yielded. Greater pump efficiency leads to improved energy retainment, thus requiring more capacity since more energy would be captured. Case Study 2 shows negligible sensitivity to the ESS to RES kWh ratio between the 3- and 7-day SMAs, meaning that a 3-day SMA would make the same ESS use as a 7-day SMA, yet with a smaller storage requirement as explained previously in Tables 7.7 and 7.8.

7.2.4 The ESS power and number of ECUs required

The application of a SMA is one method to reduce high ECU power requirements to handle the otherwise potentially curtailed powers from the RES. The number of ECUs implies the number of centrifugal pump and Pelton Wheel units required based on the ΔP requirements the ESS is to handle. This is calculated by dividing the maximum ΔP by the hydraulic machine which has a smaller rated power (i.e., the centrifugal pump as shown in Table 7.3).

Figure 7.5 shows an example of an ECU power distribution histogram for a 3-day SMA for Case Study 2, indicating a maximum instantaneous power of 55 MW during charging and a maximum instantaneous power of 35 MW during discharging. Despite the maxima, due to the SMA, Figure 7.5 shows a concentrated distribution near the lower powers up to approximately 30 MW.

Tables 7.12 and 7.13 summarise the difference in the number of ECUs required per case study. A larger SMA leads to the ESS, and thus ECU, experiencing larger powers since the power differential (ΔP) is greater when averaging over a longer timeframe. While this did not affect Case Study 2, a 1-day SMA required one less ECU compared to a 3- and 7-day SMA since powers were smaller across the data frame and the parametric analysis of Case Study 1 showed greater sensitivity to SMA compared to Case Study 2.

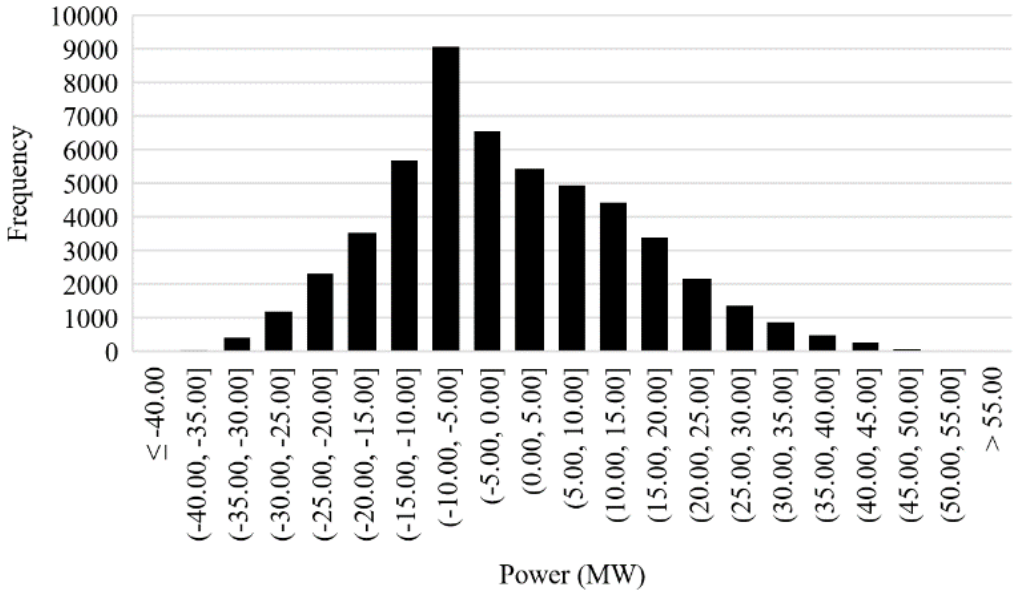

Figure 7.5: An example of the power distribution for Case Study 2 with a 3-day SMA.

Table 7.12: The number of ECUs required to reach 95% power availability for Case Study 1.

Case Study 1	SMA		
	1-day	3-day	7-day
Number of ECUs at 95% ECU Availability	4	5	5

Table 7.13: The number of ECUs required to reach 95% power availability for Case Study 2.

Case Study 2	SMA		
	1-day	3-day	7-day
Number of ECUs at 95% ECU Availability	6	6	6

7.2.5 The overall system storage efficiency

The overall system storage efficiency (η_{ovr}), defined previously in equation 7.1, provides a metric to relate the energy generated by the RES and storage system with the energy generated without an ESS. Although ECU hydraulic machinery efficiency is important, one must remember that with the SMA approach, not all power generated by the RES would be supplied into the ESS. The SMA is set to provide a smoothened power output to be fed to the grid, and the ESS is used to handle any excess power (through charging) or any power deficits in relation to the SMA power output (through discharging).

As a result, considering a 10% reduction in the centrifugal pump efficiency sensitivity study will not result in a 10% decrease in the overall system storage efficiency. The efficiency (η_{ovr}) would only reach 100% if no ESS were present or if the ESS would encounter no losses in the round-trip storage process. Tables 7.14 and 7.15 show the results of the overall efficiency for the two case studies.

The common trend between the two case studies is that a smaller SMA results in a higher overall efficiency. This occurrence further consolidates the results shown in Table 7.12, where more ECUs are needed for the 3- and 7-day SMAs compared to the 1-day SMA. The relationship is sound since greater power handling requirements by the ECU result in greater losses, thus impacting the overall system storage efficiency. Additionally, the $\Delta HPES$ also increased with increasing SMA. Case Study 2 shows a reduced sensitivity in the resulting overall system storage efficiency based on SMA, in comparison to Case Study 1. Case Study 1 out-performs Case Study 2 for a 1-day SMA where this is primarily due to the power differentials requiring two additional ECUs in Case Study 2 compared to Case Study 1. The 3- and 7-day results indicate a different trend, with Case Study 2 showing better overall system storage efficiency, improving the overall system storage efficiency gap between the two studies with lower pump efficiencies.

Table 7.14: The overall system efficiencies for Case Study 1.

Case Study 1	**Overall System Storage Efficiency**		
Pump Efficiency	1-day	3-day	7-day
60%	83.86%	74.84%	71.68%
70%	87.42%	80.12%	77.60%
80%	91.12%	85.73%	84.03%

Table 7.15: The overall system efficiencies for Case Study 2.

Case Study 2	**Overall System Storage Efficiency**		
Pump Efficiency	1-day	3-day	7-day
60%	79.54%	76.33%	75.00%
70%	83.98%	81.38%	80.28%
80%	88.63%	86.72%	85.89%

7.3 Concluding Remarks

A number of conclusions related to the case studies considered can be drawn, namely:

- The inclusion of more than one RES and increase in the RES installation size (in terms of power) improves the effect of applying a SMA. In fact, maximum reduction in the RES power standard deviation of 16.1% for Case Study 2 occurs in comparison to 11.6% for Case Study 1, thus showing that a SMA was more effective for Case Study 2 relative to Case Study 1.

- While the need for LDES is consistent across both case studies and all parametric analyses, the relationship between a SMA and LDES hours requires analysis on a case-by-case basis. In Case Study 1, an increase in LDES hours ($\geq$ 8 hours) was observed with increased SMA. Case Study 2 showed that LDES hours decreased with increased SMA. However, the LDES hours decrease did not encounter the same increase in SDES, but in the mid-range period of 4 to 8 hours, which is an ideal range (but not limited to) for the FLASC HPES system.

- Sacrificing 5% of ESS availability can reduce ESS capacity requirements by up to 71%. This would directly lead to heavy cost reductions by deliberately curtailing any energy exceeding the capacity based on the 5% ESS availability reduction.

- The inclusion of more than one RES indicates a greater need for storage, since multiple RES are also less sensitive to different SMAs, thus allowing a smaller SMA and smaller ESS capacity to yield the kWh of ESS per kWh of RES generation compared to a larger SMA and ESS capacity. Due to less sensitivity to a varied SMA when operating with multiple RES, the number of ECUs required is virtually independent of SMA. Case Study 1, however, indicates that a smaller SMA leads to less ECUs required due to a smaller power differential requirement.

- A larger SMA impacts overall system storage efficiency since losses due to larger power differential requirements are greater. A 20% increase in centrifugal pump efficiency (from 60 to 80%) can lead to a maximum improvement of 12.35% in overall efficiency based on the two case studies performed.

8 TECHNO-FEASIBILITY ASSESSMENT OF A FLOATING BREAKWATER CONCEPT INTEGRATING ENERGY STORAGE FOR SUPPORTING MARINE RENEWABLES IN DEEP WATERS

For islands such as the Maltese Islands, protecting our coastal areas from large waves in bad weather conditions has important social and environmental benefits. Floating Breakwaters (FBWs) may offer this solution given the two following advantages they offer over traditional breakwaters (BWs) [174]: (1) FBWs can be deployed in areas where traditional BWs cannot be due to poor seabed foundations; (2) FBWs are often more financially viable in sea depths exceeding 6 metres. Additionally, the installation of multiple FBWs can support the multi-use of offshore space. This chapter investigates the viability of developing an offshore project, dubbed FORTRESS (a floating offshore breakwater for supporting marine renewable energy around islands), involving the deployment of a novel, modular floating breakwater (FBW) design to create a sheltered water area in the deep sea to support multiple activities, including energy storage in the form of a HPES system. However, such projects can only become a reality if they are feasible financially. Techno-economic feasibility assessments are essential for establishing the viability of new technologies under development [175]. The rapid increase in RES plants harvesting intermittent sources of energy, such as wind and solar power is leading to grid management problems given that the energy supply often does not match the actual demand by end consumers [176]. Energy storage is essential in handling this challenge and enabling the integration of renewables on a wide scale within the electricity supply networks [177] [178]. There is a growing interest to combine offshore renewables with other activities within the same marine space, including aquaculture and energy storage. Apart from making more efficient use of marine areas, co-locating different activities offers opportunities for cost reduction by being able to share common infrastructure, such as moorings and power transmission infrastructure. Several studies involving the co-location of various activities offshore have been carried out. Ohunakin et al. [179] assessed offshore wind energy potential at seven different sites in the Gulf of Guinea, where the results revealed that due to the moderate to high offshore wind resources, the case studies located in deep waters, were still more economically viable.

Meanwhile, Rahimi et al. [180] performed a techno-economic analysis on a hybrid, onshore wind and solar farm in different cities in Australia due to their potential at providing an environmentally friendly solution for energy production. Scroggins et al. [181] assessed the role that renewable energy plays in the aquaculture and fisheries industries, concluding that the RES provide a maximum of 5% of the energy required to maintain the said industries. The study concluded that a shift to situation-specific RES is required if international decarbonization aims are to be reached. Similarly, Lilas et al. [182] highlighted that combining offshore wind turbines with aquaculture allows for carbon footprint reduction, while also meeting the energy demands of the aquaculture farm via a centralized, multi-use platform which also integrates ESSs. The study also emphasises that moving aquaculture further offshore reduces the negative environmental impact of fisheries. Bocci et al. [183] investigated opportunities for the development of multi-use space based on 10 case studies across Europe, highlighting that whilst space claiming can create conflict, the pros outweigh the cons due to the common benefits for multiple parties within the multi-use space.

Dalton et al. [184] analysed and found that combining energy, food and water in the same marine space leads to attractive system profitability. Srinivasan et al. [185] investigated the possibility of having a floating PV setup together with a BESS to be installed and used purely for an offshore oil platform facility. The study found that the economic feasibility of the project heavily relies on the optimisation of the floating platform, specifically on the anchoring and mooring systems. Environmentally, the study found that reductions in CO_2 emissions due to the inclusion of the floating PV system were obtained. Elginoz et al. [186] presented a multi-purpose platform accommodating both wave and wind energy generation. Their life-cycle assessment found that the primary source of pollution occurred during manufacturing of the platform and the decommissioning costs were affected depending on the recyclability of the platform parts. Abhinav et al. [187] reviewed platforms integrating multiple renewable energy generation sources with co-located aquaculture systems. The study concluded that such systems are still at a low technology readiness level (TRL), with multi-purpose platforms still being far from common practice.

From the above published works, one can observe that co-location, i.e., locating different technologies within the same marine space, is essential for improving the economic viability of offshore projects. Additionally, the ideal approach to such projects is one that satisfies the three pillars of sustainability, namely: environmental, social and economic.

The proposed concept being evaluated in this chapter involves the deployment of multiple FBW modules, dubbed Project FORTRESS, will enable multiple revenue streams through the co-located assets, including sales of renewable energy from floating wind and solar farms, the provision of energy storage services and the provision of sheltered waters for aquaculture cages and berthing of seafaring vessels.

It is assumed that investors develop the Project FORTRESS to own and operate the FBWs with revenue being generated from two sources: (1) provision of sheltered waters offshore and (2) energy storage services, in case of hybridisation. The chapter assesses numerous case studies for the proposed concept applied to the Maltese deep waters, located in the Central Mediterranean Sea. The first part of the study analyses the same solar farm in different offshore and onshore environments based on Malta's average land rental prices.

The study then introduces the FBW structure with the sole purpose of creating a sheltered water area for a variety of marine activities. Part B introduces the novel aspect of the FBW, which includes an ESS within the FBW design. The main objective of this study is to evaluate which cases are financially feasible and whether the considered revenue sources yield a sustainable business case to invest in the proposed FBW technology. Evaluating the environmental impacts of such infrastructure deployed at sea was outside the scope of the present study. Figure 8.1 summarises the workflow presented within this chapter. The work is set up as follows:

- Section 8.1 presents a theoretical review and the selected site within the Maltese territorial waters offering potential for developing a multi-use offshore park integrating FBWs, offshore renewable energy and other activities. The design parameters for the technologies, which were maintained constant throughout this chapter, are also presented in this section. The case studies considered for cost modelling and economic analysis are also presented here.

- Sections 8.2 and 8.3 present separate cost and revenue modelling for the solar PVs, the floating offshore wind turbine (FOWT) pilot farm and FBWs, as well as the marine park revenue streams. As shown in Figure 8.1, the case studies are split into two main parts:

- Part A (Section 8.2) focuses on different solar PV deployment technologies (land-based and rooftop PVs, floating PVs in calm waters, open seas and sheltered waters created by the FBWs) together with the FOWT pilot farm. Part A also analyses the cost reductions in floating solar PV infrastructure due to the introduction of the FBW structure without energy storage.
- Part B (Section 8.3) replicates the case study in Part A; however, it introduces hydro-pneumatic energy storage (HPES) within the FBWs. Part B also analyses the influence that sea depth and the number of FBWs have on the overall revenue generation of the multi-use marine park

- Section 8.4 summarises the conclusions derived from the techno-economic analyses.

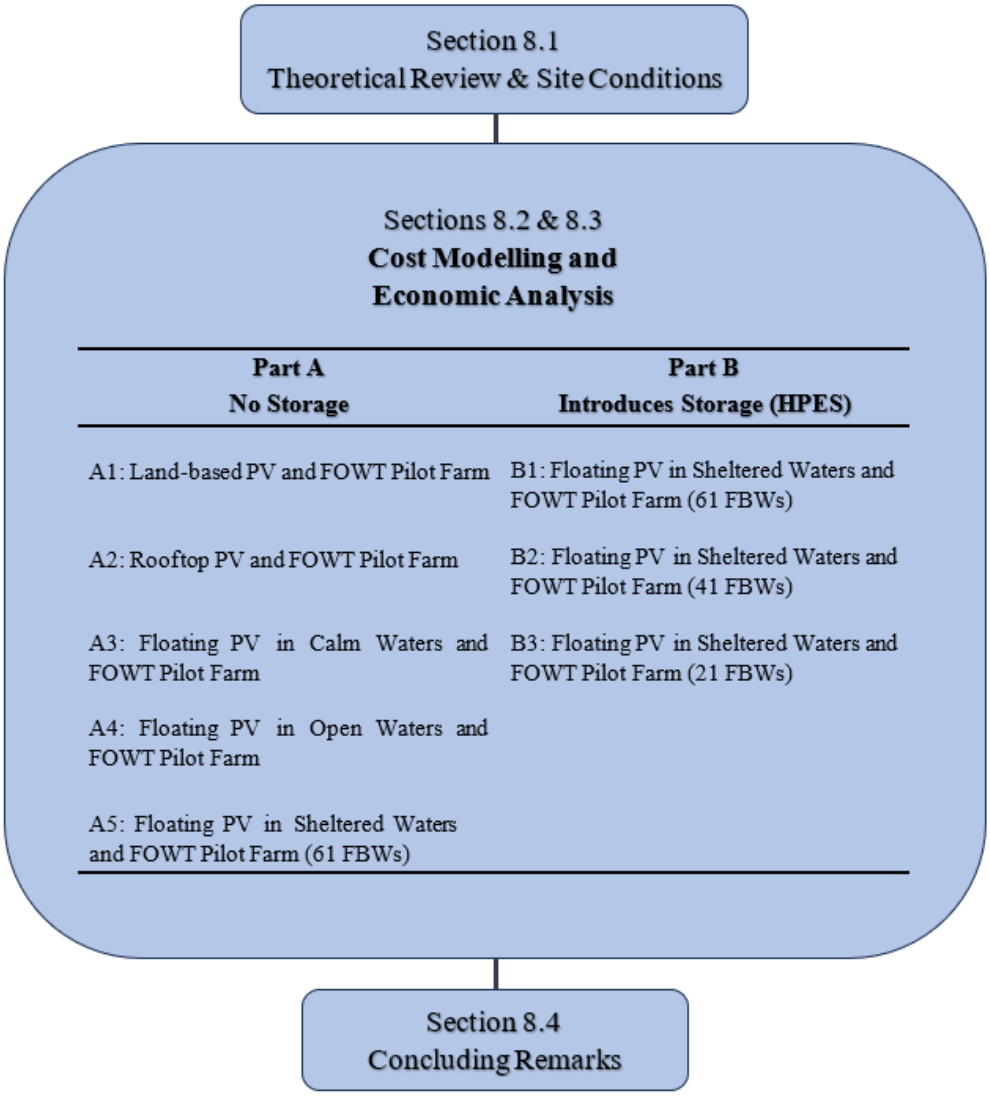

Figure 8.1: An overview of the work undertaken and presented in this Chapter.

8.1 Theoretical Review and Site Conditions

The following section presents a brief theoretical review of the equations applied for the techno-economic feasibility assessment. This section also shows the site identified for potential project development and presents the main technical parameters forming the basis for the techno-economic assessment. In order to assess whether a system will be economically feasible throughout its lifecycle, performing a techno-economic feasibility assessment is required. The main costings associated with large-scale solar PV projects and floating offshore wind turbines can be summarised in the following list [188]–[191]:

1. Project Development and Consenting
2. Capital Expenditure (CAPEX)
    a. Hardware
    b. Assembly and Installation
    c. Electrical Power Infrastructure
3. Operational Expenditure (OPEX)
4. Decommissioning

The main assessments performed to analyse the economic feasibility of a system or project are the Simple Payback Period (SPP), the Internal Rate of Return (IRR) and the Levelized Cost of Energy (LCOE). The SPP is calculated as shown in equation 8.1 hereunder:

$$SPP = \frac{Total\ Project\ Investment}{Annual\ Profits} \tag{8.1}$$

However, the SPP does not consider the time effects on the value of money and thus can be seen as a limited indicator of the true feasibility of a project. As a result, the IRR is typically preferred to accurately assess a project's potential. The IRR is calculated by applying equation 8.2 hereunder and assuming that the Net Present Value (NPV) is equal to zero:

$$0 = NPV = \sum_{n=0}^{N} \frac{C_n}{(1+r)^n} \tag{8.2}$$

Where C_n is the cash flow, r is the internal rate of return, n is a non-negative integer and N is the total number of periods. In order for a project to be deemed economically feasible, the IRR percentages must be equal or greater than the discount rate applied [192].

Additionally, the LCOE is also an important calculation which finds the ratio between the annual total cost to the electrical output of the system, thus providing a cost per unit of electricity generated ($€/kWh$). The LCOE is calculated as shown in equation 8.3:

$$LCOE = \frac{\frac{I}{a}}{E_{generated}} + \frac{OPEX}{E_{generated}} \tag{8.3}$$

Where I is the initial investment, a is the annuity factor and $E_{generated}$ is the annual energy generated [193], [194].

Figure 8.2 shows the four main sites considered for Project FORTRESS for possible implementation of a multi-use marine park using the proposed FBW technology [195]. Site 1, situated along Malta's west coast, is the most ambitious site, primarily due to the sea depth (~200 m, see bathymetric chart in Figure 8.3 [196]) and the distance from shore. Meanwhile, Sites 2 to 4 all approximately lie along the 50-metre bathymetry line, thus also being closer to shore. Furthermore, environmental consideration is another important aspect when considering such a large-scale project. Figure 8.4 presents the principal areas which are considered to be the SPAs and SACs in Maltese territorial waters. All sites except for Site 1 lie within an environmentally protected area.

Figure 8.2: Potential Sites for Project FORTRESS [195].

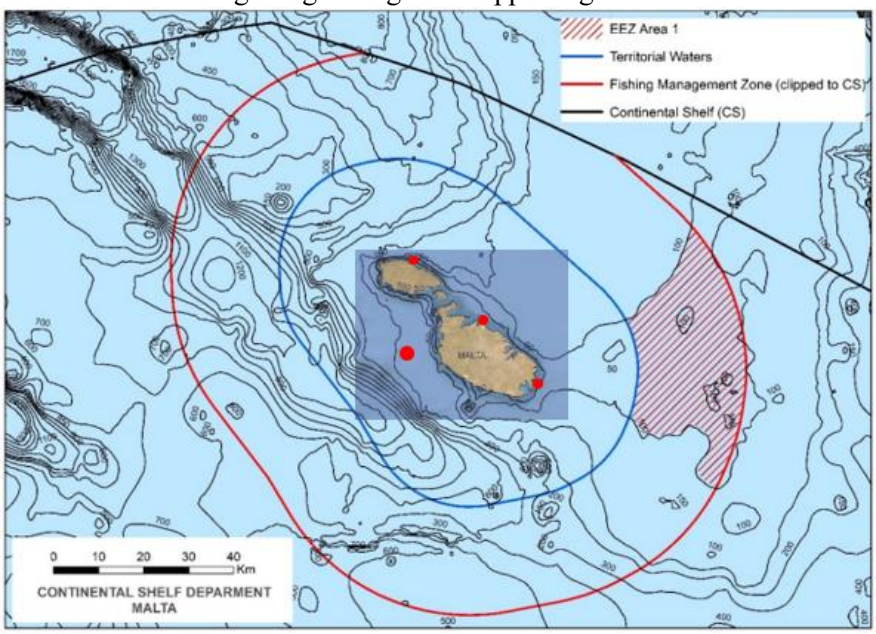

Figure 8.3: The bathymetry map of the Maltese Islands [196].

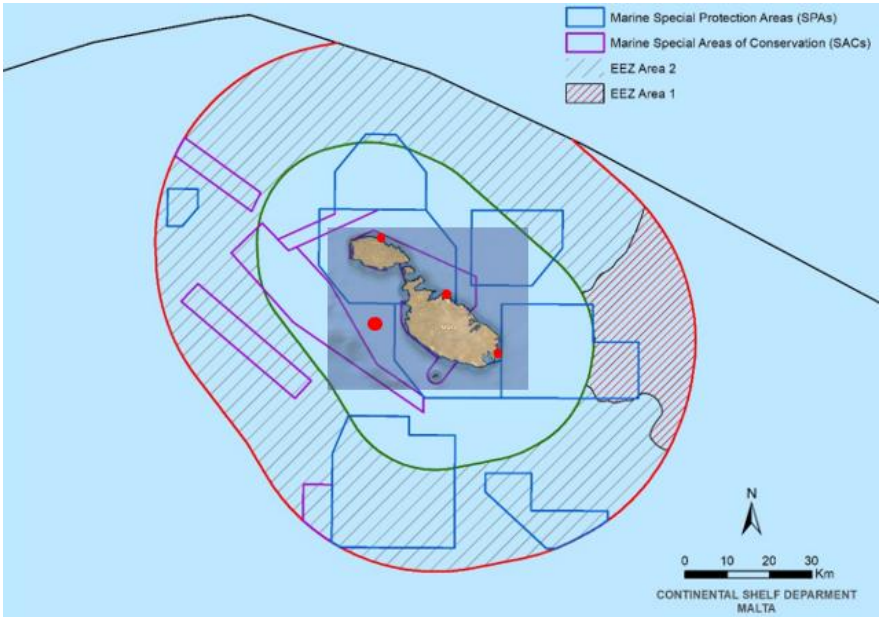

Figure 8.4: The SPA and SAC areas around the Maltese Islands [196].

It was decided to base the techno-feasibility analysis for the multi-use park on Site 1 for the following reasons:

1. The site is more distant from the coast, providing ample marine space for a large-scale multi-use park.
2. The sea depth at Site 1 reaches 200 m, thus representing a worst-case scenario with regards to the expected costs for the FBWs. The latter would be expected to be cheaper when deployed at the other sites indicated in Figures 8.2 – 8.4.
3. Site 1 does not lie within an environmentally sensitive area (Marine SPA or SAC).

8.1.1 Baseline Data

The main energy storage system (ESS) parameters which are kept constant throughout Chapter 7 are once again presented in Tables 8.1 to 8.3 below. The presented values hereunder are consistent with the values presented in Section 6.2 , since this chapter builds up on that analysis.

Table 8.1: Main parameters of the variable speed, multi-stage centrifugal pump.

Centrifugal Pump Parameter	Value
Rated Power (P_{H_p})	4.30 MW
Rated Speed (ω)	3250 RPM
Number of Stages	9
Maximum Hydraulic Efficiency (η_{pump})	82%

Table 8.2: Main parameters of the Pelton turbine.

Pelton Turbine Parameter	Value
Rated Power (P_{H_t})	5.00 MW
Rated Speed (ω_{Pelton})	426 RPM
Overall Efficiency (η_{Pelton})	85%
Runner Diameter (D)	3.78 m
Bucket to Jet Speed Ratio ($\emptyset$)	0.48
Generator Efficiency (η_{gen})	0.95
Number of Nozzles (N)	2
Skin Friction Coefficient (k)	0.97
Jet Angle (β)	165°

Table 8.3: Main parameters of the Pressure Containment System (PCS).

PCS Parameter	Value
Pre-charge (Minimum) Pressure	80 bar
Pressure Limit	200 bar
ESS Capacity (per Breakwater)	3.85 MWh

The Wind and Solar data obtained has already been explained in Section 7.1 and presented in Table 7.1. Table 8.4 and 8.5 respectively summarise the FOWT farm and solar PV performance metrics assumed and maintained constant throughout this Section. The WT power was simply multiplied by three, assuming that no partial compensation between the turbines occurs.

Table 8.4: Main parameters of the FOWT Pilot Farm.

FOWT Pilot Farm Parameters	Value	Reference
Wind Turbine Rating	10 MW	[173]
Number of Wind Turbines	3	-
Annual Energy Yield per Turbine	35.90 GWh	-
Annual Gross Wind Farm Energy Yield	107.70 GWh	-
Assumed Wake Losses	10%	[197]
Assumed Wind Farm Availability	97%	[198]
Net Capacity Factor	33%	[199]

Table 8.5: Main parameters of the solar PV Farm.

Solar PV Parameters	Value	Reference
Solar Panel Nominal Power	400 W	
Solar Panel Area	2 m^2	[200]
Solar Farm Rating	40 MWp	
Annual Energy Yield	68 GWh	-

Once the individual performance parameters for the FOWT pilot farm and for the solar PVs were established, understanding the spatial requirements of the two RES technologies related to the study was the step which followed.

Table 8.6 presents estimates for the spatial requirements for the solar PVs and the FOWT pilot farm. The ‘medium’ value for spatial requirements is simply the average of the optimistic and conservative spatial requirement scenarios.

Table 8.6: The individual and combined spatial requirements of the RES analysed in the report.

Parameter	Value	Reference
FOWT Pilot Farm		
Spatial Requirement (Optimistic)	7.20 MW/km^2	[201]
Spatial Requirement (Conservative)	4.66 MW/km^2	[202]
Spatial Requirement (Medium)	5.93 MW/km^2	-
Solar PV Farm		
Spatial Requirement (Optimistic)	200 MW/km^2	[203]
Spatial Requirement (Conservative)	80 MW/km^2	[204]
Spatial Requirement (Medium)	140 MW/km^2	-
Total Spatial Requirements (Based on a 30 MW FOWT farm and a 40 MWp floating solar PV farm)		
Optimistic	4.37 km^2	-
Conservative	6.94 km^2	-
Medium	5.35 km^2	-

The geometric parameters of a single FBW module with the integrated HPES system (presented in Figure 8.5) being adopted in the present study are presented and described in [205]. Note that the FBW floater remains unchanged when integrating the HPES system. The PCS in this case is assumed to consist of eight steel pipelines, shown in Figure 8.5 hereunder. Further detail may, however, be found in [205].

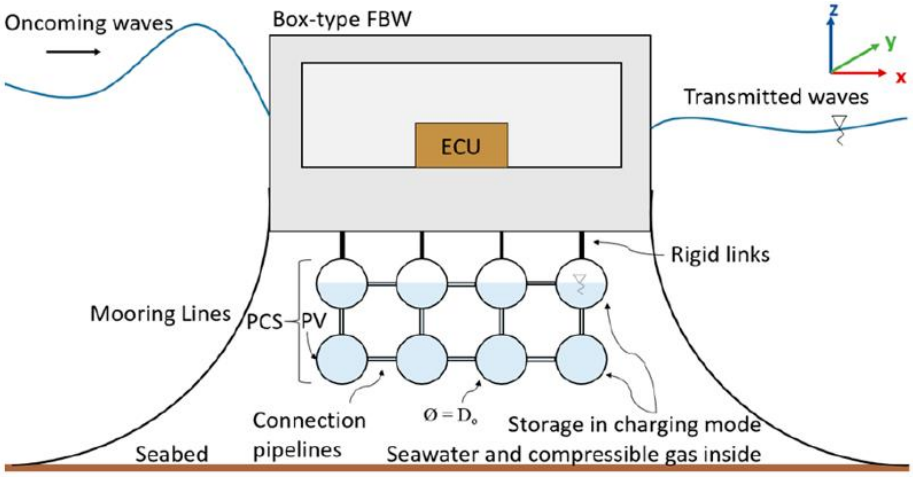

Figure 8.5: Image reproduced from [205]. A front view of the FBW with the integrated HPES system.

The total cost for one hybrid FBW module adds up to a total of €29,106,298 (€29.1 million) and includes aspects such as shipping, coatings and auxiliary items. It was observed that the moorings are the most expensive component, accounting for more than half the total hardware-attributable cost [205]. The anchors are the next most expensive component of the floating system, followed by the FBW and HPES system. From a detailed study on the logistics of installation of the hybrid FBW, the transportation and installation costs were found to add up to simply 7.2% of the total hardware-attributable costs. Considering also insurance costs during the commission phase, the total CAPEX of one FBW with the integrated HPES system has been estimated to be approximately €31,623,152 (€31.6 million). The hardware, in particular the mooring chains, are the highest expense related to a large-scale FBW. The proposed system needs very heavy chains to remain in place and experience controlled response in deep waters, leading to very expensive mooring solutions.

As explained previously in Section 7.2, the case studies considered in this study, and which will be analysed throughout this chapter, are split into two main parts. Table 8.7 summarises all case studies which have been performed. Studies A1 to A4 considered two onshore solar PV technologies (land-based and rooftop) and two floating offshore solar PV technologies (calm waters and open offshore) to analyse how the energy production, capital expenditure (CAPEX), operating expenditure (OPEX) and decommissioning expenditure (DECEX) vary from one case to another. The floating FOWT pilot farm was assumed to be the same throughout all studies. Study A5 introduced the FBWs, thus creating a sheltered region. It was assumed that the FBW owners would generate revenue by leasing the sheltered water space to operators of floating solar farms, aquaculture farms and sea faring vessels. For study A5, the FBWs serve the sole purpose of providing a sheltered area, and do not have the ESS incorporated.

Table 8.7: A summary of all the case studies performed throughout the report.

Case Study	Description
Part A – No ESS	
A1	Land-based PV and FOWT Pilot Farm
A2	Rooftop PV and FOWT Pilot Farm
A3	Floating PV in Calm Waters and FOWT Pilot Farm
A4	Floating PV in Open Waters and FOWT Pilot Farm
A5	Floating PV in Sheltered Waters and FOWT Pilot Farm (Includes 61 FBWs)
Part B – Includes FBWs and ESS	
B1	Floating PV in Sheltered Waters and FOWT Pilot Farm (61 FBWs)
B2	Floating PV in Sheltered Waters and FOWT Pilot Farm (41 FBWs)
B3	Floating PV in Sheltered Waters and FOWT Pilot Farm (21 FBWs)

Studies B1 to B3 introduce ESS which allows the FBWs to serve a dual purpose, i.e., to provide:

1. A sheltered area; and
2. Energy storage services to the electricity grid.

The inclusion of ESS services provides additional revenue streams for the FBW owners. All revenue streams are presented in Table 8.8. RS1 to RS3 are common revenue streams which were applied to case study A5 and all of Part B, since the said revenue streams are possible with the inclusion of the FBWs, yet do not require the ESS except for the charging services associated with RS1. Revenue streams RS4 to RS6 are introduced in Part B with the inclusion of the ESS incorporated in the FBWs. Figure 8.6 presents where the RSs are applied in the case studies.

Table 8.8: The different revenue streams (RSs) considered

Revenue Stream (RS)	Type	Description
RS1	Lease of marine space	Yacht Berthing
RS2	Lease of marine space	Aquaculture Farms
RS3	Lease of marine space	Solar PV Farms
RS4	Energy storage	Power Smoothing
RS5	Energy storage	Power Arbitrage
RS6	Energy storage	Berthing Electrical Supply

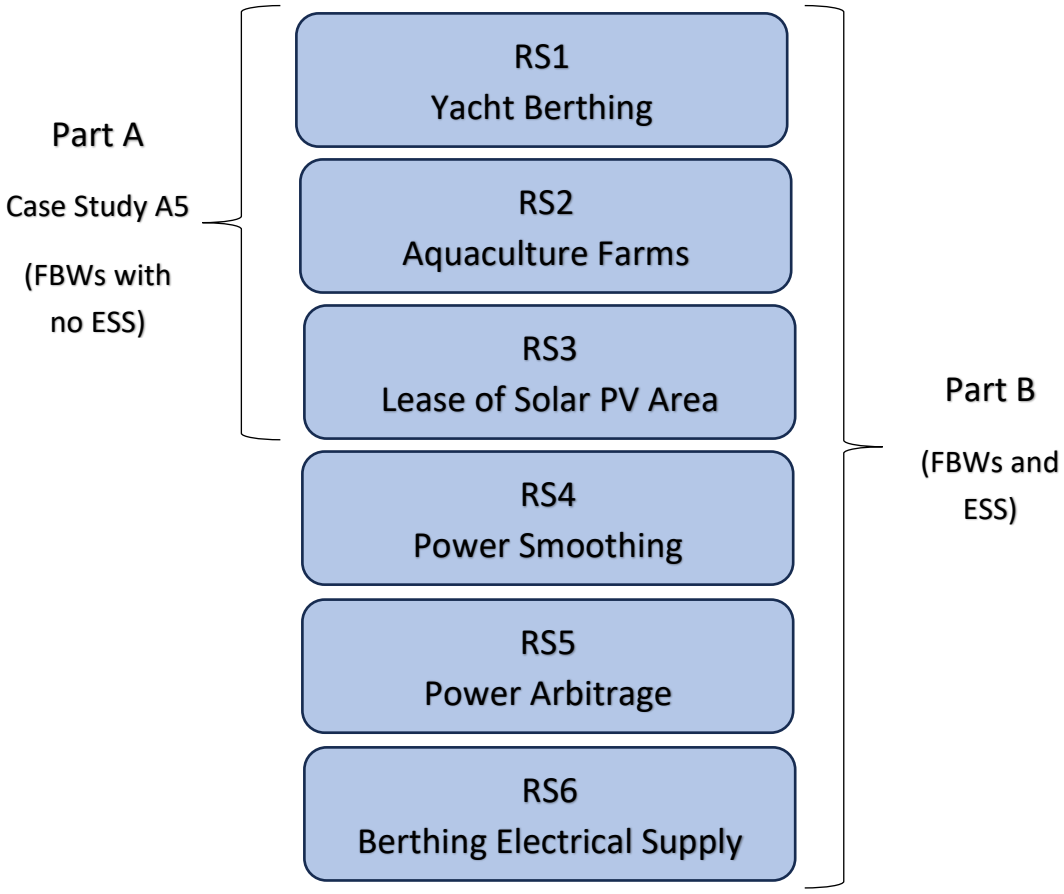

8.1.2 Techno-Economic Feasibility Case Studies

This section discusses the cost modelling of the individual RES technologies and amalgamate the different cost models into an overall IRR and LCOE comparison for the various case studies considered.

FOWT Pilot Farm Cost Modelling

Since the 30 MW FOWT Pilot Farm is assumed to be present throughout all case studies across Parts A and B, this section will separately explain the cost modelling and economic feasibility of the Pilot Farm as a stand-alone project. While Table 8.4 in Section 8.1.1 discussed the FOWT pilot farm technical details, Table 8.9 hereunder presents the main costings assumed. A report carried out by BVG Associates stated that FOWT farm costs range between 4,000 to 5,000 €/kW [206]. While CAPEX costing values were obtained from a variety of sources ([189], [190], [207]) the highest CAPEX value found from the referenced sources (which exceeds BVG Associates' cost range [206]) was considered for this particular study due to the following reasons:

1. Projects are usually large-scale, meaning that a FOWT farm would consist of at least more than ten WTs, with some projects reaching Gigawatts of installed capacity (> 1000 MW).
2. The project in question would be the first of its kind in the Maltese Islands, thus costs will be higher due to lack of previous experience in the sector.
3. Transportation and installation costs would be greater given the lack of local, adequate port facilities which are large enough to assemble the FOWTs at the quayside.

A detailed breakdown of what the CAPEX, OPEX and DECEX costs consist of may be obtained from a cost modelling study performed by Diaz et al. [189] for a FOWT farm consisting of 88 WTs each rated at 10 MW. The cost (€/kW) was calculated and is presented in Table 8.9. The CAPEX includes costs for project development, consenting, plant hardware, plant assembly and installation, electrical power hardware and installation. The OPEX costs include regular operating costs (personnel) and maintenance costs (on-site travel and inspection).

Table 8.9: The main cost parameters of the FOWT Pilot Farm.

FOWT Pilot Farm Cost Parameters	Value	Reference
CAPEX	5172 €/kW	
OPEX	50.40 €/kW	[189]
DECEX	138.23 €/kW	

The inputs required for the LCOE, IRR and SPP are listed in Table 8.10. The interest rate was selected based on the fact that the interest rate for such projects typically varies from 5 to 10% [189], [190]. Similarly, the inflation rate is typically assumed to be anywhere between 2 to 2.5% and therefore, an inflation rate of 2.5% was considered [208].

The timing of the project was assumed to be 30 years, with the first 5 years being solely dedicated to project development and consenting. Therefore, the FOWT Pilot Farm would have a lifecycle of 25 years. The CAPEX is distributed across the first 5 years, with procurement of the hardware carried out in years 3 and 4. On the 5th year, the OPEX commences, and this is applied every year up until the decommissioning of the project occurs on the final year of the FOWT farm lifecycle. With respect to the annual energy produced, Table 8.4 in Section 8.1.1 presented the optimal energy production. Staffell et al. [209] concluded that WTs lose approximately $1.6 \pm 0.2\%$ in energy production per year. As a result, this energy production loss was applied across the 25-year lifecycle of the FOWT pilot farm. FOWT farms must have an IRR value which is at least 8% [210]. Hence, the feed-in tariff (FIT) required to reach an IRR of 8% was found. Table 8.11 summarises the FOWT pilot farm's main economic feasibility results.

Table 8.10: The FOWT Pilot Farm LCOE, IRR and SPP Analysis Input parameters.

Economic Analysis Inputs	Value	Reference
Interest Rate	7.50%	[189], [190]
Inflation Rate	2.50%	[208]
Discount Rate	4.88%	-

Table 8.11: The FOWT Pilot Farm LCOE, IRR and SPP Analysis Output parameters.

Economic Analysis Outputs	Value
LCOE	13.8 €c/kWh
FIT	17.7 €c/kWh
IRR	8.0%
Simple Payback Period	9.88 years
Profit	207 M€

8.2 Part A - Storage

As explained previously in Sections 8.1.1 and 8.1.2 and as shown in Table 8.7, Part A involved a number of case studies assuming different Solar PV technologies: Case Studies A1 and A2 analyse two onshore solar PV technologies, comparing the cost difference between land-based and rooftop PVs. Meanwhile, Case Studies A3 and A4 present the cost modelling of the solar PV farm in calm and open waters respectively. Open waters would expose the solar PV structures to large waves, thus demanding robust floating support structures, similar to those used on oil and gas and floating wind turbines. Case Studies A1 to A4 provide information, which is required to perform Case Study A5, where the FBW structure is introduced.

8.2.1 Onshore Solar PV (Case Studies A1 and A2)

Case Study A1 considers the rental of unused onshore land for the development of a 40 MWp solar farm together with a 30 MW FOWT pilot farm off the West Coast of the Maltese Islands. Table 8.12 presents the main costings related to the land-based PV plant. While the CAPEX costs related to the solar PV hardware are not high, the total initial project investment required becomes excessively high since due to lease of space costs to rent out the land for a project lifetime of 25 years. Since the CAPEX cost did not include project development and consenting in this case, a study by Alsheghri et al. [211] was used, where it was assumed that such costs made up 0.56% of the total CAPEX costs of the solar farm. Meanwhile, as shown in Table 8.13, The Energy and Water Agency's National Renewable Energy Action Plan [212] showed that the CAPEX for rooftop PV systems is higher than for land-based PV systems.

Table 8.12: The main cost parameters of the Land-based PV plant (related to case study A1).

Land-based PV	Value	Reference
CAPEX	754 €/kW	[211], [212]
Land Lease	16 €/sq/a	Discussed in Section 8.2.3
OPEX	14 €/kW	[212]
DECEX	30 €/kW	[213]

Table 8.13: The main cost parameters of the Rooftop PV plant (related to case study A2).

Rooftop PV	Value	Reference
CAPEX	1609 €/kW	[212]
Rooftop Lease	6 €/sq/a	[214]
OPEX	26 €/kW/a	[212]
DECEX	30 €/kW	[213]

Since Case Studies A1 and A2 consist of onshore PV systems, the interest rate related to project investment was assumed to be 5% based on the average interest rate of European Solar PV projects [215]. While the CAPEX costs related to the solar PV hardware are not high, the total initial project investment required becomes excessively high since due to lease of space costs to rent out the land for a project lifetime of 25 years. Since the CAPEX cost did not include project development and consenting in this case, a study by Alsheghri et al. [211] was used, where it was assumed that such costs made up 0.56% of the total CAPEX costs of the solar farm.

Table 8.14 presents the inputs applied for the calculations of the LCOE, IRR and SPP. The cost parameters presented in Tables 8.12 and 8.13 were applied to the cost analysis. Additionally, a 0.2% decrease in solar panel production per annum was applied based on a study by Fraunhofer [216]. Table 8.15 presents the economic analysis outputs of the land-based and rooftop PV systems, indicating that the rooftop PV plant requires a FIT which is 46.70% less than that of the land-based PV plant in order to achieve an IRR of 8%. Once the individual economic outputs of the different onshore solar PV plant setups and the FOWT pilot farm were obtained, an overall economic output could be obtained for the two case studies (A1 and A2). Table 8.16 summarises the main economic parameters of Case Studies A1 and A2.

Table 8.14: The Onshore Solar PV Plant (40 MWp) LCOE, IRR and SPP Analysis Input parameters.

Economic Analysis Inputs	Value	Reference
Interest Rate	5.00%	[215]
Inflation Rate	2.50%	[208]
Discount Rate	2.44%	-
Annual Energy Produced	61.30 GWh	-

Table 8.15: The Onshore Solar PV Plant (40 MWp) LCOE, IRR and SPP Analysis Output parameters.

Economic Analysis Outputs	Land-based PV	Rooftop PV
LCOE	13.90 €c/kWh	7.93 €c/kWh
Feed-in Tariff	23.80 €c/kWh	12.70 €c/kWh
Internal Rate of Return	8.0%	8.0%
Simple Payback Period	9.93	8.86
Profit	204 M€	98 M€

Table 8.16: The economic results for Case Studies A1 (Land-based PV) and A2 (Rooftop PV).

Economic Analysis Outputs	A1 (Land-based PV)	A2 (Rooftop PV)
LCOE	13.80 €c/kWh	10.90 €c/kWh
Simple Payback Period	9.87	9.51
Profit	411 M€	305 M€

8.2.2 Offshore Solar PV (Case Studies A3 and A4)

Case Study A3 considers a floating offshore solar PV farm assumed to be in operation in calm waters (i.e., on reservoirs and lakes) together with the 30 MW FOWT pilot farm. Case Study A4 considers a floating offshore solar PV farm, assumed to be in operation in open waters, thus being exposed to harsher wind and wave conditions and demanding a robust support structure. As explained in Table 8.7 in Section 8.1.1, the 30 MW FOWT pilot farm is included throughout all the case studies. Tables 8.17 and 8.18 present the main costings related to the floating offshore solar PV farm assumed to be operating in calm waters and open waters respectively.

Table 8.17: The main cost parameters of the Floating PV plant in calm waters (case study A3).

FPV in Calm Waters	Value	Reference
CAPEX	693 €/kWp	[217]
Replacement Costs	109 €/kWp	[217]
OPEX	29 €/kWp/a	[217]
DECEX	42 €/kWp	[218]

Table 8.18: The main cost parameters of the Floating PV plant in open waters (case study A4).

FPV in Open Waters	Value	Reference
CAPEX	2047 €/kWp	[218]
Replacement Costs	109 €/kWp	[217]
OPEX	30 €/kWp/a	[218]
DECEX	42 €/kWp	[218]

While a number of research papers were considered to understand the typical CAPEX and OPEX costs of a floating PV (FPV) system [208], [219], the most appropriate cost breakdowns were provided by Islam et al. [217] and by Micheli et al. respectively [218]. While the CAPEX cost difference between floating PVs in calm waters and in open waters is significant due to the reasons explained above, the OPEX cost difference is negligible. Additionally, the replacement of hardware (for example PV panels, inverters and mooring chains) and decommissioning costs were assumed to be equal due to a lack of literature related to the said costs.

In the case of Case Studies A3 and A4, the interest rate related to project investment was assumed to be higher (set at 8%) than the onshore case studies to reflect the higher risk levels associated with offshore-based projects [211], [214]. On the other hand, however, the energy produced per year for the offshore solar PV case studies was assumed to be 11% more due to the reasons previously explained in Section 8.1 [11]. Table 8.19 presents the applied parameters to carry out the economic evaluation for the solar PV systems in calm waters and open seas. Table 8.20 compares the economic outputs of the solar PV system in calm waters and open seas for an IRR of 8%. Table 8.21 summarises the main economic parameters of Case Studies A3 and A4.

Table 8.19: The Offshore Solar PV Plant (40 MWp) LCOE, IRR and SPP Analysis Input parameters.

Economic Analysis Inputs	Value	Reference
Interest Rate	8.00%	[214]
Inflation Rate	2.50%	[208]
Discount Rate	5.37%	-
Annual Energy Produced	68.0 GWh	-

Table 8.20: The Offshore Solar PV Plant (40 MWp) LCOE, IRR and SPP Analysis Output parameters.

Economic Analysis Outputs	Calm Waters	Open Seas
LCOE	8.00 €c/kWh	12.00 €c/kWh
Feed-in Tariff	9.70 €c/kWh	14.90 €c/kWh
Internal Rate of Return	8.0%	8.0%
Simple Payback Period	8.14	8.86
Profit	77 M€	130 M€

Table 8.21: The economic results for Case Studies A3 (Calm Waters) and A4 (Open Seas).

Economic Analysis Outputs	A3 (Calm Waters)	A4 (Open Seas)
LCOE	11.4 €c/kWh	13.0 €c/kWh
Simple Payback Period	9.31	9.43
Profit	279 M€	332 M€

8.2.3 The Influence of Ground Rent Cost

A key finding from Case Studies A1 to A4 is that although land-based PV systems are far cheaper than those offshore in open sea, the cost advantage is easily absorbed by the high costs for renting land. In fact, Case Study A1 ended up being the most expensive project in terms of CAPEX, thus resulting in requiring the highest FIT to obtain the desired 8% IRR for investors. In order to understand if this was a case-specific issue, different coastal regions around the Mediterranean were analysed to understand the typical land rental pricing. Table 8.22 presents the average rental price per square metre per year for the different places analysed. One may observe that the rental price rises based on the regional population density. As a result, Malta and Ibiza resulted in having the greatest rental prices per year, thus heavily impacting the overall economic viability of a solar PV farm on unused, onshore territory.

Table 8.22: The average rental price per year for different coastal regions in the Mediterranean Sea.

Region	Value (€/m²/year)	References	Population Density (pers/km²)
Malta	16.0	[220]–[223]	1,649
Sicily	1.10	[224]–[227]	190
Spain (overall)	1.16	[228]–[231]	94
Ibiza	13.00	[232]	278
Crete	1.70	[233]–[236]	75

Figure 8.7 presents a graph indicating the relationship between the IRR and land rental price per year for different FITs. The results show that a FIT as low as 5 €c/kWh would not be enough to make the onshore-based PV system profitable, even if no land rental price was incurred.

Meanwhile, the only FITs which are feasible at a land rental price of 16 €/kWh fall between 20 and 25 €c/kWh. In most cases, the maximum land rental price which made the FITs ranging from 10 to 25 €c/kWh able to achieve 8% IRR or more, was 4 €/m²/year. It is important to note that the graph analysis does not apply to the onshore rooftop PV system, since a rooftop rental cost was established through a study by Rebe et al. [214]. The rooftop rental cost is also based on the assumption that the required area to house a 40 MWp solar farm would be found.

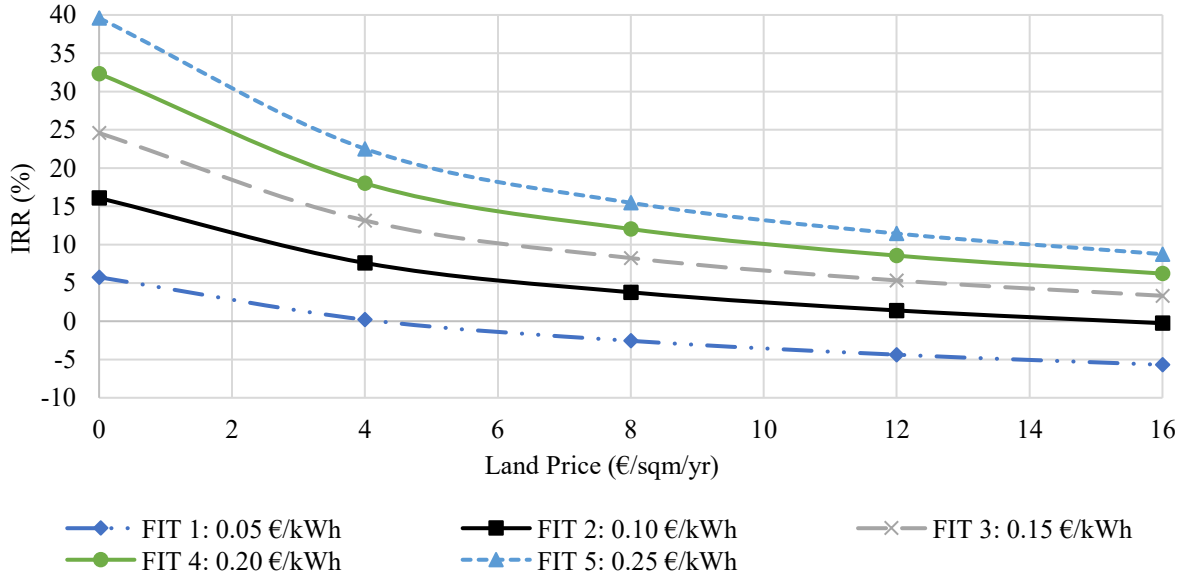

Figure 8.7: The relationship between IRR and Land Rental Price for different FITs.

Due to the wind turbine farm already being situated offshore (in waters with a sea depth of 200 m) and considering the high land prices for onshore PVs in Malta, co-locating floating wind and solar farms offshore seems to be a promising alternative. Case Study A2 provided competitive results with those in A3, however based on co-location and the assumption that a 40 MWp solar PV farm would need to be placed on rooftops, shifting offshore seems to be most sensible. As a result, Sub-section 8.2.5 will explain Case Study A5, which is titled 'Floating PV in Sheltered Waters and FOWT Pilot Farm including FBWs', as previously presented in Table 8.7 in Section 8.1.1. Prior to Section 8.2.5, Section 8.2.4 will discuss Part A of the revenue streams created as a result of the introduction of the FBWs.

8.2.4 Revenue Streams for the FBWs (Part A)

The FBWs will create a large, sheltered area in deep water to accommodate different marine activities. When assuming that the FBWs are purely structures to provide an area of sheltered waters (i.e., no storage incorporated within the FBWs), the following revenue streams may be generated:

1. Berthing of seafaring vessels (e.g., yachts),
2. Renting of space for Aquaculture cages,
3. Renting of space for floating solar PVs.

Figures 8.8 to 8.10 present an example of how the sheltered waters could be utilised, and what Project FORTRESS would look like overall. The figures assume that Site 1 was selected as the ideal site for such a project, previously shown in Figure 8.2 in Section 8.1.

The FBW array provides a sheltered area spanning 8.30 km^2, which provides space for two 40 MWp offshore floating solar PV farms (spanning 0.57 km^2 excluding spacing) , aquaculture through fish farms (peach section spanning 0.135 km^2) and a berthing section (orange and purple sections spanning 0.23 km^2); All previously described above. An additional 27 MWp of solar PVs are assumed to be placed on the FBW array surfaces, spanning an area of 0.12 km^2.

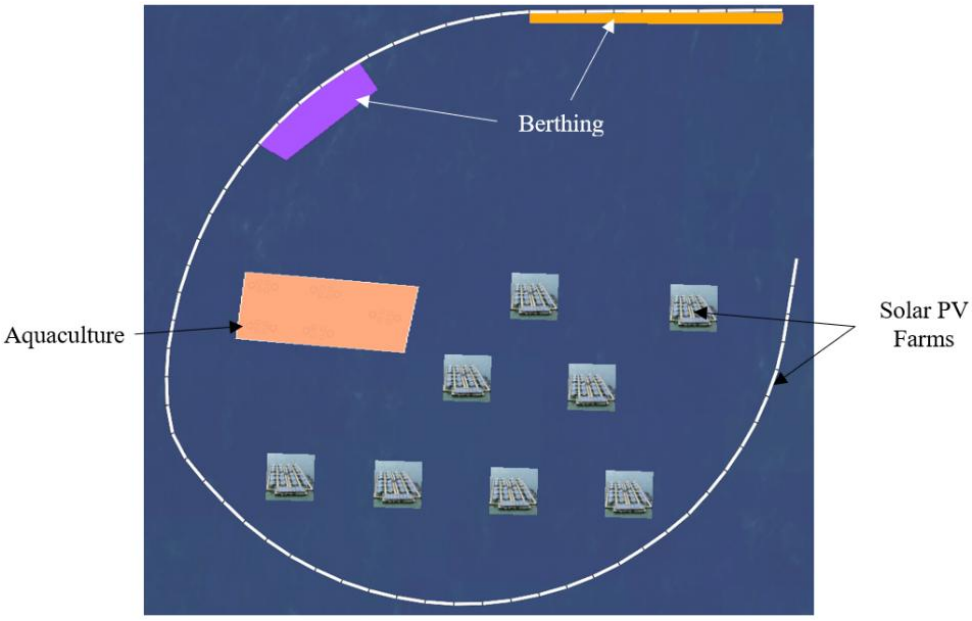

Figure 8.8: A zoomed in, plan view of the FBW array.

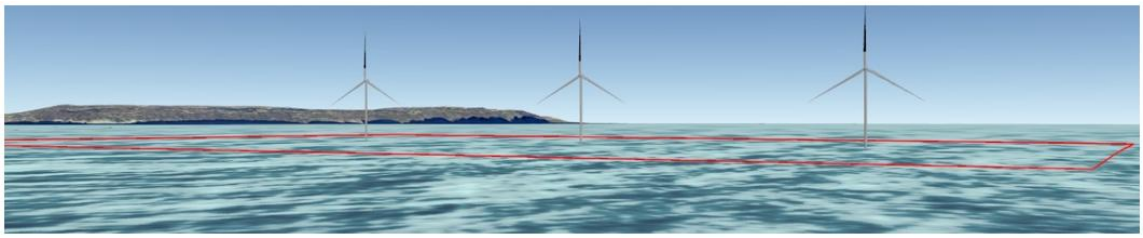

Figure 8.9: A zoomed in image of the FOWT pilot farm.

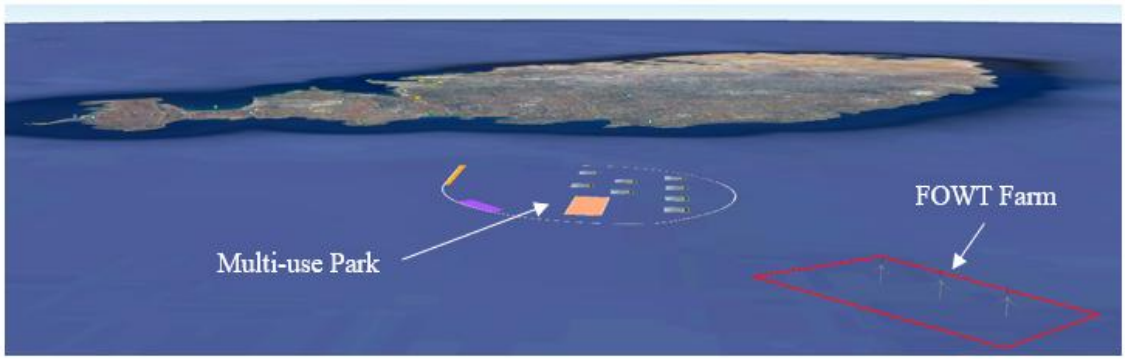

Figure 8.10: A schematic of the Project FORTRESS setup, highlighting two berthing sections (purple and orange), an aquaculture area (peach) and the 80 MWp solar PV farm all being sheltered by the FBW array.

Berthing Facilities

The first revenue stream considering is the offering of berthing facilities to seafaring vessels within a sheltered area created by the FBWs. The assumed business model is to have this area owned by the operators of the FBWs but leased to a third party operating the facilities. In order to obtain realistic pricing for the berthing services being offered, prices from different berthing locations across the Maltese Islands were reviewed, such as for example those being quoted by the, with Excelsior and Marina di Valletta marinas [237], [238]. Table 8.23 presents the assumed pricing being assumed in the presented study. These are presented at the price per day for yachts as a function of size. The pricing was set to one half of that found in [237], [238], given that Project FORTRESS will offer the berthing in offshore environment rather than at port. Additionally, the number of berth spaces and area required are also presented.

The approximate number of berth spaces were based on analyses for Universal Berth Parameters [62] and based on a report related to the development of yachting facilities in Malta [239], [240].

The berthing section was assumed to be operational for five months per year, spanning from mid-May to mid-October (153 days). The estimated revenue being generated was estimated to be based on a half-half mix: 284 yachts sized between 16 to 18 metres and 284 yachts sized between 18 to 20 metres. Since assuming that the berthing area would be fully utilised consistently for all 153 days is an unrealistic scenario, three different usage percentages were considered.

Table 8.23: A summary of the yacht berthing pricing and setup.

Berth Size	Price per Day (€)	No. of Berths	Area Required (m^2)
16 to 18 metres	38	568	115,000
18 to 20 metres	42		
Up to 35 metres	55	26	110,000
Up to 50 metres	180		

Lastly, Project FORTRESS would charge the berthing owner a percentage of the revenue generated for making use of the sheltered area created by the FBWs. The percentage charges are shown in Table 8.24 (10%, 17%, 25%). Through this charge, a cost in euro per square metre was established, which would then be utilised for the other revenue streams. The obtained cost per square metre was required to be less than the lease of land and rooftop rent. Table 8.24 also presents the results of the yacht berthing revenue stream financial analysis.

Table 8.24: The financial results related to the Yacht Berthing revenue stream financial analysis.

Main Financial Results	Value
Revenue per day assumed	€ 27,075
Revenue assuming 5 months of non-stop operation	€ 4,142,475
Revenue assuming 5 months (Berthing facility owner) (20% usage)	€ 828,495
Revenue assuming 5 months (Berthing facility owner) (40% usage)	€ 1,656,990
Revenue assuming 5 months (Berthing facility owner) (60% usage)	€ 2,485,485
Revenue to Project FORTRESS (FBWs owners) (10%)	€ 165,699
Revenue to Project FORTRESS (FBWs owners) (17%)	€ 281,688
Revenue to Project FORTRESS (FBWs owners) (25%)	€ 414,248
Price of Area (10%)	0.74 €/m^2
Price of Area (17%)	1.25 €/m^2
Price of Area (25%)	1.84 €/m^2

Aquaculture

The second possible revenue stream is to exploit the sheltered waters created by the array of FBWs for aquaculture (i.e., the operation of fish farms). Wang et al. [241] explained that while moving aquaculture further offshore increases expenses, advances in technology and the opportunity for co-location can lead to important cost reductions, hence increasing economic feasibility. Furthermore, Holmer [242] discussed how environmental detriment is predicted to decline with aquaculture moving further offshore due to greater sea depths and harsher weather conditions, leading to more efficient waste dispersion. Due to being set up further offshore, the carbon footprint of fish farms may increase due to increased transportation, unless green transportation is introduced. One small fish farm in the case of this project was assumed to consist of four 50 metre diameter cages and two 60 metre

diameter cages (shown in Table 8.25). It was assumed that ten of such small fish farms would be placed in the sheltered water area. Similar to the berthing revenue stream, Project FORTRESS' responsibility as the owner of the FBWs is to rent offshore sheltered space to be utilised by the fish farm operators. The cost in euro per square metre calculated previously in Table 8.24 was applied in this case in order to calculate the annual revenue for FORTRESS for the area utilised. Table 8.26 presents the financial results obtained.

Table 8.25: A summary of the sizing of one fish farm.

Parameter	Amount	Area Required (m^2)
Number of 50 metre diameter cages	4	7,850
Number of 60 metre diameter cages	2	5,655

Table 8.26: The financial results related to the Aquaculture revenue stream financial analysis.

Main Financial Results	Value
Price of Area (€/m^2) (10%)	0.74
Price of Area (€/m^2) (17%)	1.25
Price of Area (€/m^2) (25%)	1.84
Revenue to Project FORTRESS (€) (10%)	99,686
Revenue to Project FORTRESS (€) (17%)	169,466
Revenue to Project FORTRESS (€) (25%)	249,214

Renting of Solar PV area

The third revenue stream is the renting of sheltered water areas created by the FBWs to operators of floating solar PV farms. With the introduction of the FBW array, the offshore floating PVs have a level of protection from open sea conditions. As a result, the solar farm cannot be considered to be in calm waters but is protected from the high waves of open seas. Thus, a separate analysis assuming a compromise between Case Studies A3 and A4 was carried out to estimate the LCOE and required FIT for a minimum of 8% IRR in the case of a solar PV farm in sheltered waters. The CAPEX cost value (1,370 €/kWp) was assumed to be the average value of the CAPEX costs for the PV system in calm waters (693 €/kWp) and for the PV system in open seas (2,047 €/kWp).

All economic analysis input parameters were also maintained. Table 8.27 hereunder presents the main economic results for a PV system in sheltered waters.

Table 8.27: The sheltered waters Solar PV Plant LCOE, IRR and SPP Analysis Output parameters.

Economic Analysis Outputs	Sheltered Waters
LCOE	11.30 €c/kWh
Feed-in Tariff	13.60 €c/kWh
Internal Rate of Return	8.0%
Simple Payback Period	7.75
Profit	102 M€

Due to the CAPEX savings in designing a Floating PV system for sheltered seas, a rental price (in terms of €/m^2) is assumed to be charged by Project FORTRESS covering two different methods:

1. Locating floating PV systems in the sheltered water areas created by the FBWs, with a pricing arrangement that is similar to yacht berthing and aquaculture.

2. Locating additional solar PVs on the deck area available on the FBWs themselves. Such panels would be integrated in a similar way as roof-top systems, with no floaters and moorings required.

In the present feasibility analysis, it is assumed that the rental price for space for the second option is twice that of the first. Table 8.28 presents the power ratings and areas occupied in the sheltered waters together with the area occupied on top of the FBWs. Once again, Project FORTRESS is solely responsible for renting out the sheltered water area being utilised by the solar PV farm operators. The revenue resulting from the energy generated from the solar PV farm will be earned by its operators and not by the owners of the FBWs. Table 8.29 presents the yearly revenues for Project FORTRESS resulting from the two different area pricings enlisted in Table 8.28.

Table 8.28: A summary of the area required to accommodate the solar PV plants.

Solar PVs	Power Rating (MWp)	Amount	Area Required (m^2)
In sheltered waters	40	2	536,487
On FBWs	27	1	120,780

Table 8.29: The financial results related to the Renting of Solar PV area revenue stream financial analysis.

Solar PVs	Area price for PVs in sheltered seas (€/m^2)	Area price for PVs on FBWs (€/m^2)	Total Revenue (€)
Conservative	0.74	1.48	576,000
Medium	1.25	2.50	977,000
Optimistic	1.84	3.68	1,437,000

8.2.5 Sheltered Solar PV (Case Study A5)

Case Study A5 analyses an offshore floating solar PV system in sheltered waters and the FOWT Pilot Farm. The solar PV system is said to be sheltered due to the introduction of a FBW array, consisting of 61 FBWs. The number of FBWs was derived based on previous research, which was presented previously in Section 8.1. Table 8.30 presents the costings related to the FBW structure.

Table 8.30: The main cost parameters of the FBW structure.

FBW Costs	Value
Number of FBWs	61
FBW CAPEX	€ 27,586,954
FBW OPEX	3% of FBW CAPEX
FBW DECEX	3% of FBW CAPEX
Total Cost	€ 1.68 billion

A full economic analysis could be performed amalgamating the costings and revenue generated via the applicable revenue streams. Since the revenue streams will be applicable across the project lifetime (25 years), the annual revenue generated considered an inflation rate of 2.5% from the start to the end of the project [208]. Table 8.31 presents the results of Case Study A5, highlighting that the project would not be financially feasible with the discussed setup.

Through the economic evaluation of Case Study A5, a number of conclusions may be drawn:

1. The financial modelling shows that revenue streams RS1 (yacht berthing), RS2 (aquaculture farms) and RS3 (solar PV farms) do not provide sufficient revenue to outweigh the life cycle costs of the overall project, primarily due to the high cost of the FBW array. Figure 8.11 presents the division of the different costs associated with the FBW array and the portion of revenue generated.

2. The combined savings incurred by locating the offshore solar PV farms in sheltered waters created by the FBW array together with the additional revenue streams instead of open seas, do not justify the high capital investment required for the FBWs in deep waters.

3. Case Study A5 did not consider the integration of energy storage within the FBW array to provide additional revenue streams, which would fuel the FBW investment.

As a result, the following section (Section 8.3) will analyse new case studies whereby the FBW array will not only be utilised to create a sheltered area, but to also store energy and thus, offer the opportunity for new revenue streams.

Table 8.31: The economic results for Case Study A5.

Economic Analysis Outputs	A5
LCOE	47.34 €c/kWh
Simple Payback Period	419 years
Profit	- € 1.41 billion

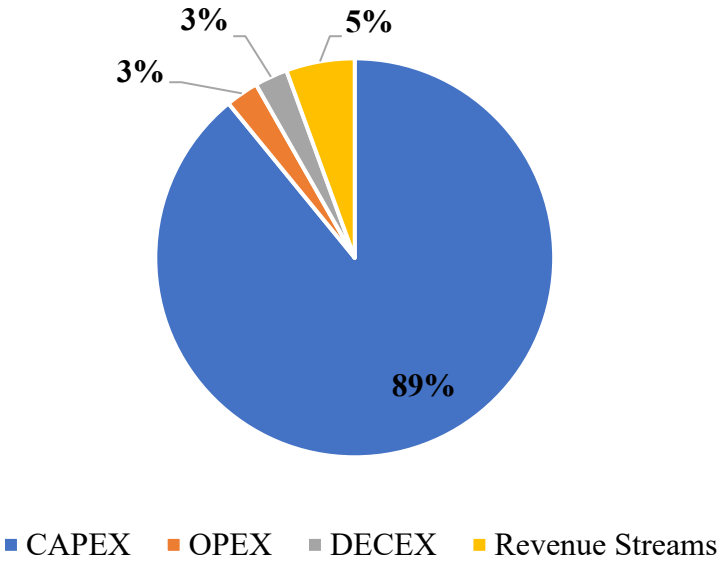

Figure 8.11: A pie chart showing the ratio between the different FBW array costs and the revenue generated as a result of the FBW array.

8.3 Part B – FBWs Integrating Energy Storage

Part B consists of repeating the final case study of Part A, Case Study A5, integrating the HPES system [243] to provide energy storage services, apart from creating sheltered water areas. This hybridisation process enables new revenue streams that are discussed further in Section 8.3.1. Throughout Part B, all FBWs have the HPES system integrated (previously shown in Figure 8.5 in Section 8.1.1 [205]). Once the revenue streams were defined, the cost modelling and techno-feasibility assessments at a sea depth of 200 m could be performed.

8.3.1 Revenue Streams for FBWs integrating Energy Storage (Part B)

Apart from the revenue streams already listed and explained previously in Section 8.2.4, a number of additional revenue streams related to the integration of energy storage within the FBWs themselves were identified:

1. Power Smoothing
2. Power Arbitrage
3. Power to Berthed Sea-Faring Vessels

Power Smoothing

The technique utilised to smoothen power from the offshore RES (30 MW FOWT pilot farm and 40 MWp solar PV farm) is done by applying a Simple Moving Average (SMA) was previously explained in detail in Section 7.1. Figure 8.12 provides a basic flowchart of the revenue generation process for the revenue stream of power smoothing, where a graph where P_{raw} is the intermittent signal, while P_{SMA} is the SMA applied

The power smoothing process involves Project FORTRESS purchasing excess energy based on the averaged FIT (calculated to be 16.11 €c/kWh based on the energy production ratio between the FOWT farm and the floating solar PV farm) between the RESs and storing that excess energy via the ESS. Once an energy deficit occurs, the ESS discharges energy and sells it to the grid at a mark-up price, since the energy discharged would be aiding in matching the power required, thus providing a smoothened power output to the grid. The power smoothing applied was that of a 1-day SMA, meaning that the previous 24 hours of power generation data is utilised to obtain a Moving Average (MA).

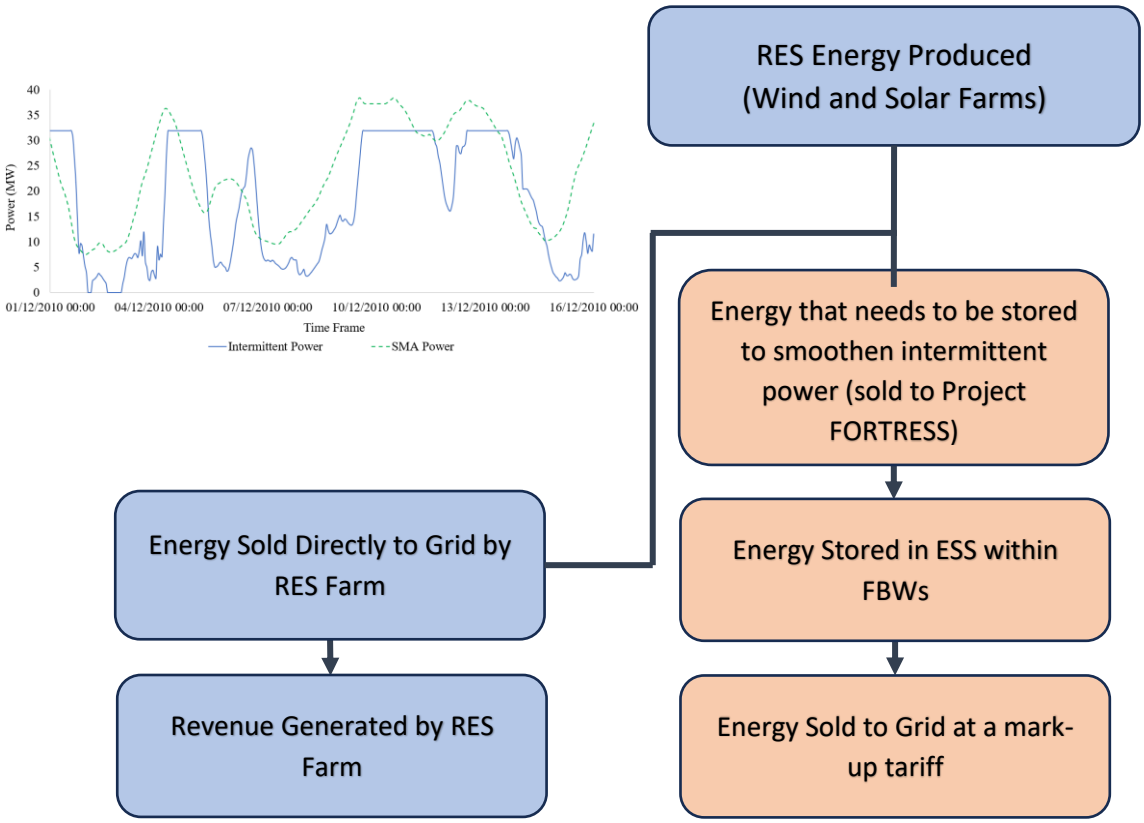

Figure 8.12: A flowchart of the revenue generation for the Power Smoothing revenue stream.

Table 8.32 presents the difference in the number of FBWs utilised for power smoothing based on the percentage of the overall RES generation to be smoothened for the grid. Tables 8.33 to 8.35 present the financial results based on applying the power smoothing revenue stream when the total number of FBWs is 61, 41 and 21 (Table 8.7, Part B). The financial study analyses how the power smoothing availability would affect the revenue generated from selling energy to smoothen the said power. Additionally, the selling price was also parameterized to analyse the profitability of the revenue stream.

Table 8.32: A summary of the number of FBWs based on Power Smoothing Availability.

Number of FBWs for Power Smoothing					
Power Smoothing Availability	**61**	**Power Smoothing Availability**	**41**	**Power Smoothing Availability**	**21**
65%	26	55%	22	30%	15
80%	35	70%	28	40%	18
95%	60	85%	40	50%	20

Table 8.33: The financial results related to the Power Smoothing revenue stream analysis for 61 FBWs.

	Mark-up Selling Price	**Profit (based on difference in selling and purchase price) (M€)**		
Power Smoothing Availability		**65%**	**80%**	**95%**
Conservative	28 €c/kWh	2.98	3.66	4.35
Medium	31 €c/kWh	4.30	5.29	6.28
Optimistic	34 €c/kWh	5.63	6.92	8.22

Table 8.34: The financial results related to the Power Smoothing revenue stream analysis for 41 FBWs.

	Mark-up Selling Price	**Profit (based on difference in selling and purchase price) (M€)**		
Power Smoothing Availability		**55%**	**70%**	**85%**
Conservative	28 €c/kWh	2.51	3.20	3.88
Medium	31 €c/kWh	3.63	4.63	5.62
Optimistic	34 €c/kWh	4.76	6.05	7.35

Table 8.35: The financial results related to the Power Smoothing revenue stream analysis for 21 FBWs.

	Mark-up Selling Price	Profit (based on difference in selling and purchase price) (M€)		
Power Smoothing Availability		**30%**	**40%**	**50%**
Conservative	28 €c/kWh	1.37	1.83	2.28
Medium	31 €c/kWh	1.98	2.64	3.30
Optimistic	34 €c/kWh	2.59	3.46	4.32

It should be noted that the above tables include the inefficiency of the ESS during both the charging (70% centrifugal pump efficiency) and discharging cycles (85% Pelton turbine efficiency). If the mark-up selling price to smoothen out the power is not sufficient, a loss can occur when considering the money spent by Project FORTRESS to purchase energy from the RESs. The mark-up prices assumed provided a profit throughout all scenarios. A common trend is that the larger the proportion of energy flowing through the ESS, the higher is the generated revenue. However, one must also consider that the remaining FBWs may also be hybridized to integrate an ESS and be used for revenue generation through power arbitrage, which is explained hereunder.

Power Arbitrage

Power or energy arbitrage is the use of ESS to store energy during periods of low market process of electricity to be sold later on during periods of high demand and higher process. This is another potential revenue stream for Project FORTRESS. Energy from the co-located RES can be purchased when demand is low, stored and kept until energy prices rise. A parametric analysis for this revenue stream was performed.

Table 8.36 presents the number of FBWs included in each study. The number of FBWs for power arbitrage is based on using the remainder of FBWs which have not been utilised for obtaining a specific percentage of power smoothing. The difference is calculated, with 1 FBW always being made available for the electrical services of berthing. Table 8.37 presents the available energy storage capacity which can be utilised for power arbitrage.

Table 8.36: The number of FBWs for Power Arbitrage based on Power Smoothing Availability.

Number of FBWs for Power Arbitrage					
Power Smoothing Availability	**61**	**Power Smoothing Availability**	**41**	**Power Smoothing Availability**	**21**
65%	34	55%	18	30%	6
80%	25	70%	12	40%	3
95%	0	85%	0	50%	0

Table 8.37: The Energy Storage Capacity for Power Arbitrage based on Power Smoothing Availability.

Energy Storage Capacity Available for Power Arbitrage (MWh)					
Power Smoothing Availability	**61**	**Power Smoothing Availability**	**41**	**Power Smoothing Availability**	**21**
65%	131	55%	69	30%	23
80%	96	70%	46	40%	12
95%	0	85%	0	50%	0

The parametric study involved considering different assumed FITs. It was assumed that the total energy storage capacity based on the amounts specified previously in Table 8.37 would be purchased by the various assumed FITs and sold at different mark-up prices. A trend could be drawn for each FIT and mark-up price, indicating where a profit or loss purely based on purchase and mark-up price was made while also including ESS inefficiencies. Figures 8.13 to 8.18 present the results obtained for the power arbitrage parametric analysis.

The common trend across all results is that it is more profitable to buy electricity at a cheaper FIT since even when the price difference between purchasing and selling is identical, the losses made when purchasing power at a high FIT are greater in comparison. The average financial value was considered when performing the techno-economic feasibility assessments in the upcoming case studies.

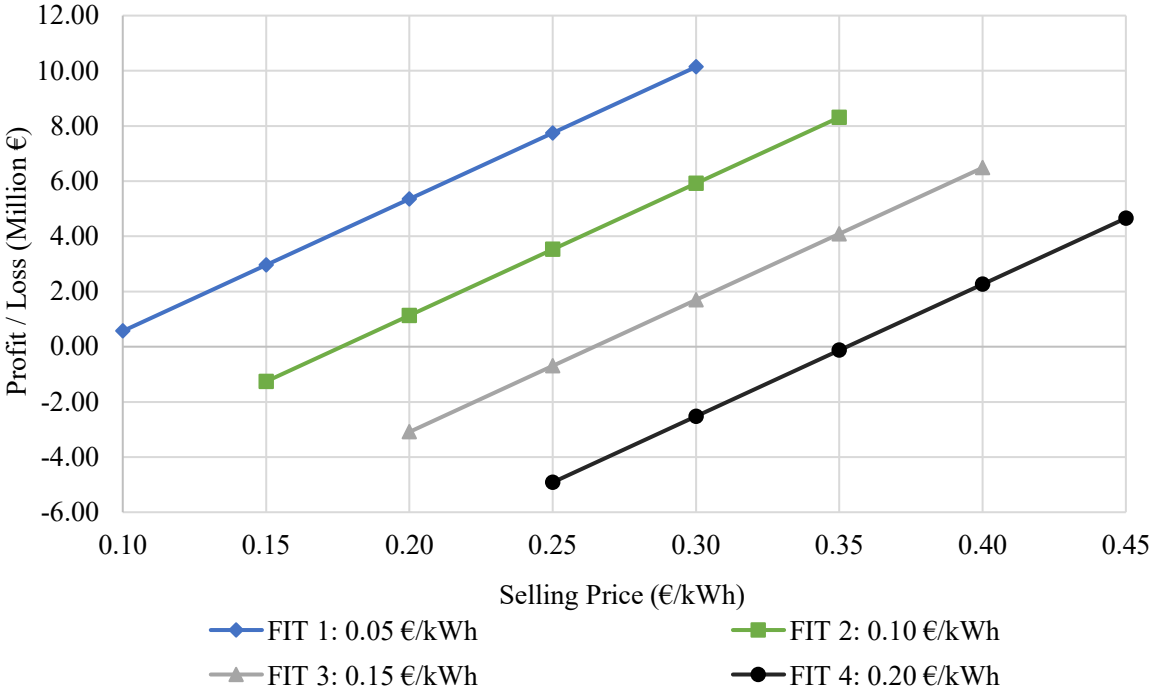

Figure 8.13: The profit and loss parametric analysis based on using 34 FBWs for Power Arbitrage.

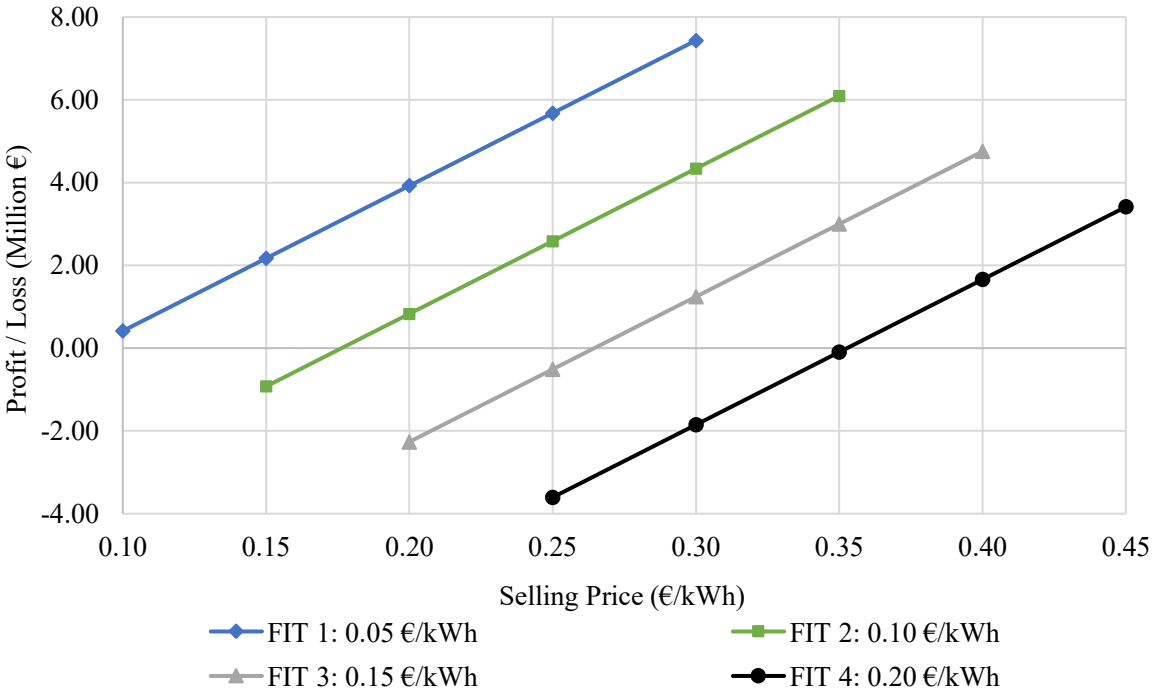

Figure 8.14: The profit and loss parametric analysis based on using 25 FBWs for Power Arbitrage.

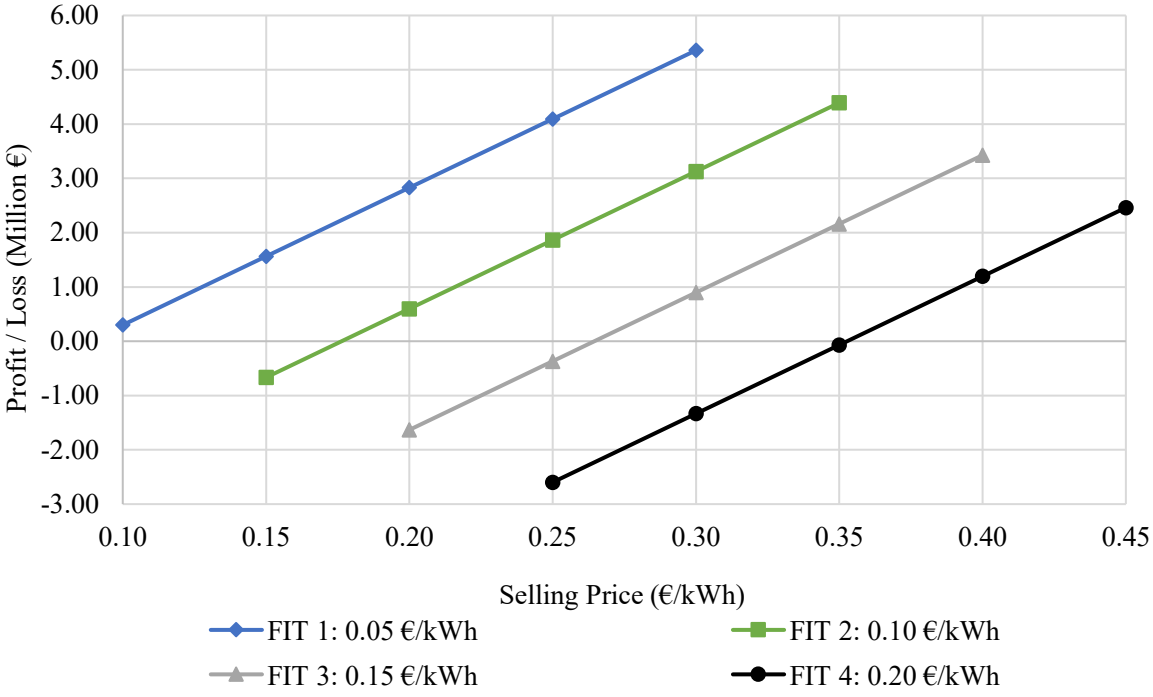

Figure 8.15: The profit and loss parametric analysis based on using 18 FBWs for Power Arbitrage.

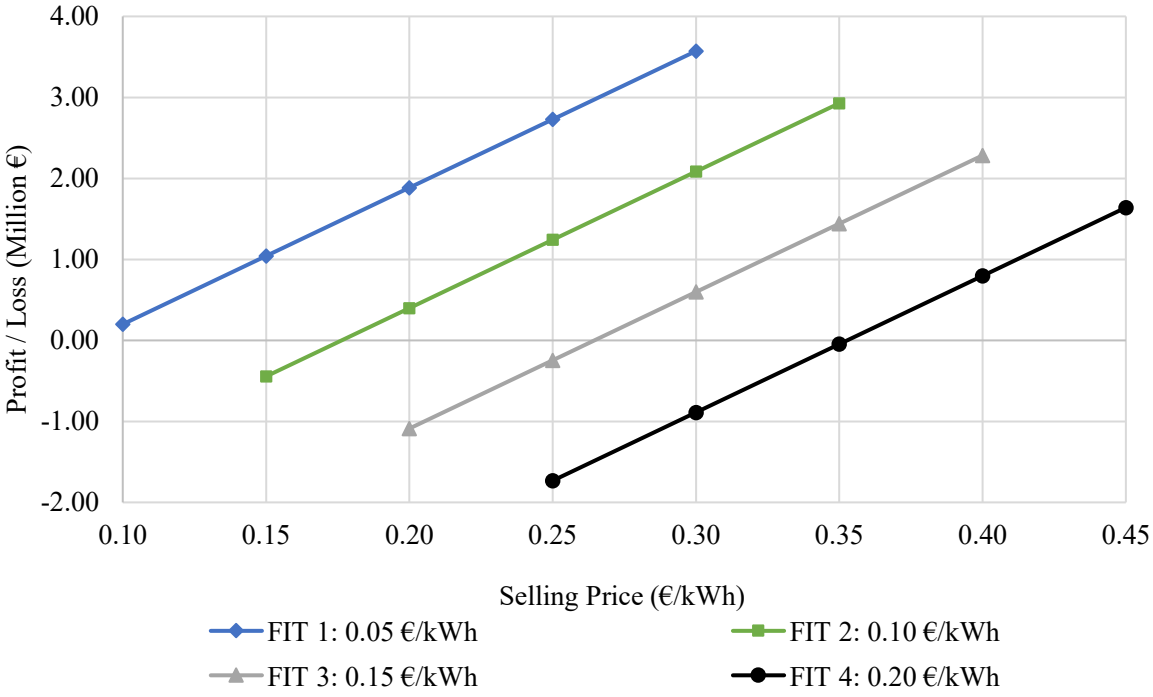

Figure 8.16: The profit and loss parametric analysis based on using 12 FBWs for Power Arbitrage.

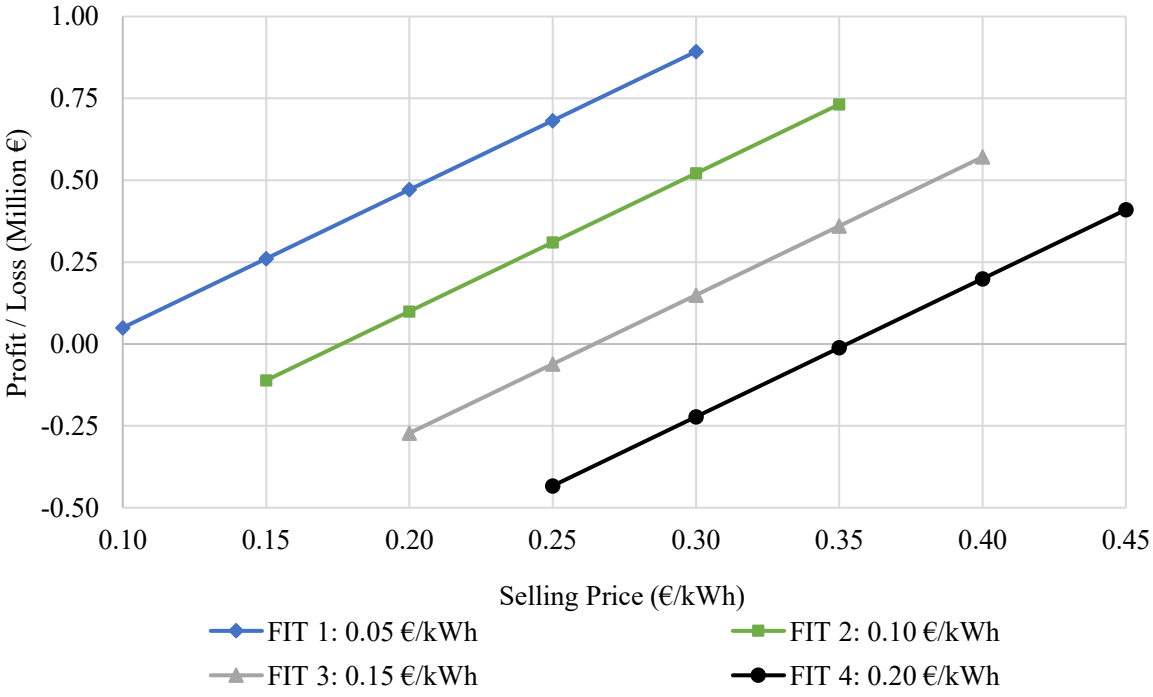

Figure 8.17: The profit and loss parametric analysis based on using 6 FBWs for Power Arbitrage.

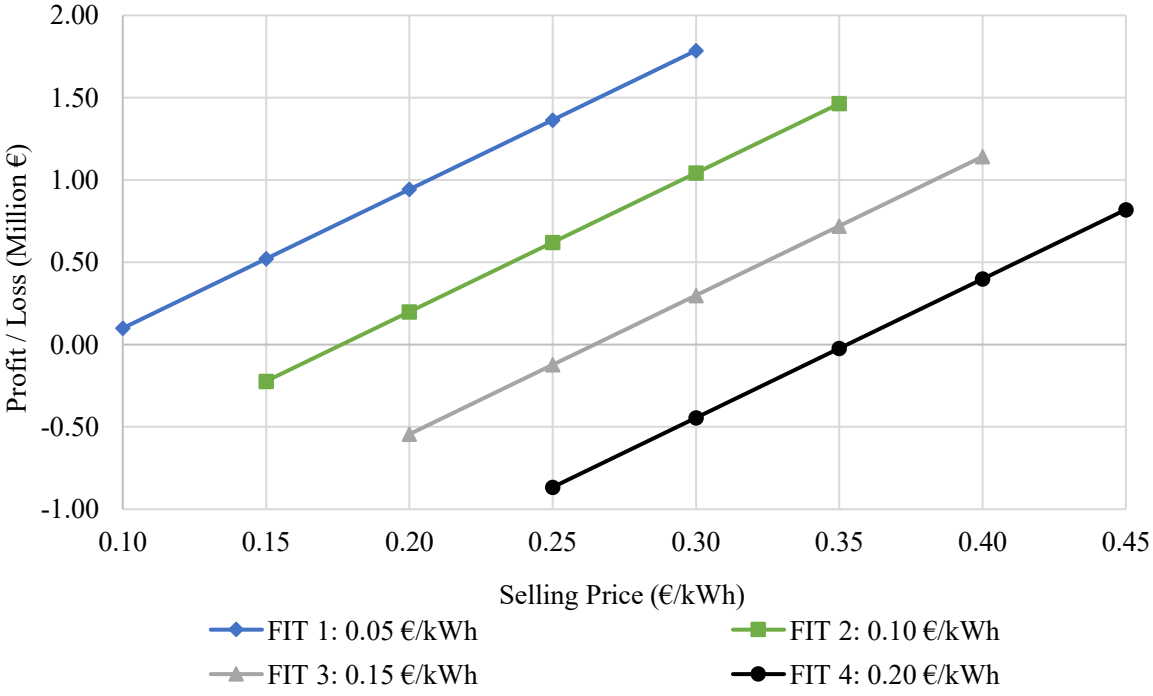

Figure 8.18: The profit and loss parametric analysis based on using 3 FBWs for Power Arbitrage.

Sales of Electricity to Seafaring Vessels berthed in the Multi-Use Marine Park

Due to the addition of energy storage within the FBWs, the area within the multi-use marine park allocated for berthing would also provide electricity to sea-faring vessels. As a result, in addition to the berthing revenue stream primarily explained in Section 8.2.4, there is the addition of selling electrical power to the boats and yachts which utilise berthing services. An electricity sale price of 0.27 €/kWh was assumed, taking into consideration the prices being charged by existing yacht marinas around the Maltese Islands [244]. When considering the daily electrical demands experienced at the Santa Barbara yacht marina in California (USA) [245], the daily average electrical requirement was quoted to be 1.72 MWh. Due to the mentioned yacht marina having just a 5% difference in occupied sea area compared to Project FORTRESS' berthing area, utilising 1 FBW (3.85 MWh) to support the electrical demands is sufficient. While 1 FBW offers 55% more than the average daily need quoted, the production influx of electric ships and the yacht size allowable at the berthing section of Project FORTRESS will increase the average electrical requirements per day. Table 8.38 presents the assumed revenue generated due to electrical services (rows 2 to 4). The difference between the conservative, medium and optimistic values is based on the percentage usage of boats which would utilise the electrical services, set at 20, 40 and 60% respectively. Table 8.38 also provides an overall update of the total revenue generated (rows 5 to 7) due to renting of berthing area (presented previously in Section 8.2.4) and electrical services combined.

Table 8.38: The updated financial results related to the Yacht Berthing financial analysis.

Main Financial Results	Value
Assumed Electrical Needs per Year (MWh)	1500
Revenue from Electrical Services (Conservative)	€ 303,750
Revenue from Electrical Services (Medium)	€ 405,000
Revenue from Electrical Services (Optimistic)	€ 506,250
Revenue to FORTRESS (Conservative)	€ 470,000
Revenue to FORTRESS (Medium)	€ 687,000
Revenue to FORTRESS (Optimistic)	€ 921,000

8.3.2 Case Studies B1, B2 and B3

Case Studies B1 to B3 (presented in Table 8.7 in Section 8.1.1) consider the co-location of a floating solar PV system (2 by 40 MWp) sheltered by a FBW array deployed in a sea depth of 200 metres, together with a FOWT pilot farm (30 MW). The surface area of the FBWs is also assumed to be covered by solar panels, providing an additional 27 MWp of power. The difference between the case studies is in the number of FBWs making up the FBW array, where Case Study B1 has 61 FBWs, Case Study B2 has 41 FBWs and Case Study B3 has 21 FBWs. Due to the addition of the ESS within the FBWs, the costings of the FBW are updated, and the inclusion of the Energy Conversion Unit (ECU) costs must also be added. Since the ECUs are being rated at 4.3 MW, each ECU accommodates the operation of multiple PCSs, and thus multiple FBWs. Table 8.39 provides an overview of the FBW costs.

When carrying out the techno-economic feasibility assessment for the different case studies (B1, B2 and B3), the sheltered area of 61 FBWs to accommodate all the revenue streams is not the same sheltered area offered by 41 FBWs and 21 FBWs. Therefore, it was assumed that while the 61 and 41 FBWs will accommodate all revenue streams, with the latter generating less revenue but also having less costs due to less FBWs, the 21 FBWs could not accommodate the aquaculture stream and the renting of the two 40 MWp solar PV farms revenue stream due to spatial restrictions.

Table 8.39: The main cost parameters of the FBW structure as a function of number of FBWs.

Parameter	Value		
Number of FBWs	61	41	21
Number of ECUs	7	5	3
Cost of ECU	€ 5,500,000		
FBW CAPEX	€ 31,623,152		
FBW OPEX	3% of FBW CAPEX		
FBW DECEX	3% of FBW CAPEX		
Total Cost (Billion €)	2.09	1.42	0.74

Table 8.40 presents the input parameters applied throughout the case study economic evaluations. The assumed inflation rate was also applied to the revenue streams, assuming that the revenue generated will also increase year on year for the same assumed sales. Meanwhile, Table 8.41 presents how the FBW array is split in terms of energy storage revenue stream generation. The FBW array was split based on maintaining as close to an even balance between power smoothing and power arbitrage as possible and based on ensuring that each revenue stream associated with energy storage made profit, thus referring to the results provided in Tables 8.33 to 8.35 and Figures 8.13 to 8.18 in Sub-section 8.3.1.

Table 8.42 presents the comparative results between the three case studies. At a sea depth of 200 metre, the results show that Project FORTRESS would not be an economically feasible project since the CAPEX, OPEX and DECEX costs of the investment made for the deployment of the FBWs outweigh the total revenue generated via the different revenue streams. The common trend observed is that when the number of FBWs in the array was decreased, although the revenue generated was also reduced, the loss in revenue generation was less than the reduction in costs due to having a lower number of FBWs. In order to obtain the conservative and optimistic loss values, the obtained financial value presented in Table 8.42 as 'medium' was multiplied by a factor of 1.25 (conservative) and 0.75 (optimistic) respectively.

Table 8.40: The LCOE, IRR and SPP Analysis Input parameters for Case Studies B1, B2 and B3.

Economic Analysis Inputs	Value	Reference
Interest Rate	7.50%	[214]
Inflation Rate	2.50%	[208]
Discount Rate	4.88%	-

Table 8.41: The setup of the FBW array for Case Studies B1, B2 and B3.

Number of FBWs			
Parameter	**B1**	**B2**	**B3**
Berthing Electrical Supply	1	1	0
Power Smoothing	26	22	15
Power Arbitrage	34	18	6

Table 8.42: The economic results for Case Studies B1, B2 and B3.

Economic Analysis Outputs	B1	B2	B3
LCOE (€c/kWh)	72.45	49.78	26.59
Profit/Loss (Billion €) – Conservative	- 2.42	- 1.63	- 0.90
Profit/Loss (Billion €) - Medium	- 1.94	- 1.30	- 0.72
Profit/Loss (Billion €) - Optimistic	- 1.45	- 0.98	- 0.54

Figures 8.19 to 8.21 present a breakdown of the portion each revenue stream takes up for 61 FBWs, 41 FBWs and 21 FBWs respectively. As the number of FBWs decreases, the revenue portion taken up by power smoothing increases, while the portion taken up by power arbitrage decreases. Additionally, the revenue generated via the berthing area rental increases, while the solar farm area rental revenue decreases as a percentage of total revenue generated. In the case of Case Study B3 (21 FBWs), two revenue streams are sacrificed due to the sheltered area decreasing in size. In fact, aquaculture is completely omitted and the two 40 MWp solar PV farms are assumed to be deployed as offshore PV systems susceptible to open seas rather than in sheltered waters.

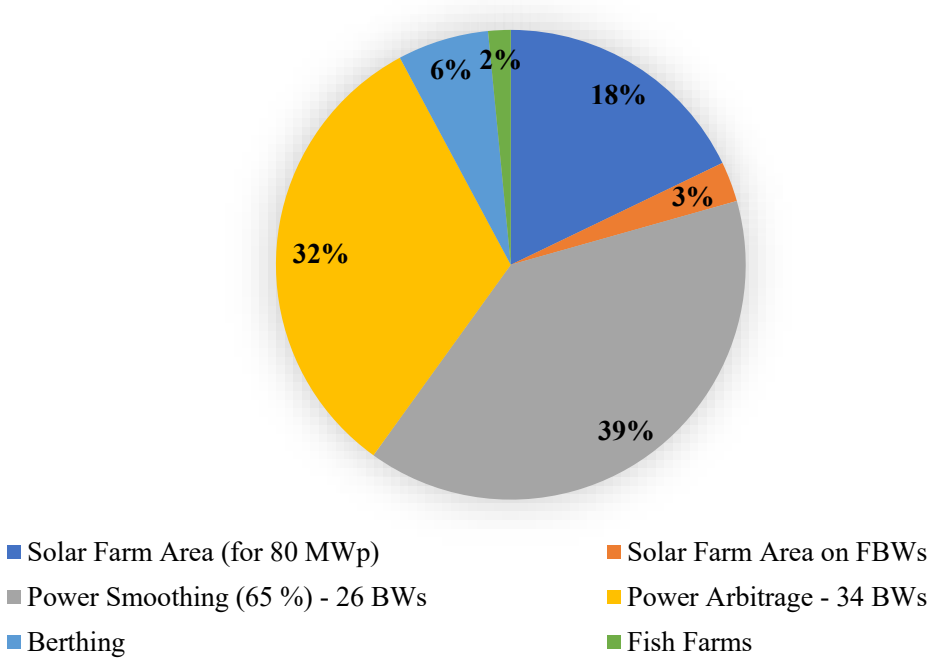

Figure 8.19: A pie chart showing the percentage contribution of each revenue stream to the overall revenues for Case Study B1.

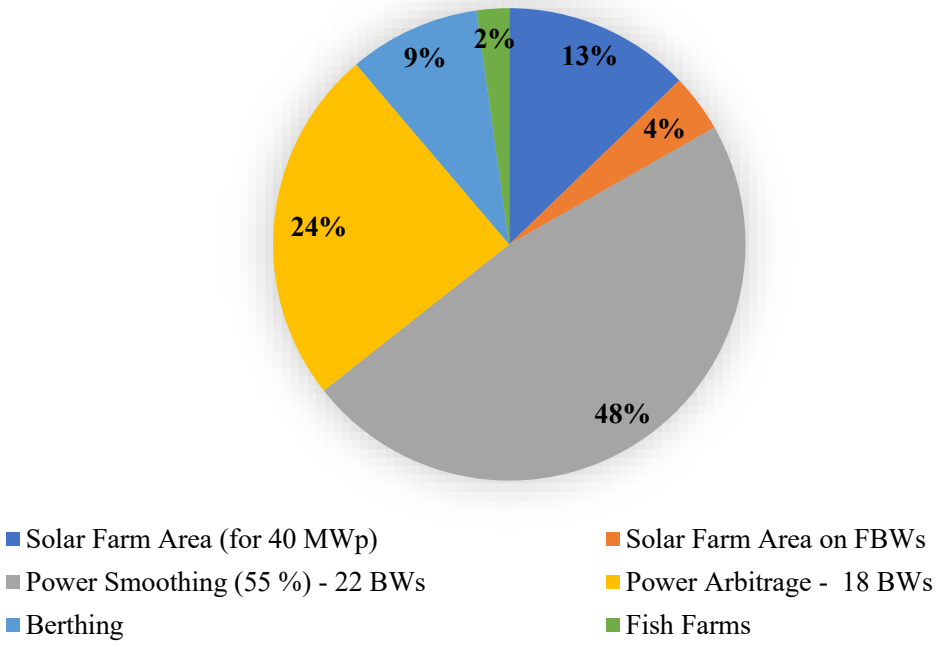

Figure 8.20: A pie chart showing the percentage contribution of each revenue stream to the overall revenues for Case Study B2.

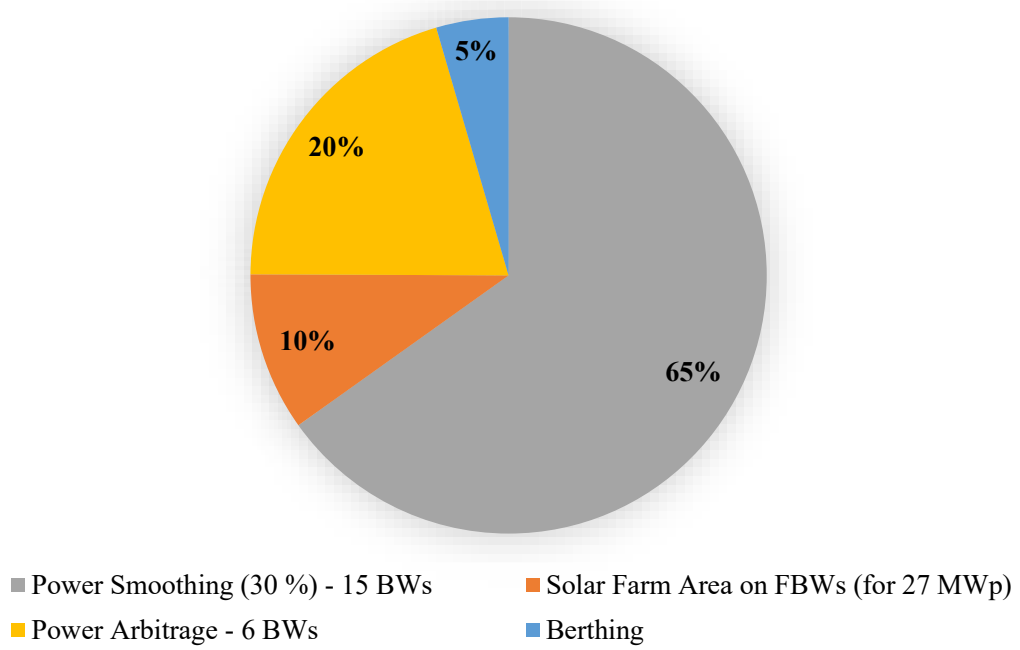

Figure 8.21: A pie chart showing the percentage contribution of each revenue stream to the overall revenues for Case Study B3.

The Influence of Sea Depth on the Techno-Economic Feasibility of the Marine Park

In order to understand the influence of sea depth on the financial results of Case Studies B1, B2 and B3, the study can be repeated with the sea depth in which the FBW arrays are deployed being changed to 50 metres. An important note to be made is that the sea depth of deployment does not have an effect on the HPES system. Since 58% of the FBW cost is related to the moorings alone [184], a shallower sea depth should result in significant savings in relation to the overall project. In order to simplify matters, the cost modelling of the individual RESs was maintained constant and was not re-analysed due to the change in sea depth. The FOWT Pilot Farm was assumed to remain at the same 200 metre sea depth, with only the FBWs, floating solar PV farm and other activities being relocated to a 50 metre depth. Table 8.43 presents an updated version of Table 8.39, indicating the new FBW CAPEX costs as a result of the shallower sea depth. Due to the shallower sea depth (from 200 to 50 metres), the FBW CAPEX cost decreases by 47%. Meanwhile, Table 8.44 presents the updated economic results for Case Studies B1, B2 and B3 deployed at a sea depth of 50 metres.

Table 8.43: The main cost parameters of the FBW structure at a sea depth of 50 metres.

Parameter	Value		
Number of FBWs	61	41	21
Number of ECUs	7	5	3
Cost of ECU	€ 5,500,000		
Cost of PCS	€ 2,647,197		
FBW CAPEX	€ 14,670,285		
FBW OPEX	3% of FBW CAPEX		
FBW DECEX	3% of FBW CAPEX		
Total Cost (Billion €)	1.22	0.82	0.52

Table 8.44: The economic results for Case Studies B1, B2 and B3 at a sea depth of 50 metres.

Economic Analysis Outputs	B1	B2	B3
LCOE (€c/kWh)	42.06	28.92	18.75
Profit/Loss (Billion €) - Conservative	- 1.20	- 0.80	- 0.59
Profit/Loss (Billion €) - Medium	- 0.96	- 0.64	- 0.47
Profit/Loss (Billion €) - Optimistic	- 0.72	- 0.48	- 0.35

8.4 Concluding Remarks

The main aim of this chapter was to carry out a techno-economic feasibility assessment to evaluate the viability of a multi-use marine park involving the use of FBWs with a built-in HPES system to support offshore wind and solar energy exploitation, as well as aquaculture and vessel berthing. The study was based on an offshore site in Maltese territorial waters that did not fall within environmentally protected areas. The assumed site has a sea depth of around 200 metres. The financial analysis compared the costs of floating solar PVs in open offshore and sheltered waters with those of onshore ground-based and rooftop systems. The study also considered the inclusion of FBWs to create the sheltered area in deep sea. It was found that:

- The investment costs required for FBWs in deep waters are significant. In fact, said costs are much larger than the expected cost savings gained by placing solar PVs in the resulting sheltered area instead of an open sea site offshore on a robust floating structure.

- The additional revenue streams from a FBW, including the addition of ESS and the renting of sheltered marine space for aquaculture and vessel berthing, are still considered to be insufficient to cover the investment costs of the FBWs. However, integration of the HPES system within the FBW structure allows for cost reductions when compared to having the HPES system or systems being deployed as stand-alone units. Additionally, the following points, however, merit further consideration:
    - It was observed that the high investment costs of FBWs are primarily due to the moorings in waters at an approximate sea depth of 200 metre (58.9% of the total FBW CAPEX), mainly due to the long catenary moorings needed to maintain the required stability. Installing FBWs closer to shore would result in a substantial reduction in CAPEX. This would offer opportunities for protecting sensitive coastal sites from wave-induced erosion.

- The presented feasibility study for the proposed FBWs was only based on direct revenue streams originating from the provision of energy storage services and on the rental of sheltered water spaces.

- There exist opportunities for reducing the costs of the FBWs through a more detailed engineering design that evaluates opportunities for reducing the mass of steel-reinforced concrete for each FBW.

Other positive socio-economic impacts of the study have not been assessed. For example, the deployment of FBWs would lead to increased luxury yacht arrivals, safer beaches for the tourism sector and increased business opportunities for the local maritime sector. These spill over benefits on the economy of island states such as Malta should not be underestimated and should provide enough justification for the long term co-investment by public bodies to render the FORTRESS hybrid floating breakwater concept viable. However, such a project can also lead to a number of negative socio-economic impacts. The main impacts can potentially include marine ecosystem disruption, visual impact due to visible FBW array and small WT farm, as well as concerns with respect to navigation and maritime safety.

9 CONCLUSION

This thesis looked into an offshore HPES system comprising of a subsea accumulator pre-charged with compressed air together with an ECU made up of megawatt-scale hydraulic machinery comprising a centrifugal pump and Pelton turbine. The main aim of the research was to investigate the behaviour of a megawatt-scale Energy Conversion Unit of the said offshore ESS. Throughout the process, three different numerical models all serving different purposes were created. Apart from developing three numerical models, additional analysis was carried out in the form of case studies to assess the ESS sizing requirements and the techno-feasibility of the offshore-based storage system. The motive of such case studies was to better-understand how to optimally size the said system and gauge its commercial feasibility in terms of revenue generation. The optimal sizing was obtained with the assumption that the primary aim of the HPES system is to smoothen the intermittent power supply of offshore floating wind and solar. The following section explains how the research questions derived in Chapter 1 have been tackled throughout this study. The points below summarise the key conclusions of this thesis:

- The Alpha model is a basic, faster version of the Beta model, which omits details such as piping, transients and secondary losses. While the Alpha model is suited towards longer simulations, the Beta model is suited towards short-term, more detailed simulations. Despite the model differences, the results obtained and presented in Section 5.3 proved the reliability of the simplified Alpha model compared to the Beta model by demonstrating that the RMSE results are all consistently exceptionally low across runs for charging and discharging simulations.

- A larger storage system provides better overall HPES system storage. Firstly, less RES power requires curtailment with a larger storage system. Additionally, pressurisation of the PCS is more gradual. As a result, a larger storage system will allow the pump to operate at this power for a longer period of time while maintaining higher efficiency.

- Increasing the size and power capability of a centrifugal pump does not mean that operating under the variable head constraints of HPES systems becomes easier. As explained previously in Section 6.3, the inherent performance characteristics of a centrifugal pump make it impossible to operate at a low power, high pressure combination.

- A 5% reduction in ESS availability for the case studies analysed had the potential of reducing ESS capacity requirements by up to 71%. This would directly lead to heavy cost reductions by deliberately curtailing any energy exceeding the capacity based on the 5% ESS availability reduction, in the scenario where the energy exceeding the capacity cannot be utilised, stored or sold elsewhere.

- The inclusion of more than one RES type indicates a greater need for storage. Additionally, when a mix of different RES is applied, there is less sensitivity to a varied SMA. This finding permits a smaller SMA and smaller ESS capacity to yield the kWh of ESS per kWh of RES generation compared to a larger SMA and ESS capacity.

- The feasibility study in Chapter 8 concluded that the initial costs of deploying a FBW array in deep waters are high. In fact, a fully offshore solar PV plant in open seas is overall cheaper compared to having a cheaper offshore solar PV array in sheltered waters due to the protection offered by the FBW array, due to the high FBW costs. Additionally, the inclusion of the HPES system and the additional revenue streams attained via the addition of the FBW array does not warrant sufficiency to cover the initial costs and commissioning of the FBW array.

9.1 Answers to Research Questions

In Section 1.4 of this thesis, a number of research questions were set out to be answered through this study. As explained previously in Section 1.4, the primary aim of this dissertation is to study a megawatt-scale ECU of an offshore HPES system. A number of objectives were set, with the aim of tackling the research questions. This section aims at explaining each research question through the work done.

Q1 What parameters will limit the pump and turbine speed variability during the charging and discharging processes respectively?

Through the literature review related to different pump types in Chapter 2 (Figures 2.11 and 2.12 in Section 2.3.4), it was made clear that out of the three main pumps assessed, centrifugal pumps have a stronger inter-dependent relationship between pressure and flow rate when compared to positive displacement pumps.

Despite this, the centrifugal pump was still the overall ideal choice due to its reliability and megawatt-scale availability when compared to its counterparts. When assessing the operation of the pump, the Beta Model exposed that, due to the wide pressure and power ranges which the pump experienced during simulations, different controller gains and a wide range of speeds were required during operation. However, speed variability was limited by the pumps' operational characteristic curves, where a combination of pressure, flow rate, power and rotational speed needed to be satisfied simultaneously (as shown via the relationships presented in equations 3.1 to 3.3 in Chapter 3). Speed variability was limited since it is physically difficult to maintain high efficiency over a wide range of speeds and pressures. As a result, desired power and the HPES systems' state of charge limit how slow or fast the pump's rotational speed may be.

With respect to discharging, while the Pelton turbine has proven to be exceptionally better at handling a wide range of pressures and flow rates, the turbine's speed variability is highly dependent on the turbine geometric design and configuration, as well as ensuring that the bucket to jet speed ratio is maintained within the optimal limits. Furthermore, correctly sizing the spear valve or valves associated with creating the jet which causes the Pelton wheel to rotate is imperative, since this spear valve is the main component which regulates pressure and flow rate to provide a power output based on the desired power requested.

Q2 What is the pump and turbine efficiency when operating with a variable speed and time-varying accumulator head while converting intermittent power into a smoothened output?

Based on the simulations performed and presented in Chapter 6, the pump efficiencies experienced are very sensitive to the specific ESS sizing or month in which the energy storage was tested for. Meanwhile, the turbine efficiency was maintained to a constant and consistent level due to the flexibility of the spear valve. The trend which was observed through Table 6.8 in Section 6.2.3 shows that the lower the standard deviation of the actual smoothened power output, the better is the overall system storage efficiency.

This finding implies that smaller power differentials incur less hydraulic machinery losses, thus resulting in a better overall efficiency. Another observation which influenced the pump efficiency when operating with a varying accumulator head is the size of the energy storage system (i.e., the size of the accumulator). If the accumulator is sized too small, several cycles across the full pressure range occur (as shown in Figure 6.10 in Section 6.2.3), thus causing a wide range of pump efficiencies to be experienced. Apart from this, more power is curtailed since the ESS ends up being fully charged or fully discharged too quickly and frequently during charging and discharging cycles respectively.

Q3 How can Time-series Forecasting be used in improving the time response of the ECU in smoothing the intermittent supply of power from RES?

As explained in Section 2.6 of the Literature Review in Chapter 2, research has repeatedly stated that time-series forecasting can allow ESSs to work in a more pro-active way, rather than simply reacting based on real-time data and responses. Throughout the study, a time-series forecasting SARIMA model was applied at 1 minute intervals to anticipate which hydraulic machinery will be required the following minute (centrifugal pump or Pelton turbine). Additionally, as highlighted previously by Wurth et al. [128] in Section 2.6, the 1 minute intervals applied were also selected intentionally for this study, since more sensitive timestamps for forecasting was considered a knowledge gap due to the scarcity of studies. Section 6.2.4 in Chapter 6 provided results which proved that due to forecasting the power requirements, the standard deviation of the power curve decreased by at least 34.80%, as shown by the difference in standard deviation between intermittent and forecasted powers in Table 6.8. A limitation of the Alpha Plus model is that the delayed response of a wind turbine's mass inertia would result in a slower rate of change in power, which would take longer than one minute to be detected. The effects of this inertia on a frequently updated forecasting model are yet to be determined.

Q4 To what extent are transient effects, such as the inertia of hydraulic machines and hydraulic lines important in modelling the unsteady operation of the ECU?

In order to assess specific situations or the ramping up or down of a system or hydraulic machinery, understanding the transient effects are important to understand how a real-life system would operate. However, when taking computational effects into consideration, the exclusion of transient effects where possible should be exploited.

As shown throughout Chapter 5, while the Alpha Model is simplified compared to the sophisticated Beta Model, the results are highly comparable, with the only difference in values or timing occurring due to the initial ramping up and transient effects implemented in the Beta Model. The maximum $RMSE_N$ was 13.9% and 6% across all analysed parameters for charging and discharging, respectively. These results also consider the initial transients and ramping up of the Beta Model versus the Alpha model starting from a quasi-steady state situation.

As a result, if the transient part were to be eliminated and the $RMSE_N$ was to be calculated again, the error in results between the Alpha and Beta models would be less than 1% for all parameters. In conclusion, transient effects are not important to model, as long as the analysis is performed for short durations to improve computational efficiency.

Q5 Can the conversion of intermittent power into a schedulable form of power be an economically profitable solution?

Chapter 7 presented a statistical analysis for the power output from two RES (wind and solar) integrating LDES through an offshore HPES system. The latter is used to smoothen the intermittent power output from the RES. The analysis provided insight about the power (MW) and energy capacity (MWh) of the ESS required to achieve different levels of power smoothing. The SMA throughout the studies was assumed to be the desired power or demand to be fed to the grid. As a result, the ESS sizing obtained would, in reality, vary based on other energy generation sources, grid support and seasonal storage assets. Additionally, the conversion of intermittent power into a schedulable form of power was assessed economically in Chapter 8. The main revenue stream applied in relation to the conversion of intermittent power into schedulable power was power smoothing, which utilised the HPES system within a floating breakwater array based on the West Coast of Malta for revenue generation. When considering the profit generated from power smoothing alone, the conversion of intermittent power into schedulable power was profitable based on the mark-up prices assumed for the service offered for smoothing the power. Despite its profitability as an individual revenue stream in the assumed scenario, this revenue stream and the other revenue streams listed and explained in Sub-Sections 8.2.4 and 8.3.1 did not generate enough revenue to overcome the capital and operational expenditure that the specific marine park analysed in Chapter 8 incurred.

9.2 Relevance to Industry

As explained throughout Chapter 1, the research within this thesis addresses real-world challenges, in this case, the energy transition. Due to RES intermittency, energy storage will be an essential tool in the coming decades to aid the business cases of offshore wind and solar farms, as well as to provide a stable output of power to the grid.

Additionally, the technical skills developed via the use of methodologies, tools and software (Python™ / MATLAB®) directly applies to industrial applications and uses. The application of such skills leads to an increase in the expertise in numerical simulations and data-driven modeling.

The research within this dissertation contributes to knowledge since it looks into a type of energy storage system (HPES) and simulates the operation of such a system at the megawatt scale. Such a step is required since it analyses system sizing, thus increasing energy storage capability and capacity. The study also provides insight on how such a system responds to transients and how such a system responds to the prediction of RES power.

While the research is novel, the study is also highly relatable due to the ease of collaboration with industry partners and the use of commercially available software tools. The research also aligns with industry trends since it focuses on aspects such as energy efficiency, sustainability and delves into finding strategies related to cost reductions. Lastly, the research also offers transferable skills such as project management, critical thinking and data interpretation; all skills which are of value in industrial research and development roles.

9.3 Limitations of the Study

A number of general limitations associated with the analyses of this study may be highlighted:

- Firstly, while experimental data of the analysed MW-scale HPES system are not available, a verification step performed within the Alpha and Beta models was that of setting the pump speed to one of the speeds from the pump curves, setting a fixed head and observing that the power, efficiency, and flow rate values outputted matched the points on the pump curves. Nonetheless, validation with experimental data would be beneficial and is, thus, a limitation of the present study.

- Secondly, isothermal conditions were assumed throughout this study. Understanding the influences of any potential thermal effects which deviate from isothermal conditions is beyond the scope of this study, however is a limitation of the work done.

- One of the limitations related to the OPEX and DECEX calculations is that the same value was assumed for PVs in calm and open waters. This is due to a lack of physical experiments both in academia and in industry. Therefore, this inaccuracy may skew results slightly, with the real difference between both systems remaining unclear, and potentially inaccurate.

- Finally, with respect to the techno-economic feasibility assessment, obtaining a quantifiable number for the spill-over benefits mentioned in Section 8.4 was also not part of the present study and is thus considered to be a limitation of this study. The spill-over benefits include more luxury yacht arrivals, safer beaches and new business opportunities for the local maritime sector.

9.4 Recommendations for Future Work

Both short and long duration energy storage systems are and will be imperative in ensuring a stable grid, especially with the increase in the installation of intermittent renewable energy sources. Due to the lack of experience and proven track records of a wide variety of new solutions, this study has contributed to research questions and knowledge gaps, however gaps and key issues continue arising within this industry.

A primary goal for further work should evaluate opportunities for improving the efficiency of the system, primarily by optimising ECU efficiency. For example, while this study considered a singular megawatt-scale centrifugal pump, future research must focus on the possibility of applying the same system but implementing a number of smaller pumps operating in series or in parallel to meet the variable power and head requirements demanded by the RES and PCS, respectively. Such a solution can potentially allow for a better balance of efficiency, while offering flexibility of amplifying pressure or flow rate attainment based on the way the pumps are connected. Additionally, contingency via multiple pumps can be a useful advantage Due to the lack of availability of MW-scale solutions on the market, ensuring that such a system is scalable in the future also requires implementing multiple pumps. Apart from this factor, the system remains widely scalable since the PCS can also be a long pipeline instead of a pressure

vessel. Another potential solution which requires further analysis is the evaluation of a positive-displacement pump instead of a centrifugal pump. Yet, a limitation with such pumps is their lack of market availability at MW-scale [246]. The Beta model is a physically comprehensive model, however still requires further development for it to be a complete digital twin of the system. Applying thermal effects to the system, as well as implementing a more detailed electrical power system would be beneficial to improve the results' accuracy, with a special focus on system start-up. A detailed electrical power system and an optimised control system would also be able to delve into the grid connectivity and system response. Additionally, a major challenge is its high computational cost, with further work being required to explore possibilities of improving the computational efficiency. One of the factors to make the Alpha Plus model more effective is the inclusion of weather forecast data to better predict future power requirements, both for wind and solar plants.

Another recommendation for future work is to explore more variations of the statistical analysis in Chapter 7. For example, calculating the impact that a change in ratio between the solar PV power and WT power, or keeping the WT power the same but using two IEA 15 MW turbines instead of three IEA 10 MW turbines. Such changes would impact ESS capacity requirements and the CAPEX and OPEX of the RES, which were an important part of the study in Chapter 8.

In relation to the techno-economic assessment, the future research should focus on the possibility of reducing the overall cost of the FBW design as well as the HPES system, with a specific focus on exploring optimal strategies for minimizing the cost benefits of HPES systems integrating the FBWs. It is imperative to study the environmental impacts resulting from such a multi-use offshore park during construction and operation, such as, for example, the impacts on avifauna and the marine habitats, and ensure appropriate mitigation measures are implemented. Quantification of the spill-over benefits mentioned in Section 8.4 can possibly lead to a much more favourable business case.

REFERENCES

[1] DNV, “Energy Transition Outlook 2022,” 2021.

[2] E. T. E. Centre, “Study on Energy Storage,” 2023.

[3] G. Chaudhary, J. J. Lamb, O. S. Burheim, and B. Austbø, “Review of energy storage and energy management system control strategies in microgrids,” *Energies*, vol. 14, no. 16, pp. 1–25, 2021.

[4] J. Twitchell, K. Desomber, and D. Bhatnagar, “Defining long duration energy storage,” *J. Energy Res.*, vol. 60, no. September 2022, p. 105787, 2023.

[5] R. Shan, J. Reagan, S. Castellanos, S. Kurtz, and N. Kittner, “Evaluating emerging long-duration energy storage technologies,” *Renew. Sustain. Energy Rev.*, vol. 159, no. February, p. 112240, 2022.

[6] M. Beuse, B. Steffen, and T. S. Schmidt, “Projecting the Competition between Energy-Storage Technologies in the Electricity Sector,” *Joule*, vol. 4, no. 10, pp. 2162–2184, 2020.

[7] O. Schmidt, S. Melchior, A. Hawkes, and I. Staffell, “Projecting the Future Levelized Cost of Electricity Storage Technologies,” *Joule*, vol. 3, no. 1, pp. 81–100, 2019.

[8] B. Cárdenas, L. Swinfen-Styles, J. Rouse, and S. D. Garvey, “Short-, medium-, and long-duration energy storage in a 100% renewable electricity grid: A UK case study,” *Energies*, vol. 14, p. 8524, 2021.

[9] M. Ruid, “Short- and Long-Duration Energy Storage Essential to the Clean Energy Transition,” 2022.

[10] C. Nichols, A. Holland, and C. Idrissov, “Long Duration Energy Storage Market 2024-2044: Technologies, Players, Forecasts.”

[11] Z. Wang, R. Carriveau, D. S.-K. Ting, W. Xiong, and Z. Wang, “A review of marine renewable energy storage,” *J. Energy Res.*, vol. 43, no. 12, pp. 1–43, 2019.

[12] Slocum et al., “Offshore energy harvesting storage and power generation system,” US8698338B2, 2014.

[13] Y. Arellano-Prieto, E. Chavez-Panduro, P. Salvo Rossi, and F. Finotti, “Energy Storage Solutions for Offshore Applications,” *Energies*, vol. 15, no. 17, 2022.

[14] Siemens, “Seeing behind the meter,” 2024.

[15] C. Vakili-Zad and J. Hoekstra, “High dwelling vacancy rate and high prices of housing in Malta a mediterranean phenomenon,” *J. Hous. Built Environ.*, vol. 26, no. 4, pp. 441–455, Nov. 2011.

[16] E. B. Barbier, “Climate change impacts on rural poverty in low-elevation coastal zones,” 2015.

[17] G. Arendal, “Coastal population and altered land cover in coastal zones (100 km off coastline).” [Online]. Available: https://www.grida.no/resources/5529. [Accessed: 12-Sep-2023].

[18] J. Petric, “Modeling of a Hydro-pneumatic Energy Storage System,” in *2013 8th EUROSIM Congress on Modelling and Simulation*, 2013, pp. 214–219.

[19] Segula Technologies, “Solution for undersea compressed air energy storage,” 2022. [Online]. Available: https://www.segulatechnologies.com/en/innovationproject/remora. [Accessed: 17-Sep-2023].

[20] E. Ortego, A. Dazin, G. Caignaert, and F. Colas, “Modeling of Hydro-Pneumatic Energy Storage Using Pump Turbines,” no. November, 2013.

[21] A. Odukomaiya, A. Abu-Heiba, S. Graham, and A. M. Momen, “Experimental and analytical evaluation of a hydro-pneumatic compressed-air Ground-Level Integrated Diverse Energy Storage (GLIDES) system,” *Appl. Energy*, vol. 221, no. November 2017, pp. 75–85, 2018.

[22] T. Sant, D. Buhagiar, R. N. Farrugia, D. Farrugia, and F. M. Strati, “Cost Evaluation of Two Concepts for the Integration of Hydro-pneumatic Energy Storage in Floating Wind Turbines,” *J. Phys. Conf. Ser.*, vol. 1037, no. 4, 2018.

[23] Q. Gao, A. Bechlenberg, B. Jayawardhana, N. Ertugrul, A. I. Vakis, and B. Ding, “Techno-economic assessment of offshore wind and hybrid wind–wave farms with energy storage systems,” *Renew. Sustain. Energy Rev.*, vol. 192, no. October 2022, p. 114263, 2024.

[24] J. Rönkkö, A. Khosravi, and S. Syri, “Techno-Economic Assessment of a Hybrid Offshore Wind–Wave Farm: Case Study in Norway,” *Energies*, vol. 16, no. 11, 2023.

[25] F. Hussain, M. Z. Rahman, A. N. Sivasengaran, and M. Hasanuzzaman, *Energy storage technologies*. Elsevier Inc., 2019.

[26] S. Koohi-Fayegh and M. A. Rosen, “A review of energy storage types, applications and recent developments,” *J. Energy Storage*, vol. 27, no. July 2019, p. 101047, 2020.

[27] M. R. Chakraborty, S. Dawn, P. K. Saha, J. B. Basu, and T. S. Ustun, “A Comparative Review on Energy Storage Systems and Their Application in Deregulated Systems,” *Batteries*, vol. 8, no. 9, 2022.

[28] P. K. Pathak and A. R. Gupta, “Battery Energy Storage System,” in *2018 4th International Conference on Computational Intelligence & Communication Technology (CICT)*, 2018, pp. 1–9.

[29] H. Zsiborács *et al.*, “Intermittent renewable energy sources: The role of energy storage in the european power system of 2040,” *Electron.*, vol. 8, no. 7, pp. 0–18, 2019.

[30] D. Q. Oliveira *et al.*, *A critical review of energy storage technologies for microgrids*. Springer Berlin Heidelberg, 2021.

[31] L. Xia, L. Yu, D. Hu, and G. Z. Chen, “Electrolytes for electrochemical energy storage,” *Mater. Chem. Front.*, vol. 1, no. 4, pp. 584–618, 2017.

[32] J. A. Jeevarajan, T. Joshi, M. Parhizi, T. Rauhala, and D. Juarez-Robles, “Battery Hazards for Large Energy Storage Systems,” *ACS Energy Lett.*, vol. 7, no. 8, pp. 2725–2733, 2022.

[33] P. Krivik and P. Baca, “Electrochemical energy storage,” in *Energy Storage*, 2013, pp. 80–99.

[34] M. Skyllas-Kazacos, M. H. Chakrabarti, S. A. Hajimolana, F. S. Mjalli, and M. Saleem, “Progress in Flow Battery Research and Development,” *J. Electrochem. Soc.*, vol. 158, no. 8, p. R55, 2011.

[35] P. Leung *et al.*, “Recent developments in organic redox flow batteries: A critical review,” *J. Power Sources*, vol. 360, pp. 243–283, 2017.

[36] A. Blakers, M. Stocks, B. Lu, and C. Cheng, “A review of pumped hydro energy storage,” *Prog. Energy*, vol. 3, no. 2, 2021.

[37] S. Rehman, L. M. Al-Hadhrami, and M. M. Alam, “Pumped hydro energy storage system: A technological review,” *Renew. Sustain. Energy Rev.*, vol. 44, pp. 586–598, 2015.

[38] A. Arabkoohsar and M. Sadi, “Flywheel energy storage,” in *Mechanical Energy*

Storage Technologies, 2020, pp. 101–124.

[39] S. Wicki and E. G. Hansen, “Clean energy storage technology in the making: An innovation systems perspective on flywheel energy storage,” *J. Clean. Prod.*, vol. 162, pp. 1118–1134, 2017.

[40] A. G. Olabi, T. Wilberforce, M. A. Abdelkareem, and M. Ramadan, “Critical review of flywheel energy storage system,” *Energies*, vol. 14, no. 8, pp. 1–33, 2021.

[41] J. Larminie and J. Lowry, “Electric Vehicle Technology Explained,” *Electr. Veh. Technol. Explain.*, Oct. 2003.

[42] B. Zakeri and S. Syri, “Electrical energy storage systems: A comparative life cycle cost analysis,” *Renew. Sustain. Energy Rev.*, vol. 42, pp. 569–596, 2015.

[43] M. Budt, D. Wolf, R. Span, and J. Yan, “A review on compressed air energy storage: Basic principles, past milestones and recent developments,” *Appl. Energy*, vol. 170, pp. 250–268, 2016.

[44] A. M. Rabi, J. Radulovic, and J. M. Buick, “Comprehensive Review of Compressed Air Energy Storage (CAES) Technologies,” *Thermo*, vol. 3, no. 1, pp. 104–126, 2023.

[45] M. Dooner and J. Wang, *Compressed-Air Energy Storage*. Elsevier Ltd, 2020.

[46] J. Wang *et al.*, “Overview of Compressed Air Energy Storage and Technology Development,” *Energies*, vol. 10, no. 7, 2017.

[47] E. Hossain, H. M. R. Faraque, S. H. Sunny, N. Mohammad, and N. Nawar, “A Comprehensive Review on Energy Storage Systems: Types, Comparison, Current Scenario, Applications, Barriers, and Potential Solutions, Policies, and Future Prospects,” *Energies*, vol. 13, no. 14, p. 3651, 2020.

[48] O. Fajinmi, J. L. Munda, Y. Hamam, and O. Popoola, “Compressed Air Energy Storage as a Battery Energy Storage System for Various Application Domains: A Review,” *Energies*, vol. 16, no. 18, p. 6653, 2023.

[49] A. S. Hazim, D. Buhagiar, and A. Gray, “Repurpose Offshore Pipeline as Energy Storage ROPES: Opening a New Market Segment Offshore,” in *Offshore Technology Conference*, 2022.

[50] D. Buhagiar and T. Sant, “Modelling of a novel hydro-pneumatic accumulator for large-scale offshore energy storage applications,” *J. Energy Storage*, vol. 14, pp. 283–

294, 2017.

[51] D. Buhagiar, T. Sant, R. N. Farrugia, L. Aquilina, D. Farrugia, and F. M. Strati, “Small-scale Experimental Testing of a Novel Marine Floating Platform with Integrated Hydro-pneumatic Energy Storage,” *J. Energy Storage*, vol. 24, p. 100774, Aug. 2019.

[52] A. Sharma, V. Sharma, J. P. Saini, and K. Prashad, “An overview on energy storage options for renewable energy systems,” *Int. J. Eng. Sci. Res. Technol.*, vol. 3, no. 8, pp. 776–788, 2014.

[53] N. Zagoras, K. Balasubramaniam, I. Karagiannidis, and E. B. Makram, “Battery Energy Storage Systems A Financial Evaluation in Microgrids,” *2015 North Am. Power Symp.*, 2015.

[54] DNV GL AS, “Offshore Standards DNVGL-OS-B101,” 2019.

[55] C. Wang, F. Wang, C. Li, W. Chen, H. Wang, and L. Lu, “Investigation on energy conversion instability of pump mode in hydro-pneumatic energy storage system,” *J. Energy Storage*, vol. 53, p. 105079, Sep. 2022.

[56] FLASC B.V., “Renewable energy storage - FLASC,” 2020. [Online]. Available: https://www.offshoreenergystorage.com. [Accessed: 17-Sep-2023].

[57] T. Sant, R. N. Farrugia, D. Farrugia, D. Buhagiar, and F. M. Strati, “Cost Analysis of Two Offshore Hydro-pneumatic Energy Storage Concepts,” 2018.

[58] I. Sarbu and C. Sebarchievici, “A Comprehensive Review of Thermal Energy Storage,” *Sustainability*, vol. 10, no. 1, 2018.

[59] S. N. Singh, P. Tiwari, and S. Tiwari, *Fundamentals and Innovations in Solar Energy*, vol. VIII. 2021.

[60] I. Dincer and M. A. Rosen, *Thermal Energy Storage Systems and Applications*, 2nd ed., vol. 6, no. August. Wiley, 2011.

[61] P. Breeze, “Hydrogen Energy Storage,” in *Power System Energy Storage Technologies*, 2018, pp. 69–77.

[62] W. F. Ekpotu, J. Akintola, M. C. Obialor, and U. Philemon, “Historical Review of Hydrogen Energy Storage Technology,” *World J. Eng. Technol.*, vol. 11, no. 03, pp. 454–475, 2023.

[63] D. Mahmoud Morsi Ali, “Hydrogen Energy Storage,” in *Energy Storage Devices*, 2019.

[64] O. Faye, J. Szpunar, and U. Eduok, “A critical review on the current technologies for the generation, storage, and transportation of hydrogen,” *Int. J. Hydrogen Energy*, vol. 47, no. 29, pp. 13771–13802, 2022.

[65] Y. Arellano-Prieto, E. Chavez-Panduro, P. S. Rossi, and F. Finotti, “Energy Storage Solutions for Offshore Applications,” *Energies*, vol. 15, p. 6153, 2022.

[66] D. A. Katsaprakakis, “Energy storage for offshore wind farms,” in *Offshore Wind Farms*, Elsevier Ltd, 2016, pp. 459–493.

[67] A. S. Hazim, D. Buhagiar, and A. Gray, “Repurpose Offshore Pipeline as Energy Storage ROPES: Opening a New Market Segment Offshore,” *Offshore Technology Conference*. p. D031S031R008, 02-May-2022.

[68] C. Maggi *et al.*, “A methodological approach to study the environmental impact of oil and gas offshore platforms,” *Rapp. Comm. int. Mer Medit.*, vol. 38, pp. 285–300, Jan. 2007.

[69] M. Child, C. Kemfert, D. Bogdanov, and C. Breyer, “Flexible electricity generation, grid exchange and storage for the transition to a 100% renewable energy system in Europe,” *Renew. Energy*, vol. 139, pp. 80–101, 2019.

[70] C. K. Nayak, M. R. Nayak, and R. Behera, “Simple moving average based capacity optimization for VRLA battery in PV power smoothing application using MCTLBO,” *J. Energy Storage*, vol. 17, pp. 20–28, Jun. 2018.

[71] J. Marcos, I. de La Parra, M. García, and L. Marroyo, “Control strategies to smooth short-term power fluctuations in large photovoltaic plants using battery storage systems,” *Energies*, vol. 7, no. 10, pp. 6593–6619, 2014.

[72] J. Torres, M. Blanco, M. Lafoz, G. Navarro, J. Nájera, and M. Santos-Herran, “Dimensioning methodology of energy storage systems for power smoothing in a wave energy conversion plant considering efficiency maps and filtering control techniques,” *Energies*, vol. 13, no. 13, Jul. 2020.

[73] M. Stewart, “Centrifugal pumps,” in *Surface Production Operations*, Gulf Professional Publishing, 2019, pp. 61–309.

[74] E. B. Maxime Binama, Alex Muhirwa, “Cavitation effects in centrifugal pumps - A review,” *Int. J. Eng. Res. Appl.*, vol. 6, no. 5, pp. 52–63, 2016.

[75] American Petroleum Institute, *Centrifugal Pumps for Petroleum, Petrochemical and Natural Gas Industries*. 2004.

[76] T. H. Lee, “Centrifugal Pumps,” in *Drilling Fluids Processing Handbook*, 1st ed., Gulf Professional Publishing, 2005, pp. 465–514.

[77] M. Gambini and M. Vellini, *Turbomachinery*. Springer Nature Switzerland AG, 2021.

[78] R. Bullert *et al.*, *Reciprocating positive displacement pumps*, 1st ed. LEWA GmbH, 1988.

[79] H. Anderson, *Losses in Centrifugal Pumps*, 4th ed. Elsevier Science, 1994.

[80] P. Girdhar, O. Moniz, and S. Mackay, “Centrifugal pump operation and characteristics,” in *Practical Centrifugal Pumps*, 2005, pp. 89–120.

[81] M. GÜNER and M. M. ÖZBAYER, *Centrifugal Pump Design Materials and Specifications*, no. March. 2020.

[82] J. F. Gulich, *Centrifugal Pumps*, 4th ed. Springer Nature Switzerland AG, 2020.

[83] American Petroleum Institute, *Positive Displacement Pumps - Reciprocating*, 2nd ed. 1995.

[84] E. S. Menon, “Pump Stations,” in *Pipeline Planning and Construction Field Manual*, Gulf Professional Publishing, 2011, pp. 223–258.

[85] G. T. P. Ltd, “Introduction to the purpose, use and care of centrifugal pumps,” 2020. [Online]. Available: https://lifetime-reliability.com/training/learn-engineering-in-an-hour/PGT006_Centrifugal_pumps_intro_training.pdf. [Accessed: 25-Oct-2023].

[86] N. R. Pumps, “Multistage pump guide,” 2020. [Online]. Available: https://www.northridgepumps.com/article-216_multistage-pump-guide. [Accessed: 25-Oct-2023].

[87] J. Pepper and M. Moore, “Consider Screw Pumps in Oil & Gas Applications,” 2017. [Online]. Available: https://www.pumpsandsystems.com/consider-screw-pumps-oil-gas-applications. [Accessed: 25-Oct-2023].

[88] L. K. Gudukeya and C. Mbohwa, “Improving the efficiencies of pelton wheel in

Micro-Hydro Power plants," in *Proceedings of the International Conference on Industrial Engineering and Operations Management*, 2017, vol. 2017, no. OCT, pp. 1089–1100.

[89] M. Hana, "Numerical analysis of non-stationary free surface flow in a Pelton bucket," 1999.

[90] Y. Beucher, E. B. Ksayer, and D. Clodic, "Characterization of Friction Loss in Pelton Turbine," in *Proc. of the 13th International Refrigeration and Air Conditioning Conference at Purdue*, 2010, pp. 1–8.

[91] Z. Zhang, *Pelton turbines*, 1st ed. Springer Cham, 2016.

[92] F. White, "Fluid Mechanics," 7th ed., McGraw-Hill, 2011, pp. 93–97.

[93] L. F. Barstad, "CFD Analysis of a Pelton Turbine," 2012.

[94] I.U. Atthanayake, "Analytical Study On Flow Through a Pelton Turbine Bucket Using Boundary Layer Theory," *Int. J. Eng. Technol.*, vol. 09, no. 09, pp. 11–15, 2009.

[95] D. Buhagiar and M. K. Bugeja, "Control Of An Open-Loop Hydraulic Offshore Wind Turbine Using A Variable-Area Orifice," in *ASME 2015 34th International Conference on Ocean, Offshore and Arctic Engineering*, 2015, pp. 1–10.

[96] A. H. Elbatran, M. W. Abdel-Hamed, O. B. Yaakob, Y. M. Ahmed, and M. Arif Ismail, "Hydro power and turbine systems reviews," *J. Teknol.*, vol. 74, no. 5, pp. 83–90, 2015.

[97] A. Abgottspon, T. Staubli, and D. Felix, "Erosion of Pelton buckets and changes in turbine efficiency measured in the HPP Fieschertal," in *IOP Conference Series: Earth and Environmental Science*, 2016, vol. 49, no. 12.

[98] J. Gomes Pereira, L. Andolfatto, and F. Avellan, "Monitoring a Francis turbine operating conditions," *Flow Meas. Instrum.*, vol. 63, no. August, pp. 37–46, 2018.

[99] T. Zhang, G. He, W. Guang, J. Lu, X. Song, and D. Zhu, "Investigation of the Internal Flow in a Francis Turbine for Comparing the Flow Noise of Different Operation Conditions," pp. 1–14, 2023.

[100] Y. A. Cengel and J. M. Cimbala, *Fluid Mechanics Fundamentals and Applications*. 2014.

[101] N. Khakurel, "Analysis on effects and limitations of cavitation in design and operation

of Francis turbine," 2016.

[102] W. Duncan Jr., "Turbine Repair," Denver, Colorado, 2000.

[103] F. Avellan, "Introduction to cavitation in hydraulic machinery," in *6th Int. Conf. on Hydraulic Machinery and Hydrodynamics*, 2004, no. February, pp. 11–22.

[104] C. G. Duan *et al.*, *Abrasive Erosion and Corrosion of Hydraulic Machinery*. Imperial College Press, 2002.

[105] J. Nicolle, J. F. Morissette, and A. M. Giroux, "Transient CFD simulation of a Francis turbine startup," in *IOP Conference Series: Earth and Environmental Science*, 2012, vol. 15, no. PART 6.

[106] W. Rahmann and F. Khan, "Modeling and Simulation of Kaplan Turbine," in *4Th Conference on Sustainability in Process Industry*, 2020, no. September, p. 7.

[107] A. H. P. T. Committee, *The Guide To Hydropower Mechanical Design*. HCI Publications, 1996.

[108] K. Hirtenlehner, "Real Efficiency of a Pelton Turbine in Back Pressure Operation," 2006.

[109] D. Zaniewski, P. Klimaszewski, Ł. Witanowski, Ł. Jędrzejewski, P. Klonowicz, and P. Lampart, "Comparison of an impulse and a reaction turbine stage for an ORC power plant," *Arch. Thermodyn.*, vol. 40, no. 3, pp. 137–157, 2019.

[110] B. Chhetry, "Assembly design of Francis turbine from maintenance perspective in context to sediment-laden river projects," no. March, 2017.

[111] J. Chauhan, "Difference Between The Impulse And Reaction Turbine," 2017. [Online]. Available: https://www.askpowerplant.com/difference-impulse-reaction-turbine/.

[112] S. Huang, Y. Wei, C. Guo, and W. Kang, "Numerical Simulation and Performance Prediction of Centrifugal Pump's Full Flow Field Based on OpenFOAM," *Process. 2019, Vol. 7, Page 605*, vol. 7, no. 9, p. 605, Sep. 2019.

[113] J. Zhao, J. Pei, J. Yuan, and W. Wang, "Structural optimization of multistage centrifugal pump via computational fluid dynamics and machine learning method," *J. Comput. Des. Eng.*, vol. 10, no. 3, pp. 1204–1218, Apr. 2023.

[114] P. E. Jenkins and A. Kuryachy, "Simulink/MATLAB Model for Assessing the Use of a Centrifugal Pump as a Hydraulic Turbine," *World J. Mech.*, vol. 08, no. 07, pp. 253–

271, 2018.

[115] M. H. Bhuyan, S. Hossain, and A. Islam, “Design of a Pelton Turbine using SOLIDWORKS for Ocean Wave Energy Design of a Pelton Turbine using SOLIDWORKS for Ocean Wave Energy Harvesting in MATLAB Simulink,” no. May, 2021.

[116] J. Decaix, M. Mettille, and C. Münch-Alligné, “Simulation of a Pelton turbine using the moving particle simulation method: application to two challenging situations,” *J. Hydraul. Res.*, Jul. 2024.

[117] E. Y. Setyawan, A. U. Krismanto, Mujiono, S. Djiwo, C. Saleh, and T. Hidayat, “Optimizing Pelton turbine performance: unveiling the power of three nozzles for maximum efficiency and sustainable hydropower generation,” *J. Meas. Eng.*, vol. 12, no. 3, pp. 469–484, Jul. 2024.

[118] J. L. Chukwuneke, C. H. Achebe, M. C. NWOSU, and J. E. Sinebe, “Analysis and Simulation on Effect of Head and Bucket Splitter Angle on the Power Output of a Pelton Turbine,” *Int. J. Eng. Appl. Sci.*, vol. 5, no. 03, pp. 1–8, 2014.

[119] F. Y. Edouard Duchesnay, Tommy Löfstedt, *Statistics and Machine Learning in Python (Release 0.3 beta)*. 2020.

[120] V. Sharma, A. Cortes, and U. Cali, “Use of Forecasting in Energy Storage Applications: A Review,” *IEEE Access*, vol. 9, pp. 114690–114704, 2021.

[121] M. Ghofrani and M. Alolayan, “Time Series and Renewable Energy Forecasting,” *Time Ser. Anal. Appl.*, 2018.

[122] H. R. Yatish and S. R. Swamy, “Recent Trends in Time Series Forecasting - a Survey,” *Int. Res. J. Eng. Technol.*, vol. 07, no. 04, pp. 5623–5628, 2020.

[123] P. J. Brockwell and R. A. Davis, *Introduction to Time Series and Forecasting*, vol. 45, no. 1. 2003.

[124] A. M., “Artificial Intelligence vs Machine Learning vs Data Science.” [Online]. Available: https://towardsdatascience.com/artificial-intelligence-vs-machine-learning-vs-data-science-2d5b57cb025b. [Accessed: 15-Aug-2024].

[125] S. G. Solanki, V. K. Ramachandaramurthy, N. Y. K. Shing, R. H. G. Tan, M. Tariq, and S. B. Thanikanti, “Power smoothing techniques to mitigate solar intermittency,”

Proc. - 2019 Int. Conf. Electr. Electron. Comput. Eng. UPCON 2019, pp. 1–6, 2019.

[126] X. Chen, K. C. Leung, and A. Y. S. Lam, "Power Output Smoothing for Renewable Energy System: Planning, Algorithms, and Analysis," *IEEE Syst. J.*, vol. 14, no. 1, pp. 1034–1045, 2020.

[127] P. H. A. Barra, W. C. de Carvalho, T. S. Menezes, R. A. S. Fernandes, and D. V. Coury, "A review on wind power smoothing using high-power energy storage systems," *Renew. Sustain. Energy Rev.*, vol. 137, no. April 2020, p. 110455, 2021.

[128] I. Würth *et al.*, "Minute-scale forecasting of wind power—results from the collaborative workshop of IEA Wind task 32 and 36," *Energies*, vol. 12, no. 4, 2019.

[129] J. Johnson *et al.*, "PV output smoothing using a battery and natural gas engine-generator," *Conf. Rec. IEEE Photovolt. Spec. Conf.*, no. February, pp. 1811–1816, 2013.

[130] M. J. E. Alam, K. M. Muttaqi, and D. Sutanto, "A novel approach for ramp-rate control of solar PV using energy storage to mitigate output fluctuations caused by cloud passing," in *IEEE Transactions on Energy Conversion*, 2014, vol. 29, no. 2, pp. 507–518.

[131] L. Dannecker, *Energy Time Series Forecasting: Efficient and Accurate Forecasting of Evolving Time Series from the Energy Domain*. 2015.

[132] C. Matthews, "Engineers' Guide to Rotating Equipment," *Eng. Guid. to Rotating Equip.*, 2001.

[133] KSB Centrifugal Pump Lexicon, "Efficiency scale-up." [Online]. Available: https://www.ksb.com/en-global/centrifugal-pump-lexicon/article/efficiency-scale-up-1116642. [Accessed: 31-Oct-2023].

[134] MathWorks, "Centrifugal Pump," 2007. [Online]. Available: https://www.mathworks.com/help/hydro/ref/centrifugalpump.html. [Accessed: 09-Nov-2023].

[135] T. Hansen, "Pump Filters / Strainers," 2023. [Online]. Available: https://www.dultmeier.com/technical-library/pump-filters-strainers.php. [Accessed: 13-Nov-2023].

[136] H. Sun, S. Bu, and Y. Luan, "A high-precision method for calculating the pressure drop

across wire mesh filters," *Chem. Eng. Sci.*, vol. 127, no. May, pp. 143–150, 2015.

[137] H. A. Shah, G. C. Chaudhari, and V. D. Dhima, "Parametric Optimization & Design of Pelton Turbine Wheel for Hydraulic Efficiency Improvement," in *Journal of Physics: Conference Series*, 2021, vol. 2007, no. 1.

[138] T. Zaw Oo, N. Nyi, and C. C. Khaing, "Design Calculation of Pelton Turbine for 220 kW," *Int. J. Sci. Res. Publ.*, vol. 9, no. 7, p. p9131, 2019.

[139] C. G. Rodriguez, D. Zambrano, S. Reyes, J. Tapia, M. Egusquiza, and E. Egusquiza, "Dynamic model for axial motion of horizontal pelton turbine and validation in actual failure case," *Shock Vib.*, vol. 2020, 2020.

[140] S. Petley and G. A. Aggidis, "Estimating the Energy Loss in Pelton Turbine Casings by Transient CFD and Experimental Analysis," *Int. J. Fluid Mach. Syst.*, vol. 12, no. 4, pp. 400–417, 2019.

[141] SKF, "SKF Bearing Select." [Online]. Available: https://www.skfbearingselect.com/#/bearing-selection-start. [Accessed: 01-Nov-2023].

[142] Z. Zhang, "Flow friction theorem of Pelton turbine hydraulics," *Proc. Inst. Mech. Eng. Part A J. Power Energy*, vol. 221, no. 8, pp. 1173–1180, 2007.

[143] MathWorks, "Needle Valve," 2020. [Online]. Available: https://www.mathworks.com/help/hydro/ref/needlevalve.html. [Accessed: 09-Nov-2023].

[144] F. F. Farshad, L. C. Choate, R. H. Winters, and J. D. Garber, "Pipeline Optimization - A Surface Roughness Approach," 2017, no. December, p. 24.

[145] MathWorks, "Hydraulic Resistive Tube," 2020. [Online]. Available: https://www.mathworks.com/help/simscape/ref/hydraulicresistivetube.html. [Accessed: 09-Nov-2023].

[146] MathWorks, "Gas-Charged Accumulator." [Online]. Available: https://www.mathworks.com/help/hydro/ref/gaschargedaccumulator.html. [Accessed: 10-Nov-2023].

[147] L. J. Briffa, C. Cutajar, T. Sant, and D. Buhagiar, "Numerical Modeling of the Thermal Behavior of Subsea Hydro-Pneumatic Energy Storage Accumulators Using Air and CO2," *Energies*, vol. 15, no. 22, pp. 1–19, 2022.

[148] C. Cutajar, T. Sant, R. N. Farrugia, and D. Buhagiar, “A Software Tool for the Design and Operational Analysis of Pressure Vessels used in Offshore Hydro-pneumatic Energy Storage,” *J. Energy Storage*, vol. 40, no. May, p. 102750, 2021.

[149] MathWorks, “Check Valve.” [Online]. Available: https://www.mathworks.com/help/hydro/ref/checkvalve.html. [Accessed: 15-Nov-2023].

[150] A. Borg, “Adaptive illumination control for improved underwater imaging,” University of Southampton, 2020.

[151] D. Corrigan, “Characterising the Response of a Closed Loop System,” 2012.

[152] I. Tools, “Open Loop and Closed Loop Animation,” 2023. [Online]. Available: https://instrumentationtools.com/open-loop-and-closed-loop-animation/. [Accessed: 16-Nov-2023].

[153] Omega Engineering, “Tuning a PID Controller,” 2023. [Online]. Available: https://www.omega.com/en-us/resources/tuning-a-pid-controller#:~:text=Manual tuning methods consist of,offset within an acceptable period. [Accessed: 16-Nov-2023].

[154] Red Lion, “Manual Tune Procedures - PID Controllers,” 2023. [Online]. Available: https://www.redlion.net/sites/default/files/1300/4432/PID. [Accessed: 16-Nov-2023].

[155] MathWorks, “Three-Phase Source.” [Online]. Available: https://www.mathworks.com/help/sps/powersys/ref/threephasesource.html. [Accessed: 15-Nov-2023].

[156] MathWorks, “DTC Induction Motor Drive.” .

[157] W. Li, G. Li, K. Ni, Y. Hu, and X. Li, “Sensorless control of late-stage offshore DFIG-WT with FSTP converters by using EKF to ride through hybrid faults,” *Energies*, vol. 10, no. 12, 2017.

[158] M. L. De Klerk and A. K. Saha, “Performance analysis of DTC-SVM in a complete traction motor control mechanism for a battery electric vehicle,” *Heliyon*, vol. 8, no. 4, p. e09265, 2022.

[159] E. Jääskeläinen and P. Pohjalainen, “DTC: A motor control technique for all seasons,” 2016.

[160] L. Seymour, P. J. Brockwell, and R. A. Davis, *Introduction to Time Series and Forecasting.*, vol. 92, no. 440. 1997.

[161] J. Durbin and S. J. Koopman, *Time Series Analysis by State Space Methods*, vol. 47, no. 3. 2005.

[162] S. Chantasiriwan, "Performance of variable-speed centrifugal pump in pump system with static head," *Int. J. Power Energy Syst.*, vol. 33, no. 1, pp. 15–21, 2013.

[163] D. J. Brasch and D. Whyman, "Pumping of liquids," in *Ludwig's Applied Process Design for Chemical and Petrochemical Plants*, G. P. Publishing, Ed. 2007, pp. 303–369.

[164] M. S. Ramsey, *Chapter Eight - Pumps*. 2019.

[165] Y. J. Fan, A. Le Mu, and T. Ma, "Modeling and control of a hybrid wind-tidal turbine with hydraulic accumulator," *Energy*, vol. 112, pp. 188–199, 2016.

[166] E. Sletfjerding, J. S. Gudmundsson, and K. Sjoen, "Friction factor in high-pressure gas pipelines in the North Sea," *SPE Proc. - Gas Technol. Symp.*, pp. 459–467, 2000.

[167] F. Farshad and J. Garber, "Relative roughness chart for internally coated pipes (OCTG)," *Proc. - SPE Annu. Tech. Conf. Exhib.*, vol. 1 (PI), no. October 1999, pp. 579–586, 1999.

[168] P. Bortolotti *et al.*, "IEA Wind TCP Task 37 Systems Engineering in Wind Energy-WP2.1 Reference Wind Turbines Technical Report," 2019.

[169] R. N. Farrugia and T. Sant, "A wind resource assessment at Aħrax point: A node for central Mediterranean offshore wind resource evaluation," *Wind Eng.*, vol. 40, no. 5, pp. 438–446, Oct. 2016.

[170] L. Svenningsen, "Power Curve Air Density Correction And Other Power Curve Options In WindPRO," 2010.

[171] J. G. Ziegler and N. B. Nichols, "Optimum settings for automatic controllers," *J. Dyn. Syst. Meas. Control. Trans. ASME*, vol. 115, no. 2B, pp. 220–222, 1993.

[172] K. Hirtenlehner, "The initial experience of the start-up and the first operation of Pelton Turbine in Back Pressure Operation," 2008.

[173] P. Bortolotti *et al.*, "IEA Wind TCP Task 37 Systems Engineering in Wind Energy-WP2.1 Reference Wind Turbines Technical Report," 2019.

[174] H. F. Burcharth *et al.*, *Innovative Engineering Solutions and Best Practices to Mitigate Coastal Risk*. 2014.

[175] A. C. Eloka-Eboka, S. Maroa, and A. E. Taiwo, *Biobutanol from agricultural and municipal solid wastes, techno-economic, and lifecycle analysis*, no. 2015. Elsevier Inc., 2023.

[176] DNV, "Energy Transition Outlook," 2022.

[177] P. Denholm and T. Mai, "Timescales of energy storage needed for reducing renewable energy curtailment," *Renew. Energy*, vol. 130, pp. 388–399, Jan. 2019.

[178] THE EUROPEAN COMMISSION, "Energy Storage-Underpinning a decarbonised and secure EU energy system," 2023.

[179] O. S. Ohunakin *et al.*, "Techno-economic assessment of offshore wind energy potential at selected sites in the Gulf of Guinea," *Energy Convers. Manag.*, vol. 288, no. January, 2023.

[180] I. Rahimi, M. R. Nikoo, and A. H. Gandomi, "Techno-economic analysis for using hybrid wind and solar energies in Australia," *Energy Strateg. Rev.*, vol. 47, no. February, 2023.

[181] R. E. Scroggins *et al.*, "Renewable energy in fisheries and aquaculture: Case studies from the United States," *J. Clean. Prod.*, vol. 376, no. September, p. 134153, 2022.

[182] T. LILAS, E. Antoniou, A. Kotrikla, A. Vatistas, and I. Dagkinis, "Improving aquaculture environmental footprint utilizing offshore renewable energy," *Proc. 16th Int. Conf. Environ. Sci. Technol.*, vol. 16, no. September, 2022.

[183] M. Bocci *et al.*, *Multi-use of the sea: A wide array of opportunities from site-specific cases across Europe*, vol. 14, no. 4. 2019.

[184] G. Dalton *et al.*, "Feasibility of investment in Blue Growth multiple-use of space and multi-use platform projects; results of a novel assessment approach and case studies," *Renew. Sustain. Energy Rev.*, vol. 107, no. December 2018, pp. 338–359, 2019.

[185] V. C. C. Srinivasan, P. Kumar Soori, and F. A. Ghaith, "Techno-Economic Feasibility of the Use of Floating Solar PV Systems in Oil Platforms," 2024.

[186] N. Elginoz and B. Bas, "Life Cycle Assessment of a multi-use offshore platform: Combining wind and wave energy production," *Ocean Eng.*, vol. 145, no. July, pp.

430–443, 2017.

[187] K. A. Abhinav *et al.*, “Offshore multi-purpose platforms for a Blue Growth: A technological, environmental and socio-economic review,” *Sci. Total Environ.*, vol. 734, p. 138256, 2020.

[188] L. Castro-Santos, D. Silva, A. R. Bento, N. Salvação, and C. Guedes Soares, “Economic feasibility of floating offshore wind farms in Portugal,” *Ocean Eng.*, vol. 207, 2020.

[189] H. Díaz and C. Guedes Soares, “Cost and financial evaluation model for the design of floating offshore wind farms,” *Ocean Eng.*, vol. 287, no. P2, p. 115841, 2023.

[190] T. Stehly, P. Beiter, and P. Duffy, “2019 Cost of Wind Energy Review,” no. December, p. 68, 2020.

[191] V. Ramasamy and R. Margolis, “Floating Photovoltaic System Cost Benchmark: Q1 2021 Installations on Artificial Water Bodies,” *Natl. Renew. Energy Lab.*, vol. 1, no. 10, pp. 1–15, 2021.

[192] I. Dincer and A. Abu-Rayash, *Sustainability modeling*. 2020.

[193] M. Kamran, “Microgrid and hybrid energy systems,” in *Fundamentals of Smart Grid Systems*, Academic Press, 2023, pp. 299–363.

[194] M. Aquilina, “Investigating the Impact of Wind Turbine Rotor Up-Scaling on the Viability of Floating Wind Farms,” University of Malta, 2014.

[195] Google, “Google Earth.” [Online]. Available: https://earth.google.com/web/. [Accessed: 15-Apr-2024].

[196] Government of Malta, “The proposal of economic activities within Malta’s Exclusive Economic Zone.” [Online]. Available: https://www.etenders.gov.mt/epps/pmc/listPmcContractDocuments.do?resourceId=8628319#. [Accessed: 15-Apr-2024].

[197] C. L. Archer *et al.*, “Review and evaluation of wake loss models for wind energy applications,” *Appl. Energy*, vol. 226, no. May 2018, pp. 1187–1207, 2018.

[198] N. Conroy, J. P. Deane, and B. P. O Gallachoir, “Wind turbine availability: Should it be time or energy based? - A case study in Ireland,” *Renew. Energy*, vol. 36, no. 11, pp. 2967–2971, 2011.

[199] E. Sesto and N. H. Lipman, “Wind energy in Europe,” 2023.

[200] M. S. Technologies, “SunPower Maxeon Solar Panels.” [Online]. Available: https://sunpower.maxeon.com/int/solar-panel-products/maxeon-solar-panels. [Accessed: 13-Feb-2024].

[201] P. Enevoldsen and M. Z. Jacobson, “Data investigation of installed and output power densities of onshore and offshore wind turbines worldwide,” *Energy Sustain. Dev.*, vol. 60, pp. 40–51, 2021.

[202] B. H. Bulder, E. T. G. Bot, and G. Bedon, “Optimal wind farm power density analysis for future offshore wind farms ECN cost model evaluation for large wind farms,” 2018.

[203] D. F. Silalahi and A. Blakers, “Global Atlas of Marine Floating Solar PV Potential,” *Solar*, vol. 3, no. 3, pp. 416–433, 2023.

[204] K. Trapani, D. L. Millar, and H. C. M. Smith, “Novel offshore application of photovoltaics in comparison to conventional marine renewable energy technologies,” *Renew. Energy*, vol. 50, no. August 2020, pp. 879–888, 2013.

[205] C. Cutajar, T. Sant, R. N. Farrugia, and D. Buhagiar, “Analysis of the Wave Attenuating and Dynamic Behaviour of a Floating Breakwater Integrating a Hydro-Pneumatic Energy Storage System,” *J. Mar. Sci. Eng. 2023, Vol. 11, Page 2189*, vol. 11, no. 11, p. 2189, Nov. 2023.

[206] A. BVG, “Guide to a Floating Offshore Wind Farm Published on behalf of the Offshore Renewable Energy Catapult, The Crown Estate and Crown Estate Scotland,” no. May, 2023.

[207] K. Nieradzinska, C. MacIver, S. Gill, G. A. Agnew, O. Anaya-Lara, and K. R. W. Bell, “Optioneering analysis for connecting Dogger Bank offshore wind farms to the GB electricity network,” *Renew. Energy*, vol. 91, no. March, pp. 120–129, 2016.

[208] J. Baptista, P. Vargas, and J. R. Ferreira, “A techno-economic analysis of floating photovoltaic systems, for southern european countries,” *Renew. Energy Power Qual. J.*, vol. 19, no. September, pp. 57–62, 2021.

[209] I. Staffell and R. Green, “How does wind farm performance decline with age?,” *Renew. Energy*, vol. 66, pp. 775–786, 2014.

[210] W. Zhao, Y. Han, and D. Niu, “Analysis of economic benefit of wind power based on

system dynamics," *AIP Conf. Proc.*, vol. 1955, 2018.

[211] A. Alsheghri, S. A. Sharief, S. Rabbani, and N. Z. Aitzhan, "Design and Cost Analysis of a Solar Photovoltaic Powered Reverse Osmosis Plant for Masdar Institute," *Energy Procedia*, vol. 75, pp. 319–324, 2015.

[212] Minister - Office of the Prime Minister and The Energy & Water Agency, "The National Renewable Energy Action Plan," 2017.

[213] D. C. Invernizzi, G. Locatelli, A. Velenturf, P. E. Love, P. Purnell, and N. J. Brookes, "Developing policies for the end-of-life of energy infrastructure: Coming to terms with the challenges of decommissioning," *Energy Policy*, vol. 144, no. May, 2020.

[214] M. Gomez Rebe, L. Mule' Stagno, and C. Yousif, "Optimising Photovoltaic Power Generation and Useable Area By Varying the Solar Module Tilt," 2013, pp. 4102–4108.

[215] D. Feldman, M. Bolinger, and P. Schwabe, "Current and Future Costs of Renewable Energy Project Finance Across Technologies," no. July, p. 53, 2020.

[216] Fraunhofer ISE, "Current and Future Cost of Photovoltaics," *Agora Energiewende*, no. February, p. 82, 2015.

[217] M. I. Islam *et al.*, "Techno-Economic and Carbon Emission Assessment of a Large-Scale Floating Solar PV System for Sustainable Energy Generation in Support of Malaysia's Renewable Energy Roadmap," *Energies*, vol. 16, no. 10, pp. 1–32, 2023.

[218] A. Ghigo, E. Faraggiana, M. Sirigu, G. Mattiazzo, and G. Bracco, "Design and Analysis of a Floating Photovoltaic System for Offshore Installation: The Case Study of Lampedusa," *Energies*, vol. 15, no. 23, 2022.

[219] M. F. I. Faruqui, A. Jawad, and N. Al Masood, "Techno-economic assessment of power generation potential from floating solar photovoltaic systems in Bangladesh," *Heliyon*, vol. 9, no. 6, 2023.

[220] propertymarket, "Land Plot for rent - Attard," 2023. [Online]. Available: https://www.propertymarket.com.mt/view/land-to-rent-attard-4122532301898864109/%0A. [Accessed: 17-Oct-2023].

[221] indomio, "Land Plot for rent - Marsa," 2023. [Online]. Available: https://www.indomio.com.mt/7643547?position=8%0A. [Accessed: 17-Oct-2023].

[222] indomio, “Land Plot for rent - Marsa,” 2023. [Online]. Available: https://www.indomio.com.mt/9086496?position=9. [Accessed: 17-Oct-2023].

[223] indomio, “Land Plot for rent - Attard,” 2023. [Online]. Available: https://www.indomio.com.mt/14656685?position=6%0A. [Accessed: 17-Oct-2023].

[224] idealista, “Land plots in Erice,” 2023. .

[225] idealista, “Land plots in Cinisi,” 2023. [Online]. Available: https://www.idealista.it/en/immobile/27367665/. [Accessed: 17-Oct-2023].

[226] idealista, “Land plots in Mascalucia,” 2023. .

[227] idealista, “Land plots in Monreale,” 2023. [Online]. Available: https://www.idealista.it/en/immobile/23098412/. [Accessed: 17-Oct-2023].

[228] idealista, “Land plot for rent in camino Cortijo Los Arias,” 2023. [Online]. Available: https://www.idealista.com/en/inmueble/95312351/. [Accessed: 17-Oct-2023].

[229] idealista, “Land plot for rent in camino de casabermeja,” 2023. [Online]. Available: https://www.idealista.com/en/inmueble/34786165/. [Accessed: 17-Oct-2023].

[230] idealista, “Land plot for rent in camino de las Carmelitas,” 2023. .

[231] idealista, “Land plot for rent in calle Campanillas,” 2023. [Online]. Available: https://www.idealista.com/en/inmueble/98617836/. [Accessed: 17-Oct-2023].

[232] idealista, “Land plot for rent in calle des Pou de na Maciana,” 2023. [Online]. Available: https://www.idealista.com/en/inmueble/87604704/%0A. [Accessed: 17-Oct-2023].

[233] Spiti24, “Other Land property for rent - Nea Alikarnassos, Karteros,” 2023. [Online]. Available: https://www.spiti24.gr/en/97282925?position=27. [Accessed: 17-Oct-2023].

[234] Spiti24, “Land Plot for rent - Souda, Center,” 2023. [Online]. Available: https://www.spiti24.gr/en/94221175?position=13. [Accessed: 17-Oct-2023].

[235] Spiti24, “Land Plot for rent - Heraclion Cretes, Giofirakia,” 2023. [Online]. Available: https://www.spiti24.gr/en/97412383?position=10#photo2%0A. [Accessed: 17-Oct-2023].

[236] Spiti24, “Land Plot for rent - Heraclion Cretes, Silamos,” 2023. [Online]. Available: https://www.spiti24.gr/en/99854320?position=7. [Accessed: 17-Oct-2023].

[237] Excelsior, “Yacht Marina,” 2024. [Online]. Available: https://excelsior.com.mt/leisure/yacht-marina. [Accessed: 29-Dec-2023].

[238] M. Di Valletta, “Berthing Tariffs,” 2019. [Online]. Available: https://marinadivalletta.com/wp-content/uploads/2019/04/Marina-Di-Valletta-Berthing-Tariffs-1.pdf. [Accessed: 29-Dec-2023].

[239] Maltese Parliament, “Development of Yachting Facilities in Malta,” 2009.

[240] U. B. Parameters, “Universal Berth Parameters,” pp. 1–13.

[241] C. Wang, “Moving offshore for fish farming,” *J. Aquac. Mar. Biol.*, vol. 8, no. 2, pp. 38–39, 2019.

[242] M. Holmer, “Sustainable development of marine aquaculture off-the-coast and offshore - a review of environmental and ecosystem issues and future needs in temperate zones,” *Expand. Maric. farther offshore Tech. Environ. Spat. Gov. challenges*, pp. 135–171, 2013.

[243] “Renewable Energy Storage - FLASC.” [Online]. Available: https://www.offshoreenergystorage.com/. [Accessed: 20-Oct-2018].

[244] M. Di Valletta, “Superyacht Berthing,” 2023. [Online]. Available: https://marinadivalletta.com/berthing/superyacht-berthing/. [Accessed: 17-Oct-2023].

[245] S. Riedman, “City of Santa Barbara Waterfront Department Memorandum,” 2019.

[246] A. Cassar, T. Sant, and A. Borg, “Modelling the hydraulic performance of an array of centrifugal pumps operating under a variable pressure in a hydro-pneumatic energy storage system,” *J. Phys. Conf. Ser.*, vol. 2929, no. 1, p. 012004, Dec. 2024.